

UNIVERSITAT DE VALÈNCIA

Departament de Física Atòmica, Molecular i Nuclear

INSTITUTO DE FÍSICA CORPUSCULAR

CSIC-UVEG

**Experimental Studies of Neutrino Nature:
from K2K to SuperNEMO**

TESIS DOCTORAL EN CIENCIAS FÍSICAS



Pau Novella i Garijo

València 2008

ABSTRACT

Experimental Studies of Neutrino Nature: from K2K to SuperNEMO

Pau Novella i Garijo

The experimental approaches to understand neutrino nature, namely oscillation and neutrino-less beta double decay experiments, are reviewed. As paradigmatic examples, K2K, HARP, NEMO and SuperNEMO experiments are described, along with their published or expected results. We report on the HARP π^+ production cross-section measurement in Aluminum, and its contribution to the K2K oscillation analysis. We also analyze the limitations of NEMO experiment in the search for the $\beta\beta^{0\nu}$ decay, with the goal of finding the best design for the SuperNEMO project; we present an exhaustive analysis of the physics case of SuperNEMO depending on several parameters, and study its particular potential operating at Canfranc Underground Laboratory.

Contents

<i>Preface</i>	ix
<i>Acknowledgments</i>	xi
1 Introduction	1
2 Massive neutrino physics	7
2.1 Introducing Massive neutrinos to the Standard Model	8
2.2 Neutrino oscillations in vacuum	14
2.3 Neutrinoless double beta decay	16
3 Experimental approaches to neutrino physics	25
3.1 Overview	25
3.2 Neutrino oscillations	26
3.2.1 Solar neutrinos	28
3.2.2 Atmospheric neutrinos	31
3.2.3 Reactor neutrinos	33
3.2.4 Accelerator neutrinos	35
3.3 Direct determination of m_ν	37
3.3.1 Kinematic constraints from Weak Decays	37
3.3.2 Cosmological bounds	39
3.3.3 Searching for the $\beta\beta0\nu$ decay	40
3.4 Summary of experimental results	49
3.5 Open issues in neutrino physics	53
4 Evidence of massive neutrinos: the K2K experiment	57
4.1 Overview	58

4.2	Neutrino beam	59
4.2.1	K2K neutrino beam	59
4.2.2	Summary of beam operation	62
4.2.3	K2K neutrino beam simulation	62
4.3	Neutrino detectors	63
4.3.1	Near neutrino detector system	65
4.3.2	Far detector: Super-Kamiokande	67
4.4	Oscillation analysis technique: the Far/Near flux ratio	67
4.4.1	Definition of the far-to-near flux ratio	68
4.4.2	Prediction of the far-to-near ratio	68
4.4.3	Impact of far-to-near ratio uncertainties	69
4.5	Understanding K2K neutrino flux: HARP experiment	71
4.5.1	Need for HARP experiment	71
4.5.2	Experimental apparatus	72
4.5.3	Tracking with the forward spectrometer	75
4.5.4	Particle identification	80
4.5.5	Calculation of the cross-section	84
4.5.6	Results	89
4.6	Neutrino flux predictions based on HARP results	100
4.6.1	Prediction of the flux central value	100
4.6.2	Systematic uncertainties of the flux predictions	104
4.6.3	Prediction of the far-to-near ratio from the HARP result .	123
4.6.4	Summary of flux predictions based on HARP	126
4.7	Measurements at near and far detectors	129
4.7.1	Measurement at the near detector system	129
4.7.2	Measurement at Super-Kamiokande	134
4.8	Neutrino Oscillation Analysis	137
4.8.1	Predictions at Super-Kamiokande	138
4.8.2	Likelihood definition	140
4.8.3	Results	141
4.9	K2K Summary	143
5	Nature of neutrino mass: SuperNEMO experiment	149
5.1	Overview	149
5.2	The NEMO experience	152
5.2.1	NEMO detector	153
5.2.2	NEMO (and SuperNEMO) backgrounds	154
5.2.3	Limitations of the NEMO-3 experiment	160
5.2.4	Results of the search for the $\beta\beta^{0\nu}$ decay	162

5.3	SuperNEMO project	165
5.3.1	SuperNemo goals	165
5.3.2	Detector standard design	166
5.3.3	Choice of isotopes	169
5.3.4	R&D and expected time scale	171
5.4	Simulation and data reconstruction	173
5.4.1	SuperNEMO simulation	173
5.4.2	Event reconstruction	175
5.5	Event selection	179
5.5.1	Event selection cuts	179
5.5.2	Overall detection efficiency	188
5.6	Computing SuperNEMO sensitivity	193
5.6.1	Sensitivity to a light Majorana neutrino	193
5.6.2	Nuclear matrix elements	194
5.6.3	Likelihood analysis	197
5.6.4	Computing the discovery potential	200
5.7	The physics case of SuperNEMO	203
5.7.1	Physics case of ^{82}Se	203
5.7.2	Dependence of the sensitivity with the exposure	205
5.7.3	Dependence of the sensitivity with the experimental setup	207
5.7.4	Internal backgrounds	213
5.7.5	Sensitivity for overall internal background	218
5.7.6	External backgrounds: ^{222}Rn	220
5.7.7	Physics case of ^{150}Nd	225
5.7.8	Possible improvements to the standard setup	233
5.8	Summary of SuperNEMO sensitivity results	235
6	Feasibility of the SuperNEMO physics case	239
6.1	Feasibility of SuperNEMO experimental targets	240
6.2	Canfranc Underground Laboratory and BiPo	246
6.3	Physics case at LSC	249
7	Summary and Conclusions	253
A	Resumen en castellano	261
A.1	Introducción	261
A.2	Modelo Estándar y neutrinos masivos	262
A.3	Situación actual de la física experimental de neutrinos	266
A.4	Evidencia de neutrinos massivos: K2K	268

A.4.1	Predicción de flujos en K2K: el experimento HARP	269
A.4.2	Ánálisis de oscilaciones	269
A.5	Naturaleza de la masa de los neutrinos: SuperNEMO	270
A.5.1	Simulación y reconstrucción de datos	273
A.5.2	Sensibilidad al proceso $\beta\beta^{0\nu}$	274
A.6	SuperNEMO en el Laboratorio Subterráneo de Canfranc	274
A.7	Recapitulación y conclusiones	280

Preface

In the last few years, several results from oscillation experiments have demonstrated that neutrinos are massive, providing a clear proof of physics beyond the Standard Model. Moreover, models from Grand Unified theories provide natural frameworks for neutrino masses and lepton number violation, and in particular the seesaw model explains the smallness of the neutrino mass by requiring the existence of Majorana neutrinos. As a direct consequence, there is a renewed interest in double beta decay experiments, since the observation of the neutrino-less mode of this decay would prove the Majorana nature of neutrino masses.

The Neutrino Physics group led by J.J. Gómez-Cadenas at IFIC has been not only an excited witness of this sort of revolution, but also a part of it. It was 5 years ago when we joined the K2K collaboration, with the main goal of providing neutrino flux predictions based on the HARP experiment. As we stand now, our oscillation physics project has been successful since K2K published two years ago a clear evidence of massive neutrinos, taking into account the HARP contribution. As further confirmation of oscillations in the atmospheric sector shown up since that time, we decided to move to the subsequent open issue: the nature of neutrino masses. Hence, we joined the NEMO and SuperNEMO collaborations with the aim of searching for the neutrino-less double beta decay. By now, the new Canfranc Underground Laboratory offers us an extraordinary chance to play a leading role in the search for $\beta\beta^{0\nu}$ process in the context of the European underground physics, and consequently among our current and next future plans there is the goal of defining the best experimental alternative for the Canfranc laboratory.

Being a PhD student since 5 years ago, I had the opportunity of working in all the above, and thus moving from oscillation experiments to $\beta\beta$ ones. This is the ultimate reason explaining the kind of work I am defending for my PhD. This thesis is meant to draw a general view of the past and present experimental approaches to understand the actual neutrino nature, mainly focusing on those experiments in which the Neutrino Physics group at IFIC has been involved in the last years.

*Pau Novella i Garijo
Valencia, February 2008*

Acknowledgments

It has been a long time since started my PhD,... or at least so it seems to me. And during this time I had the pleasure of working with several people around the world. Each one of the people I met provided a piece of this thesis, and thus I am indebted to all of them. Thank you!

All this is about a chance J.J. Gómez-Cadenas offered me some years ago. It is thanks to him that I am now defending my PhD; he has been my advisor, but also the person who made me believe that I could do it. I am quite sure everybody would love physics after listening to him for half an hour (that's enough, don't let him talk so much!) and this is one of the main reasons why he is (and will be) a really good advisor. Although doing a PhD only with J.J. as advisor would have been really nice, it turns out that it has been even better working also with Michel Sorel and Anselmo Cervera, who joined the group as post-docs some time after me. They have been always there to help me and show me the way, and indeed I consider them co-advisors of my work. I would also like to remark that new students will be even luckier than me, as the family has grown up recently with Markus Ball and Christian Hansen.

The current work has been possible thanks to people from three different collaborations: HARP, K2K and NEMO/SuperNEMO. Hence, I would like to thank the whole three collaborations. However, there is always somebody who works closer to you: this is the case of Dave Schmitz (from HARP), and Vladimir Vasiliev and Federico Nova (from NEMO/SuperNEMO). Without them, this thesis would not exist.

I really need to thank the help and friendship from all those students in the Neutrino Physics group of the IFIC: Jordi Burguet, Ana Tornero, Elena Couce, Joan Català, Javier Muñoz, Justo Martín Albo, Laura Monfregola and Francesc Monrabal (in order of appearance...). Moreover, even not working on the same issues, people around the IFIC also deserve my warm thanks, as all of them provided throughout these years a really nice place to work. I am very

grateful specially to those who rather than colleagues are indeed close friends: Neus López, Ana Ros and Laura Moliner, who by some kind of magic turned the IFIC into a strange beautiful place where one can meet friends every day.

Last but by no means least, I would also like to thank all those living outside this "Physicist's World", but who have been more or less involved just because they stood too close to me. I wish to extend my thanks (and apologies) to my friends and family. First of all, to my girlfriend, for her patience and encouragement (and for all those times I could not spend with her). Then, to the Campanar and Canyada crews, for the fresh air they brought me each weekend (and for all those beers I could not have with them). Finally, to my family, to those who still remain and specially to those who would have liked to read these lines, for the environment where I can always have a rest (and for all those evenings I could not stay longer). Their support is for sure one of the building blocks of this work.

Chapter 1

Introduction

It was Pauli who first suggested that neutrinos were emitted together with electrons in the nuclear beta decay to provide both energy and angular momentum conservation in the process. That was the first time that a theorist proposed the existence of a new (undetected) particle in order to guarantee the validity of a symmetry principle. Although this happened in 1930, the neutrino remained invisible for another twenty five years. Experimental confirmation of Pauli's hypothesis required a long time of experimental effort, but the discovery of the antineutrino finally took place in the fifties, thanks to the experiment by Reines and Cowan [1]. It is now more than 70 years that neutrinos have played a major role in the quest to understand elementary particles and their interactions, and indeed the relevant effort in trying to understand the nature of these particles and the information that they can provide has ultimately led to some Nobel Prizes: it was for Reines in 1995, and for Lederman, Schwartz and Steinberger in 1988; more recently, the 2002 Nobel prize was awarded to Davis and Koshiba for their seminal roles in the development of neutrino astrophysics.

From the theoretical point of view, the standard model of electroweak interactions was developed in the late 1960's, providing a framework in which neutrinos were incorporated as left-handed partners of the charged leptons, in turn organized in two generations along with the quarks. The subsequent discovery of the charmed quarks and the third generation of quarks and leptons completed the current scenario of the electroweak interactions within the standard model. Nevertheless, by that time neutrinos were introduced as mass-less Dirac fermions, for which no gauge invariant renormalizable mass term can be constructed. Consequently, in the Standard Model there is neither mixing nor

CP violation in the leptonic sector.

After the success of the Big-Bang nucleosynthesis (BBN) and the discovery of the cosmic microwave background, it became clear that neutrinos had also a major role in the history of the early universe: indeed, their own history dates back to a small fraction of a second after the Big Bang. As the evidence of the existence of dark matter in the universe increased, the hypothesis that neutrinos, although with a really small mass, may provide an explanation for the dark matter also arisen. This led to a massive assault on the issue of neutrino mass and its role in cosmology, and provided a large program of experiments addressing the issues of finite neutrino mass and the possibility of mixing between generations. Although it seems now that neutrinos are not likely the source of dark matter in the universe, the experimental evidence obtained in the last decade for finite neutrino masses and mixing is strong, since it comes from different types of neutrino sources. Neutrinos from both sun and atmosphere were first observed in the 1960's. Since that time, experiments measuring atmospheric neutrino fluxes have reported results pointing to the disappearance of muon neutrinos (ν_μ) when propagating over distances of hundreds of kilometers. Besides, experiments measuring solar neutrino fluxes found results that suggested the disappearance of electron neutrinos (ν_e) while propagating within the Sun or between the Sun and the Earth.

It was 1968 when Gribov and Pontecorvo [2, 3] pointed out that flavor oscillations arise if neutrinos are massive and mixed. The easiest explanation to the deficit in the atmospheric ν_μ and solar ν_e fluxes was that of neutrino oscillation, leading to at least two massive neutrinos unlike what it is predicted in the Standard Model. Since the Standard Model had introduced neutrinos as mass-less particles, the observation of neutrino oscillation became of uppermmost importance. As we stand now, the experimental evidence of neutrino masses and mixing is an unambiguous signal of new physics, that need to be fit beyond the Standard Model. Further theoretical works meant to extend the model finally led to Grand Unified Theories (GUTs) which provide a natural framework for nucleon decay and neutrino masses. These theories still need to be tested by a new round of experiments.

A new set of more precise neutrino oscillation experiments have shown up in the last decade, bringing to light the scenario of three massive neutrinos. Results from solar and atmospheric experiments have been confirmed using terrestrial neutrino beams, namely nuclear reactor and accelerator-based beams. Neutrinos coming from these sources have been detected at distances up to hundreds of kilometers, evidencing oscillation effects that can be fit within the scenario of

three flavor oscillations.

However, even the minimal picture of three massive neutrinos is still not complete. We do not have direct evidence of one of the three mixing angles and we are far from a precise determination of the other two. In addition, we don't know if there is CP violation in the leptonic sector. Furthermore, although it is true that oscillations have allowed us to prove that neutrinos are massive, they do not tell us anything about their absolute mass scale or about its *nature*. All the fermions in the Standard Model, with the exception of neutrinos, are Dirac particles with their antiparticles being the charge conjugates of the particles and with opposite quantum numbers. Neutrinos, however, have an extra possibility due to their neutral charge. Neutrinos may have a Majorana mass, which would imply that the neutrino and antineutrino are effectively the same particle and cannot be distinguished. The fundamental distinction of being Dirac or Majorana particles becomes only important for massive particles, becoming irrelevant in the mass-less limit. The possibility of Majorana neutrinos seems to be favored by the theoretical community and indeed it is a requirement in some GUTs such as SO(10) or strings.

The scale of neutrino mass differences and the possible CP violation motivates new experimental searches for double beta decay and end-point anomalies in beta decay, as well as new studies of oscillation phenomena using accelerators, nuclear reactors, and astrophysical sources of neutrinos. Meanwhile a better knowledge of the mixing parameters will be obtained with a new generation of high precision oscillation experiments, the absolute mass scale and the actual nature of neutrino mass (Dirac or Majorana) may be inferred from $\beta\beta$ experiments. The observation of the neutrino-less double beta decay ($\beta\beta^{0\nu}$) would imply that neutrinos are Majorana particles and would help to resolve the neutrino mass scale in combination with the oscillation data.

Double beta decay ($\beta\beta$) is a nuclear transition $(Z, A) \rightarrow (Z + 2, A)$ in which two neutrons bound in a nucleus are simultaneously transformed into two protons plus two electrons (and eventually other light neutral particles). This transition is possible and potentially observable because nuclei with even Z and N are more bound than the odd-odd nuclei with the same $A = N + Z$. So far, we have observed the $\beta\beta$ decay in many nuclei, but always through the mode in which two neutrinos are emitted: this is the $\beta\beta^{2\nu}$ decay. Meanwhile the $\beta\beta^{2\nu}$ process can be described within the Standard Model, the neutrino-less beta double decay $\beta\beta^{0\nu}$ cannot. No matter what mechanism is responsible for the $\beta\beta^{0\nu}$ decay, it is only possible if neutrinos are massive Majorana particles.

The detection of the $\beta\beta^{0\nu}$ process will give us two main valuable pieces of

informations: it will prove the Majorana nature of neutrinos and will provide a measurement of the so-called *neutrino effective mass* ($\langle m_\nu \rangle$), which is a linear combination of the neutrino masses, Majorana phases and oscillation parameters. In case no signal is observed, any $\beta\beta$ experiment can infer an upper value of $\langle m_\nu \rangle$. Of course, the goal of neutrino-less double beta decay experiments is to measure (or set a lower limit for) the half-life $T_{1/2}^{0\nu}$ of the process, but it turns out that $T_{1/2}^{0\nu}$ is a function of the neutrinos effective mass, along with the Nuclear Matrix Elements (NME). The value of $\langle m_\nu \rangle$ (or even an upper limit) adds an extra handle to constrain the absolute mass scale of neutrinos, so in combination with results from oscillation experiments and cosmological bounds it may ultimately lead to the resolution of the neutrino mass pattern. However, one has to notice that $\langle m_\nu \rangle$ depends on the NME's, which are computed theoretically within a big uncertainty and indeed different theoretical models can provide quite different values for the same NME.

Currently there are many experiments searching for neutrino-less double-beta decay in several selected nuclei, and some of them plan to scale up their experimental setup in order to achieve better sensitivities. Basically, all of them search for the distortion of the well known spectrum of the $\beta\beta^{2\nu}$ decay, since it could be understood in terms of the contribution of the 0ν mode. So far, there is no clear signal of the $\beta\beta^{0\nu}$ process, although a particular group of the Heidelberg-Moscow [4] experiment has claimed to observe this decay in ^{76}Ge : $\langle m_\nu \rangle = 200\text{-}600$ meV, depending on the NME considered. This result has been very controversial, being one of the goals of the next generation of $\beta\beta$ experiments to test it.

The current $\beta\beta$ experiments are sensitive to about 100-500 meV in terms of $\langle m_\nu \rangle$. The next generation is meant to reach sensitivities around 50 meV, but this is a tough job. It is worth noticing that the half-life of the $\beta\beta^{0\nu}$ decay, or equivalently the number of expected events, is suppressed quadratically with the effective Majorana neutrino mass $\langle m_\nu \rangle$, which is known to be very small. On the other hand, the normal $\beta\beta^{2\nu}$ mode stays constant (does not depend on $\langle m_\nu \rangle$) and it is an intrinsic background which can only be eliminated partially by means of a good energy resolution. Furthermore, any other kind of events with an energy release around $Q_{\beta\beta}$ is a potential background: due to the slow rate of the $\beta\beta^{0\nu}$ process (in case it exists), a few background events per year will be enough to hide the desired signal. Even if the backgrounds are kept under control, it could well be that $\langle m_\nu \rangle$ is far below the 50 meV range, and in this case the next generation of $\beta\beta$ experiments, projected for a time scale of few years, would fail detecting the $\beta\beta^{0\nu}$ decay. If this happens, next stage would

be to design detectors capable of reaching the sensitivities of a few meV, but this would require several tons of $\beta\beta$ source and completely new experimental techniques. However, we recall that even a negative result in the search of the $\beta\beta^{0\nu}$ process offers valuable information to resolve the neutrino mass pattern by combining the lower limits in $T_{1/2}^{0\nu}$ with results from other types of experiments.

The purpose of this work is to analyze, from an experimental point of view, two fundamental issues concerning the nature of neutrinos: the oscillation between different flavors and their mass. The work is focused on those experiments in which the Neutrino Physics group at IFIC, led by J.J. Gómez-Cadenas, has been involved for the last 5 years. Concerning neutrino oscillations, we describe the K2K experiment, which reported evidence of muon neutrino oscillation, and the input to the K2K analysis provided by the HARP experiment. Then, regarding the search for the neutrino mass nature, we focus on the NEMO and SuperNEMO experimental approach to the detection of the neutrino-less beta double decay. This work is organized as follows. Chapter 2 reviews the Standard Model and how massive neutrinos can be introduced in order to take into account the current data from neutrino oscillation experiments. Chapter 3 describes the various experimental approaches to neutrino physics, developed since the discovery of the anti-neutrino in 1956 by Cowan and Reines, paying special attention to oscillation and $\beta\beta^{0\nu}$ experiments. To show an evidence of non-vanishing neutrino masses, we describe in Chapter 4 the K2K experiment along with the HARP contribution: this can be treated as an illustrating example of how a full set of oscillation experiments have currently proved that neutrinos are massive particles. Then, we discuss in Chapter 5 the NEMO-3 results regarding the search for the $\beta\beta^{0\nu}$ process, and the physics case of its natural evolution: the SuperNEMO experiment. Since up to now SuperNEMO has been considered as one possibility for the new underground laboratory at Canfranc (Spain), the LSC, we analyze in Chapter 6 its case at this particular laboratory. Finally, Chapter 7 summarizes the whole work and draws the current scenario of the experimental neutrino physics and the efforts to keep on searching for the actual neutrino nature.

Chapter 2

Massive neutrino physics

In the Standard Model (SM), neutrinos were introduced as mass-less particles. However, it is more natural to expect them to be massive, since there is no symmetry principle or gauge invariance requiring neutrinos to have vanishing masses. Moreover, we know that all other fermions, quarks and charged leptons are massive. Oscillation experiments have proven in the last years that neutrinos have indeed a mass, and consequently it is a must to extend the SM to take this fact into account. It turns out that neutrinos are very light with respect to the other fermions, and this striking qualitative feature needs to be understood. Furthermore, the issue of the actual nature of neutrino mass also arises when extending the SM. Whereas the charged leptons are Dirac particles, distinct from their antiparticles, neutrinos may be the ultimate neutral fermions, as envisioned by Majorana, identical to their antiparticles. The see-saw mechanism is the most simple scenario explaining why neutrinos are so light, and it predicts Majorana neutrinos.

Along this chapter, we review the possible ways in which the SM can be modified or extended in order to accommodate massive neutrinos, leading to leptonic mixing and neutrino oscillation. We also discuss about the so-called Dirac or Majorana nature of the neutrinos, focusing in the neutrino-less beta double decay since this process may give us an answer to this issue. The phenomenology of massive neutrinos has been described in several works, although in the current document we mainly follow Ref. [5, 6].

2.1 Introducing Massive neutrinos to the Standard Model

The major success of the Standard Model is the connection between forces mediated by spin-1 particles and local (gauge) symmetries. The strong, weak and electromagnetic interactions are connected to $SU(3)$, $SU(2)$ and $U(1)$ gauge groups, respectively, being the characteristics of the different interactions explained by the symmetry which they are related to. Thus, the SM is based on the gauge group:

$$G_{\text{SM}} = SU(3)_C \times SU(2)_L \times U(1)_Y, \quad (2.1)$$

where $SU(3)$ belongs to the color group of quantum chromodynamics; $SU(2)$ to the weak isospin; and $U(1)$ to the hypercharge. That is, the strong, weak and electromagnetic interactions.

In the standard model individual lepton charges ($L_e = 1$ for e^- and ν_e and $L_e = -1$ for e^+ , and $\bar{\nu}_e$ and analogously for L_μ and L_τ) are conserved. Thus, processes such as $\mu^+ \rightarrow e^+ + \gamma$, or $K_L \rightarrow e^\pm + \mu^\mp$ are forbidden. Indeed, there is no experimental evidence of such processes. Based on these empirical facts, the standard model places the left-handed components of the charged lepton and neutrino fields into the doublets of the group $SU(2)_L$,

$$L_L = \begin{pmatrix} \nu_\ell \\ \ell_L \end{pmatrix}_L, \quad \ell = e, \mu, \tau, \quad (2.2)$$

while the right-handed components of the charged lepton fields are singlets. The right-handed components of the neutrino fields are *absent* in the standard electroweak model by definition.

Thus, the matter content of the SM remains as shown in Table 2.1. As can be seen, there are three matter fermion generations. Each one consists of five different representations of the SM gauge group. The elementary particles are arranged as doublets for chiral left-handed fields and singlets for right-handed fields except for neutrinos (ν_ℓ). These are fermions that have neither strong nor electromagnetic interactions, i.e., they are singlets of $SU(3)_C \times U(1)_Y$. These three neutrinos that have weak interactions are known as *active*.

In order to provide masses to fermions in the SM, the model also contains a single Higgs boson doublet, ϕ with charges $(1, 2, 1/2)$, whose vacuum expectation value breaks the gauge symmetry,

$$\langle \phi \rangle = \begin{pmatrix} 0 \\ \frac{v}{\sqrt{2}} \end{pmatrix} \implies G_{\text{SM}} \rightarrow SU(3)_C \times U(1)_{\text{EM}}. \quad (2.3)$$

$L_L(1, 2, -\frac{1}{2})$	$Q_L(3, 2, \frac{1}{6})$	$E_R(1, 1, -1)$	$U_R(3, 1, \frac{2}{3})$	$D_R(3, 1, -\frac{1}{3})$
$\begin{pmatrix} \nu_e \\ e \\ \nu_\mu \\ \mu \\ \nu_\tau \\ \tau \end{pmatrix}_L$	$\begin{pmatrix} u \\ d \\ c \\ s \\ t \\ b \end{pmatrix}_L$	e_R	u_R	d_R
		μ_R	c_R	s_R
		τ_R	t_R	b_R

Table 2.1: Matter contents of the Standard Model. Numbers in parenthesis represent the corresponding charges under the group 2.1.

This is the only piece of the SM which still misses experimental confirmation. In the SM, fermion masses arise from the Yukawa interactions which couple a right-handed fermion with its left-handed doublet and the Higgs field,

$$-\mathcal{L}_{\text{Yukawa}} = Y_{ij}^d \bar{Q}_{Li} \phi D_{Rj} + Y_{ij}^u \bar{Q}_{Li} \tilde{\phi} U_{Rj} + Y_{ij}^\ell \bar{L}_{Li} \phi E_{Rj} + \text{h.c.} \quad (2.4)$$

(where $\tilde{\phi} = i\tau_2 \phi^*$) which after spontaneous symmetry breaking (Higgs mechanism) lead to charged fermion masses

$$m_{ij}^f = Y_{ij}^f \frac{v}{\sqrt{2}}. \quad (2.5)$$

However, since no right-handed neutrinos exist in the model, the Yukawa interactions leave the neutrinos massless. Furthermore, neutrino masses cannot arise either from loop corrections, according to the following considerations. The SM gauge symmetries and particle content induce an accidental global symmetry (*i.e.*, it is not imposed):

$$G_{\text{SM}}^{\text{global}} = U(1)_B \times U(1)_{L_e} \times U(1)_{L_\mu} \times U(1)_{L_\tau}. \quad (2.6)$$

$U(1)_B$ is the baryon number symmetry and $U(1)_{L_e, L_\mu, L_\tau}$ are the three lepton flavor symmetries, with total lepton number given by $L = L_e + L_\mu + L_\tau$. Loop corrections cannot provide neutrino masses because the only possible neutrino mass term that can be constructed with the SM fields is the bilinear $\bar{L}_L L_L^C$ which violates the total lepton symmetry by two units. Being the total lepton number a global symmetry of the model, L -violating terms cannot be induced by loop corrections.

Regarding interactions between neutrinos and their corresponding charged leptons, we have in the SM charged current (CC) and neutral currents (NC):

$$-\mathcal{L}_{\text{CC}} = \frac{g}{\sqrt{2}} \sum_{\ell} \bar{\nu}_{L\ell} \gamma^{\mu} \ell_L^- W_{\mu}^+ + \text{h.c.} \quad (2.7)$$

$$-\mathcal{L}_{\text{NC}} = \frac{g}{2 \cos \theta_W} \sum_{\ell} \bar{\nu}_{L\ell} \gamma^{\mu} \nu_{L\ell} Z_{\mu}^0. \quad (2.8)$$

It is important to notice here that studies of e^+e^- annihilation at the Z -resonance peak have determined the invisible width of the Z boson, caused by its decay into unobservable channels. One can interpret this width as a measurement of the number of neutrino active flavors: $N_{\nu} = 2.984 \pm 0.008$ is obtained from the four LEP experiments [7]. Therefore, it can be concluded that there are just three active neutrinos with masses of less than $M_Z/2$. Besides these three active neutrino flavors there could be other neutrinos which do not participate in weak interactions. Such neutrinos are called *sterile*. This kind of neutrinos is defined as having no SM gauge interactions (singlets of the full SM gauge group). Notice that as defined, the SM contains no sterile neutrinos.

Summarizing all the above discussion, one can say that neutrinos are deemed to be massless in the SM, and the individual lepton numbers, as well as the total one, are strictly conserved. With the fermionic content and gauge symmetry of the SM one cannot construct a renormalizable mass term for the neutrinos. In order to introduce a neutrino mass, one must either extend the particle contents of the model or abandon the gauge invariance and/or renormalizability. Concerning experimental tests, observation of neutrino oscillations proves non-conservation of neutrino flavor and the massive nature of these particles, leading to physics beyond the Standard Model.

Introducing massive neutrinos

In a field theory of neutrinos the mass is determined by the mass term in the Lagrangian. Since the right-handed neutrinos are absent in the standard electroweak model, one can add more possibilities by adding to the three known neutrino fields $\nu_{\ell L}$ new fields corresponding to sterile neutrinos $\nu_{s i}$. Keeping the gauge symmetry and the particle contents of the SM, and assuming an arbitrary number m of sterile neutrinos, one can construct two types of mass terms:

$$-\mathcal{L}_{M_\nu} = M_{Dij} \bar{\nu}_{si} \nu_{Lj} + \frac{1}{2} M_{Nij} \bar{\nu}_{si} \nu_{sj}^c + \text{h.c.} \quad (2.9)$$

where ν^c indicates a charge conjugated field, $\nu^c = C\bar{\nu}^T$ and C is the charge conjugation matrix. M_D is a complex $m \times 3$ matrix and M_N is a symmetric matrix of dimension $m \times m$.

The first term is what we call a Dirac mass term, analogous to the mass term of charged leptons. It conserves the total lepton number, but it might violate the individual lepton flavor numbers.

The second term is a Majorana mass term which breaks the total lepton number conservation by two units. It is allowed only if the neutrinos have no additive conserved charges of any kind.

In general Eq. (2.9) can be rewritten as:

$$-\mathcal{L}_{M_\nu} = \frac{1}{2} \bar{\nu}^c M_\nu \vec{\nu} + \text{h.c.} \quad (2.10)$$

where

$$M_\nu = \begin{pmatrix} 0 & M_D^T \\ M_D & M_N \end{pmatrix}, \quad (2.11)$$

and $\vec{\nu} = (\vec{\nu}_L, \vec{\nu}_s^c)^T$ is a $(3+m)$ -dimensional vector. The matrix M_ν is complex and symmetric. It can be diagonalized by a unitary matrix of dimension $(3+m)$, V^ν , so that

$$(V^\nu)^T M_\nu V^\nu = \text{diag}(m_1, m_2, \dots, m_{3+m}). \quad (2.12)$$

The corresponding $3+n$ eigenstates ν_M represent Majorana neutrinos, obeying the condition:

$$\nu_M = \nu_M^c \quad (2.13)$$

Now, depending on the scale of M_N , one can analyze different cases:

- **Dirac neutrinos:**

this happens when $M_N = 0$, so second term in Eq. 2.9 vanishes, and therefore there is lepton number symmetry in the model. The quantum number L distinguishes a neutrino from an anti-neutrino. For $m = 3$ we can identify the three sterile neutrinos with the right-handed component of a four-spinor neutrino field. In this case the Dirac mass term can be diagonalized with two 3×3 unitary matrices, V^ν and V_R^ν as:

$$V_R^{\nu\dagger} M_D V^\nu = \text{diag}(m_1, m_2, m_3). \quad (2.14)$$

The neutrino mass term can be written as:

$$-\mathcal{L}_{M_\nu} = \sum_{k=1}^3 m_k \bar{\nu}_{Dk} \nu_{Dk} \quad (2.15)$$

where

$$\nu_{Dk} = (V^{\nu\dagger} \vec{\nu}_L)_k + (V_R^{\nu\dagger} \vec{\nu}_s)_k, \quad (2.16)$$

so the weak-doublet components of the neutrino fields are

$$\nu_{Li} = L \sum_{j=1}^3 V_{ij}^\nu \nu_{Dj}, \quad i = 1, 3. \quad (2.17)$$

In this case the SM is not a good low-energy effective theory since both the matter content and the assumed symmetries are different. In addition, there is no explanation to the fact that neutrino masses are much lighter than the corresponding charged fermion masses, although in this case all acquire their mass via the same mechanism.

- **Majorana neutrinos in the Seesaw model:**

in this case M_N is much higher than the scale of electroweak symmetry breaking $\langle\phi\rangle$. The diagonalization of M_ν leads to three light, ν_l , and m heavy, N , neutrinos:

$$-\mathcal{L}_{M_\nu} = \frac{1}{2} \bar{\nu}_l M^l \nu_l + \frac{1}{2} \bar{N} M^h N \quad (2.18)$$

with

$$M^l \simeq -V_l^T M_D^T M_N^{-1} M_D V_l, \quad M^h \simeq V_h^T M_N V_h \quad (2.19)$$

and

$$V^\nu \simeq \begin{bmatrix} \left(1 - \frac{1}{2} M_D^\dagger M_N^{*-1} M_N^{-1} M_D\right) V_l & M_D^\dagger M_N^{*-1} V_h \\ -M_N^{-1} M_D V_l & \left(1 - \frac{1}{2} M_N^{-1} M_D M_D^\dagger M_N^{*-1}\right) V_h \end{bmatrix} \quad (2.20)$$

where V_l and V_h are 3×3 and $m \times m$ unitary matrices respectively. So the heavier are the heavy states, the lighter are the light ones. Also as seen from Eq. (2.20) the heavy states are mostly right-handed while the light ones are mostly left-handed. Both the light and the heavy neutrinos are Majorana particles. In this case the SM is a good effective low energy theory. For further details, see [8].

- **Light sterile Majorana neutrinos:**

this happens if the scale of some eigenvalues of M_N is not higher than the electroweak scale. As in the case with $M_N = 0$, the SM is not even a good low energy effective theory: there are more than three light neutrinos, and they are admixtures of doublet and singlet fields.

From experimental data, we know that neutrinos masses are much smaller than the masses of the associated lepton in the weak isodoublet (Eq.2.2). Even the mass of the lightest charged lepton (the electron) is at least 10^5 times larger than the neutrino mass. Such a large factor is difficult to explain unless within some symmetry principle, and thus the assumption that neutrinos are Majorana particles arises. Moreover, several theoretical models explaining neutrinos masses lead to the conclusion that neutrinos are massive Majorana fermions.

Neutrino mixing

If neutrinos are massive particles and there is neutrino mixing, the left-handed components of the neutrino fields $\nu_{\alpha L}$ ($\alpha = e, \mu, \tau, s_1, s_2, \dots$) are unitary linear combinations of the left-handed components of the n (Dirac or Majorana) neutrino fields ν_k ($k = 1, \dots, n$) with masses m_k :

$$\nu_{\alpha L} = \sum_{k=1}^n U_{\alpha k} \nu_{k L}. \quad (2.21)$$

The number n of massive neutrinos is 3 for the cases with only three active flavour neutrinos. The number n is more than three in the case of a Dirac-Majorana mass term with a mixing of both active and sterile neutrinos.

In particular, if there are only three neutrinos, U is a 3×3 unitary matrix analogous to the CKM matrix for the quarks. It is known as the PMNS matrix to Pontecorvo, Maki, Nakagawa and Sakata. It can be written in terms of six independent parameters: three mixing angles and three phases. If neutrinos are Dirac particles, two phases can be eliminated by redefinition of the massive states. For Majorana neutrinos, this is not possible.

In the case of Majorana neutrinos, the PMNS matrix can be conveniently

parametrized as:

$$U = \begin{pmatrix} 1 & 0 & 0 \\ 0 & c_{23} & s_{23} \\ 0 & -s_{23} & c_{23} \end{pmatrix} \begin{pmatrix} c_{13} & 0 & s_{13}e^{-i\delta} \\ 0 & 1 & 0 \\ -s_{13}e^{i\delta} & 0 & c_{13} \end{pmatrix} \begin{pmatrix} c_{21} & s_{12} & 0 \\ -s_{12} & c_{12} & 0 \\ 0 & 0 & 1 \end{pmatrix} \begin{pmatrix} e^{i\alpha_1} & 0 & 0 \\ 0 & e^{i\alpha_2} & 0 \\ 0 & 0 & 1 \end{pmatrix} \quad (2.22)$$

where $c_{ij} \equiv \cos \theta_{ij}$ and $s_{ij} \equiv \sin \theta_{ij}$. The angles θ_{ij} can be taken without loss of generality to lie in the first quadrant, $\theta_{ij} \in [0, \pi/2]$ and the phases $\delta, \alpha_i \in [0, 2\pi]$. The presence of these phases causes the violation of CP invariance in the lepton sector. The two Majorana phases $\alpha_{1,2}$ affect only lepton number violating processes and are very hard to measure (oscillation experiments are not sensitive to them). Since in this parameterization of the mixing matrix the CP-violating phase δ is associated with s_{13} , it is clear that CP violation is negligible in the lepton sector if the mixing angle θ_{13} is small.

PMNS matrix parameterization of Eq. (2.22) can be understood as a 3D rotation matrix, product of three independent rotations, one in the plane 23, another in the plane 12 and a third that connects both (Fig. 2.1). As it will be described in chapter 3, the current experimental data can be accommodated to this 3- ν scheme. Atmospheric neutrino experiments are sensitive to the mixing angle θ_{23} (and thus to the rotation in the plane 23), while solar neutrino experiments can measure θ_{12} (rotation in the plane 12).

2.2 Neutrino oscillations in vacuum

In the case of massive neutrinos, the weak eigenstates, ν_α , produced in weak interactions are, in general, linear combinations of the mass eigenstates ν_i :

$$|\nu_\alpha\rangle = \sum_{i=1}^n U_{\alpha i}^* |\nu_i\rangle \quad (2.23)$$

where n is the number of light neutrino species and U is the mixing matrix. After traveling a distance L , a neutrino originally produced with a flavor α evolves as:

$$|\nu_\alpha(t)\rangle = \sum_{i=1}^n U_{\alpha i}^* |\nu_i(t)\rangle, \quad (2.24)$$

and it can be detected in the charged-current (CC) interaction

$$\nu_\alpha(t)N' \rightarrow \ell_\beta N$$

with a probability

$$P_{\alpha\beta} = |\langle \nu_\beta | \nu_\alpha(t) \rangle|^2 = \left| \sum_{i=1}^n \sum_{j=1}^n U_{\alpha i}^* U_{\beta j} \langle \nu_j | \nu_i(t) \rangle \right|^2. \quad (2.25)$$

Using the standard approximation that $|\nu\rangle$ is a plane wave

$$|\nu_i(t)\rangle = e^{-iE_i t} |\nu_i(0)\rangle,$$

that neutrinos are relativistic with $p_i \simeq p_j \equiv p \simeq E$,

$$E_i = \sqrt{p_i^2 + m_i^2} \simeq p + \frac{m_i^2}{2E}, \quad (2.26)$$

and the orthogonality relation $\langle \nu_j | \nu_i \rangle = \delta_{ij}$, we get the following transition probability:

$$\begin{aligned} P_{\alpha\beta} = \delta_{\alpha\beta} - 4 \sum_{i < j} & \operatorname{Re}[U_{\alpha i} U_{\beta i}^* U_{\alpha j}^* U_{\beta j}] \sin^2 X_{ij} \\ & + 2 \sum_{i < j} \operatorname{Im}[U_{\alpha i} U_{\beta i}^* U_{\alpha j}^* U_{\beta j}] \sin 2X_{ij}, \end{aligned} \quad (2.27)$$

where

$$X_{ij} = \frac{(m_i^2 - m_j^2)L}{4E}. \quad (2.28)$$

The first line in (2.27) is CP conserving while the second one is CP violating and has opposite sign for neutrinos and antineutrinos. This transition probability has an oscillatory behavior, with amplitudes that are proportional to elements in the mixing matrix and oscillation lengths

$$L_{0,ij}^{\text{osc}} = \frac{4\pi E}{\Delta m_{ij}^2}, \quad (2.29)$$

where $\Delta m_{ij}^2 \equiv m_i^2 - m_j^2$.

Thus, in order to undergo flavour oscillations, neutrinos must have different masses and they must mix. Also, as can be seen from Eq. (2.27), the Majorana

phases cancel out in the oscillation probability as expected because flavour oscillation is a total lepton number conserving process.

When neutrinos propagate in dense matter, the interaction with the medium affects their properties and the corresponding effects can be observed in oscillation experiments. Although this is an interesting issue, it is out of the scope of this work since we will focus on an oscillation experiment (K2K) in which matter effects are negligible. For further details, we refer to [5].

2.3 Neutrinoless double beta decay

If neutrinos are massive, the issue of their nature (whether they are Majorana or Dirac particles) becomes of uppermost importance. If neutrinos are Majorana particles, thus identical to their antiparticles, then neutrino-less beta double decay processes may be observed.

Majorana neutrinos and $\beta\beta^{0\nu}$

Double beta decay ($\beta\beta$) is a *rare* transition between two nuclei with the same mass number A that changes the nuclear charge Z by two units. The decay can occur only if the initial nucleus is less bound than the final nucleus, and both more than the intermediate one. Many even-even nuclei can undergo a $\beta\beta$ transition, and indeed this decay involving the emission of two neutrinos has been observed in several isotopes. Analogous transitions of two protons into two neutrons are also, in principle, possible in several nuclei, but phase space considerations give preference to the former decay. An example is shown in Fig. 2.2, from [9].

One can distinguish two different modes of the $\beta\beta$ decay:

1. *Double beta decay with emission of two neutrinos $\beta\beta^{2\nu}$:*
the emission of two beta particles involves also two neutrinos:

$$(Z, A) \rightarrow (Z + 2, A) + e_1^- + e_2^- + \bar{\nu}_{e_1} + \bar{\nu}_{e_2}, \quad (2.30)$$

lepton number is conserved and, being this mode allowed in the SM. This decay has been observed in isotopes such ^{76}Ge , ^{100}Mo , ^{82}Se and ^{150}Nd , and it has been measured with typical half-lives of 10^{18} – 10^{20} years. The inverse of the lifetime for $\beta\beta^{2\nu}$ processes can be expressed in terms of an

exactly calculable phase-space factor $G^{2\nu}(E_0, Z)$, and the nuclear matrix element (NME) $|M^{2\nu}|$ [10]:

$$\frac{1}{T^{2\nu}} = |M^{2\nu}| G^{2\nu}(E_0, Z), \quad (2.31)$$

where E_0 is the available reaction energy, $E_0 = Q_{\beta\beta} + 2m_e$. The calculation of NMEs is performed theoretically, although it is affected by relatively large uncertainties.

2. Neutrino-less beta double decay $\beta\beta^{0\nu}$:

in this mode there are no neutrinos emitted,

$$(Z, A) \rightarrow (Z + 2, A) + e_1^- + e_2^-, \quad (2.32)$$

violating thus lepton number conservation and requiring massive Majorana neutrinos. Hence, its observation would be a signal of physics beyond the Standard Model. One can visualize this process by assuming the exchange of various virtual particles: the most simple mechanism is the exchange of a light Majorana neutrino, although one can also assume the emission of a neutral boson B, a Majoron, as it will be described below. The half-life of the $\beta\beta^{0\nu}$ decay depends on the type of particle exchange.

The $\beta\beta^{2\nu}$ and $\beta\beta^{0\nu}$ modes involve different total energy (sum of the two emitted electrons) spectrum, no matter what the mechanism for the $\beta\beta^{0\nu}$ decay is. Therefore, one can separate them experimentally by means of a good energy resolution. Fig. 2.3 shows the energy sum of the two emitted electrons for both $\beta\beta^{2\nu}$ and $\beta\beta^{0\nu}$ decays. In the case of $\beta\beta^{0\nu}$ process, the spectrum associated with the exchange of a light Majorana neutrino and the one associated to the Majoron emission are shown.

Exchange of a light Majorana neutrino

The most simple way in which $\beta\beta^{0\nu}$ decay may occur is via the exchange of a light Majorana neutrino. As shown in Fig. 2.4, the parent nucleus emits a pair of virtual W bosons, and then these W exchange a Majorana neutrino ν^M to produce the outgoing electrons. The exchange of the neutrino can be understood as a two-step process:

1. at first vertex a right-handed neutrino is emitted, created together with an e^- via a beta decay. There, lepton number should be conserved and this neutrino would have to be an antineutrino $\bar{\nu}$,

2. then, at a second vertex the same particle behaves as a left-handed neutrino, being absorbed and creating a second e^- via a quasi-elastic scattering $\nu + n \rightarrow e^- + p$.

It is clear that the diagram vanishes unless $\nu = \bar{\nu}$, that is, the neutrino is a Majorana particle. The process is suppressed by a helicity mismatch at the two vertices touched by the virtual ν . Obviously, the required helicity flip is possible only if neutrinos have mass.

The $\beta\beta^{0\nu}$ process differs from the $\beta\beta^{2\nu}$ one in several aspects, although they have common features as both are $\beta\beta$ decays. In both modes, the two emitted electrons take almost all the available energy,

$$Q_{\beta\beta} \equiv M(A, Z) - M(A, Z + 2),$$

in a transition that involves the 0^+ ground state of the initial nucleus and most likely the 0^+ ground state of the final nucleus. It is also possible the transition to an excited state of the final nucleus, but it is suppressed by the smaller phase space (indeed, the $\beta\beta^{2\nu}$ decay to excited states has been observed in some nuclei). On the other hand, there are two points distinguishing between $\beta\beta^{2\nu}$ and $\beta\beta^{0\nu}$ decays:

- In the $\beta\beta^{2\nu}$ mode, the two neutrons undergoing the transition are uncorrelated and simultaneously, while in the $\beta\beta^{0\nu}$ the two neutrons are correlated.
- In the $\beta\beta^{2\nu}$ mode, the spectrum of the sum of the energies of the two electrons emitted is continuous and peaked below $Q_{\beta\beta}/2$. The spectrum approaches to zero approximately as $(\Delta E/Q_{\beta\beta})^6$. From the other side, the theoretical spectrum of the $\beta\beta^{0\nu}$ mode is a delta at $Q_{\beta\beta}$. This point has special interest since it allows us to separate experimentally both modes, as shown in Fig. 2.4.

Assuming that the $\beta\beta^{0\nu}$ decay is mediated by the exchange of a light Majorana neutrino, the inverse of the half-life for the process is [11]

$$\frac{1}{T_{1/2}^{0\nu}} = G^{0\nu}(Q, Z) |M^{0\nu}|^2 \langle m_\nu \rangle^2, \quad (2.33)$$

where $G^{0\nu}(Q, Z)$ is a phase space factor that depends on the transition $Q_{\beta\beta}$ value and on the nuclear charge Z , and can be calculated analytically; $M^{0\nu}$ is the

nuclear matrix element that can be evaluated in nuclear models, although with a considerable uncertainty; finally, the quantity $\langle m_\nu \rangle$ is the effective neutrino Majorana mass, defined as:

$$\begin{aligned}
 \langle m_\nu \rangle &= \left| \sum_j m_j |U_{ej}|^2 e^{i\alpha_j} \right| \\
 &= \left| |U_{e1}|^2 m_1 + |U_{e2}|^2 m_2 e^{i\alpha_1} + |U_{e3}|^2 m_3 e^{i\alpha_2} \right| \\
 &= \left| c_{13}^2 (|m_1| c_{12}^2 + |m_2| e^{2i\alpha_1} s_{12}^2) + |m_3| e^{2i(\alpha_2 - \delta)} s_{13}^2 \right|
 \end{aligned} \tag{2.34}$$

being $c_{ij} \equiv \cos \theta_{ij}$ and $s_{ij} \equiv \sin \theta_{ij}$, and where we assume only three light Majorana neutrinos. Consequently, the effective mass is related to the mixing angles that are determined or constrained by the oscillation experiments, to the absolute neutrino masses m_i of the mass eigenstates ν_i , and to the Majorana phases α_i . Although $\langle m_\nu \rangle$ depends on the by now unknown quantities θ_{13} , δ , α_1 and α_2 of the PMNS matrix, the lower and upper limits of $\langle m_\nu \rangle$ are independent of the Majorana phases, and therefore one can use measured values of the mixing angles to deduce a range of the absolute mass scale of neutrinos. This discussion will be extended in section 3.3.

Other mechanisms for $\beta\beta^{0\nu}$ decay

As previously pointed out, the exchange of light Majorana neutrinos is not the only possible mechanism inducing neutrino-less double beta decay [9]. In general, in theories beyond the Standard Model there may be other sources of total lepton number violation which can lead to $\beta\beta^{0\nu}$. Nevertheless, as it was first pointed out in Ref. [12], irrespective of the mechanism, $\beta\beta^{0\nu}$ necessarily implies a Majorana neutrino mass. The reason is that any diagram contributing to the decay can be inserted into a neutrino propagator, with outgoing electron lines closed appropriately with SM interactions as in Fig. 2.5.

As examples, we cite the following mechanisms:

- emission of a Majoron J , the Goldstone boson associated with spontaneous symmetry breaking of lepton number, as shown in left panel of Fig.

2.6. Depending on the theoretical model, one or more Majorons can be emitted in the process. Thus, the $\beta\beta J$ decay involves at least three body decay spectrum (as seen in Fig. 2.3), with the Majorons avoiding detection.

- exchange of super-symmetric (SUSY) particles (gluinos or neutralinos) through R-parity violation, as shown in right panel of Fig. 2.6. R-parity is associated with the quantum number $R_p = (-1)^{3B+L+2S}$, where B, L and S are baryon, lepton and spin numbers, respectively. In this case, $\beta\beta^{0\nu}$ decay is sensitive to SUSY coupling constants.

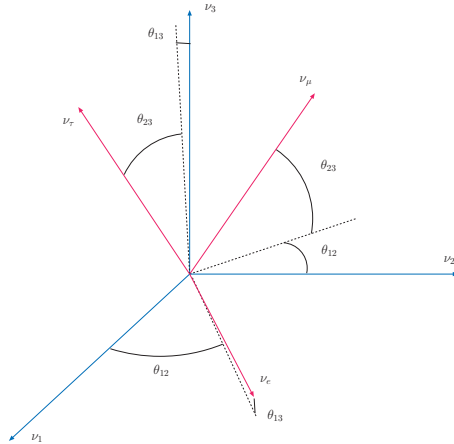


Figure 2.1: Neutrino mixing scheme.

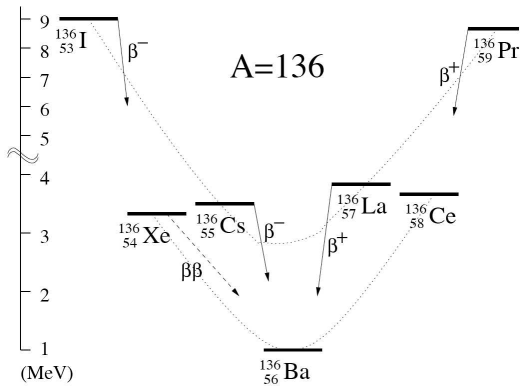


Figure 2.2: Simplified atomic mass scheme for isotopes with $A = 136$. Nuclei ^{136}Xe , ^{136}Ba and ^{136}Ce are stable against the ordinary β decay. However, energy conservation alone allows the transition $^{136}\text{Xe} \rightarrow ^{136}\text{Ba} + 2\text{e}^-$ and the analogous decay of ^{136}Ce with positron emission. From Ref. [9].

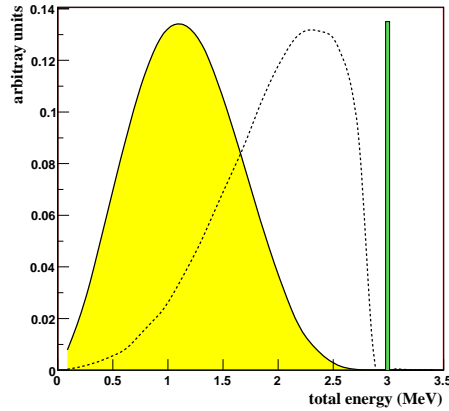


Figure 2.3: Energy sum of the two emitted electrons in both $\beta\beta^{2\nu}$ (lines) and $\beta\beta^{0\nu}$ (filled spike) decays. Two different mechanisms for the $\beta\beta^{0\nu}$ process are considered: exchange of a light Majorana neutrino (solid line) and the emission of a Majoron (dashed line). Assumed isotope is ^{82}Se .

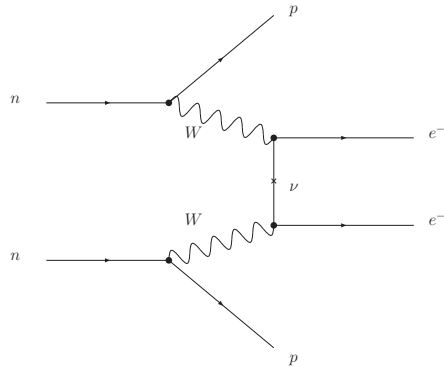


Figure 2.4: Feynman diagram for a $\beta\beta^{0\nu}$ process mediated by the exchange of light Majorana neutrinos.

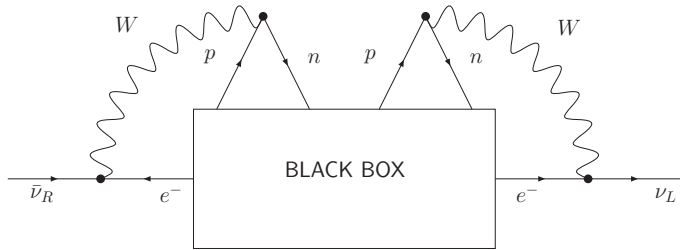


Figure 2.5: Diagram showing how any neutrino-less double beta decay process induces a $\bar{\nu}$ -to- ν transition, that is, an effective Majorana mass term. This is the so-called “Black box theorem” [12].

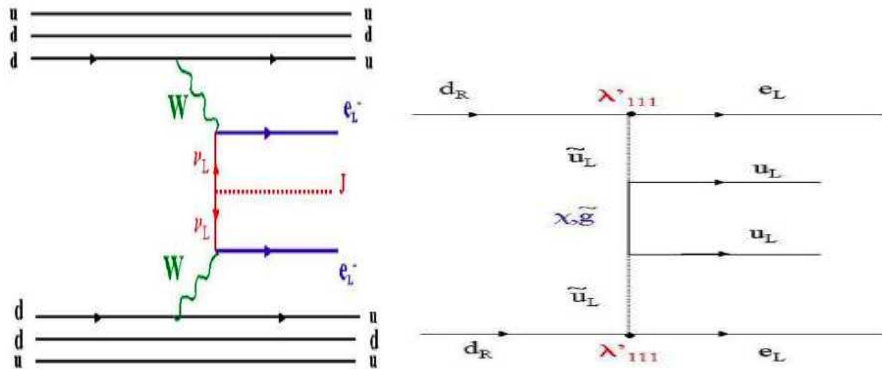


Figure 2.6: Two of the possible underlaying mechanisms for the $\beta\beta^{0\nu}$ process. Left: $\beta\beta^{0\nu}$ decay involving emission of a Majoron J. Left: $\beta\beta^{0\nu}$ decay mediated by SUSY particles.

Chapter 3

Experimental approaches to neutrino physics

3.1 Overview

The experimental studies aiming to understand neutrino nature can be divided into two different fields. First, neutrino oscillation experiments aim to measure the oscillation parameters appearing in the three first terms of Eq.2.22. Depending on the neutrino energy and the distance between the neutrino source and the detectors, one is able to measure one or another parameter. This is why we distinguish between different kinds of neutrino oscillation experiments, being sensitive to the solar, atmospheric or interference regimes.

Second, since neutrino oscillation data are only sensitive to neutrino mass differences, another kind of experiments are needed in order to search for the absolute neutrino mass m_ν . In particular, oscillation experiments are not sensitive to the Majorana phases in Eq.2.22, and therefore the fundamental issue of whether neutrinos are Dirac or Majorana particles is out of their scope. As it will be described in this chapter, upper values for m_ν have been set thanks to kinematics constraints of weak decays and cosmological bounds. Furthermore, $\beta\beta^{0\nu}$ decay experiments may prove that neutrinos are Majorana particles and estimate absolute neutrino mass by combining their results with the oscillation parameters measured in oscillation experiments.

The following sections summarize different experimental approaches to neu-

trino physics, from the oscillation experiments to those experiments looking for the absolute mass scale and the nature of neutrino masses. An extended description of these experiments and their results can be found at [5] and [13].

3.2 Neutrino oscillations

Neutrino oscillations experiments are characterized by the typical neutrino energy E_ν and by the distance L between neutrino source and detector. In order to be sensitive to a given value of Δm_{ij}^2 , the experiment has to be set up with $E/L \approx \Delta m_{ij}^2$.

Oscillation experiments can be divided into four categories, depending on the neutrino source under study. Typically, each neutrino source implies a given range of energy and a distance between the source and the detector (as an example, solar neutrinos have much longer flight distances than atmospheric neutrinos), although for neutrinos generated on Earth one has some freedom to choose the source-detector distance L . Consequently, oscillation experiments are sensitive to a certain set of oscillation parameters, depending on the neutrino source.

According to the above criteria, we have the following type of experiments:

- solar neutrinos
- atmospheric neutrinos
- reactor neutrinos
- accelerator neutrinos

In the case of reactor and accelerator experiments, one can set L depending on the range of Δm^2 to be explored. This is why we distinguish between short and long baseline (LBS and SBL) experiments. Furthermore, oscillation in atmospheric neutrinos can be analyzed in a wide range of L , since one can detect neutrinos coming from the top of the detector (they travel about 15 km in the atmosphere), or neutrinos coming from the bottom (they have traversed the full diameter of the Earth). Table 3.1 shows the typical parameters of L and E_ν , and the corresponding values of Δm^2 , for the kinds of experiments listed above.

Concerning experimental issues, PMNS matrix in Eq. 2.22 can be understood as the convolution of three different terms (apart from the Majorana phases, which cannot be observed by oscillation experiments). Each term (or rotation,

Experiment	L (m)	E (MeV)	Δm^2 (eV ²)
Solar	10^{10}	1	10^{-10}
Atmospheric	$10^4 - 10^7$	$10^2 - 10^5$	$10^{-1} - 10^{-4}$
Reactor SBL	$10^2 - 10^3$	1	$10^{-2} - 10^{-3}$
Reactor LBL	$10^4 - 10^5$		$10^{-4} - 10^{-5}$
Accelerator SBL	10^2	$10^3 - 10^4$	> 0.1
Accelerator LBL	$10^5 - 10^6$	10^4	$10^{-2} - 10^{-3}$

Table 3.1: Characteristic values of L and E_ν for various types of neutrino experiments and the corresponding ranges of Δm^2 which can be explored. SBL and LBL stand for short and long baselines.

as explained in section 2.1) contains the mixing angle controlling one of the so-called *oscillation sectors*: atmospheric, solar and interference. Thus, first sub-matrix in Eq. 2.22 holds the angle which can be measured in atmospheric and accelerator neutrinos (at long baselines) experiments:

$$U_{atm} = \begin{pmatrix} 1 & 0 & 0 \\ 0 & c_{23} & s_{23} \\ 0 & -s_{23} & c_{23} \end{pmatrix} \quad (3.1)$$

and we use the following convection for the mixing angle: $\theta_{23} \equiv \theta_{atm}$.

On the other hand, solar and reactor neutrino experiments are sensitive to the parameter in third term of Eq. 2.22, that is, to the solar sector:

$$U_{sol} = \begin{pmatrix} c_{12} & s_{12} & 0 \\ -s_{12} & c_{12} & 0 \\ 0 & 0 & 1 \end{pmatrix} \quad (3.2)$$

In this work we use the following convection for the corresponding mixing angle: $\theta_{12} \equiv \theta_{sol}$.

Finally, mixing or interference between atmospheric and solar sectors is controlled by the second term in Eq. 2.22:

$$U_{inter} = \begin{pmatrix} c_{13} & 0 & s_{13}e^{-i\delta} \\ 0 & 1 & 0 \\ -s_{13}e^{i\delta} & 0 & c_{13} \end{pmatrix} \quad (3.3)$$

Summarizing, the current experimental data can be fit to a 3- ν scenario: two mixing angles (θ_{sol} and θ_{atm}) and two mass square differences (Δm_{sol}^2 and Δm_{atm}^2) are measured by solar and atmospheric experiments respectively.

The third mixing angle (θ_{13}) is known to be small or even null. Therefore, one is allowed to analyze atmospheric and solar data assuming a two-neutrino scenario within good approximation. For a two-neutrino case, the overall mixing matrix depends on a single parameter (θ_{sol} or θ_{atm}),

$$U = \begin{pmatrix} \cos \theta & \sin \theta \\ -\sin \theta & \cos \theta \end{pmatrix}, \quad (3.4)$$

and there is a single mass-squared difference Δm^2 (Δm_{sol}^2 or Δm_{atm}^2). Then $P_{\alpha\beta}$ of Eq. 2.27 takes the well known form

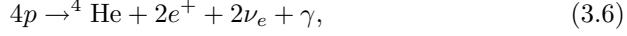
$$P_{\alpha\beta} = \delta_{\alpha\beta} - (2\delta_{\alpha\beta} - 1) \sin^2 2\theta \sin^2 X. \quad (3.5)$$

The physical parameter space is covered with $\Delta m^2 \geq 0$ and $0 \leq \theta \leq \frac{\pi}{2}$ (or, alternatively, $0 \leq \theta \leq \frac{\pi}{4}$ and either sign for Δm^2).

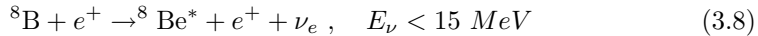
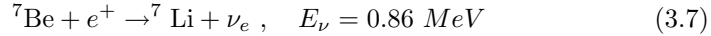
Neutrino oscillation experiments usually analyze their data inside this scenario of only two-flavour neutrino oscillation.

3.2.1 Solar neutrinos

Solar neutrinos are electron neutrinos produced in the thermonuclear reactions which generate the solar energy. All the reaction chains result in the overall fusion of protons into ${}^4\text{He}$:



where the energy release is $Q = 4m_p - m_{{}^4\text{He}} - 2m_e \simeq 26$ MeV. It is mostly radiated through the photons and only a small fraction is carried by the neutrinos, $\langle E_{2\nu_e} \rangle = 0.59$ MeV. Due to their low energy, neutrinos from this fusion are not easy to detect. Neutrinos coming from the following secondary reactions were the first to be observed:



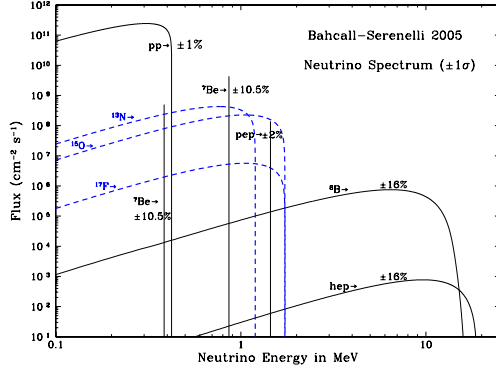


Figure 3.1: Neutrino fluxes predicted by the SSM as a function of the neutrino energy. From [16].

The so-called solar neutrino problem [14, 15] came from the fact that several experiments observed a solar neutrino flux Φ^{obs} that was smaller than the predicted by the Standard Solar Model (SSM) [16]. Moreover, different experiments have shown different deficits, indicating that the effect is energy dependent. Fig. 3.1 shows the solar ν_e fluxes as predicted by the SSM. The following list summarizes results from solar neutrino experiments since 1968:

- **Chlorine experiment at Homestake:**

The first result announced by Ray Davis took place in 1968 [17]. The detector, placed at Homestake mine (South Dakota), was a tank filled with ~ 615 Tons of C_2Cl_4 , in which solar ν_e were captured via $^{37}\text{Cl}(\nu, e^-) ^{37}\text{Ar}$. The energy threshold for this reaction is 0.814 MeV, so the relevant fluxes are those of neutrinos coming from the ^7Be and ^8B (Eq. 3.7 and 3.8). The average event rate measured during the more than 20 years of operation is [18]

$$R_{\text{Cl}} = 2.56 \pm 0.16 \pm 0.16 \text{ SNU} \quad \Rightarrow \quad \frac{R_{\text{Cl}}}{\text{SSM}} = 0.30 \pm 0.03 \quad (3.9)$$

where 1 SNU = 10^{-36} captures/atom/sec.

- **Gallium experiments (SAGE and GALLEX/GNO):**

SAGE [19] and GALLEX/GNO [20] (GNO experiment is the successor

of GALLEX) are operated at Baksan (Russia) and Gran Sasso (Italy) respectively. Both are radiochemical experiments using ^{71}Ga target: solar neutrinos are captured via $^{71}\text{Ga}(\nu, e^-)^{71}\text{Ge}$. The threshold of this reaction is 0.233 MeV and this allows to detect neutrinos from 3.6. The averaged event rates measured by SAGE and GALLEX+GNO are [21]:

$$R_{\text{GALLEX+GNO+SAGE}} = 68.1 \pm 3.75 \text{ SNU} \Rightarrow \frac{R_{\text{Ga}}}{\text{SSM}} = 0.52 \pm 0.03. \quad (3.10)$$

- **Water Cherenkov detector (Kamiokande and SK):**

Super-Kamiokande [22] (SK) is the evolution of the Kamiokande [23] detector. It is a tank filled with 50 kilotons of water that allows to detect in real time electrons produced by the elastic scattering (ES) of the solar neutrinos, $\nu_a + e^- \rightarrow \nu_a + e^-$, thanks to the emission of Cherenkov light. While the detection process in radiochemical experiments is purely a charge current (CC) interaction (W-exchange), the detection ES process goes through both CC and neutral current (NC) (Z-exchange) interactions. Consequently, the ES detection process is sensitive to all active neutrino flavors. The detection threshold in SK is 5 MeV, and therefore it is sensitive to neutrino flux coming from Eq. 3.8. The measured flux is:

$$\begin{aligned} \Phi_{\text{SK}} &= (2.35 \pm 0.02 \pm 0.08) \times 10^6 \text{ cm}^{-2}\text{s}^{-1} \Rightarrow \\ &\Rightarrow \frac{\Phi_{\text{SK}}}{\Phi_{\text{SSM}}} = 0.413 \pm 0.014. \end{aligned} \quad (3.11)$$

- **The Sudbury Neutrino Observatory (SNO):**

The SNO detector [24, 25, 26] is a great sphere surrounded by photomultipliers, which contains approximately 1000 Tons of heavy water, D_2O , and is located at the Creighton mine (Canada). SNO is sensitive to all flavors of active neutrinos and not just to ν_e . This is possible because energetic neutrinos can interact in the D_2O of SNO via three different reactions. Electron neutrinos may interact via the CC reaction $\nu_e + d \rightarrow p + p + e^-$, and can be detected above an energy threshold of a few MeV (presently $T_e > 5$ MeV). All active neutrinos ($\nu_a = \nu_e, \nu_\mu, \nu_\tau$) interact via the NC reaction $\nu_a + d \rightarrow n + p + \nu_a$ with an energy threshold of 2.225 MeV. Finally, the non-sterile neutrinos can also interact via ES, $\nu_a + e^- \rightarrow \nu_a + e^-$. SNO can test if the deficit of solar ν_e is due to changes in the flavor composition of the solar neutrino beam, since the ratio CC/NC compares the

number of ν_e interactions with those from all active flavors. This comparison is independent of the overall flux normalization. SNO latest solar flux predictions are:

$$\begin{aligned}\Phi_{\text{SNO}}^{\text{CC}} &= (1.68_{-0.06}^{+0.06}_{-0.09}) \times 10^6 \text{ cm}^{-2}\text{s}^{-1} \Rightarrow \frac{\Phi_{\text{SNO}}^{\text{CC}}}{\Phi_{\text{SSM}}} = 0.29 \pm 0.02, \\ \Phi_{\text{SNO}}^{\text{ES}} &= (2.35 \pm 0.22 \pm 0.15) \times 10^6 \text{ cm}^{-2}\text{s}^{-1} \Rightarrow \frac{\Phi_{\text{SNO}}^{\text{ES}}}{\Phi_{\text{SSM}}} = 0.41 \pm 0.05, \\ \Phi_{\text{SNO}}^{\text{NC}} &= (4.94 \pm 0.21_{-0.34}^{+0.38}) \times 10^6 \text{ cm}^{-2}\text{s}^{-1} \Rightarrow \frac{\Phi_{\text{SNO}}^{\text{NC}}}{\Phi_{\text{SSM}}} = 0.87 \pm 0.08.\end{aligned}\tag{3.12}$$

The simplest mechanism for the solar neutrino flavor transition is that of oscillations of ν_e into ν_μ and/or ν_τ , in a two-neutrino scenario. The measurements of the neutral current flux by SNO confirm that the ν_e deficit corresponds to a ν_μ/ν_τ flux appearance. Top left panel of Fig. 3.3 shows combined analysis results from SNO, SK, Gallium and Chlorine experiments. These compatible results yield:

$$\begin{aligned}\Delta m_{\text{sol}}^2 &\sim 6 \times 10^{-5} \text{ eV}^2, \\ \theta_{\text{sol}} &\sim 33^\circ\end{aligned}$$

It is worth noticing that the interpretation of the solar data led to a set of possible solutions of mass square difference and mixing angle, which indeed were far away one from another. The degenerate solutions were the so-called *MSW small mixing angle* (SMA), *MSW large mixing angle* (LMA), *MSW low mass* (LOW) and *vacuum oscillations* (VAC) [5]. Only with further SK and SNO data analysis, in particular the inclusion of the time and energy dependence of the ${}^8\text{B}$ neutrino fluxes, this situation was solved by pointing the LMA solution as the most likely to explain the solar neutrino problem.

3.2.2 Atmospheric neutrinos

When cosmic rays interacts with the nitrogen and oxygen in the Earth's atmosphere at an average height of 15 kilometers, pions and some kaons are produced.

These hadrons decay into electron and muon neutrinos and anti-neutrinos. Atmospheric neutrinos are observed in underground experiments using different techniques and leading to different type of events depending on their energy. They can be detected by the direct observation of their CC interaction inside the detector. Modern experiments (since the 1970's) follow mainly two directions, allowing both of them flavor classification of the events as well as the measurement of the energy and angle of the outgoing lepton:

- **Water Cherenkov detectors:**

Cherenkov light produced in water by charged leptons is registered by photomultipliers. This is the case of Kamiokande and Super-Kamiokande [28, 27]. Both detectors observed ν_μ fluxes smaller than expected by theoretical calculations. Indeed, the event distribution as a function of the zenith angle θ suggested that the deficit increased with the distance between the neutrino production and interaction points. Comparing the observed and the expected distributions, the following statements can be inferred:

1. ν_e distributions are well described by the MC while ν_μ presents a deficit. Consequently, the atmospheric neutrino deficit is mainly due to disappearance of ν_μ and not the appearance of ν_e .
2. The suppression of contained μ -like events is stronger for larger $\cos \theta$, which implies that the deficit grows with the distance traveled by the neutrino from its production point to the detector.
3. disappearance probability is higher for larger energy neutrinos

- **Iron calorimeters:**

An iron calorimeter is composed of a set of alternating layers of iron which act as a target and some tracking element (such as plastic drift tubes) which allows the reconstruction of the shower produced by the electrons or the tracks produced by muons. Detectors Soudan2 [29] and MACRO [30] have confirmed the same effects observed by SK.

SK, Macro and Soudan experiments have found definitive evidence of atmosphere ν_μ disappearance. The simplest and most direct interpretation of the atmospheric neutrino anomaly is that of muon neutrino oscillations (in a two-neutrino scenario). On the other hand, there is no observation of ν_e oscillation,

leading to the conclusion that mixing angle θ_{13} is small. Combined analysis for the oscillation parameter space can be seen in top right plot of Fig. 3.3. Atmospheric neutrinos experiments show that

$$\Delta m_{atm}^2 \sim 2 \times 10^{-3} \text{ eV}^2, \\ \theta_{atm} \sim 45^\circ$$

3.2.3 Reactor neutrinos

Another source of neutrino fluxes are nuclear reactors. They produce $\bar{\nu}_e$ beams with $E_\nu \sim \text{MeV}$. This low energy only allows to produce e 's in the neutrino CC interaction that takes place in the detector. In case $\bar{\nu}_e$ oscillates, the remaining neutrino cannot interact via CC and is not detected. Therefore, the oscillation signature in experiments using reactor neutrinos is a disappearance effect, or in other words a deficit in the expected reactor flux. These kind of experiments have the advantage that smaller values of Δm^2 can be accessed due to the lower neutrino beam energy. As previously said, one can choose the distance L between the neutrino source and the detector, and this allows to set the Δm^2 range to be explored. We can distinguish between SBL (CHOOZ [31]) and LBL (KamLAND [32]) experiments:

- **CHOOZ:**

it searched for disappearance of $\bar{\nu}_e$'s coming from a nuclear plant in France, using a detector located at $L \simeq 1 \text{ km}$ from the reactors. The $\bar{\nu}_e$ interaction signature is the delayed coincidence between the prompt e^+ signal and the signal due to the neutron capture in the Gd-loaded scintillator. The ratio between the measured and expected fluxes averaged over the neutrino energy spectrum is given by

$$R_{\text{CHOOZ}} = 1.01 \pm 2.8\%(\text{stat}) \pm 2.7\%(\text{syst}). \quad (3.13)$$

Thus no evidence was found for a deficit in the flux. Furthermore CHOOZ also presented their results in the form of the antineutrino energy spectrum which showed no distortion.

There are other short baseline reactor experiments which did not find a signal of oscillation: Gosgen [33], Krasnoyarsk [34], Bugey [35] and Palo Verde [36]. We recall that the common point to all of them was the short distance L (few km at most from nuclear reactor to neutrino detector).

They are sensitive to $\Delta m^2 \gtrsim 7 \times 10^{-3}$ eV², far away from the values obtained in the solar neutrino experiments.

- **KamLAND:**

it uses a longer baseline: detector (1 kiloton of liquid scintillator) is placed inside Kamioka mine (Japan), at an average distance of 150-210 km from several nuclear power stations. Such a distance between neutrino source and detector allows to be sensitive to smaller values of Δm^2 . It can test oscillations with $\Delta m^2 \gtrsim 10^{-5}$ eV², so KamLAND is operating in the same range as solar neutrino experiment. The ratio of the number of observed events to the number of events expected without oscillations is:

$$R_{\text{KamLAND}} = 0.611 \pm 0.094 \quad (3.14)$$

for $E_{\bar{\nu}_e} > 3.4$ MeV [32]. This deficit is inconsistent with the expected rate for massless $\bar{\nu}_e$'s at the 99.95% confidence level. Kamland analysis published at [37] also presents energy dependence of the events in the form of the prompt energy ($E_{\text{prompt}} \simeq E_{\bar{\nu}_e} + m_p - m_n$) spectrum, showing clearly an energy dependent deficit.

From KamLAND analysis one gets $\Delta m_{\text{sol}}^2 \sim 7 \times 10^{-5}$ eV². However, its results can be combined with the solar data achieving the allowed range for oscillation parameters shown in bottom left panel of Fig. 3.3 (from [5]). This combined analysis yields:

$$\begin{aligned} \Delta m_{\text{sol}}^2 &\sim 8 \times 10^{-5} \text{ eV}^2, \\ \theta_{\text{sol}} &\sim 34^\circ \end{aligned}$$

It is important to notice that CHOOZ provides an interesting result regarding the $3 - \nu$ scenario in which the solar and atmospheric sectors interfere via the mixing angle θ_{13} . The fact that $\bar{\nu}_e$ does not disappear in this experiment leads to the following conclusion:

$$\theta_{13} \lesssim 13^\circ, \quad \text{for} \quad \Delta m_{\text{atm}}^2 \sim 2 \times 10^{-3} \text{ eV}^2$$

3.2.4 Accelerator neutrinos

Conventional accelerator-based neutrino beams come from the decay of light hadrons produced on a fixed target, when a primary proton beam collides with it. Neutrinos come mostly from pion decay, although kaons give also a contribution:

$$\begin{aligned} p + \text{target} &\rightarrow \pi^\pm + X \\ \pi^\pm &\rightarrow \mu^\pm + \nu_\mu (\bar{\nu}_\mu) \\ \mu^\pm &\rightarrow e^\pm + \nu_e (\bar{\nu}_e) + \bar{\nu}_\mu (\nu_\mu) \end{aligned} \quad (3.15)$$

The beam contains both μ - and e -neutrinos and antineutrinos. The final composition and energy spectrum of the neutrino beam is determined by selecting the sign of the decaying π and by stopping the produced μ in the beam line. The beam intensity depends on the energy of the primary proton beam. There is an additional contribution to the electron neutrino and antineutrino flux from kaon decay.

Accelerator neutrino beams can be used to test oscillation of atmospheric neutrinos taking advantage of the controlled neutrino source. Energy of accelerator neutrinos is about a few GeV, and thus distance between accelerator and neutrino detector has to be of the order of hundred kilometers in order to be sensitive to the same Δm^2 involved in atmospheric neutrino oscillation. These are therefore LBS experiments.

The analysis technique of accelerator neutrino beam experiments relies on the comparison between neutrino flux measured at a far detector, where oscillation is expected to take place according to atmospheric neutrinos experiments, and the predicted flux at the same detector in absence of oscillation. Any discrepancy between the observation and the prediction can be described in terms of neutrino oscillation. Therefore, the key point of these experiments is to be able to predict with high accuracy the un-oscillated flux at the far detector. To get such a prediction, neutrino flux is measured at a near detector (close to the beam source), where neutrinos have not oscillated yet, and then flux is extrapolated somehow to the far detector.

The first LBS experiments with accelerator beams are K2K [38] and MINOS [39].

- **K2K:**

it run with a baseline of about 250 km from KEK to SK. Fig. 3.2 shows an schematic view of the K2K experiment: an accelerator-based neutrino beam and two detector sites. We describe the K2K last analysis in this work (chapter 4). 107 events were observed at the far detector while the

expected number for the null oscillation hypothesis is 151^{+12}_{-10} . In addition, a distortion of the neutrino energy spectrum was also observed. Best fit value of Δm_{atm}^2 is $2.8 \times 10^{-3} \text{ eV}^2$ in the two-neutrino scenario.

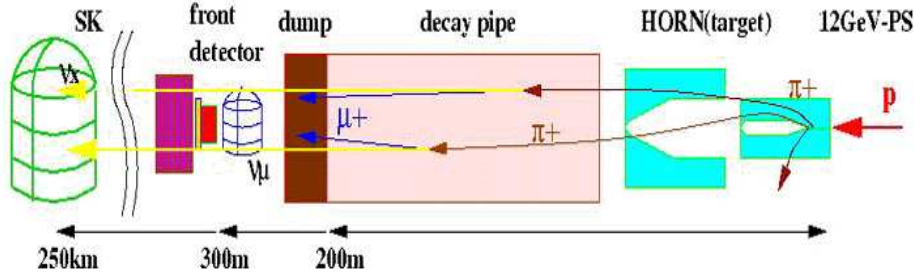


Figure 3.2: Schematic view of the K2K experiment. Neutrino beam is generated by hitting an aluminum target with a primary proton beam of $12 \text{ GeV}/c$. Neutrino fluxes are measured at near and far detectors.

- **MINOS:**

it is currently running with a baseline of 730 km from Fermilab, where the near detector is placed, to the Soudan mine where the far detector is located. MINOS has observed a total of 122 events below 10 GeV while the expectation without oscillations is 238.7 ± 10.7 [40]. A preliminary analysis reports $\Delta m_{atm}^2 = 2.38^{+0.20}_{-0.16} \times 10^{-3} \text{ eV}^2$ in the two-neutrino scenario. Bottom right plot of Fig. 3.3 (from [5]) shows MINOS results for the oscillation parameters.

Both K2K and MINOS observed deficit of events with energy dependence, yielding compatible results with those inferred from the atmospheric neutrino data:

$$\Delta m_{atm}^2 \sim 2.6 \times 10^{-3} \text{ eV}^2, \\ \theta_{atm} \sim 45^\circ$$

Apart from the LBS experiments, there is also another set of experiments working with accelerator beams but with shorter baselines (hundreds of meters). They are not sensitive to the low values of Δm^2 estimated in atmospheric neutrinos experiments, and have not seen oscillation signal. The only exception is the Liquid Scintillator Neutrino Detector (LSND) [41] running at Los Alamos, where an excess of events compatible with $\bar{\nu}_\mu \rightarrow \bar{\nu}_e$ oscillations was observed. However, KARMEN [42] and MiniBooNE [43] experiments have completely tested the corresponding phase space of the oscillation parameter with negative results.

3.3 Direct determination of m_ν

Although oscillation experiments have demonstrated that neutrinos have masses and mix, they are not sensitive to the absolute mass scale of the neutrinos (m_ν). Results of oscillation experiments provide a lower bound on the heavier mass in Δm_{ij}^2 , $|m_i| \geq \sqrt{\Delta m_{ij}^2}$ for $\Delta m_{ij}^2 > 0$. However, there is no upper bound on this mass, and there is neither upper nor lower bound on the lighter mass m_j . In particular, one can distinguish between three different mass patterns, arising from the fact that the sign of Δm_{31}^2 is still not known:

- Normal hierarchy: $m_3 \gg m_2 \sim m_1$
- Inverted hierarchy: $m_1 \sim m_2 \gg m_3$
- Degenerate hierarchy: $m_1 \sim m_2 \sim m_3$

In addition, if neutrinos are massive, the issue of their nature (whether they are Majorana or Dirac particles) becomes of uppermost importance. If neutrinos are Majorana particles, thus identical to their antiparticles, then $\beta\beta^{0\nu}$ processes may be observed. Successful $\beta\beta^{0\nu}$ experiment results would provide an extra handle to estimate the absolute mass scale.

The following subsections will describe briefly the experimental tests searching for the absolute neutrino mass and its Dirac or Majorana *nature*.

3.3.1 Kinematic constraints from Weak Decays

Kinematic tests explore processes which are allowed in the Standard Model with $m_\nu = 0$. Analyzing effects of such processes as a function of neutrino mass provides new information if the experimental observation differs from the Standard Model prediction. Specifically, upper bounds for m_{ν_e} , m_{ν_μ} and m_{ν_τ} are obtained from the below decays:

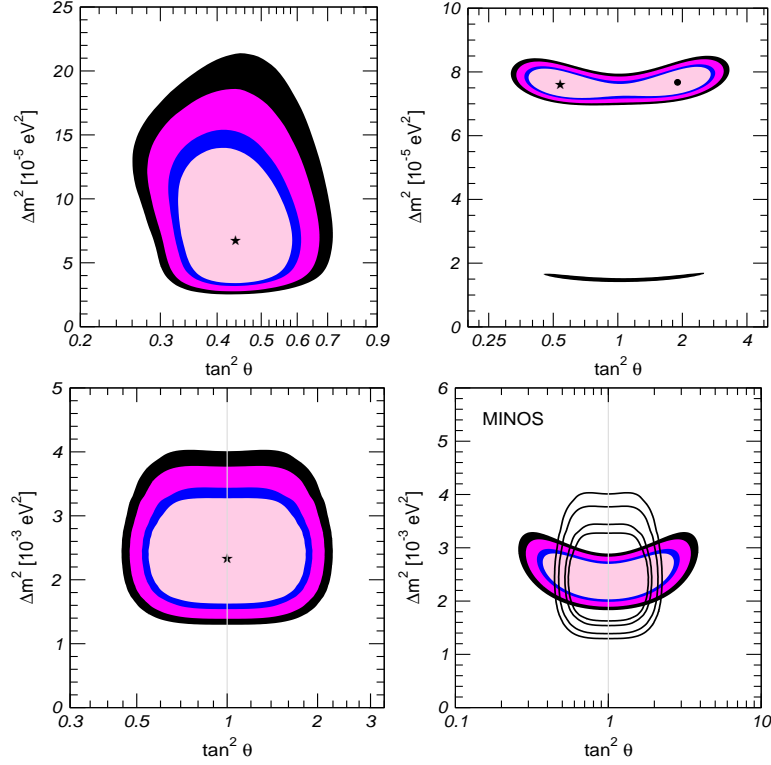
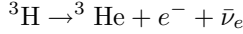


Figure 3.3: Allowed regions of oscillation parameters, at 90%, 95%, 99% and 99.7% C.L. Top right: allowed region for Δm_{sol}^2 and θ_{sol} from global analysis of solar neutrino data. Top left: allowed region for Δm_{sol}^2 and θ_{sol} from kamLAND data, based on calculations by T. Schwetz. Bottom right: allowed region for Δm_{atm}^2 and θ_{atm} from global analysis of atmospheric neutrino data. Bottom left: allowed region for Δm_{atm}^2 and θ_{atm} from MINOS data; for comparison purposes atmospheric neutrino results are also shown with lines. Figures from [5].

- **Tritium β -decay:**

The absolute electron neutrino mass m_{ν_e} can be searched from the beta decay spectrum, in particular from the tritium decay:



Discrepancy on the electron spectrum between prediction for $m_{\nu_e} = 0$ and the experimental result may allow a measurement of m_{ν_e} . By now, the most precise determination from the Mainz [44] and Troitsk [45] experiments gives no indication in favor of $m_{\nu_e} \neq 0$ and consequently an upper limit has been set

$$m_{\nu_e} < 2.2 \text{ eV} \quad (3.16)$$

at 95% confidence level (CL).

- **Pion decay:**

the muon energy in the pion decay $\pi^- \rightarrow \mu^- + \bar{\nu}_\mu$ can provide a measurement of m_{ν_μ} , although with less accuracy than the one for m_{ν_e} from tritium decay. Current limit is [7]:

$$m_{\nu_\mu} < 190 \text{ keV} \quad (3.17)$$

- **Tau decay:**

Upper limit for m_{ν_τ} is inferred from τ decay: $\tau^- \rightarrow n\pi + \nu_\tau$. Current limit is [7]:

$$m_{\nu_\tau} < 18.2 \text{ MeV} \quad (3.18)$$

3.3.2 Cosmological bounds

Neutrinos contribute to the total energy density of the Universe. As a consequence they can play a relevant role in large scale structure formation and leave clear signatures in several cosmological observables. Although in an indirect way, it is possible to infer constraints on the neutrino masses by comparing the most recent cosmological data with the theoretical predictions. The relevant quantity in these studies is the total neutrino energy density in our Universe, $\Omega_\nu h^2$ (where h is the Hubble constant normalized to $H_0 = 100 \text{ km s}^{-1} \text{ Mpc}^{-1}$). Currently, $\Omega_\nu h^2$ is related to the total mass in the form of neutrinos:

$$\Omega_\nu h^2 = \sum_i m_i / (94 \text{ eV}). \quad (3.19)$$

Therefore cosmological data puts a limit on the sum of neutrino masses, not being sensitive to the neutrino mixing.

The most relevant data come from the Large Scale Structures (LSS) as obtained from large redshift surveys of galaxies by the 2 degree Field survey [46] and the Sloan Digital Sky Survey [47] and from Cosmic Microwave Background (CMB) anisotropies which at present are most precisely determined by the WMAP experiment [48]. Additional information can also be extracted from the so-called Lyman- α forest [49, 50].

A single cosmological bound on neutrino masses does not exist. The bound depends on the data included in analysis as well as on details on the biases assumed and on the statistical treatment. One can say that cosmological bound is within the following range:

$$\sum m_\nu < 0.3 - 3.0 \text{ eV} \quad (3.20)$$

3.3.3 Searching for the $\beta\beta0\nu$ decay

Experiments searching for the neutrino-less beta double decay have a major role in neutrino physics. No matter which virtual particle is exchanged in the process (see Sec. 2.3), $\beta\beta0\nu$ decay only happens if neutrinos are Majorana particles. So far, this is the only way one can try to discover the actual nature of neutrino masses. In addition, the observation of this decay also provides an estimation of the neutrino effective mass $\langle m_\nu \rangle$ defined in section 2.3. Such an estimation can be combined with the oscillation parameters values obtained from oscillation experiments. In particular, one can infer from equation 2.34 the upper and lower limits for $\langle m_\nu \rangle$ [51]:

$$\langle m_\nu \rangle_{max} = \sum_i |U_{ei}|^2 m_i \quad (3.21)$$

$$\langle m_\nu \rangle_{min} = \max[2|U_{ei}|^2 m_i] \quad (3.22)$$

which do not depend on Majorana phases. If the value of $\langle m_\nu \rangle$ is determined in a $\beta\beta0\nu$ experiment and at the same time the mixing angles θ_{ij} and the mass square differences Δm_{ij} are known from oscillation experiments, a range of absolute values of the neutrinos masses can be deduced [51]. Furthermore, taking advantage of an additional information, like the one coming from tritium beta decay, one can determine or at least constrain the Majorana phases.

Although $\beta\beta$ experiments may provide such relevant results, searching for $\beta\beta^{0\nu}$ processes is a tough job, since the half-life of this decay, or equivalently the number of expected events, is suppressed quadratically with the effective Majorana neutrino mass $\langle m_\nu \rangle$, which is known to be very small. On the other hand, the normal $\beta\beta^{2\nu}$ mode stays constant (does not depend on $\langle m_\nu \rangle$) and it is an intrinsic background which can only be eliminated partially by means of a good energy resolution. In addition, any other kind of events with an energy release around $Q_{\beta\beta}$ is a potential background.

In the case of the exchange of a light Majorana neutrino (see Sec. 2.3), the search for neutrino-less double beta decay relies on finding a peak in the region around the transition end-point value ($Q_{\beta\beta}$). If one had a perfect detector (infinite resolution and no background), the experiment would be almost straightforward: the $\beta\beta^{0\nu}$ events will accumulate in a spike at Q and no $\beta\beta^{2\nu}$ event will fall in this exact position thanks to the outstanding resolution. The key issues of any $\beta\beta^{0\nu}$ experiment can be summarized as follows:

1. **Statistics:** in order to acquire enough statistics, any $\beta\beta$ experiment needs a large exposure, defined as the product of isotope mass M by the data taking time t . According to the radioactive decay law in the approximation of $T_{1/2} \gg t$, the number of $\beta\beta$ decays $N_{\beta\beta}$ (both $\beta\beta^{0\nu}$ and $\beta\beta^{2\nu}$) can be expressed in terms of $T_{1/2}$ as follows:

$$N_{\beta\beta} = \ln 2 \frac{N_A \times 10^3}{A T_{1/2}} Mt \quad (3.23)$$

where t is the measuring time, M is the detector useful mass, N_A is the Avogadro number, A is the atomic weight and $N_{\beta\beta}$ is the number of $\beta\beta$ decays. In the case of $\beta\beta^{0\nu}$ process, the half-life $T_{1/2}$ is a function of $\langle m_\nu \rangle$ (Eq.2.33). With reasonable assumptions on the nuclear matrix element it can be estimated that neutrino effective masses around 50-100 meV corresponds to half-lives of about $10^{26} - 10^{27}$ years. As an example, using 100 kg of ^{82}Se isotope implies only 4 events per year of measurement, if $T_{1/2}^{0\nu} = 10^{26} \text{ y}$. Fig. 3.4 shows the number of expected $\beta\beta^{0\nu}$ events as a function of $\langle m_\nu \rangle$ (for a fixed exposure of 500 kg · year) and as a function of the exposure (for a fixed effective mass of 200 meV), corresponding to three different isotopes, and according to Nuclear Matrix Elements (NME) quoted in Ref. [52]. One can notice how number of decays is suppressed quadratically as $\langle m_\nu \rangle$ tends to zero, meanwhile it increases linearly with the exposure.

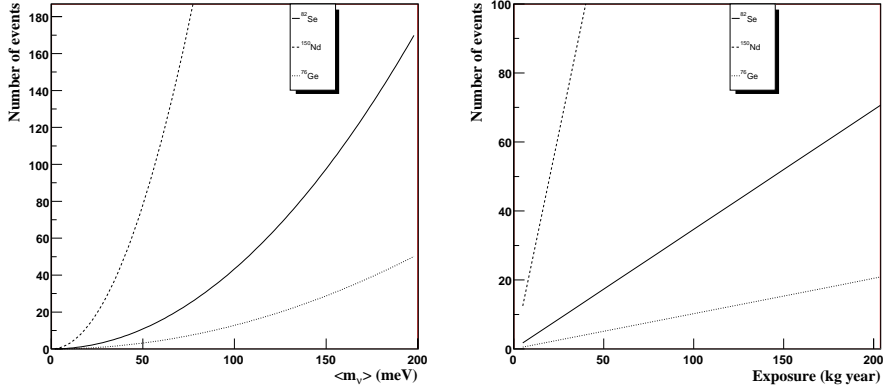


Figure 3.4: Number of expected $\beta\beta^{0\nu}$ events $N_{\beta\beta}$ for ^{76}Ge , ^{82}Se and ^{150}Nd isotopes. Left: $N_{\beta\beta}$ as a function of $\langle m_\nu \rangle$. Right: $N_{\beta\beta}$ as a function of exposure. Results according to nuclear matrix elements listed in Ref. [52] for $g_A = 1.25$.

2. **Experimental conditions:** taking into account the experimental conditions of a background limited experiment, the sensitivity to $T_{1/2}^{0\nu}$ not only depends on the exposure:

$$T_{1/2}^{0\nu} \propto \frac{a \ \varepsilon}{A} \sqrt{\frac{M \ t}{b \ \delta E}} \quad (3.24)$$

being a the isotopic abundance of the parent nuclide, ε the detection efficiency, b the rate of background counts (in events/keV/kg/year) and δE the energy window at the $\beta\beta^{0\nu}$ peak position (proportional to the energy resolution of the detector). As soon as one assumes a limited energy resolution, $\beta\beta^{2\nu}$ spectrum becomes a background since its tail overlaps the $\beta\beta^{0\nu}$ signal, as can be seen in Fig. 3.5. In this case, the sensitivity to $T_{1/2}^{0\nu}$ increases with the square root of the exposure. This can be understood as follows: the signal sensitivity is approximately determined by the statistical precision (i.e., square root) of the background determination. Because the number of background counts increases linearly with time, the decay rate sensitivity scales as the square root of time. In turn, the

$\langle m_\nu \rangle$ sensitivity scales as the square root of the decay rate, and therefore as the fourth root of the counting time.

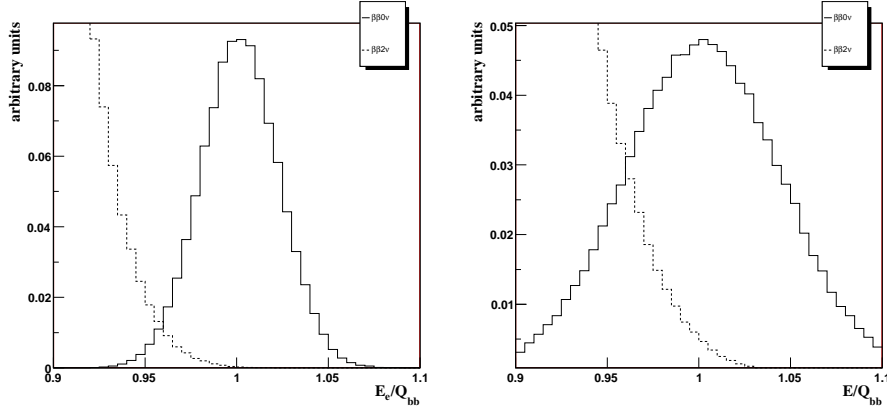


Figure 3.5: Separation between the $\beta\beta^{0\nu}$ and $\beta\beta^{2\nu}$ spectra, as a function of the sum electron energy (kinetic energy E_e of the two electrons) over $Q_{\beta\beta}$. Left plot includes an effect of 5% FWHM resolution smearing, while right one includes 10% FWHM resolution smearing. The assumed $2\nu/0\nu$ ratio is 10.

3. Backgrounds: Apart from the $\beta\beta^{2\nu}$ spectrum, any process releasing an energy around $Q_{\beta\beta}$ fakes the $\beta\beta^{0\nu}$ signal. The following lists the most common sources of backgrounds other than the $\beta\beta^{2\nu}$ one:

- *Natural activity*:

The isotopes of the thorium and radium series are present as impurities in all materials. The half-life of U and Th isotopes is comparable to the age of the universe but very short compared to the half-life sensitivity of the $\beta\beta^{0\nu}$ experiments. Therefore, even a small quantity of them will create a significant background. In particular, ^{214}Bi and ^{208}Tl (also coming from radon gas decay) have large Q -values, and the decay spectra will overlap the endpoint of almost all the $\beta\beta$ candidates.

- *Cosmogenic and induced activities*:

$\beta\beta$ experiments are operated deep underground to avoid cosmic ray

interactions. At these depths, muons are the only surviving cosmic ray particles, but their interactions can produce high-energy secondaries of neutrons, bremsstrahlung γ rays and electromagnetic showers.

Taking into account all the above discussion, one can define the criteria to optimize the setup of a $\beta\beta$ experiment. The following summarize the main points to achieve the best experiment as possible:

- **Calorimeter resolution:**

the only way to avoid (or indeed reduce) background coming from $\beta\beta^{2\nu}$ spectrum is to achieve a good energy resolution. The better resolution, the better signal-to-background ratio in the energy region where the peak of the $\beta\beta^{0\nu}$ decay is searched for.

- **Extra handles for background rejection:**

in order to reject background events other than the ones coming from the $\beta\beta^{2\nu}$ decay, one needs extra handles to tag them, since a good energy resolution may not be enough. In addition to the total energy measurement, information coming from event reconstruction (tracking of the charged particles, kinematic data,...) can be used to identify background events. Another possibility is to detect the $\beta\beta$ -decay daughter in coincidence with the decay energy release, thus allowing rejection of non- $\beta\beta$ events.

- **Choice of isotope:**

choosing an adequate $\beta\beta$ source isotope is very important. There are several criteria to use one or another isotope, but some of the most important are the following. An isotope with a large Q value places the region of interest above many potential backgrounds and a relatively slow $\beta\beta^{2\nu}$ rate also helps to keep this background under control. Moreover, a relevant natural abundance of the isotope or the capability to enrich the source is desirable. On the other hand, purity of the source must be ensured in order to avoid the so-called internal backgrounds.

- **Radio-purity of detector materials:**

radioactive impurities in detector material leads to an extra source of background and consequently one needs to ensure the radio-purity of each piece of the detector.

- **External shielding:**

the detector must be protected from the environment and its associated

radioactivity. This is why typically $\beta\beta$ detectors are operated at underground laboratories and, in addition, surrounded by some kind of shield (iron, water,...).

- **Detection efficiency:**

the detector design has to optimize the detection efficiency. As shown in Eq.3.24, sensitivity to $T_{1/2}^{0\nu}$ is proportional to the detection efficiency of the $\beta\beta^{0\nu}$ events.

- **Detector size:**

typically it is an advantage to minimize the detector size. As already said, $\beta\beta$ detectors are placed at underground laboratories, where the available space is limited. In addition, smaller detectors are cheaper and with less background due to impurities in the materials. On the other hand, a very large source may have some advantage due to self shielding of a fiducial volume.

A positive result of an experiment searching for the neutrino-less beta double decay would need supporting evidences to strengthen the argument and become universally accepted: the above characteristics would provide such evidences.

Different approaches to the search of $\beta\beta^{0\nu}$ decay

1. *Calorimetric experiments:*

Released energy of $\beta\beta$ events is measured with ionization detectors, bolometers or liquid scintillators. Their obvious advantages are the following:

- very good energy resolution (1% FWHM at 2 MeV), reducing $\beta\beta^{2\nu}$ background,
- high detection efficiency (75%), since detector and source are the same,
- easy to scale up, so can be extrapolated to higher amounts of isotope mass.

On the other hand, the main disadvantage are the absence of extra handles to reject the non- $\beta\beta$ background (any event in the energy region of the $\beta\beta^{0\nu}$ peak fakes the signal) and the high cost of the ^{76}Ge enrichment and radio-purification of the surrounding materials. The most restricted limits to the neutrino effective mass come from the following experiment:

- **Heidelberg-Moscow experiment [53]:**

searched the $\beta\beta^{0\nu}$ decay of ^{76}Ge using five high-purity Ge semiconductor detectors enriched to 87% in ^{76}Ge . The experiment run in the Gran Sasso Underground Laboratory (Italy) from 1990 to 2003, totaling an exposure of 71.7 kg·y. It is by far the longest running $\beta\beta$ decay experiment with the largest exposure. After the conclusion of the data taking period, a group led by H. V. Klapdor-Kleingrothaus (KK) has reanalyzed the data three times [4] claiming 4σ evidence for ^{76}Ge $\beta\beta^{0\nu}$ decay with a lifetime of about 1.2×10^{25} y, corresponding to a $\langle m_\nu \rangle$ of 0.24–0.58 eV (best value: 0.44 eV). This claim has sparked a debate (see, for example, Ref. [54]) in the neutrino physics community because the signal peak is faint and the spectrum contains other unexplained peaks (Fig. 3.6).

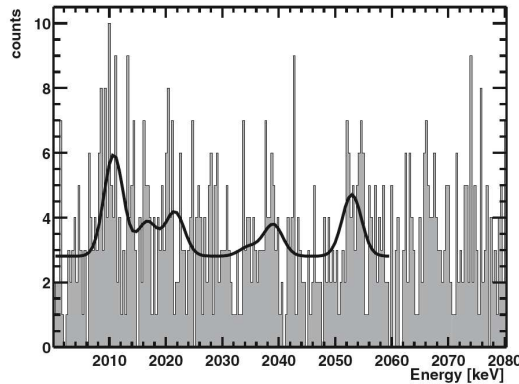


Figure 3.6: The spectrum from the Heidelberg-Moscow experiment upon which the claim for $\beta\beta^{0\nu}$ is based. In the region between 2000 and 2100 keV, KK's first analysis found a total of 7 peaks. Four of these were attributed to ^{214}Bi (2011, 2017, 2022, 2053 keV), one was attributed to the ^{76}Ge $\beta\beta^{0\nu}$ decay (2039 keV), and two were unidentified (2066 and 2075 keV). Later analyses do not discuss the spectrum above 2060 in detail. From [4].

2. *tracko-calor experiments:*

in addition to the total energy measurement, they provide tracking of the

involved particles. The typical configuration of these experiments consists of foil-shaped sources with some detectors (e.g. scintillators, TPCs, drift chambers, ...) analyzing the electrons emerging from the foil. The main advantages of this kind of detectors are:

- both electrons are detected and their kinematic properties measured,
- three different measurements: single energy, angular correlation and energy sum,
- several isotopes can be studied since source and detector are separated
- e^-, e^+, γ and α can be identified.

The tracking of charged particles provides a good extra handle for non- $\beta\beta$ background rejection. Furthermore, in case a $\beta\beta^{0\nu}$ signal is detected, the reconstruction of the electron tracks would also provide a unique tool to distinguish the decay mechanism from the electron angular correlation. From the other side, the limitations of this experimental approach are the poor energy resolution and the difficulties to scale up the source mass.

The first tracko-calo experiment providing results for several $\beta\beta$ isotopes is the last one of the NEMO series:

- **NEMO-3 [96]:**

This experiment is currently running at Modane Underground Laboratory (LSM), although it has already published some results for the search of the $\beta\beta^{0\nu}$ process in ^{82}Se and ^{100}Mo sources. Source foils are surrounded by a tracking device (geiger wires) and by a calorimeter that allows the energy measurement of the tracked particles. In this work, an extended description of NEMO-3 is given in section 5.2, since the SuperNEMO project, another tracko-calo experiment, is somehow its natural evolution.

As a summary, we present in table 3.2 a list of past and present experiments searching for the neutrino-less beta double decay. Table shows the isotope used and the experimental technique developed to detect the $\beta\beta$ events, along with the published results.

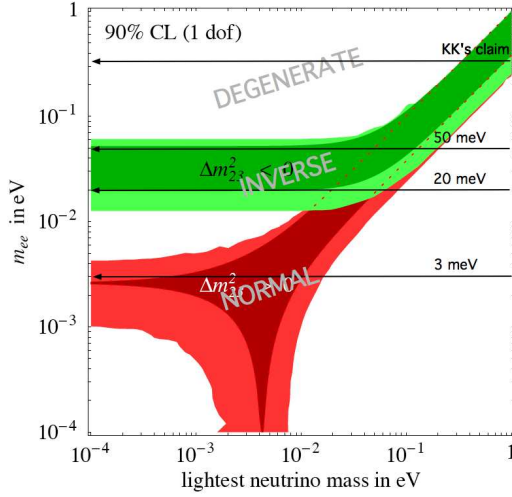


Figure 3.7: Neutrino effective mass as a function of the lightest neutrino mass. The objectives of the future experiments are twofold: first, the exploration of the claimed evidence (degenerate-hierarchy region) and, later, to increase the sensitivity for neutrino masses down to 20–50 meV (inverse-hierarchy region). Figure from [55].

Objectives of the next generation

Measurements or upper limits of the effective neutrino mass $\langle m_\nu \rangle$ should help to resolve the scheme of neutrino mass scale, which is unknown due to its dependence on the still not measured sign of Δm_{31} . Since $\langle m_\nu \rangle$ is a function of mixing angles and absolute neutrino masses, one can establish a relationship between $\langle m_\nu \rangle$ and the lightest neutrino mass which depends on the mass hierarchy, and therefore define the goals of the future $\beta\beta^{0\nu}$ experiments. A good description of the objectives of the next generation of experiments can be found at [13]: in terms of $\langle m_\nu \rangle$, there are three ranges of increasing sensitivity, related to the neutrino-mass scales inferred from neutrino oscillations data:

- The ~ 100 –500 meV range corresponds to the quasi-degenerate spectrum of neutrino masses. The motivation for reaching this scale has been strengthened by the claim of observation of $\beta\beta^{0\nu}$ decay in ${}^{76}\text{Ge}$; the only certain

way to confirm or refute it is with another experimental result.

- The $\sim 20\text{--}50$ meV range arises from the atmospheric neutrino oscillation results. Observation of $\langle m_\nu \rangle$ at this mass scale would imply the inverted neutrino mass hierarchy or the normal-hierarchy mass spectrum very near the quasi-degenerate region. To establish the correct mass pattern, additional input from the overall neutrino physics program would be needed. The study of this mass range will require, at least, 1-ton experiments.
- The $\sim 1\text{--}5$ meV range arises from the solar neutrino oscillation results and corresponds to the normal hierarchy. This goal would require ~ 100 tons of the decaying isotope, and no current technique provides such a leap in sensitivity.

Fig. 3.7 from [55] shows the above three ranges, plotting neutrino effective mass as a function of the lightest neutrino mass. The degenerate region will be explored easily by several experiments scaling up the “old techniques”, meanwhile the inverse region will require some years of R&D.

3.4 Summary of experimental results

The simplest explanation of the solar neutrino data described in Sec. 3.2.1 is the oscillations of ν_e into an active (ν_μ and/or ν_τ). Moreover, the simplest and most direct interpretation of the atmospheric neutrino data described in Sec. 3.2.2 is that of muon neutrino oscillations.

From the results previously described it is obvious that the minimum joint description of solar and atmospheric evidences requires that all three known neutrinos take part in the oscillations. Recall that we have two different Δm^2 , from solar and atmospheric experiments:

$$\Delta m_{21}^2 = \Delta m_{sol}^2 \ll \Delta m_{atm}^2 = |\Delta m_{31}^2| \simeq |\Delta m_{32}^2|. \quad (3.25)$$

In this case, the mixing parameters are encoded in the 3×3 lepton mixing PMNS matrix. As far as neutrino oscillation concerns, one can add or not a term containing Majorana phases since they are not observable. As soon as one considers the 3 neutrino scheme ($3 - \nu$), the interference between solar and atmospheric sectors (Eq.3.3) has to be taken into account. Regarding the interference parameters (θ_{13} and δ_{CP}), one has to notice that we still have almost no information. From global data analysis, one can extract that θ_{13} (see [5]) is compatible with zero. Furthermore, if there is a non-vanishing δ_{CP} , the

feasibility of a measurement depends on the actual value of θ_{13} , since it enters the PMNS matrix only through the combination with $\sin \theta_{13}$ (see Eq.2.22). The results of the global combined analysis assuming a $3-\nu$ scenario are summarized in Fig. 3.8 (from [5]) in which different projections of the allowed 6-dimensional parameter space are shown.

From the global combined analysis of the oscillation experimental data, the derived ranges for the six oscillation parameters at 1σ (3σ) are [5]:

$$\begin{aligned}\Delta m_{21}^2 &= 7.9^{+0.27}_{-0.28} ({}^{+1.1}_{-0.89}) \times 10^{-5} \text{ eV}^2, \\ |\Delta m_{31}^2| &= 2.6 \pm 0.2 (0.6) \times 10^{-3} \text{ eV}^2, \\ \theta_{12} &= 33.7 \pm 1.3 ({}^{+4.3}_{-3.5}), \\ \theta_{23} &= 43.3^{+4.3}_{-3.8} ({}^{+9.8}_{-8.8}), \\ \theta_{13} &= 0.0^{+5.2}_{-0.0} ({}^{+11.5}_{-0.0}), \\ \delta_{\text{CP}} &\in [0, 360].\end{aligned}\tag{3.26}$$

Oscillation experiments cannot determine the absolute magnitude of the masses, or differentiate between different mass patterns. In particular, if $\nu_i, i = 1, 2, 3$ are the mass eigenstates, such that $m_1 < m_2 < m_3$, one could have:

$$\begin{aligned}\Delta m_{\text{sol}} &= m_2 - m_1, & \Delta m_{\text{atm}} &= m_3 - m_2 \\ \Delta m_{\text{atm}} &= m_1 - m_3, & \Delta m_{\text{sol}} &= m_2 - m_1\end{aligned}\tag{3.27}$$

The first situation corresponds to the neutrino pattern known as *normal* hierarchy (the gap between the two lightest states corresponds to the small mass difference measured by solar experiments) while the second is known as *inverted* hierarchy (the gap between the two lightest states corresponds to the large mass difference measured by atmospheric experiments). This is shown in Fig. 3.9.

On the other hand, kinematical tests and cosmological data provide upper limits to the absolute neutrinos mass scale, as described in section 3.3. Results can be summarized as follows:

$$\begin{aligned}m_{\nu_e} < 2.2 \text{ eV} &\quad \text{from } {}^3\text{H} \rightarrow {}^3\text{He} + e^- + \bar{\nu}_e \\ m_{\nu_\mu} < 190 \text{ keV} &\quad \text{from } \pi^- \rightarrow \mu^- + \bar{\nu}_\mu \\ m_{\nu_\mu} < 18.2 \text{ MeV} &\quad \text{from } \tau^- \rightarrow n\pi + \nu_\tau \\ \sum m_\nu < 0.3 - 3.0 \text{ eV} &\quad \text{from } \Omega_\nu h^2 = \sum_i m_i / (94 \text{ eV})\end{aligned}$$

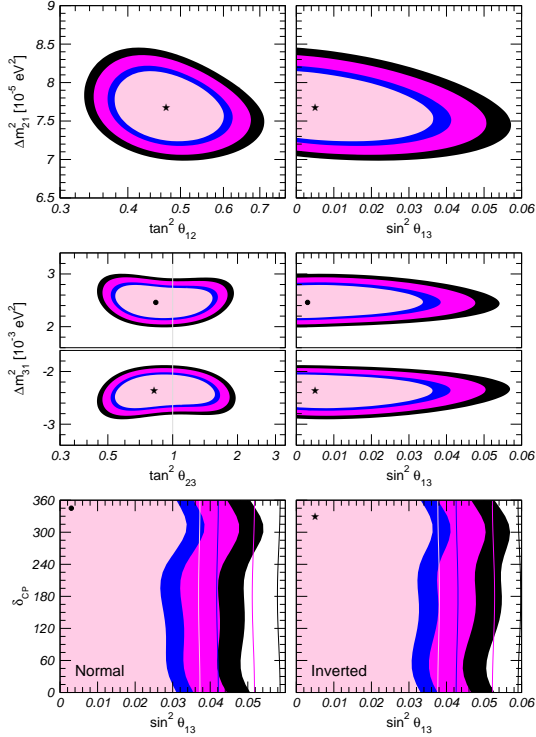


Figure 3.8: Global 3ν oscillation analysis. Each panels shows 2-dimensional projection of the allowed 5-dimensional region after marginalization with respect to the undisplayed parameters. The different contours correspond to the two-dimensional allowed regions at 90%, 95%, 99% and 3σ CL. In the lowest panel the vertical lines correspond to the regions without inclusion of the atmospheric neutrino data. Figure from [5]

isotope	experiment, date	exp. (kg·y)	technique	$T_{1/2}^{0\nu}$ (10 ²³ y)	$\langle m_\nu \rangle$ (eV)
⁴⁸ Ca	Elegant VI, 2004	4.2	scintillator	0.14	<(7.2-44.7)
⁷⁶ Ge	H.-Moscow, 2001	35.5.0	ionization	190	< 0.35
⁷⁶ Ge	H.-Moscow, 2004	71.7	ionization	(119 ⁺²⁹⁹ ₋₅₀)	0.24-0.58
⁸² Se	NEMO-3, 2007	1.8	tracking	2.1	<(1.2-3.2)
¹⁰⁰ Mo	NEMO-3, 2007	13.1	tracking	5.8	<(0.6-2.7)
¹¹⁶ Cd	Solotvina, 2003	0.5	scintillator	1.7	<1.7
¹²⁸ Te	Cuoricino, 2007	11.8	bolometer	30.0	<(0.41-0.98)
¹³⁶ Xe	DAMA, 2002	4.5	scintillator	12.0	<(0.8-5.6)
¹⁵⁰ Nd	Irvine TPC, 1997	0.01	tracking	0.012	
¹⁶⁰ Gd	Solotvina, 2001	1.0	scintillator	0.013	

Table 3.2: A selection of the past and present experiments giving the best result per isotope to date [7]. All given $T_{1/2}^{0\nu}$ are lower limits, with the exception of the Heidelberg-Moscow (2004) experiment where the 99.997% CL value is given.

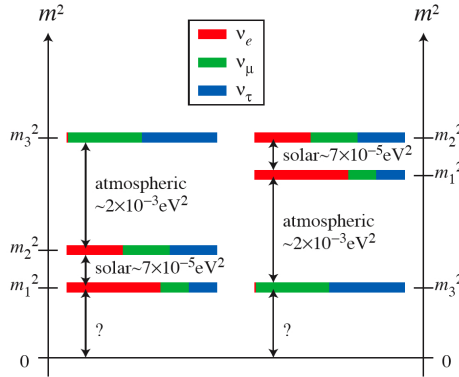


Figure 3.9: The two possible configurations of neutrino masses, normal (left) and inverted (right) hierarchies, as suggested by oscillation experiments. The flavour composition of the mass states is shown as well.

Finally, concerning the search for the neutrino-less beta double decay, a group from the Heidelberg-Moscow experiment [4] has claimed to observe a 4σ signal in ^{76}Ge , corresponding to:

$$\langle m_\nu \rangle = 0.24 - 0.58 \text{ eV} \quad (3.28)$$

This is the so-called Klapdor's claim. NEMO-3 detector will be the first approach to check this controversial result, and for sure the next generation of $\beta\beta^{0\nu}$ experiments, like SuperNEMO, contain within their goals the exclusion or confirmation of Klapdor's claim with relevant confidence levels.

3.5 Open issues in neutrino physics

To conclude this chapter, we summarize now the open issues concerning neutrino physics and the ways in which they can be solved. On one side, the next generation of accelerator and reactor neutrino experiments, like T2K [56] or Double-Chooz [57], will provide better accuracy for the oscillation parameters, and improved sensitivity to the mixing angle θ_{13} ; in order to observe CP violation (measurement of the phase δ in PMNS matrix) and to resolve neutrino mass pattern, a new generation of experiment will need to be projected: the so-called Beta Beams [58], Neutrino Factories [59] or very long baselines experiments are the possibilities under study. On the other side, new $\beta\beta$ experiments (like SuperNEMO) will keep on searching for the $\beta\beta^{0\nu}$ process to test the Majorana nature of neutrinos. From the theoretical point of view, the models explaining neutrino masses will need to be revisited as new experimental results show up. More specifically, the following is the list of the open issues in experimental neutrino physics:

1. Precision measurements of the oscillation parameters:

Now that oscillation of both solar and atmospheric has been confirmed, the goal regarding oscillation experiments is to measure the known oscillation parameters (θ_{12} , θ_{23} , Δm_{21}^2 , $|\Delta m_{31}^2|$) with better accuracy. This task will be performed by experiments like T2K [56] or OPERA [60].

2. Measurements of the mixing angle θ_{13} :

θ_{13} is still unknown, although we know it is really small or even vanishing. Its measurement is a major issue since this parameter will open the doors

for an observation of the CP violation characterized by the phase δ : we recall that δ only appears in the PMNS matrix in combination with $\sin \theta_{13}$. In a near future, T2K and Double Chooz experiments will search for θ_{13} down to sensitivities of 2 degrees. As an example, Double Chooz will be able to analyze the survival probability of reactor antineutrinos in a short baseline:

$$P_{ee} \simeq 1 - \sin^2 2\theta_{13} \sin^2 \left(\frac{\Delta m_{31}^2 L}{4E} \right). \quad (3.29)$$

At a future stage, long baseline accelerator experiments will use Superbeams, with major intensity upgrades with respect to current beams, thus reaching better sensitivities to θ_{13} . The ultimate accelerator facility for neutrino oscillation experiments will be a neutrino factory, where ν_e and $\bar{\nu}_\mu$ ($\bar{\nu}_e$ and ν_μ) beams of high intensity will be obtained from the decay of stored μ^+ (μ^-), along with new detector technologies.

3. Mass hierarchy:

The current knowledge of the oscillation parameters leads to two possible orderings of the neutrino mass eigenstates: the so-called normal and inverse hierarchies. These two mass patterns can be distinguished by means of matter effects in long-baseline experiments, which enhance the probability $P(\nu_\mu \rightarrow \nu_e)$ and suppress $P(\bar{\nu}_\mu \rightarrow \bar{\nu}_e)$ or vice versa depending on the sign of Δm_{31}^2 . Long baselines are needed in order to observe such matter effects.

4. CP violation:

If there is intrinsic CP violation in the neutrino sector, then $P(\nu_\mu \rightarrow \nu_e) \neq P(\bar{\nu}_\mu \rightarrow \bar{\nu}_e)$, depending on the difference in these CP -conjugate vacuum probabilities on the oscillation parameters:

$$\Delta P \propto \left(\frac{\Delta m_{21}^2}{\Delta m_{31}^2} \right) \sin \delta \sin^2 \theta_{13}, \quad \frac{\Delta P}{P} \propto \frac{X_{21} \sin \delta}{\theta_{13}} \quad (3.30)$$

Thus, as previously pointed out, the feasibility of a measurement of the CP phase δ depends on the value of the mixing angle θ_{13} . Moreover, actual CP violation has to be distinguished from the faked one coming from matter effects by means of the proper choice of the baseline length.

5. Unitarity of the 3x3 mixing matrix:

In order to test the unitarity of the neutrino mixing matrix and thereby determine if there is room for the existence of sterile neutrinos, one needs to measure all its elements. Again, a neutrino factory could measure the needed six oscillation probabilities ($\nu_\mu \rightarrow \nu_\nu$, $\nu_\mu \rightarrow \nu_e$, $\nu_\mu \rightarrow \nu_\tau$, $\bar{\nu}_e \rightarrow \bar{\nu}_e$, $\bar{\nu}_e \rightarrow \bar{\nu}_\mu$, $\bar{\nu}_e \rightarrow \bar{\nu}_\tau$) through the detection of the six corresponding charged leptons.

6. Dirac or Majorana masses:

The only way to discover the actual nature of neutrino masses is by the measurement of the $\beta\beta^{0\nu}$ decay, since it occurs only if neutrinos are Majorana particles. In addition, the observation of such a process would provide a measurement of the neutrino effective mass $\langle m_\nu \rangle$, offering a valuable information to constrain neutrino absolute mass scale. As described in the current chapter, there are several projects for the $\beta\beta^{0\nu}$ search using different experimental approaches, and in this work we focus on the SuperNEMO proposal. No matter which technology is used, $\beta\beta^{0\nu}$ experiments face the same kind of problems: the background has to be reduced almost to zero, meanwhile the amount of isotope used has to be really large (hundreds of kg) if one wants to test the inverse hierarchy.

The fact that neutrinos are massive particles is the first discovery beyond the Standard Model. Although first round of oscillation experiments have provided a measurement of the parameters involved in the so-called solar and atmospheric sectors, the projected experiments for the near future (few years) have great potential for another breakthrough in the measurement of the mixing angle θ_{13} that connects both sectors. The same is also true for $\beta\beta^{0\nu}$ experiments: there is no reason to think that the actual neutrino mass pattern is not the inverted one, and therefore a discovery may arise within the next generation of experiments. On the other hand, a larger time scale is needed in order to test the CP -violation in oscillation experiments, as well as to reach sensitivity to the normal hierarchy region in $\beta\beta$ experiments.

Chapter 4

Evidence of massive neutrinos: the K2K experiment

As previously described in Section 3.2, several experiments have published evidences of neutrino oscillations. Along this chapter, we present results of the ν_μ disappearance analysis in K2K, the KEK to Kamioka long-baseline neutrino oscillation experiment [38]. K2K has measured neutrino oscillations with very high accuracy, proving that these particles are massive.

The sensitivity of this experiment relies strongly on a good characterization of the accelerator neutrino beam which is used. This beam is generated from hadron decays produced in an aluminum target, when a primary proton beam collides with it. Therefore a good knowledge of the hadron production cross-section is required to achieve an accurate prediction of the neutrino fluxes. HARP experiment is meant to measure such cross-sections, and indeed its first published results are of important relevance for K2K [61].

The latest K2K results were published in October 2006 [38], and they take into account results from HARP experiment, providing an increased sensitivity to the ν_μ disappearance. In fact, HARP results have allowed K2K to exclude the null oscillation hypothesis with 4.3σ . In this chapter, we describe how HARP measurements are included into K2K analysis and how the final results for the oscillation analysis are obtained.

4.1 Overview

The KEK to Kamioka long-baseline neutrino oscillation experiment (K2K) uses an accelerator-produced beam of nearly pure ν_μ with a neutrino flight distance of 250 km to probe the same Δm^2 region as that explored with atmospheric neutrinos. Neutrinos are measured first by a suite of detectors located approximately 300 meters away from the beam source and then by the Super-Kamiokande (SK) detector which is 250 km away. The near detector site consists of a 1-kiloton water Cherenkov detector (1KT) and a fine grained detector system. SK is a 50 kiloton water Cherenkov detector, located 1000 m underground.

For neutrinos of a few GeV, the dominant oscillation takes place between ν_μ and ν_τ flavor states and two-flavor oscillations are enough to describe and analyze the data. In the two-flavor neutrino oscillation framework the probability that a neutrino of energy E_ν with a flavor state ν_μ will later be observed in the ν_τ flavor eigenstate after traveling a distance L in vacuum is:

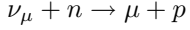
$$P(\nu_\mu \rightarrow \nu_\tau) = \sin^2 2\theta \sin^2 \left(\frac{1.27 \Delta m^2 (\text{eV}^2) L (\text{km})}{E_\nu (\text{GeV})} \right), \quad (4.1)$$

where θ is the mixing angle between the mass eigenstates and the flavor eigenstates and Δm^2 is the difference of the squares of the masses of the mass eigenstates.

The above neutrino oscillation probability causes both a suppression in the total number of ν_μ events observed at SK and a distortion of the measured energy spectrum compared to that measured at the production point. Therefore, K2K analyzes both effects separately and then joins the overall information to estimate oscillation parameters:

1. all of the beam-induced neutrino events observed at SK are used to measure the overall suppression of flux
2. the subset of these events for which the incoming neutrino energy can be reconstructed are taken into account to study the energy spectrum distortion
3. both flux reduction and spectral distortion are used to obtain best fit oscillation parameters

The neutrino energy can be reconstructed at SK, using two body kinematics, when it takes place via a charged-current (CC) quasi-elastic (QE) interaction:



In order to select the CC-QE events in the data sample, one-ring events identified as a muon ($1R\mu$) are chosen. For these events, the energy of the parent neutrino is calculated by using the observed momentum of the muon, assuming QE interactions, and neglecting Fermi momentum:

$$E_\nu^{\text{rec}} = \frac{m_N E_\mu - m_\mu^2/2}{m_N - E_\mu + P_\mu \cos \theta_\mu}, \quad (4.2)$$

where m_N , E_μ , m_μ , P_μ and θ_μ are the nucleon mass, muon energy, the muon mass, the muon momentum and the scattering angle relative to the neutrino beam direction, respectively.

The following sections describe briefly the K2K experiment and the oscillation analysis performed with data taken between June 1999 and November 2004, focusing also on the HARP experiment and its contribution to the K2K analysis.

4.2 Neutrino beam

4.2.1 K2K neutrino beam

The accelerator and the neutrino beam line for K2K consist of a 12 GeV proton synchrotron (KEK-PS), a primary proton transportation line, a hadron production target, a set of focusing horn magnets for secondary particles, a decay volume, and a beam dump. A schematic view of the KEK-PS and neutrino beam line is shown in Fig. 4.1.

Protons are accelerated by the KEK-PS to a kinetic energy of 12 GeV. After acceleration, all protons are extracted in a single turn to the neutrino beam line. The duration of an extraction, or a “spill”, is $1.1 \mu\text{sec}$, which contains 9 bunches of protons with a 125 ns time interval between them. As shown in Fig. 4.1, the beam is extracted toward the north, bent by 90° toward the direction of SK, and transported to the target station. There is a final steering magnet just before the target which directs the beam to SK at an angle of about 1° downward from horizontal.

The beam intensity is monitored by 13 current transformers (CTs) installed along the neutrino beam line as shown in Fig. 4.1. In order to measure the

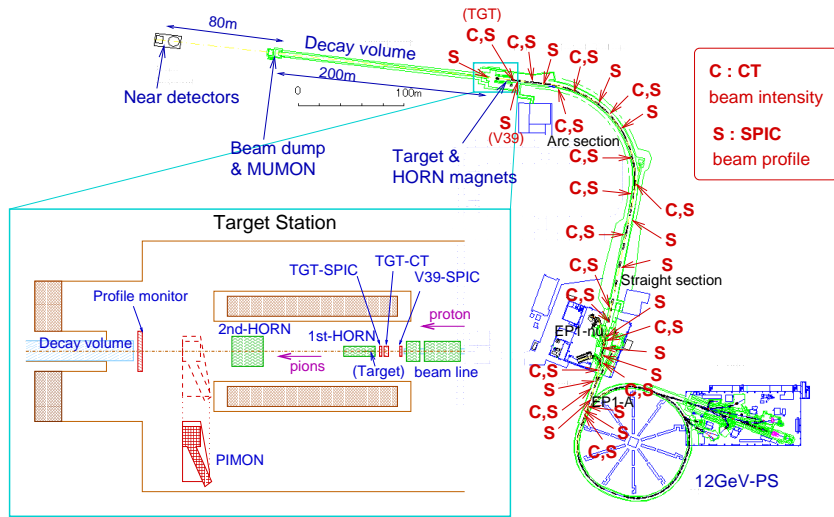


Figure 4.1: A schematic view of the KEK-PS and neutrino beam line and the location of beam line components. The lower-left inset is a magnified view of the target station. The production target and a set of horn magnets are located in the target station. A pion monitor was installed on two occasions downstream the horn magnets. Figure from [38].

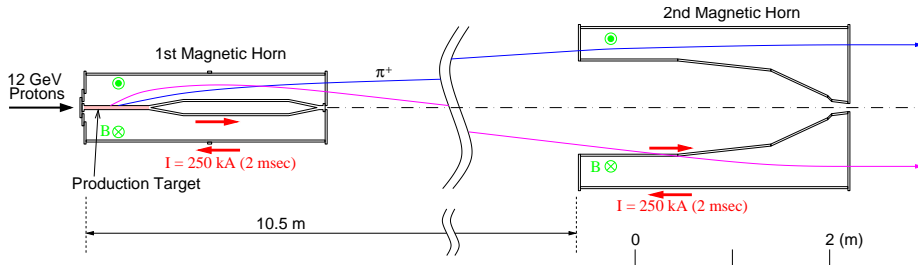


Figure 4.2: Schematic view of the two horn magnets. The production target, an aluminum rod, is embedded inside the first horn magnet. Figure from [38].

profile and the position of the beam, 28 segmented plate ionization chambers (SPICs) are also installed (Fig. 4.1). They allow the estimation of the beam size and divergence, which is used as an input to the beam MC simulation.

A hadron production target and a set of horn magnets are placed in the target station. Protons hit the target and a number of secondary particles are generated at the production target. Two toroidal magnetic horns are employed to focus positively charged particles, mainly π^+ 's, in the forward direction, increasing thus the fluxes at near and far detectors. The momentum of focused pions are around $2-3 \text{ GeV}/c$, which corresponds to about $1.0-1.5 \text{ GeV}$ of energy for those neutrinos decaying in the forward direction. A schematic view of the horn magnets is shown in Fig. 4.2. The production target, made of aluminum, is embedded inside the first horn.

A pion monitor (PIMON) was installed on two occasions just downstream the horn magnets, as shown in Fig. 4.1, in order to measure the momentum and angular distributions of pions coming through the horn magnets. The PIMON will be described in detail later in Sec. 4.4.

The positive pions focused by the horn magnets go into a 200 m long decay volume which starts 19 m downstream of the production target, where the π^+ decay: $\pi^+ \rightarrow \mu^+ \nu_\mu$. The decay volume is filled with helium gas of 1 atm (rather than air) to reduce the loss of pions by absorption and to avoid uncontrollable pion production in the gas. The beam dump made of iron is located at the end of the decay volume to absorb all the particles but neutrinos. Downstream

Periods	Ia	Ib	IIa	IIb	IIc	TOTAL
Delivered POT ($\times 10^{18}$)	6.21	49.85	24.91	20.15	3.78	104.90
POT analysis ($\times 10^{18}$)	3.10	44.83	22.57	18.61	3.12	92.23
Horn current	200 kA	250 kA	250 kA	250 kA	250 kA	
Target diameter	2 cm	3 cm	3 cm	3 cm	3 cm	
SK config.	SK-I	SK-I	SK-II	SK-II	SK-II	
LG/SciBar config.	LG	LG	SciBar	SciBar	SciBar	
SciFi Target material	water	water	water	water	Al	

Table 4.1: Summary of the number of protons on target and the experimental configuration for each running period, as defined in the text. Table from [38].

of the beam dump there is a pit containing two detectors (MUMONS), meant to measure the profile and intensity of muons with momentum greater than $5.5 \text{ GeV}/c$.

4.2.2 Summary of beam operation

K2K took data from June 1999 to November 2004. This period is divided into five according to different experimental configurations: June 1999 (Ia), November 1999 to July 2001 (Ib), December 2002 to June 2003 (IIa), October 2003 to February 2004 (IIb), and October 2004 to November 2004 (IIc). The horn current was 200 kA (250 kA) and the diameter of the production target was 2 cm (3 cm) in the Ia (other) period. The SK PMTs were full density for Ia and Ib, but were half density for IIa, IIb and IIc. There was a lead-glass calorimeter (LG) installed in between a scintillating-fiber/water-target tracker (SciFi) and a muon range detector (MRD) during the Ia and Ib periods; it was replaced by a totally active fine-segmented scintillator tracker (SciBar) for IIa, IIb and IIc. The different experimental configurations for the different periods are briefly summarized in Table 4.1, along with the number of protons delivered to the target and the number of protons used for the analysis.

4.2.3 K2K neutrino beam simulation

In order to study neutrino beam properties and to predict neutrino fluxes at the K2K detectors, a Monte Carlo (MC) simulation of the beam is used. The beam line geometry is implemented in GEANT3 [62] and particles are tracked in materials until they decay into neutrinos or are absorbed in the material. The

tracks of neutrinos are extrapolated along a straight line to the near detector (ND) and Super-Kamiokande (SK) and the fluxes and the energy spectrum at these locations are determined.

In the simulation program, protons with a kinetic energy of 12 GeV are injected into the aluminum production target. Then, an empirical formula for the differential cross-section by J. R. Sanford and C. L. Wang [63] is used to simulate the primary hadron production in the target. Parameters of this formula are obtained from a fit of two data sets: the Cho-CERN compilation, mainly from [64], and HARP data [61]. Further details on Sanford-Wang formula will be given in section 4.5.6, while differences between parameters coming from Cho-CERN and HARP will be discussed in sections 4.4 and 4.6.

Generated secondary particles are tracked by GEANT according to the GCALOR/FLUKA [65, 66] hadron model through the two horn magnets and the decay volume until they decay into neutrinos or are absorbed in materials. The produced neutrinos are extrapolated to the ND and SK according to a straight line and the energy and position of the neutrinos entering the ND and SK are stored to be used in later neutrino interaction and detector simulations.

The composition of the neutrino beam is dominated by muon neutrinos (99%) since the horn magnets mainly focus the positive pions, as can be seen in figure 4.3, where left plot shows the energy spectra of each type of neutrino at ND estimated by the beam MC simulation. The beam is contaminated with small fractions of ν_e ($\nu_e/\nu_\mu \sim 0.013$) , $\bar{\nu}_\mu$ ($\bar{\nu}_\mu/\nu_\mu \sim 0.015$) and $\bar{\nu}_e$ ($\bar{\nu}_e/\nu_\mu \sim 1.8 \times 10^{-4}$). About 97.3% of the ν_μ neutrinos come from positive pion decays, as shown in right plot of figure 4.3, being the contributions from K^+ and K_L^0 much more smaller below three GeV.

The validity of the K2K beam MC simulation has been confirmed by both HARP experiment and PIMON measurements, which will be described in detail in Sec. 4.4. Further details about Sanford-Wang parameterization and K2K beam simulation are given in sections 4.5 and 4.6.

4.3 Neutrino detectors

A near neutrino detector system (ND) is placed 300 m away from the proton target. The main purpose of the ND is to measure the direction, flux, and the energy spectrum of neutrinos before they oscillate. The schematic view of the ND during the K2K-IIb period is shown in Fig. 4.4.

The ND can be divided into two different detector systems:

- one kiloton water Cherenkov detector (1KT)

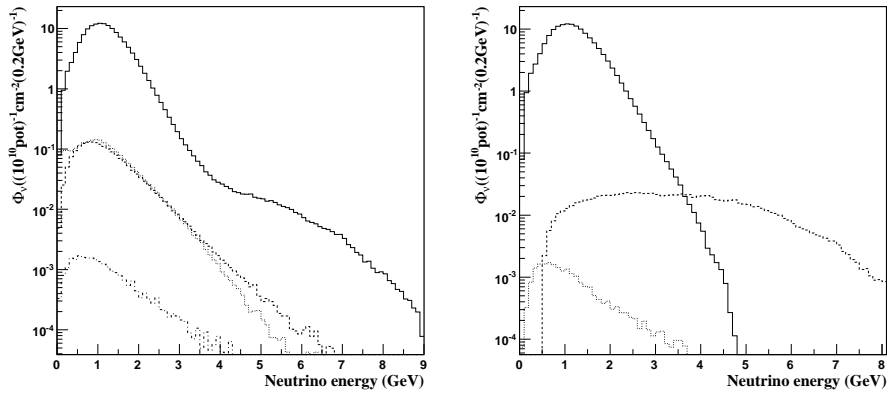


Figure 4.3: K2K neutrino beam composition. Left: The energy spectrum for each type of neutrino at ND; contributions from ν_μ , ν_e and $\bar{\nu}_e$ are shown with solid, dashed, dotted and dot-dashed lines, respectively. Right: energy spectra of ν_μ from decayed π^+ (solid line), K^+ (dashed line) and K_L^0 (dotted line).

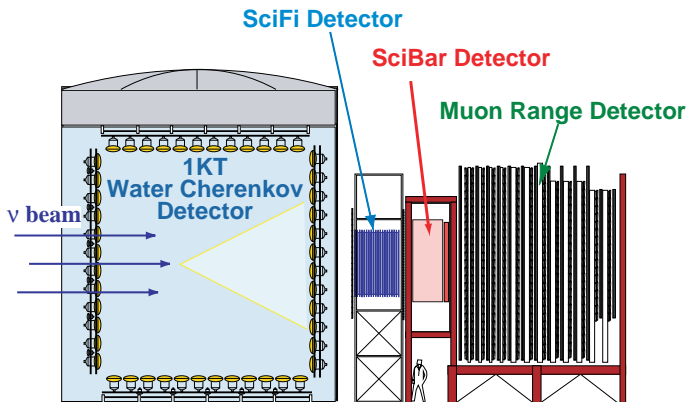


Figure 4.4: Schematic view of the near neutrino detectors for K2K-Ib period. In K2K-I, the Lead-Glass calorimeter was located at the position of the SciBar detector.

- fine-grained detector system (FGD), composed of a scintillating-fiber/water-target tracker (SciFi), a Lead-Glass calorimeter (LG) in K2K-I period, a totally active fine-segmented scintillator tracker (SciBar) in K2K-IIb and K2K-IIc periods, and a muon range detector (MRD).

Super-Kamiokande (SK) is the far detector of the K2K experiment. It is located 250 km away from the neutrino beam source at KEK, and 1000 m (2700 m water equivalent) below the peak of Mt. Ikeno-yama in Gifu prefecture.

4.3.1 Near neutrino detector system

1 kiloton water Cherenkov detector

The 1KT detector is a miniature version of SK, and uses the same neutrino interaction target material and instrumentation. The main goal of the 1KT detector is to measure the ν_μ interaction rate and the ν_μ energy spectrum.

The 1KT is a cylindrical tank containing about 1 kiloton of pure water. The tank is optically separated into the inner detector (ID) and the outer detector (OD). The walls of the ID are covered with 680 PMTs, meant to detect Cherenkov light from neutrino events taking place inside the detector. The PMTs and their arrangement are identical to those used at SK. On the other side, 68 PMTs cover the walls of the OD with the goal of vetoing incoming particles.

Reconstruction of 1KT events is performed with the same algorithms as in SK. The reconstructed quantities that define a given event are the following:

- vertex position
- number of Cherenkov rings
- particle direction

Each ring is then classified as e -like, or μ -like, using its ring pattern and Cherenkov opening angle. The momentum corresponding to each ring is determined from the Cherenkov light intensity. We define as *fully contained* (FC) those events depositing all their Cherenkov light inside the inner detector, while those depositing only a fraction of their light are classified as *partially contained* (PC).

The vertex resolution is estimated to be 14.7 cm for FC single-ring events and 12.5 cm for PC single-ring events. The angular resolution for single-ring CC-QE events is estimated to be 1.05° for FC events and 0.84° for PC events.

Regarding the quality of the particle identification, 0.3% of muon neutrino CC quasi-elastic events with a single ring are misidentified as e -like while 3.3% of electron neutrino CC quasi-elastic events with a single ring are misidentified as μ -like. The momentum resolution for muons is estimated to be 2.0-2.5% in the whole momentum range of the 1KT.

Fine-grained detector system

The FGD system consists of four different detectors, whose main goals are to measure the un-oscillated neutrino energy spectrum, and to control the stability and profile of the neutrino beam. The following gives a brief description of them:

- **scintillating fiber (SciFi) detector:**

It is a 6 ton tracking detector with integral water target layers. the SciFi detector is used to measure the neutrino spectrum and to reconstruct with high resolution the charged particle tracks produced in neutrino interactions. It can estimate the rates for quasi-elastic and inelastic interactions and it is complementary to the 1KT detector since it has sensitivity to higher energies.

- **Scintillating Bar (SciBar) detector:**

This detector was constructed as an upgrade of the near detector system. The purpose of the SciBar detector is to measure the neutrino energy spectrum and to study the neutrino interaction with high detection efficiency for low momentum particles. The main part of the SciBar detector consists of an array of plastic scintillator strips. Its totally active and finely segmented design allows to detect all the charged particles produced in a neutrino interaction. An electromagnetic calorimeter (EC) is installed downstream of the tracker part of SciBar to study the amount of the electron neutrino contamination in the beam and π^0 production in neutrino interactions. The EC is made of bars of lead and scintillating fibers, and it was originally built for the CHORUS experiment [67].

- **Muon Range (MRD) detector:**

The MRD has two purposes. The first one is to monitor the stability of the neutrino beam direction, profile and spectrum by measuring the energy, angle and vertex of muons produced in charged-current neutrino interactions. The second is to identify the muons produced in the upstream detectors and to measure their energy and angle in combination with the

other detectors in the FGD. This provides the measurement of the neutrino energy. The MRD consists of 12 layers of absorber iron.

- **Lead glass (LG) calorimeter:**

The Lead Glass (LG) calorimeter was located between SciFi and MRD in K2K-I period. The purpose of LG is to distinguish electrons from muons by measuring the energy deposit.

We refer to [38] for further details on the fine-grained detector system.

4.3.2 Far detector: Super-Kamiokande

The SK detector is a cylindrically shaped water Cherenkov detector, holding a total mass of 50 kilotons of water. The water tank is optically separated into a cylindrically-shaped inner detector (ID) and outer detector (OD). The ID is viewed by 11,146 PMTs facing inward covering 40% of the ID surface from June 1999 to 2001 (called SK-I and K2K-I), while it is viewed by 5,182 PMTs covering 19% of the ID surface from December 2002 (SK-II and K2K-II). In the OD region, outward-facing 1,885 PMTs are attached to the outer side of the supporting structure. Momentum resolution for SK-II is slightly worse than SK-I; 2.4% and 3.6% for $1 \text{ GeV}/c$ muons in SK-I and SK-II, respectively. This is because the number of ID PMTs in SK-II is about a half of SK-I. However, the performance of the vertex reconstruction, the ring counting, and the particle identification in SK-II are almost the same as in SK-I. The purity of the QE interaction in 1-ring μ -like events is 58%. The uncertainty in the energy scale is estimated to be 2.0% for SK-I and 2.1% for SK-II.

4.4 Oscillation analysis technique: the Far/Near flux ratio

The K2K experiment uses an accelerator-produced ν_μ beam with an average energy of 1.3 GeV directed at the Super-Kamiokande detector. The K2K analysis compares the observed ν_μ spectrum in Super-Kamiokande (SK), located at a distance of about 250 km from the neutrino source, with the predicted spectrum in the absence of oscillations. Thus, the main key of the analysis is the accurate prediction of the un-oscillated neutrino flux at SK. This prediction is obtained with a measurement of the spectrum near the neutrino source (with the so-called near detector system or ND) and a Monte-Carlo estimation of the ratio between SK and NSD fluxes. The last is called *far-to-near flux ratio*.

4.4.1 Definition of the far-to-near flux ratio

The effects of neutrino oscillation (ν_μ disappearance) appear in two different ways in SK measurement:

1. a reduction in the number of neutrino events
2. distortion of the neutrino energy spectrum

The observations for these quantities are compared to their expectations in SK to study neutrino oscillation. In order to obtain these expectations, we proceed as follows. The ND measures the neutrino flux and spectrum before neutrinos oscillate, and then those measurements are extrapolated by the expected ratio of muon neutrino fluxes at the far and near detector locations, the far-to-near (F/N) flux ratio, to predict the number of neutrino events and energy spectrum in SK.

The neutrino flux at any distance from its source can be predicted when the geometry of the decay volume and the momenta and directions of the pion parents of neutrinos are provided. Due to the finite size of the decay volume and the detectors, the neutrino flux does not simply obey an L^{-2} rule (where L is distance from the neutrino source); rather the flux ratio between far and near detectors has some dependence on neutrino energy, correcting for the fact that at the ND, the neutrino source is not point-like, but sensitive to effects such as the finite size of the decay tunnel, etc., whereas at the SK site the neutrino source can be considered as point-like.

Therefore, we define the F/N flux ratio, $R^{F/N}$, as

$$R^{F/N} = \frac{\Phi^{SK}(E_\nu)}{\Phi^{ND}(E_\nu)}, \quad (4.3)$$

where $\Phi^{SK(ND)}(E_\nu)$ is the neutrino energy spectrum at SK (ND).

4.4.2 Prediction of the far-to-near ratio

The F/N flux ratio is estimated by the beam MC simulation. Assuming a given model for hadron production in the aluminum target, it is straight forward to compute the ratio between fluxes at SK and ND, according to the simulation. The key point here is that different hadron models lead to different F/N flux ratios, and thus one realizes that there may be an important systematic error associated to $R^{F/N}$.

The K2K beam Monte-Carlo used to have the Cho-CERN compilation as the reference model to simulate hadron generation, using the Sandford-Wang parameterization as explained in Section 4.2.3. However, this model comes from really old data [64] and needs to be rescaled since data was taken on beryllium target. Consequently, F/N ratio suffers from big systematic errors when using this model. To fix this situation, latest analysis from K2K [38] takes HARP experiment results to simulate positive pion production, as it will be described in Sections 4.5 and 4.6.

An experimental validation of the hadron model used in the simulation has been carried out by the pion monitor (PIMON). It provides *in-situ* information on the momentum and the direction of pions entering the decay volume after they are focused by the horn magnetic fields. However, PIMON is not sensitive to pions below $2 \text{ GeV}/c$ (corresponding to neutrinos below 1 GeV) due to the threshold set to avoid background from primary protons of $12 \text{ GeV}/c$, so we have to rely completely on a model prediction for this region. Recall maximum of the oscillation is within 0.5 and 1.0 GeV , and therefore pions below $2 \text{ GeV}/c$ are indeed very important for the flux.

A schematic view of PIMON is shown in Fig. 4.5.

PIMON is a gas Cherenkov imaging detector which consists of a gas vessel, a spherical mirror, and an array of 20 photomultiplier tubes. The Cherenkov photons emitted by pions passing through the gas vessel are reflected toward and focused onto the PMT array by the spherical mirror. Then, the PMT array on the focal plane detects the Cherenkov image. Due to the characteristics of the spherical mirror, photons propagating in the same direction are focused to the same position on the focal plane, giving us information on the direction of the pions. The pion momentum is also obtained from the size of the Cherenkov ring. Furthermore, a momentum scan can be done by varying the refractive index of the inner gas. Therefore, the momentum and direction of pions can be measured separately by looking at the Cherenkov light distribution on the focal plane.

4.4.3 Impact of far-to-near ratio uncertainties

To get an idea of the relevance of the F/N uncertainties, regarding the final oscillation analysis results, one has to recall K2K publications before 2006 [68], when the Cho model was still being used to simulate hadron production.

Uncertainties on $R^{F/N}$ above $E_\nu = 1 \text{ GeV}$ were estimated from PIMON measurements, while estimation of errors below 1 GeV relied completely on the hadron production model. The expected number of fully contained events at

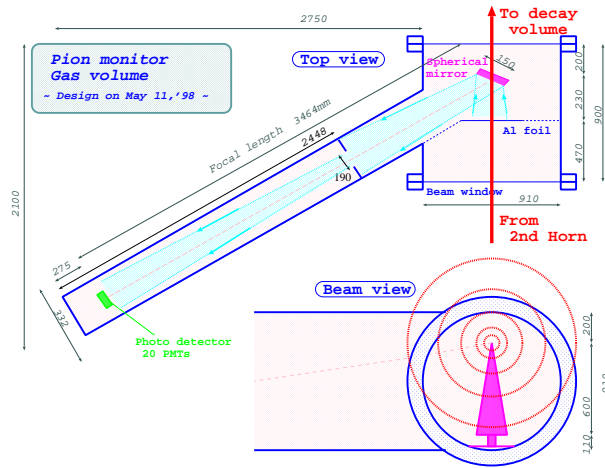


Figure 4.5: A schematic view of the pion monitor (PIMON). The PIMON consists of a gas vessel, a spherical mirror, and an array of 20 photomultiplier tubes. The gas vessel is filled with freon gas R-318 (C_4F_8). A wedge-shaped spherical mirror is set inside the gas vessel and Cherenkov light produced by the pions in the beam, represented by the concentric circles in the figure, is reflected by the mirror and directed to the array of photo-multiplier tubes which is set in the focal plane.

SK was 151^{+12}_{-10} (syst), where the major contributions to the errors came from the F/N flux ratio (5.1%) and the normalization (5.1%). Table 4.2 shows errors on $R^{\text{F}/\text{N}}(\%)$ in the analysis published in [68], when Cho model was used.

It is clear from these numbers that errors on $R^{\text{F}/\text{N}}$ have a big impact on the oscillation analysis. In fact, they are the dominant ones concerning the oscillation analysis based on the number of expected events. This is the main reason to include HARP results into the K2K analysis: a better knowledge of production hadronic cross-sections leads to more accurate estimation of the F/N flux ratio, and consequently to a higher sensitivity to neutrino oscillations. In the next Sections 4.5 and 4.6 we present the work developed to use HARP cross-sections as the new hadron production model of the K2K beam Monte-Carlo. As will be shown, using the HARP model will reduce uncertainties on $R^{\text{F}/\text{N}}$ down to the point in which they are not dominant anymore.

E_ν (GeV)	0-0.5	0.5-0.75	0.75-1.0	1.0-1.5	1.5-2.0	2.0-2.5	2.5-3.0	3.0 -
$\Delta(F/N)(\%)$	2.6	4.3	4.3	4.9	10	11	12	12

Table 4.2: Percentages of uncertainties in F/N flux ratio ratio, in each energy bin of the *old* K2K analysis [68].

4.5 Understanding K2K neutrino flux: HARP experiment

As explained in section 4.2.3, K2K beam Monte-Carlo needs as an input a model describing hadron (mainly positive pions) production in the aluminum target. K2K Monte-Carlo used to rely on old measurements for beryllium targets [64], and this led to big uncertainties in the predicted fluxes. In fact, errors coming from predicted fluxes were one of the dominant errors in the K2K analysis [68].

The objective of the HARP experiment is a systematic study of hadron production for beam momenta from $1.5 \text{ GeV}/c$ to $15 \text{ GeV}/c$ for a large range of target nuclei [69]. The main motivations are: a) to measure pion yields for a quantitative design of the proton driver of a future neutrino factory, b) to improve substantially the calculation of the atmospheric neutrino flux and c) to provide input for the flux calculation of accelerator neutrino experiments, such as K2K and MiniBooNE.

A precision measurement of the double-differential production cross-section for pions of positive charge, performed in the HARP experiment is presented in this section. The incident particles are protons of $12.9 \text{ GeV}/c$ momentum impinging on an aluminium target of 5% nuclear interaction length. The measurement of this cross-section has a direct application to the calculation of the neutrino flux of the K2K experiment. Results of this analysis were published in [61], so we refer to this publication for further details.

4.5.1 Need for HARP experiment

The dominant uncertainty in neutrino flux predictions for conventional neutrino beams is due to the pion production uncertainty in the hadronic interactions of primary beam protons with the nuclear target material. The measurement of the π^+ production cross-section is of particular relevance in the context of the recent results presented by the K2K experiment [68], which have shown evidence for neutrino oscillations at a confidence level of four standard deviations.

The neutrino beam of the K2K experiment originates from the decay of light hadrons, mainly pions, produced by exposing an aluminium target to a proton beam of momentum $12.9 \text{ GeV}/c$. In this section, the measurement of the double-differential cross-section, $d^2\sigma^{\pi^+}/dpd\Omega$ of positive pion production for protons of $12.9 \text{ GeV}/c$ momentum impinging on a thin Al target of 5% nuclear interaction length (λ_I) is presented, *i.e.* reproducing closely the conditions of the K2K beam-line for the production of secondaries.

According to the neutrino oscillation parameters measured in atmospheric neutrino experiments [28] the distortion of the spectrum measured with the far detector is predicted to be maximal in the energy range between 0.5 and 1 GeV. The determination of F/N ratio is the leading energy-dependent systematic error on the number of expected events in the K2K analysis presented in [68].

In particular, the recent HARP pion production measurement [61] is directly relevant for the K2K F/N flux ratio because it is obtained for the same proton beam momentum ($12.9 \text{ GeV}/c$) and nuclear target material (aluminum) as those used to produce the K2K neutrino beam. Moreover, beam MC simulations show that the forward pion production region measured in HARP, $30 < \theta_\pi < 210 \text{ mrad}$, $0.75 < p_\pi < 6.5 \text{ GeV}/c$, matches well the pion production phase space responsible for the dominant fraction of the K2K muon neutrino fluxes at both the near and far detector locations. Fig. 4.6 shows (p, θ) distribution of pions decaying into neutrinos reaching near and far detectors. HARP phase space covers 80% of the total neutrino flux in the near detector and in the relevant region for neutrino oscillations. Thus, it can provide an independent, and more precise, measurement of the pion yield needed as input to the calculation of the K2K F/N flux ratio than that currently available.

4.5.2 Experimental apparatus

The HARP detector, shown in Fig. 4.7, consists of forward and large-angle detection systems. The convention used for the coordinate system is also given in the Figure. In the large-angle region a TPC positioned in a solenoidal magnet is used for tracking. The forward spectrometer is built around a dipole magnet with an integral field of $\int B_y dL = 0.66 \text{ T m}$ for momentum analysis, with large planar drift chambers (NDC) for particle tracking, and three detectors used for particle identification: a time-of-flight wall (TOFW), a threshold Cherenkov detector (CHE), and an electromagnetic calorimeter (ECAL). The target itself is located inside the TPC. Beam instrumentation, including three timing detectors (BTOF) and two threshold Cherenkov detectors (BCA and BCB), provides identification of the incoming particle and the determination of the interaction

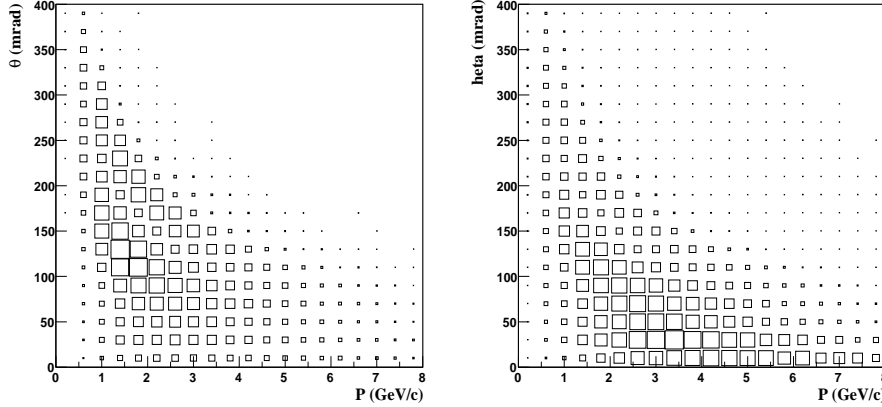


Figure 4.6: Distribution of pions (p vs (θ)) decaying into neutrinos reaching near (left) and far (right) K2K detectors.

time at the target. The impact point of the beam particle on the target and its direction are measured by a set of multi-wire proportional chambers (MWPCs). Several trigger detectors are available to select events with an interaction and to define the normalization. One of them is a double plane of scintillation counters (FTP), placed upstream of the dipole magnet, which is used to select events with an interaction in the target and outgoing charged particles in the forward region. The plane covers the full aperture of the dipole magnet, with the exception of a central hole with a diameter of 60 mm to let the beam particles pass.

Data were taken with several beam momenta and target configurations. In addition to the data taken with the thin aluminium target of 5% λ_I at an incident proton momentum of 12.9 GeV/c , runs were also taken with an empty target holder. These data allow a subtraction to be made of the interactions occurring in the material on the path of the incident beam. Other relevant configurations for the measurement described here are the data taken with and without target with other beam momenta (1.5, 3.0, 5.0, 8.0, 8.9 and 15 GeV/c) with electrons, pions and protons. These settings have been used to determine the response of the spectrometer to these particles in terms of efficiency, momentum resolution and particle identification capability. The momentum definition of the T9 beam is known with a precision of the order of 1% [70].

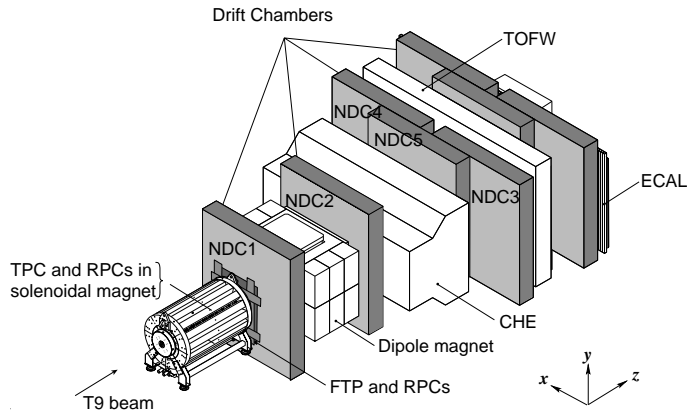


Figure 4.7: Schematic layout of the HARP spectrometer. The convention for the coordinate system is shown in the lower-right corner. The three most downstream (unlabeled) drift chambers are only partly equipped with electronics and not used for tracking.

A detailed description of the HARP spectrometer is given in Ref. [71]. In this analysis we utilize primarily the detector components of the forward spectrometer and the beam instrumentation.

Drift chambers

The main tracking device of the HARP forward spectrometer is a set of large drift chambers (NDC) placed upstream and downstream of the dipole magnet.

The spectrometer contains five NDC modules, each of which is made of four chambers. The chambers consist of three wire planes, with one plane (x) of wires oriented vertically; the other two (u and v) are rotated with respect to the vertical by ± 5 degrees. The spatial resolution of the chamber is about $340 \mu\text{m}$. The hit efficiency varies between 80% and 85% in the central NDC modules.

PID detectors

Particle identification is performed in the forward spectrometer through the combination of several detectors downstream of the dipole magnet (CHE, TOFW and ECAL). We refer to [71] for a detailed description of the three systems.

A large scintillator wall (TOFW) covering the full acceptance of the downstream tracking system is used in conjunction with the timing information from the beam detectors to measure the time-of-flight of the secondary particles for momenta up to $5 \text{ GeV}/c$. The TOFW measures the time-of-flight of particles emanating from the target, and this, together with the charged track trajectory length, l , determines the velocity, β , of the particle. A time-of-flight resolution better than 180 ps is achieved using this detector in combination with the BTOF system.

The threshold Cherenkov detector (CHE) separates pions from protons for momenta above the pion threshold ($2.6 \text{ GeV}/c$) and identifies electrons below the pion threshold. The radiator gas (perfluorobutane C_4F_{10}) is chosen for its high refractive index, which allows the detector to be operated at atmospheric pressure.

Finally, the electromagnetic calorimeter (ECAL) provides electron rejection. It is segmented longitudinally into two planes. The ratio of the energy deposition in the two planes is different for electrons compared to hadrons. In addition, the comparison of the momentum of the particle measured by the curvature of its trajectory and the energy deposition in the calorimeter provides another way to identify electrons. The ECAL complements the electron rejection of the Cherenkov above the pion Cherenkov threshold.

4.5.3 Tracking with the forward spectrometer

The track reconstruction algorithm starts by building three dimensional segments (3D) per NDC module. Once track segments are formed in the individual modules they are combined (downstream of the dipole magnet) to obtain longer track segments. Finally, downstream tracks are connected with either the interaction vertex or a 3D track segment in NDC1 (the NDC module upstream the dipole magnet, see Fig. 4.7) to measure the momentum. All these tasks are performed by a sophisticated fitting, extrapolation and matching package called RecPack [72], which is based on the well known Kalman Filter technique [73].

The interaction vertex in this analysis is well defined. The transverse coordinates (x, y) are obtained by extrapolating the trajectory of the incoming beam particle, measured with the MWPCs (with an error of the order of 1 mm), and

the z coordinate can be taken as that of the nominal plane of the target (which is 19.80 mm thick).

Consequently, the momentum of a track can be determined by imposing the constraint that it emanates from the vertex, that is, by connecting a 3D segment downstream of the dipole magnet with a 3D point upstream of the magnet. Tracks of this type are called ‘VERTEX2 tracks’, and the estimator of the momentum obtained by connecting a 3D segment with the vertex 3D point is denoted ‘ p_2 ’.

Alternatively, one can measure the momentum connecting a 3D segment downstream of the dipole with a 3D segment in the NDC1 module. These are called ‘VERTEX4 tracks’, and the estimator of the momentum is denoted ‘ p_4 ’.

The availability of two independent momentum estimators allows the tracking efficiency to be measured from the data themselves. This is possible, since

1. the reconstruction methods providing the estimators p_2 and p_4 are independent,
2. p_2 and p_4 have a Gaussian distribution around the true momentum p (the distribution is expected to be Gaussian in the variable $1/p$ rather than p , but with the relatively good resolution the difference is negligible).

This makes it possible to use one of the estimators (p_2) to measure the yields while the other (p_4) is used to measure tracking efficiency. The estimator p_2 is preferred to measure yields since it does not involve the use of the NDC1 module, where tracking efficiency is lower than in the downstream modules.

The linear correlation between p_2 and p_4 , shown in Fig. 4.8 (left panel) for simulated tracks, illustrates the fact that both are estimators of the same quantity, while the correlation between p_4 and p (Fig. 4.8, right panel) shows that both are unbiased estimators of p . The small non-linearities and disagreements between p_2 and p_4 and between p_4 and p have negligible contribution to the total systematic uncertainty.

Momentum and angular resolution

The momentum resolution as a function of the momentum is shown in Fig. 4.9 (left panel), for the case of p_2 . The resolution can be measured using beam particles of several momenta. Also shown (open circles) is the corresponding resolution found using the Monte Carlo.

Figure 4.9 (right panel), shows the angular resolution. Both the momentum and angular resolutions are small compared with the size of the bins used in

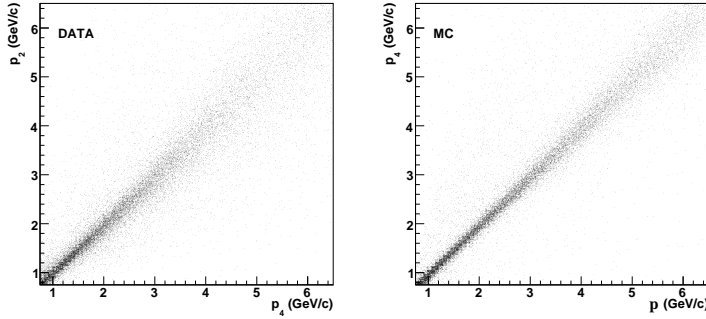


Figure 4.8: Left panel: The correlation between p_2 and p_4 , showing that both are estimators of the same quantity; right panel: the correlation between p_4 and p shows that p_4 is an unbiased estimator of the momentum p within the momentum resolution and binning (from 500 MeV/c up to 1.5 GeV/c) used in the analysis.

this analysis (500 MeV/c momentum bins, up to 4 GeV/c, 1000 MeV/c from 4 to 5 GeV/c, 1500 MeV/c from 5 to 6.5 GeV/c, and 30 mrad angular bins). In the region of interest, the agreement between data and Monte Carlo is good for the momentum resolution, while for the angular resolution the difference is less than 1 mrad, negligible compared to the bin size. Thus effects due to the finite resolution are small, and it is safe to apply a Monte Carlo based correction.

The charge misidentification rate has been estimated by computing the fraction of protons that are reconstructed with negative charge. This is done by measuring the fraction of negative particles with momenta above the pion CHE threshold that give no signal in CHE. The upper limit of 0.5% for the charge misidentification probability is found to be consistent with the known CHE inefficiency.

Definition of kinematical variables

The final cross section, being rotationally invariant around the beam axis, can be expressed in polar coordinates (p, θ) , where p is the true total momentum of the particle and θ is the true angle with respect to the beam axis (approximately equivalent to the z axis). However, given the rectangular geometry of the dipole and of the drift chambers, some of the corrections needed to com-

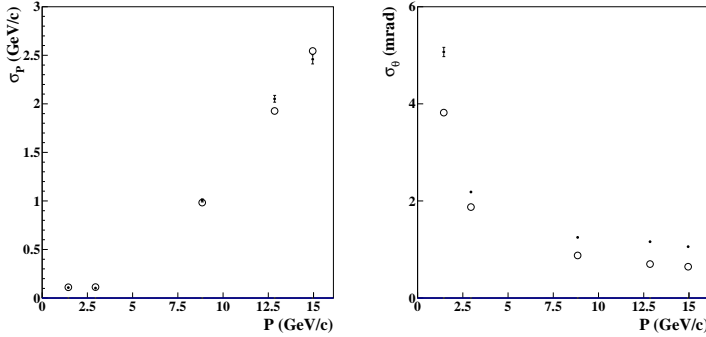


Figure 4.9: Left panel: momentum resolution (p_2) obtained from fits to data (points with error bars) taken using several well-defined discrete beam momenta and no target. Also shown (open circles) is the corresponding resolution found using the Monte Carlo. Right panel: angular resolution obtained from fits to data (points with error bars) taken using several well-defined discrete beam momenta and no target. The open circles show again the corresponding resolution found using the Monte Carlo. In the region of interest, the agreement between data and Monte Carlo is good for momentum resolution with values much smaller than the binning used in the analysis (from 500 MeV/c for $p < 4$ GeV/c up to 1.5 GeV/c at $p = 6.5$ GeV/c). Similarly the difference between measured and predicted angular resolution is negligible compared to the 30 mrad binning adopted in the analysis.

pute the cross-section are most naturally expressed in terms of (p, θ_x, θ_y) , where $\theta_x = \arctan(p_x/p_z)$ and $\theta_y = \arctan(p_y/p_z)$. Thus the conversion from rectangular to polar coordinates is carried out at a later stage of the analysis.

Track reconstruction efficiency

The track reconstruction efficiency, $\varepsilon^{\text{track}}(p, \theta_x, \theta_y)$, is defined as the fraction of tracked particles (with position and momentum measured) N^{track} with respect to the total number of particles N^{parts} reaching the fiducial volume of the HARP spectrometer as a function of the true momentum, p , and angles, θ_x, θ_y :

$$\varepsilon^{\text{track}}(p, \theta_x, \theta_y) = \frac{N^{\text{track}}(p, \theta_x, \theta_y)}{N^{\text{parts}}(p, \theta_x, \theta_y)} . \quad (4.4)$$

The track reconstruction efficiency can be computed using the redundancy of the drift chambers taking advantage of the multiple techniques used for the track reconstruction.

The total tracking efficiency can be expressed as the product of two factors. One factor represents the downstream (of the dipole magnet) tracking efficiency and the other represents the efficiency for matching a downstream segment to a vertex (for tracks originating inside the target volume):

$$\varepsilon^{\text{track}} = \frac{N^{\text{down}}}{N^{\text{parts}}} \cdot \frac{N^{\text{vertex2}}}{N^{\text{down}}} = \varepsilon^{\text{down}} \cdot \varepsilon^{\text{vertex2}} , \quad (4.5)$$

where N^{vertex2} is the number of VERTEX2 tracks, which corresponds to N^{track} in Eq. 4.4. In the momentum range of interest for this analysis, a good time-of-flight measurement is essential for particle identification. Therefore, one also requires a good TOFW hit matched to the track.

The TOFW hit matching efficiency ε^{ToF} was computed using the same track sample as for the tracking efficiency. Thus, the total reconstruction efficiency is found from:

$$\varepsilon^{\text{recon}} = \varepsilon^{\text{track}} \cdot \varepsilon^{\text{ToF}} . \quad (4.6)$$

The total reconstruction efficiency is shown in Fig. 4.10.

The total reconstruction efficiency as a function of θ_x has a slight slope and drops for positive θ_x above 100 mrad. This drop is due to the momentum-dependent acceptance limitation imposed by the dipole magnet, as clearly demonstrated by Fig. 4.10 (upper-right), which shows a flat distribution in the non-bending plane θ_y and Fig. 4.10 (lower-left), which shows the efficiency as a

function of p , integrated for all θ_x . The drop of the efficiency for large values of θ_x is fully correlated with the drop at low p . This can be seen in Fig. 4.10 (lower-right), where the reconstruction efficiency as a function of p for negative θ_x (particles fully contained in the dipole acceptance) is shown. On the other hand, efficiency drops for high momenta due to a weakness in the reconstruction algorithm (notice drop is well reproduced by the MC). The total reconstruction efficiency as a function of p for negative θ_x is flat (and about 90%) for momenta below 4 GeV/ c . The inefficiency of about 10% is mainly due to the inefficiency in matching tracks to a TOFW hit. The agreement between data and Monte Carlo for the total reconstruction efficiency is excellent, except in the last momentum bin, where there is a 6% difference. This bin is not used in the current analysis.

4.5.4 Particle identification

A set of efficient PID algorithms to select pions and reject other particles is required for the current analysis. A Monte Carlo prediction of the differential yields of the various particle types shows that the pion production cross-section is small above 6.5 GeV/ c , which is set as the upper limit of this analysis. The electron distribution peaks at low energy, while the proton background increases with momentum. The kaon yield is expected to be only a small fraction of the pion yield. In the momentum and angular range covered by the present measurements the proton yield is of a similar order of magnitude as the pion yield.

The PID strategy is based on the expectation of the yields of different particle types predicted by the Monte Carlo, and also on the momentum regions covered by the available PID detectors.

Response of PID detectors

The time-of-flight measurement with the combination of BTOF and TOFW systems (referred to as the TOFW measurement in what follows) allows pion–kaon and pion–proton separation. We use the particle velocity, β , to characterize the TOFW response. Its distribution is nearly Gaussian and it discriminates very effectively between pions and protons up to momenta around 5 GeV/ c (at this energy the separation between the average values of the proton and pion Gaussians is around 2.2σ). Figure 4.11 shows the mean value of β and its

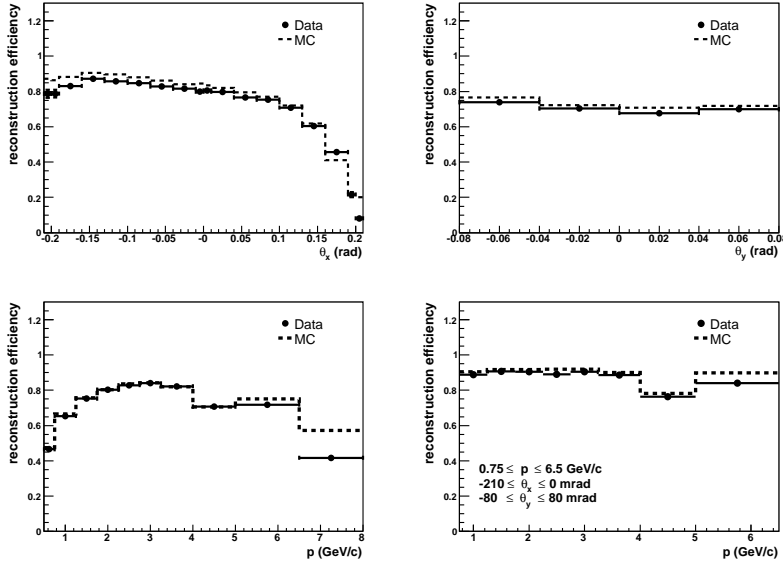


Figure 4.10: Total reconstruction efficiency as a function of kinematic variables, p , θ_x , and θ_y , at production for positively charged particles emanating from the vertex. Upper-left panel: as a function of θ_x . Upper-right panel: as a function of θ_y . Lower-left panel: as a function of p . Lower-right panel: as a function of p averaged over the θ_x and θ_y regions used in the present analysis only. The efficiency is close to 90% for negative θ_x and momenta less than 4 GeV/c , and drops for high values of θ_x (due to the TOFW and NDC acceptances) and for high momenta (due to a weakness in the reconstruction algorithm). Points with error bars correspond to data, the dashed line to Monte Carlo. The agreement is excellent, except in the bin with highest momentum, where the difference is 6%.

standard deviation as a function of momentum for protons and pions. As can be seen, data and Monte-carlo agree quite well.

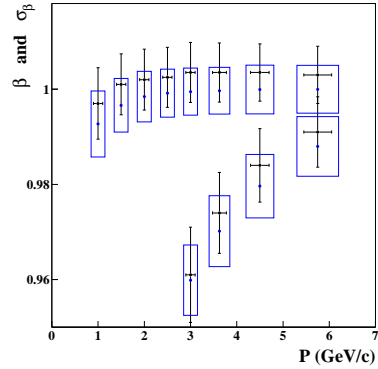


Figure 4.11: Mean value of β (points) and its standard deviation (error bars and rectangles) as a function of momentum for protons and pions. Points with error bars correspond to selected events from real data, while rectangles correspond to MC events. The centres of the rectangles are indicated with points.

The Cherenkov is used for hadron-electron separation below $2.5 \text{ GeV}/c$ and pion–proton/kaon separation above $2.5 \text{ GeV}/c$ in conjunction with the TOFW. The Cherenkov detector (CHE) is used digitally in this analysis: a signal is accepted if the number of photoelectrons is larger than 2. In the momentum range studied no signal is expected in the CHE for protons. However, in a fraction of events, the reconstruction algorithm wrongly associates the CHE hit from a pion or an electron to the proton and consequently, a fraction of protons has a non-negligible amount of associated photoelectrons. This is a potential source of background (as well as of pion inefficiency), particularly important at high momentum, where the TOFW is not applicable. The efficiency of the CHE for protons has been measured as a function of momentum and angle. The results are shown in Fig. 4.12 (right panel). This non-zero efficiency is fully taken into account in this analysis as explained in Ref. [74].

In the current analysis, the ECAL is used only to separate hadrons from electrons below $2.5 \text{ GeV}/c$ to study the Cherenkov performance.

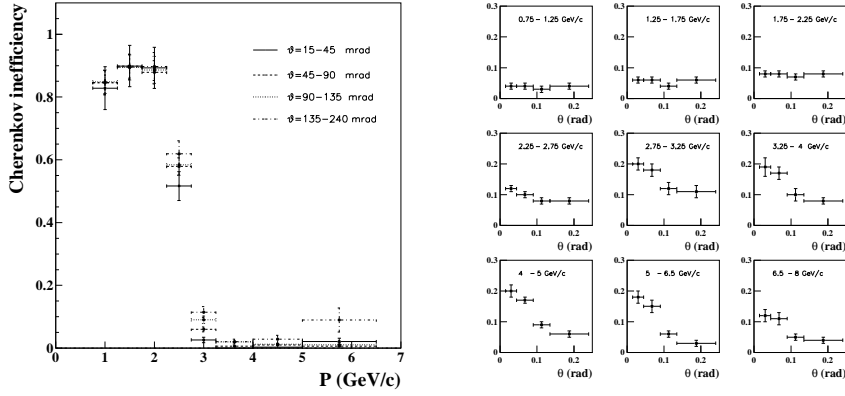


Figure 4.12: Left panel: CHE pion inefficiency as a function of the momentum for different angular regions. Right panel: CHE proton efficiency as a function of the angle for different momentum regions.

As mentioned above, the electron(positron) background is concentrated at low momentum ($p < 2.5$ GeV/c). It can be suppressed to negligible level with an upper limit on the CHE signal, given the fact that electrons are the only particles giving signal in the Cherenkov below the pion Cherenkov light emission threshold, which is equal to 2.6 GeV/c for the gas mixture used in HARP. In practice, any particle that has a momentum below 2.5 GeV/c and a signal in the CHE exceeding 15 photo-electrons is called an electron. In the following we will refer to this cut as the e-veto cut. The remaining electron background after the e-veto cut is negligible. Figure 4.13 shows ratio between e and π yields before and after e-veto application.

Particle identification strategy

Having applied the e-veto cut to reject electrons and keeping in mind that there is a small fraction of kaons, one builds PID estimators for protons and pions by combining the information from TOFW and CHE using likelihood techniques. Then, a cut on these PID estimators is applied to select pions or protons. The selected samples (raw pion and proton samples) will contain a

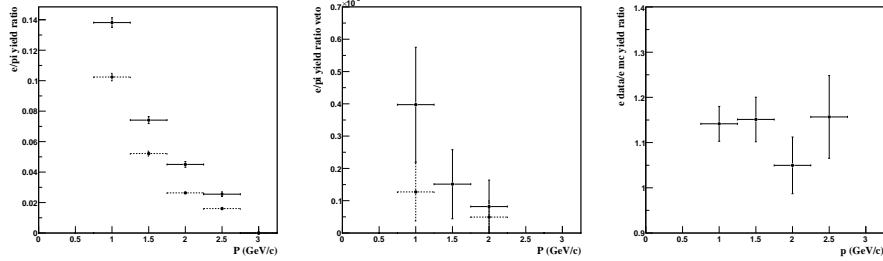


Figure 4.13: Ratio between e and π yields (e/π). Solid and dashed lines correspond to e^- and e^+ respectively Left: e/π ratio before application of the e-veto, according to Monte-Carlo Center: e/π ratio after application of the e-veto, according to Monte-Carlo Right: ratio between e yields in data and Monte-carlo.

small fraction of kaons, which can be estimated from the data, as described in Ref. [74]. This background is subtracted from the dominant yields of pions and protons.

The quantities that enter the cross-section calculation are the raw pion and proton yields and the PID efficiencies and purities (PID corrections, including kaon subtraction) obtained by the application of the e-veto cut and cuts in the PID estimators.

More details are given in Ref. [74].

4.5.5 Calculation of the cross-section

The double-differential cross-section for the production of a particle of type α can be expressed in the laboratory system as:

$$\frac{d^2\sigma_\alpha}{dp_i d\theta_j} = \frac{1}{N_{\text{pot}}} \frac{A}{N_A \rho t} M_{ij\alpha i' j' \alpha'}^{-1} \cdot N_{i' j'}^{\alpha'}, \quad (4.7)$$

where $\frac{d^2\sigma_\alpha}{dp_i d\theta_j}$ is expressed in bins of true momentum (p_i), angle (θ_j) and particle type (α), and the terms on the right-hand side of the equation are:

- $N_{i' j'}^{\alpha'}$ is the number of particles of observed type α' in bins of reconstructed momentum ($p_{i'}$) and angle ($\theta_{j'}$). These particles must satisfy the event,

track and PID selection criteria, explained below. This is the so called ‘raw yield’.

- $M_{ij\alpha i'j'\alpha'}^{-1}$ is a correction matrix which corrects for finite efficiency and resolution of the detector. It unfolds the true variables $ij\alpha$ from the reconstructed variables $i'j'\alpha'$ and corrects the observed number of particles to take into account effects such as reconstruction efficiency, acceptance, absorption, pion decay, tertiary production, PID efficiency and PID misidentification rate.
- $\frac{A}{N_A \rho t}$ is the inverse of the number of target nuclei per unit area (A is the atomic mass, N_A is the Avogadro number, ρ and t are the target density and thickness).
- N_{pot} is the number of incident protons on target.

The summation over reconstructed indices $i'j'\alpha'$ is implied in the equation. It should be noted that the experimental procedure bins the result initially in terms of the angular variable θ , while the final result will be expressed in terms of the solid angle Ω . Since the background from misidentified protons in the pion sample is not negligible, the pion and proton raw yields ($N_{i'j'}^{\alpha'}$, for $\alpha' = \pi, p$) have to be measured simultaneously.

For practical reasons, the background due to interactions of the primary proton outside the target (called ‘Empty target background’) has been taken out of the correction matrix M^{-1} . Instead, a subtraction term is introduced in Eq. 4.7:

$$\frac{d^2\sigma_\alpha}{dp_i d\theta_j} = \frac{1}{N_{\text{pot}}} \frac{A}{N_A \rho t} M_{ij\alpha i'j'\alpha'}^{-1} \cdot \left[N_{i'j'}^{\alpha'}(\text{T}) - N_{i'j'}^{\alpha'}(\text{E}) \right], \quad (4.8)$$

where (T) refers to the data taken with the aluminium target and (E) refers to the data taken with no target (Empty target).

Measurement of the raw yields

First step to measure the raw yields $N^{\alpha'}$ is to select events. Beam instrumentation allows identification of beam protons. Only protons with a good timing signal and leaving a single track in the MWPC’s are selected. These two cuts are meant to ensure a good measurement of the time and vertex (impact point on the aluminium target) of the event. The purity of the proton sample obtained in such a way is 99.5%. In order to ensure the interaction of the proton with

Data Set	Al 5%	Empty Target
Protons on target	17,954,688	4,769,408
Total events processed	4,710,609	771,330
Events with accepted beam proton	3,404,372	547,838
FTP triggers	2,087,732	225,639
FTP trigger rate = (FTP triggers / pot)	0.116	0.047
Total good tracks	209,929	11,704

Table 4.3: Total number of events in the 12.9 GeV/ c aluminium 5% λ_I target and empty target data sets.

the target, events used in this analysis are required to have one or more hits in the forward trigger plane (FTP).

Applying the above selection cuts to the 12.9 GeV/ c aluminium 5% λ_I target data set and the 12.9 GeV/ c empty target data set results in the total statistics listed in Table 4.3. The total number of protons on target (N_{pot} in Eq. 4.7) listed in the table is exactly the number to be used in the overall normalization of the cross-section results, and is known to better than 1%.

Next step is to apply selection cuts to the tracks in the events. The recorded events have been processed according to the track selection criteria listed below:

- VERTEX2 track momentum is measured (see Section 4.5.3).
- A track segment in NDC2 or in the back-plane is used in track reconstruction.
- Number of hits in a road around the track in NDC1 ≥ 4 (this is applied to reduce non-target interaction backgrounds).
- average χ^2 for hits with respect to the track in NDC1 ≤ 30 ,
- Number of hits in the road around the track in NDC2 ≥ 6 (this is applied to reduce background of tracks not coming from the target).
- The track has a matched TOFW hit.

The result of applying these cuts to the entire 12.9 GeV/ c aluminium 5% λ_I and empty target data sets is listed in Table 4.3.

In addition, geometrical cuts are applied. As described in Sec. 4.5.3 for positive θ_x the efficiency is momentum dependent. This region is avoided in the analysis by defining the fiducial volume as $-210 \leq \theta_x < 0$ mrad (thus, only particles in the negative half of the bending plane of the dipole are accepted) and $-80 < \theta_y < 80$ mrad. The restricted acceptance in θ_y is imposed to avoid edge effects of the dipole, possible fringe effects in the magnetic field, etc. Since the behavior of the spectrometer is calibrated with beam particles (at $\theta_y = 0$) the analysis restricts θ_y to a rather small region around the horizontal mid-plane of the spectrometer. In order to avoid a correction for the acceptance of the FTP-trigger and to avoid background from beam protons, cross-sections are given for $\theta > 30$ mrad.

Finally, PID algorithms are applied to the tracks in order to identify particles. In the current analysis only positive pions have been considered.

Calculation of the correction matrix

As discussed in section 4.5.3, both the momentum and angular resolution are small compared with the binning of the cross-section. Migration effects are, therefore, small. In particular, angular migration can be neglected. In addition, kinematic migration is almost decoupled from pion–proton PID migration. As explained in Sec. 4.5.4 electron and kaon ID has been decoupled from the dominant pion–proton ID so that electron and kaon correction factors are diagonal in the PID variables. With the above considerations the correction matrix M^{-1} can be written as:

$$M_{ij\alpha i' j' \alpha'}^{-1} = (M_{ij;\alpha\alpha'}^{id})^{-1} \cdot \varepsilon_{ij\alpha'}^{-1} \cdot (M_{jj'}^{\theta})^{-1} \cdot (M_{ii'}^p)^{-1}, \quad (4.9)$$

where again reconstructed indices are indicated with a prime. The corrections are applied in the order from right to left as they appear in the equation. The symbols in Eq. (4.9) have the following meaning:

- $\varepsilon_{ij\alpha'}^{-1}$ is the collection of factors applying the corrections that are diagonal in the PID indices: reconstruction efficiency, acceptance, physical loss of particles (absorption, decay), background from tertiary interactions, e–veto efficiency and kaon subtraction;
- $(M_{ii'}^p)^{-1}$ is the simplified unfolding matrix correcting for the momentum smearing which only depends of the indices i and i' representing the true and reconstructed momentum bins, respectively;

- $(M_{jj'}^\theta)^{-1}$ is the identity matrix, representing the assumption that the smearing effect in the angular measurement is negligible; and
- $(M_{ij;\alpha\alpha'}^{id})^{-1}$ is the matrix which corrects for pion–proton PID inefficiency and migration, which is diagonal in i, i' and j, j' , but built of two-by-two sub-matrices, each different and non-diagonal in the PID variables α, α' .

The diagonal efficiency correction

$$\varepsilon_{ij\alpha'}^{-1} = w_{ij}^{\text{recon}} \cdot w_{ij}^{\text{acc}} \cdot w_{ij\alpha'}^{\text{absorption}} \cdot w_{ij\alpha'}^{\text{tertiaries}} \cdot \eta_{ij\alpha'}^{\text{K}} \cdot \eta_{ij\alpha'}^{\text{e}} \quad (4.10)$$

is composed of the following factors:

w_{ij}^{recon} the correction for the overall reconstruction efficiency;

w_{ij}^{acc} the correction for the acceptance;

$w_{ij\alpha'}^{\text{absorption}}$ the correction for the loss of particles due to absorption and decay;

$w_{ij\alpha'}^{\text{tertiaries}}$ the correction for the background of tertiary particles generated by the secondaries produced in the target;

$\eta_{ij\alpha'}^{\text{K}}$ is the factor correcting for the kaon background; and

$\eta_{ij\alpha'}^{\text{e}}$ is the factor correcting for the effects of the electron veto.

The first two corrections are the same for pions and protons while the latter four also depend on the particle type. It is worth noting that the efficiency correction is expressed in terms of the true momentum and angle, and in terms of the reconstructed particle type (α'). This is because these corrections are applied before PID unfolding.

As advanced in Sec. 4.5.3, some of the above corrections are computed as a function of p, θ_x and θ_y , while some others are directly expressed in the final variables (p, θ) . In the first case, the transformation to polar coordinates (p, θ) is done integrating over all θ_x and θ_y resulting in a given θ bin. In particular, the four first corrections of Eq. (4.10), denoted by w , are computed as a function of (p, θ_x, θ_y) .

Further details on how all these correction factors are computed are described in [61].

4.5.6 Results

Figure 4.14 and Table 4.4 show the measurement of the double-differential cross-section for positive pion production in the laboratory system as a function of the momentum and the polar angle. Only diagonal errors are shown in the plots and table (a full discussion of the error evaluation is given below). Also shown in Figure 4.14 is a fit to a Sanford-Wang parameterization, which will also be discussed in this section.

Error estimates

A detailed error analysis has been performed to evaluate the accuracy of the pion cross-section measurement. The main errors entering in this measurement are listed below.

- *statistics*:
the statistical uncertainties associated with the track yields measured from the aluminium target setting and from the empty target setting (needed for subtraction) have been included in the pion production cross-section uncertainty estimates.
- *track corrections*:
several uncertainties associated with the corrections needed to convert the measured track yields to true track yields have been evaluated. The track reconstruction efficiency correction is based on the combination of thin target aluminium and beryllium data sets. The main error associated with this computation is given by the size of the statistical sample. The correction to the pion and proton yields due to absorption or decay is computed via a Monte Carlo simulation. An uncertainty of 10% for both proton and pion yields has been assumed for this correction, in addition to the uncertainty due to the finite size of the simulated data sample used to estimate this correction. Similarly, simulated data (and their associated uncertainties) were used to estimate the correction for the contamination in the sample due to tertiary particles that are not produced in the target, but rather by the decay of secondaries, or by the interaction of secondaries in the spectrometer material. An uncertainty of 100% has been assumed for this subtraction, for both proton and pion yields. Furthermore, an uncertainty has been assigned to the empty target subtraction, in order to account for the effect of the target itself which attenuates the proton beam.

θ_{\min} (mrad)	θ_{\max} (mrad)	p_{\min} (GeV/c)	p_{\max} (GeV/c)	$d^2\sigma\pi^+/(dpd\Omega)$ (mb/(GeV/c sr))
30	60	0.75	1.25	410 \pm 56
		1.25	1.75	473 \pm 49
		1.75	2.25	465 \pm 41
		2.25	2.75	441 \pm 33
		2.75	3.25	464 \pm 29
		3.25	4.00	346 \pm 18
		4.00	5.00	284 \pm 18
		5.00	6.50	129.7 \pm 8.1
60	90	0.75	1.25	412 \pm 42
		1.25	1.75	456 \pm 42
		1.75	2.25	456 \pm 36
		2.25	2.75	407 \pm 24
		2.75	3.25	381 \pm 19
		3.25	4.00	249 \pm 13
		4.00	5.00	176 \pm 13
		5.00	6.50	68.9 \pm 6.3
90	120	0.75	1.25	429 \pm 45
		1.25	1.75	442 \pm 36
		1.75	2.25	384 \pm 26
		2.25	2.75	330 \pm 20
		2.75	3.25	287 \pm 15
		3.25	4.00	164.7 \pm 9.8
		4.00	5.00	105.4 \pm 8.1
		5.00	6.50	41.4 \pm 4.3
120	150	0.75	1.25	434 \pm 44
		1.25	1.75	404 \pm 31
		1.75	2.25	329 \pm 23
		2.25	2.75	258 \pm 18
		2.75	3.25	213 \pm 13
		3.25	4.00	119.1 \pm 7.9
		4.00	5.00	62.8 \pm 5.2
		5.00	6.50	24.2 \pm 3.4
150	180	0.75	1.25	441 \pm 47
		1.25	1.75	371 \pm 31
		1.75	2.25	275 \pm 21
		2.25	2.75	203 \pm 17
		2.75	3.25	153 \pm 10
		3.25	4.00	77.5 \pm 7.1
		4.00	5.00	35.5 \pm 4.5
		5.00	6.50	13.3 \pm 1.7
180	210	0.75	1.25	332 \pm 35
		1.25	1.75	270 \pm 26
		1.75	2.25	189 \pm 19
		2.25	2.75	130 \pm 14
		2.75	3.25	87.8 \pm 7.1
		3.25	4.00	38.3 \pm 3.4
		4.00	5.00	16.6 \pm 1.7
		5.00	6.50	10.4 \pm 3.2

Table 4.4: HARP results for the double-differential π^+ production cross-section in the laboratory system, $d^2\sigma\pi^+/(dpd\Omega)$. Each row refers to a different ($p_{\min} \leq p < p_{\max}, \theta_{\min} \leq \theta < \theta_{\max}$) bin, where p and θ are the pion momentum and polar angle, respectively. The central values quoted are the ones obtained via the Atlantic analysis discussed in the text. The square-root of the diagonal elements of the covariance matrix are also given.

- *particle identification:*

uncertainties associated with the PID of tracks, and with the corrections needed to convert yields of tracks identified as pions to true pion yields, have been included. Among the several error sources associated with the pion–proton PID selection, the dominant one is due to the uncertainty in the (small) fraction of pions and protons with an associated anomalous TOFW β measurement, that is a β measurement which exhibits a non-Gaussian behavior.

- *momentum reconstruction:*

uncertainties associated with the momentum reconstruction performance of the spectrometer, and with the corrections needed to convert the measured momenta to ‘true’ momenta. Concerning the momentum, biases and resolution effects are taken into account using both real and simulated data. It was found that momentum biases do not exceed the 5% level from a study of beam particles at different momenta and from a comparison between the reconstructed momenta and the momenta inferred from β measurements with the TOFW and the threshold curves in the Cherenkov.

- *overall normalization:*

uncertainty of 4% has been estimated. The dominant sources for this uncertainty are the targeting efficiency uncertainty, which is deduced from the measurement of transverse beam spot size on target, as well as the reconstruction and PID uncertainties that are fully correlated across different (p, θ) pion bins. On the other hand, the aluminium target thickness and density were carefully measured, and the effect on the overall cross-section normalization due to these uncertainties is negligible.

The impact of the error sources discussed in the previous section on the final cross-section measurement has been evaluated, either by analytic error propagation, or by Monte Carlo techniques. Correlation effects among different particle types, and among different (p, θ) bins, have also been taken into account.

The cross-section uncertainty level is quantified by adopting two different conventions. The rationale is that both the errors on the ‘point-to-point’, double-differential cross-section, and the error on the cross-section integrated over the entire pion phase space measured, might be of interest.

Error Category	Error Source	$\delta_{\text{diff}} (\%)$	$\delta_{\text{int}} (\%)$
Statistical	Al target statistics	1.6	0.3
	Empty target subtraction (stat.)	1.3	0.2
	Sub-total	2.1	0.4
Track yield corrections	Reconstruction efficiency	0.8	0.4
	Pion, proton absorption	2.4	2.6
	Tertiary subtraction	3.2	2.9
	Empty target subtraction (syst.)	1.2	1.1
	Sub-total	4.5	4.1
Particle identification	PID Probability cut	0.2	0.2
	Kaon subtraction	0.3	0.1
	Electron veto	2.1	0.5
	Pion, proton ID correction	2.5	0.4
	Sub-total	3.5	0.7
Momentum reconstruction	Momentum scale	3.0	0.3
	Momentum resolution	0.6	0.6
	Sub-total	3.2	0.7
Overall normalization	Sub-total	4.0	4.0
All	Total	8.2	5.8

Table 4.5: Summary of the uncertainties affecting the double-differential cross-section (δ_{diff}) and integrated cross-section (δ_{int}) measurements. See text for details.

First, the dimensionless quantity δ_{diff} is defined, expressing the typical error on the double-differential cross-section, as follows:

$$\delta_{\text{diff}} \equiv \frac{\sum_i (\delta[\Delta^2\sigma^\pi/(\Delta p \Delta \Omega)])_i}{\sum_i (\Delta^2\sigma^\pi/(\Delta p \Delta \Omega))_i}, \quad (4.11)$$

where i labels a given pion (p, θ) bin, $(\Delta^2\sigma^\pi/(dp \cdot d\Omega))_i$ is the central value for the double-differential cross-section measurement in that bin, and $(\delta[\Delta^2\sigma^\pi/(dp \cdot d\Omega)])_i$ is the error associated with this measurement.

The individual and cumulative effect of the error sources discussed above on the δ_{diff} quantity are shown in Table 4.5. The typical error on the double-differential cross-section is about 8.2%. The dominant error contributions to δ_{diff} arise from overall normalization (4%), subtraction of tertiary tracks (3.2%), and momentum scale (3.0%). In Tab. 4.5, the individual cross-section uncertainties are grouped into five categories: statistical, track yield corrections, particle identification, momentum reconstruction, and overall normalization uncertainties. Uncertainties associated with the track yield corrections discussed above dominate the cross-section uncertainties in the low momentum region, while

the dominant errors in the high momentum region are due to the momentum reconstruction and to the overall normalization.

Second, we define the dimensionless quantity δ_{int} , expressing the fractional error on the integrated pion cross-section, σ^π ($0.75 \text{ GeV}/c \leq p < 6.5 \text{ GeV}/c$, $30 \text{ mrad} \leq \theta < 210 \text{ mrad}$), as follows:

$$\delta_{\text{int}} \equiv \frac{\sqrt{\sum_{i,j} (\Delta p \Delta \Omega)_i C_{ij} (\Delta p \Delta \Omega)_j}}{\sum_i (\Delta^2 \sigma^\pi)_i}, \quad (4.12)$$

where $(\Delta^2 \sigma^\pi)_i$ is the double-differential cross-section in bin i , $(\Delta^2 \sigma^\pi / (\Delta p \Delta \Omega))_i$, multiplied by its corresponding phase space element $(\Delta p \Delta \Omega)_i$. Here, C_{ij} is the covariance matrix of the double-differential cross-section obtained by summing thirteen matrices from the error sources listed in Table 4.5, and whose square root of the diagonal elements, $\sqrt{C_{ii}}$, corresponds to the error $(\delta(\Delta^2 \sigma^\pi / (\Delta p \Delta \Omega)))_i$ appearing in Eq. 4.11. This covariance matrix is used to compare the two independent analyses of the same cross-section measurement, and to obtain the best-fit values, errors, and correlations for the coefficients entering into the Sanford-Wang formula used to parameterize the HARP measurements. The correlation coefficients among distinct (p, θ) bins in C_{ij} vary between -0.19 and $+0.95$.

The contributions to δ_{int} from all the error sources considered, as well as the total error estimate on the integrated cross-section, are also given in Table 4.5. As expected, (mostly) correlated errors such as the one from the normalization or tertiary subtraction remain (almost) as large as they were for the point-to-point error. On the other hand, the contribution of the momentum scale uncertainty is negligible here, since its effect tends to be anti-correlated among different phase space bins. In addition to the normalization and tertiary subtraction, other uncertainty sources which have some impact on the integrated cross-section include the pion absorption correction and the empty target subtraction systematic uncertainty. Overall, the total uncertainty on the pion production cross-section measured over the entire phase space ($0.75 \leq p < 6.5 \text{ GeV}/c$, $30 \leq \theta < 210 \text{ mrad}$) is estimated to be about 6%.

In the following section, the cross-section results are also expressed in a parameterized form.

Sanford-Wang parameterization

The π^+ production data was fitted with a Sanford-Wang parameterization [63]. Recall this is the parameterization used in the K2K beam Monte-Carlo to simu-

late primary hadron production in the aluminum target. Fitting Sanford-Wang formula to HARP data allows for a straight forward application of HARP results to the K2K analysis, as will be described in section 4.6. This formula has the following functional form:

$$\frac{d^2\sigma(p+A \rightarrow \pi^+ + X)}{dpd\Omega}(p, \theta) = c_1 p^{c_2} \left(1 - \frac{p}{p_{\text{beam}}}\right) \cdot \exp\left[-c_3 \frac{p^{c_4}}{p_{\text{beam}}^{c_5}} - c_6 \theta(p - c_7 p_{\text{beam}} \cos^{c_8} \theta)\right], \quad (4.13)$$

where X denotes any system of other particles in the final state, p_{beam} is the proton beam momentum in GeV/c , p and θ are the π^+ momentum and angle in units of GeV/c and radians, respectively, $d^2\sigma/(dpd\Omega)$ is expressed in units of $\text{mb}/(\text{GeV}/c \text{ sr})$, $d\Omega \equiv 2\pi d(\cos \theta)$, and the parameters c_1, \dots, c_8 are obtained from fits to π^+ production data.

The *meaning* of these eight parameters is the following:

- c_1 accounts for the overall normalization factor,
- c_2, c_3, c_4, c_5 can be interpreted as describing the momentum distribution of the secondary pions,
- c_6, c_7, c_8 describe the angular distribution for fixed secondary and proton beam momenta, p and p_{beam} .

This formula is purely empirical. In the χ^2 minimization procedure, seven out of these eight parameters were allowed to vary. The parameter c_5 was fixed to the conventional value $c_5 \equiv c_4$, since the cross-section dependence on the proton beam momentum cannot be addressed by the present HARP data-set, which includes exclusively measurements taken at $p_{\text{beam}} = 12.9 \text{ GeV}/c$. In the χ^2 minimization, the full error matrix was used.

Concerning the Sanford-Wang parameters estimation, the best-fit values of the Sanford-Wang parameters are reported in Table 4.6, together with their errors. The fit parameter errors are estimated by requiring $\Delta\chi^2 \equiv \chi^2 - \chi^2_{\text{min}} = 8.18$, corresponding to the 68.27% confidence level region for seven variable parameters. Significant correlations among fit parameters are found, as shown by the correlation matrix given in Table 4.7.

The HARP cross-section measurement is compared to the best-fit Sanford-Wang parameterization of Table 4.6 in Figs. 4.14 and 4.15.

The goodness-of-fit of the Sanford-Wang parameterization hypothesis for the HARP results can be assessed by considering the best-fit χ^2 value of $\chi^2_{\text{min}} = 305$

Parameter	Value
c_1	$(4.4 \pm 1.3) \cdot 10^2$
c_2	$(8.5 \pm 3.4) \cdot 10^{-1}$
c_3	(5.1 ± 1.3)
$c_4 = c_5$	(1.78 ± 0.75)
c_6	(4.43 ± 0.31)
c_7	$(1.35 \pm 0.29) \cdot 10^{-1}$
c_8	$(3.57 \pm 0.96) \cdot 10^1$

Table 4.6: Sanford-Wang parameters and errors obtained by fitting the data set. The errors refer to the 68.27% confidence level for seven parameters ($\Delta\chi^2 = 8.18$).

Parameter	c_1	c_2	c_3	$c_4 = c_5$	c_6	c_7	c_8
c_1	1.000						
c_2	-0.056	1.000					
c_3	-0.145	-0.691	1.000				
$c_4 = c_5$	-0.322	-0.890	0.831	1.000			
c_6	-0.347	0.263	-0.252	-0.067	1.000		
c_7	-0.740	0.148	-0.067	0.077	0.326	1.000	
c_8	0.130	-0.044	0.205	-0.040	-0.650	0.189	1.000

Table 4.7: Correlation coefficients among the Sanford-Wang parameters, obtained by fitting the data.

for 41 degrees of freedom, indicating a very poor fit quality. We note that the goodness-of-fit strongly depends on the correlations among the HARP cross-section uncertainties in different (p, θ) bins, and therefore cannot be inferred from Fig. 4.14 alone. If these uncertainties were (incorrectly) treated as completely uncorrelated, the best-fit χ^2 value would decrease from 305 to 57. A more comprehensive study of π^+ production at various beam momenta and from various nuclear targets in HARP is planned and will follow in a subsequent analysis, and should hopefully shed more light on the cause of the poor quality of the Sanford-Wang hypothesis reported here.

Comparison with existing forward pion production data on aluminum

Finally the HARP results are compared with existing π^+ production data available in the literature directly from aluminum targets [75, 76, 77, 78]. The comparison is restricted to proton beam momenta between 10 and 15 GeV/c (close to the K2K beam momentum of 12.9 GeV/c), and for pion polar angles below 200 mrad (the range measured by HARP and of relevance to K2K).

The comparison is based on the HARP Sanford-Wang parameterization rather than on the HARP data points themselves, in order to match pion momenta and angles measured in past Al experiments. Furthermore, a correction to rescale the HARP Sanford-Wang parameterization at 12.9 GeV/c beam momentum to the 10–15 GeV/c beam momenta of the past Al data sets is applied [64].

Given these model-dependent corrections, it was found that the HARP results are consistent with Ref. [76] and Refs. [77], agree rather well with [78] and are somewhat lower than, but still marginally consistent with, Ref. [75]. Figure 4.16 shows the comparison between HARP and the above datasets.

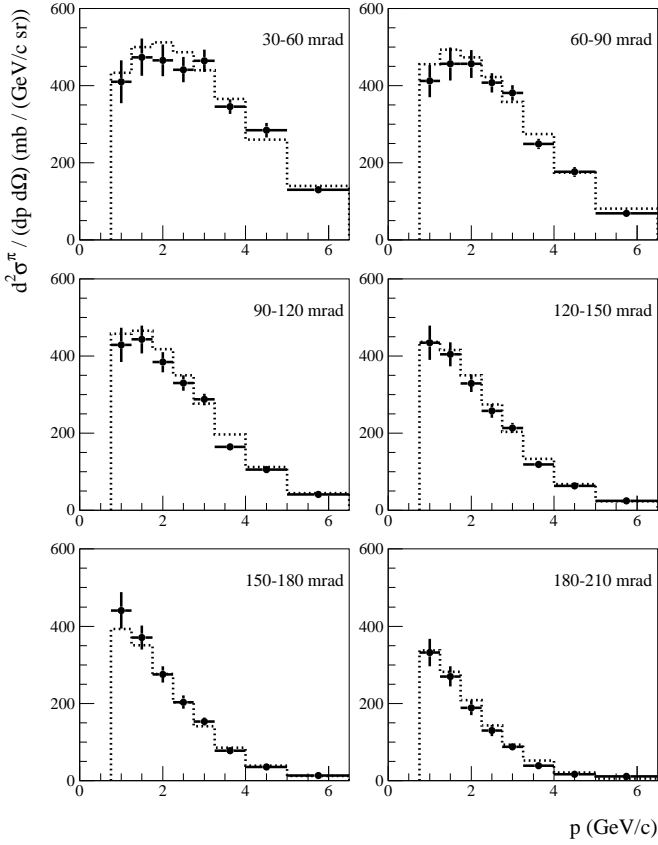


Figure 4.14: Measurement of the double-differential π^+ production cross-section in the laboratory system $d^2\sigma/(dpd\Omega)$ for incoming protons of $12.9 \text{ GeV}/c$ on an aluminium target as a function of pion momentum p , in bins of pion polar angle θ . The data points are the measurements, the histogram represents the Sanford-Wang parameterization fitted to the data.

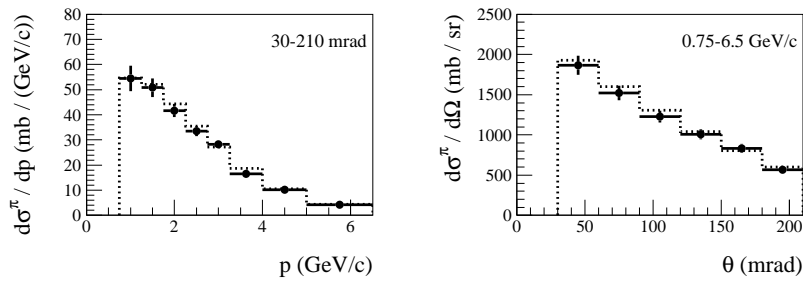


Figure 4.15: Projections of the differential light hadron production cross-section as a function of p integrated over the range $30 \leq \theta < 210$ mrad (left panel), and production cross-section as a function of θ in the range $0.75 \leq p < 6.5$ GeV/c (right panel). The points show the HARP measurements, the dotted curve the best-fit Sanford-Wang parameterization.

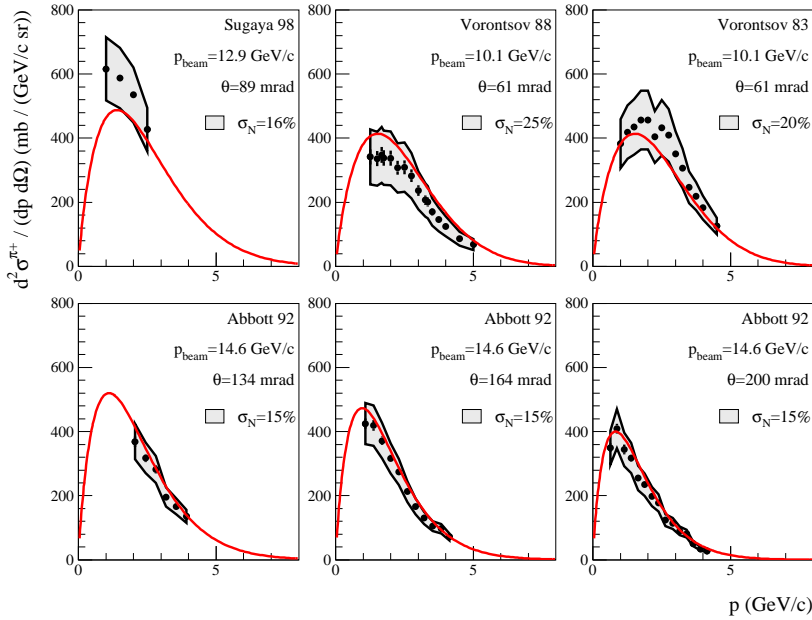


Figure 4.16: Comparison of the double-differential pion production cross-section measured in HARP, and the one measured in past experiments using an aluminum target and 10-15 GeV/c momentum beam protons. The points are the data from past experiments, and the shaded area reflect their normalization uncertainty. The solid line is the HARP Sanford-Wang parameterization rescaled to the beam momentum of past experiments, as discussed in the text.

4.6 Neutrino flux predictions based on HARP results

In this section, we predict the neutrino flux in the K2K experiment, using the measurement by the HARP experiment on the inclusive production cross-section of positive pions in p-Al collisions at 12.9 GeV/c [61]. We compute both flux central values and systematic uncertainties.

For our central value predictions, we switch from a parameterization of π^+ production in the collisions of primary protons in aluminum based on a CERN compilation of mostly Cho *et al.* p-Be data [64] plus a nuclear correction to account for the different nuclear target material, to a parameterization based on the HARP result. All other aspects of the simulations are left unchanged: primary beam optics, description of other hadronic processes, horn focusing, geometry, particle decays, etc.

Systematic uncertainties coming from HARP measurement have been computed. A full set of K2K beam systematic uncertainties has also been taken into account, to obtain an accurate estimation of overall error in the K2K flux. We recall that previous systematic evaluations used to rely on PIMON measurement for neutrinos above 1 GeV, and on the CERN compilation for energies below 1 GeV, leading to big uncertainties in neutrino fluxes. None of these have been used in the current analysis, since HARP results are much more precise. Since no input from PIMON data has been used in this study, neither to compute central values nor systematics, these two approaches to determine flux predictions (HARP and PIMON) contain independent information and are complementary.

4.6.1 Prediction of the flux central value

In this Section, flux predictions obtained with the best-fit parameterization of the HARP results are discussed. We also briefly summarize the other assumptions in the simulations, emphasizing the aspects that are varied in Section 4.6.2 for systematic error studies.

The neutrino beam simulation of the K2K experiment can be divided in the following steps:

1. **Injection of primary 12.9 GeV/c protons into aluminum target:** deviations from a perfect beam are described by eight beam optics parameters. The coordinate reference system is such that the target center is

located at $(x,y,z)=(0,0,27.5 \text{ cm})$, with the z -axis corresponding to the target axis. Two parameters describe the mean x and y positions of the beam impact point on the upstream face of the target; their default value is $\text{Mean}(x)=\text{Mean}(y)=0$, that is, the average beam impact point is perfectly centered on target. Two parameters describe the mean θ_x and θ_y directions of the beam aiming; their default value is $\text{Mean}(\theta_x)=\text{Mean}(\theta_y)=0$, that is, the beam average direction is perfectly parallel to the target axis. Four parameters describe the spill-by-spill variations in the impact point spread and angular divergence. These variations are described by gaussian distributions, with the following widths: $\text{RMS}(x)=3.4 \text{ mm}$, $\text{RMS}(y)=7.2 \text{ mm}$, $\text{RMS}(\theta_x)=8.6 \text{ mrad}$, $\text{RMS}(\theta_y)=1.0 \text{ mrad}$. Given the optics properties of the beam, the x and θ_x parameters are assumed to be fully anticorrelated with each other on a spill-by-spill basis, as the y and θ_y parameters.

2. Simulation of primary interaction vertex:

primary hadronic interactions are defined as the hadronic interactions of protons with more than 10 GeV total relativistic energy in aluminum; secondary hadronic interactions are defined as hadronic interactions that are not primary ones. The primary hadronic interaction length (or rate) is simulated according to GCALOR. The GCALOR option activates the same routines of GFLUKA for projectile energies greater than 10 GeV, or anyway for incident projectiles other than pions and nucleons. Therefore, the GFLUKA model is used to simulate the interaction length of primary hadronic interactions.

3. Production of secondary particles:

secondaries with user-specified average multiplicities and kinematics are produced. Seven types of secondaries are produced: π^\pm , K^\pm , K_0 , \bar{K}_0 , secondary protons. The π^+ production is of the most importance for muon neutrino flux predictions, since ν_μ comes mainly from pion decay. In order to describe π^+ production we use the best parameterization of the HARP data to the Sanford-Wang formula, described in section 4.5.6. This is what we call *HARP model*. Recall K2K flux predictions used to rely on the Cho/CERN compilation data (*Cho model*), which uses the same parameterization to describe π^+ production in p-Be interactions. The Sanford-Wang coefficients of the Cho/CERN π^+ model are given in Tab. 4.8, along with the ones from HARP measurement.

Parameter	c_1	c_2	c_3	c_4	c_5	c_6	c_7	c_8
Cho-CERN	238.4	1.01	2.26	2.45	2.12	5.66	0.14	27.3
HARP	440	0.85	5.1	1.78	1.78	4.43	0.14	35.7

Table 4.8: Sanford-Wang parameters for the Cho-CERN parameterization of inclusive π^+ production in p-Be interactions. For comparison purposes, values from HARP measurement are also shown.

A nuclear rescaling to convert pion production in beryllium, to production in aluminum, is then applied in the K2K beam Monte Carlo code. The rescaling proceeds by applying the following weight to the double-differential cross-section on beryllium [79]:

$$w = \left(\frac{A_{\text{Al}}}{A_{\text{Be}}}\right)^{\alpha(x_F)} \quad (4.14)$$

where the polynomial α is defined as:

$$\alpha(x_F) = 0.74 + x_F(-0.55 + 0.26x_F) \quad (4.15)$$

where x_F is the Feynman x variable, defined as:

$$x_F \equiv \frac{p_z^{\text{CM}}}{p_{\text{max}}^{\text{CM}}} \quad (4.16)$$

where CM refers to the center-of-mass frame, and p_Z to the momentum component along the beam direction. Obviously, this nuclear correction is not needed for the HARP π^+ data. For secondaries other than π^+ , the same approach is taken in both cases, and production in p-Be is estimated first, and then a nuclear correction as described above is applied.

Once the inclusive π^+ production cross-sections are computed in the HARP- or Cho/CERN-based models, the π^+ average multiplicities per inelastic interaction are computed by simply dividing these cross-sections by the total p-Al inelastic cross-section, $\sigma(\text{p-Al} \rightarrow \text{inelastic}) \simeq 420 \text{ mb}$, according to the **GHSIG** model.

4. Tracking of secondaries and hadronic reinteraction:

secondaries produced in the aluminum target are tracked and may interact hadronically. These secondary hadronic interactions are described by

the GCALOR model, both for what concerns the rate of the interactions (interaction length of secondary hadronic interactions), as well as for the multiplicity and kinematics of tertiary particles produced. The relevant GCALOR routines called are `CALSIG` and `GCALOR`, respectively. Below 10 GeV, and down to a threshold set at 2.5 GeV for pions and 3.5 GeV for nucleons, GCALOR uses a hybrid treatment, in which a fraction α of the interactions is performed as in `GFLUKA` and a fraction $1 - \alpha$ is simulated by the so called *scaling model*, which was initially developed for HETC and is an extension of the Bertini Intra-Nuclear Cascade model to higher energies. The value of α varies linearly with energy, going from 0 at threshold to 1 at 10 GeV. Below threshold, the Bertini Intra-Nuclear cascade model is used in GCALOR.

5. Focusing of charged particles:

charged particles are deflected by the magnetic field in the two horns. The field between the horns inner and outer conductor is described by the formula for an infinitely-long current-carrying wire, with $1/r$ dependence where r is the distance from the horn axes, and with an azimuthal component only. The magnetic field strength is set to 250 kA in both horns. No perturbations in the magnetic field strength as a function of azimuth are simulated for the central value flux predictions.

6. Propagation to the decay volume:

mesons and muons are tracked in the decay volume, and their decays to neutrinos are simulated according to custom-defined routines. Each neutrino parent is redecayed 1000 times in the simulation, to boost the neutrino statistics. The physics of these decays is not summarized here, since we are interested mostly in the simple two-body decay $\pi^+ \rightarrow \mu^+ \nu_\mu$ (and to a lesser extent $K^+ \rightarrow \mu^+ \nu_\mu$), fully specified by phase space arguments.

7. Neutrino propagation to the near and far detectors:

neutrinos crossing the near and far detector acceptances are accumulated to predict the neutrino fluxes at these two locations. The near detector flux acceptance is defined as a disk of 3 m in radius located at 300 m from the production target; the far detector acceptance is a disk of 250 m in radius located at 250 km (1 mrad angular aperture).

The flux predictions as a function of neutrino energy of our K2K beam Monte Carlo simulations based on the HARP- and Cho/CERN-based π^+ production models are shown in Fig. 4.17. The number of protons on target that were

simulated is $3 \cdot 10^8$ in both cases. The predictions for the neutrino fluxes at the near and far detectors are shown on the left and right of the plot respectively. The two predictions are very similar for what concerns the flux energy shape, while the overall flux normalizations are different, the HARP-based one being significantly lower. Although this difference needs to be analyzed in further studies, it will have no impact on the far to near flux ratio F/N (see 4.4.1), since it is dependent on the energy shape and not on the normalization.

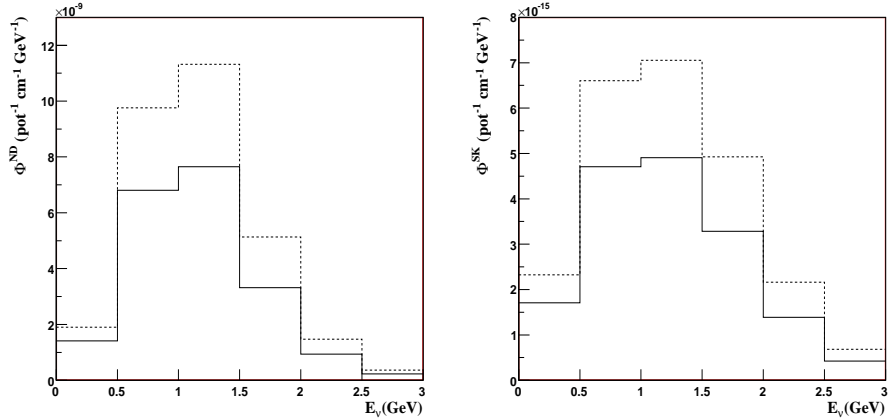


Figure 4.17: Summary of flux prediction central values for (left) K2K near detector and (right) the SK far detector, based on the HARP inputs as described in the text. Solid histogram shows the HARP-based central value, while dashed one shows the central value flux predictions based on the Cho/CERN model for π^+ production.

4.6.2 Systematic uncertainties of the flux predictions

In this Section, we describe the systematic uncertainties affecting the muon neutrino flux predictions. Those can be subdivided into four different groups:

- Beam optics
- Primary hadronic interactions

- Secondary hadronic interactions
- Horn magnetic fields

In particular, we assume that uncertainties associated with the beamline geometry specifications and particle decays (*e.g.*, branching ratios) are negligible, which should be a good approximation as far as muon neutrino flux predictions are concerned. Also, we make the approximation of considering every systematic variation as having a symmetric uncertainty associated with it (plus error equal minus error).

Each systematic uncertainty is estimated by comparing the flux predictions obtained by simulating 10^8 protons on target with a systematically varied beam Monte Carlo setting, and 10^8 protons on target with the central value setting.

Primary Beam Optics

We studied the effect that the uncertainties on the measured primary beam optics parameters have on the neutrino flux predictions. In this study, we follow the work done in Ref. [80]. These uncertainties are estimated from the measurements taken with two segmented plate ionization chambers (SPIC) located upstream of the target. We consider three systematics in this category:

- primary proton mean impact point
- primary proton mean injection angle
- beam profile width and angular divergence

The top panel in Figure 4.18 shows the flux uncertainty associated with varying the mean impact point of the primary beam from $\text{Mean}(x)=\text{Mean}(y)=0$ (central value settings), to $\text{Mean}(x)=0.8$ mm, $\text{Mean}(y)=0.9$ mm. Bottom panel in Figure 4.18 shows the flux uncertainty associated with varying the mean injection angle of the beam from $\text{Mean}(\theta_x)=\text{Mean}(\theta_y)=0$ (central value settings), to $\text{Mean}(\theta_x)=1.8$ mrad, $\text{Mean}(\theta_y)=0.8$ mrad. As can be seen in the Figure, the above uncertainties have a negligible effect on the neutrino flux predictions, as it was obtained in Ref. [80].

On the other hand, Figure 4.19 shows the flux uncertainty associated with varying the profile width and angular divergence parameters from $\text{RMS}(x) = 3.4$ mm, $\text{RMS}(y) = 7.2$ mm, $\text{RMS}(\theta_x) = 8.6$ mrad, $\text{RMS}(\theta_y) = 1.0$ mrad (central value settings), to $\text{RMS}(x) = 2.3$ mm, $\text{RMS}(y) = 5.0$ mm, $\text{RMS}(\theta_x) = 9.2$ mrad,

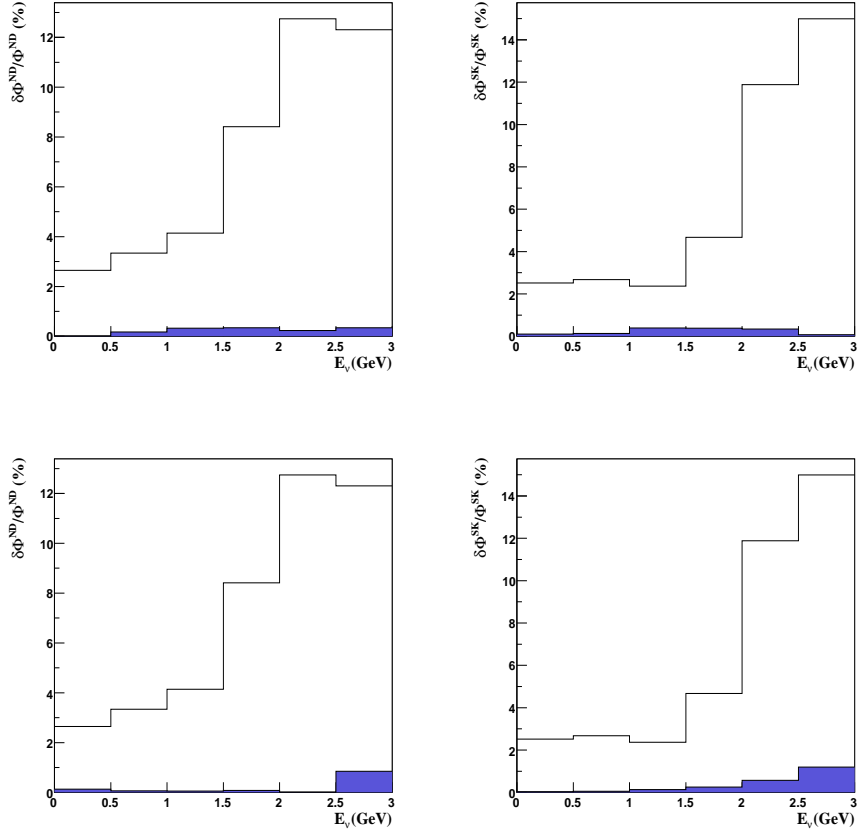


Figure 4.18: Beam optics uncertainties in the muon neutrino flux predictions at near (left) and far (right) detectors, as a function of neutrino energy E_ν . Top: uncertainties corresponding to varying the mean impact point of the primary beam as defined in the text. Bottom: uncertainties corresponding to varying the mean injection angle of the beam as defined in the text. The filled and empty histograms show the errors from each error source alone and all errors in this error category (beam optics), respectively. This systematic variations are motivated in Ref. [80].

$\text{RMS}(\theta_y) = 3.2$ mrad. The varied parameters were obtained by modifying the functional form of the SPIC profile width fits, to include a flat background to simulate electrical noise. This is the dominant primary beam optics systematic uncertainty, in terms of its effect on the neutrino flux predictions. The obtained uncertainty is very close to the one quoted in Ref. [80].

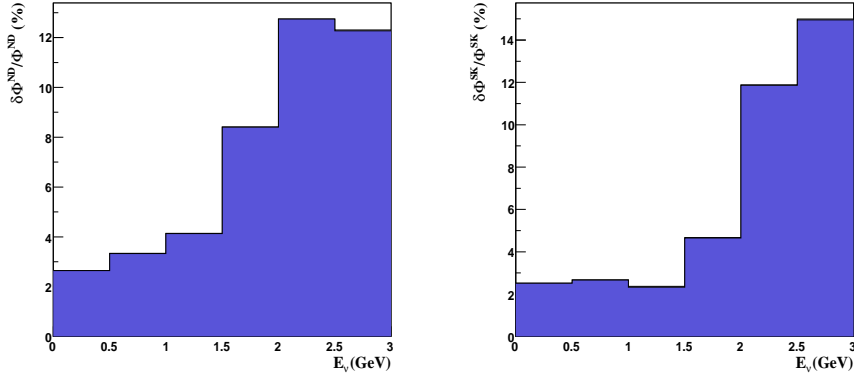


Figure 4.19: Uncertainties in the muon neutrino flux predictions as a function of neutrino energy E_ν associated with a systematic change in the primary beam optics setting, corresponding to varying the profile width and angular divergence parameters as defined in the text. Left: uncertainties on the near flux. Right: uncertainties on the far flux. The filled and empty histograms show the errors from this error source alone and all errors in this error category (beam optics), respectively. This systematic variation is motivated in Ref. [80]

Primary Hadronic Interactions

We consider now the effect of three systematic variations in the description of primary hadronic interactions on the neutrino flux predictions. Three sources of uncertainties are studied:

- proton-aluminum hadronic interaction length
- multiplicity and kinematics of π^+ production
- multiplicity of kaon production

A 32% uncertainty in the interaction length of primary hadronic interactions has been estimated. This uncertainty is larger than the actual experimental uncertainty, and has to do with a deficiency in the hadronic model in the beam Monte Carlo simulation. Hadronic interactions can be roughly classified as inelastic or elastic interactions. As explained in Section 4.6.1, a custom-defined model is adopted to simulate inelastic interactions. However, this same model is used to simulate all hadronic interactions, and no distinction between an elastic and an inelastic channel is made. Therefore, the rate of inelastic primary hadronic interactions is over-estimated in the simulation, while the rate of elastic primary hadronic interactions is zero.

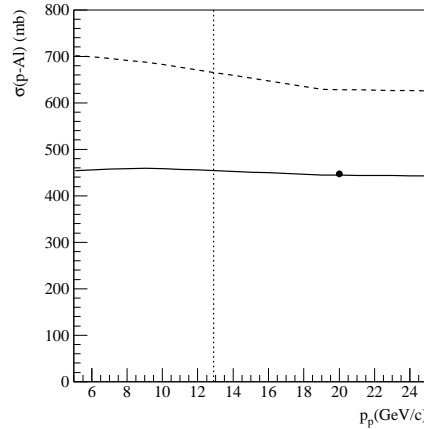


Figure 4.20: Comparisons on the proton-Al hadronic cross-section, as a function of proton momentum. The solid (dashed) line is the GCALOR/GFLUKA prediction in the beam Monte Carlo simulation for the inelastic (total) hadronic cross-section, the full circle point is a measurement of the inelastic cross-section from Ref. [81].

Figure 4.20 shows both the total hadronic cross-section, and the inelastic-only contribution to the total cross-section, for protons in aluminum, as a function of proton momentum. The curves are taken from the **GFLUKA** model used in the simulation. The data point for the inelastic cross-section is from Ref. [81]. There is good agreement between this experimental point and the **GFLUKA** prediction for the inelastic cross-section. Moreover, **GFLUKA** predicts that 67.9% of all hadronic interactions of 12 GeV kinetic energy protons in aluminum proceed inelastically.

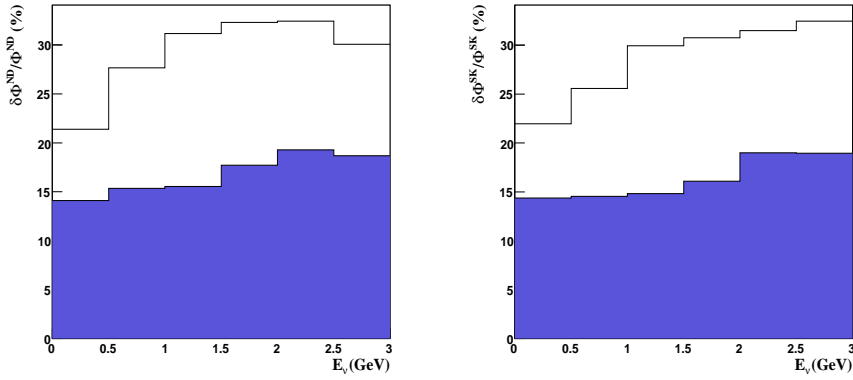


Figure 4.21: Uncertainties in the muon neutrino flux predictions as a function of neutrino energy E_ν associated with a systematic change in the description of primary hadronic interactions, corresponding to varying the p+Al total hadronic cross-section to 0.679 of its nominal value (**GFLUKA/CALOR**, taken as 1.0). The fraction 0.679 is the fraction that a hadronic interaction is supposed to proceed inelastically according to the **GFLUKA/CALOR** model. Left: uncertainties on the near flux. Right: uncertainties on the far flux. The filled and empty histograms show the errors from this error source alone and all errors in this error category (primary interactions), respectively. This systematic variation is motivated in the text and by Fig. 4.20.

We estimated that the deficiency in the beam Monte Carlo simulation described above would have a small enough effect on the far-to-near flux ratio prediction, and rather than changing the behavior of the “central value” simulation, we quantified the uncertainty associated with this deficiency. To this end, we made the approximation that elastic interactions would have a small effect on the primary proton angular distribution, and we studied the effect of reducing the rate of hadronic interactions to 67.9% of their nominal value, where the implicit assumption is that in the remaining 32.1% fraction, an elastic interaction with no effect on the projectile proton proceeds. The effect on the neutrino flux predictions is shown in Fig. 4.21. This reduction in the rate causes about a 15% decrease in the overall flux normalization at both the near and far detectors. If the K2K target were thin rather than thick, this effect would have been twice as large ($\simeq 32\%$).

The following simple procedure was followed to translate the HARP π^+ production uncertainties into flux uncertainties. Central values are extracted by running the beam Monte Carlo simulation with the parameters c_1, \dots, c_8 that fit best the HARP data, in order to obtain $\phi_\alpha(c_i)$, where α now labels a bin in generated neutrino energy, i labels the eight Sanford-Wang parameters, and ϕ is the flux prediction at either the near or far detector location, or the far/near flux ratio.

In order to extract the flux covariance matrix due to HARP π^+ production uncertainties, $M_{\alpha\beta}^\phi \equiv \langle \delta\phi_\alpha \delta\phi_\beta \rangle$, seven additional beam Monte Carlo simulations were performed, where each of the Sanford-Wang parameters is individually varied by some amount ϵ_i with respect to its best-fit value (seven simulations and not eight, since the HARP π^+ production assumes $c_4 = c_5$). The error matrix is then obtained by standard error propagation:

$$M_{\alpha\beta}^\phi = \sum_{i,j=1}^{N_c} D_{\alpha,i} M_{i,j}^\pi D_{\beta,j}^T \quad (4.17)$$

where $N_c = 7$, $M_{i,j}^\pi \equiv \rho_{i,j} \delta c_i \delta c_j$ is the covariance matrix in the Sanford-Wang parameters obtained from the HARP fit and specified in Ref. [61] via the parameter errors and correlations, and the derivatives $D_{\alpha,i}$ are:

$$D_{\alpha,i} \equiv \frac{\phi_\alpha(c_{k \neq i}, c_i + \epsilon_i) - \phi_\alpha(c_i)}{\epsilon_i} \quad (4.18)$$

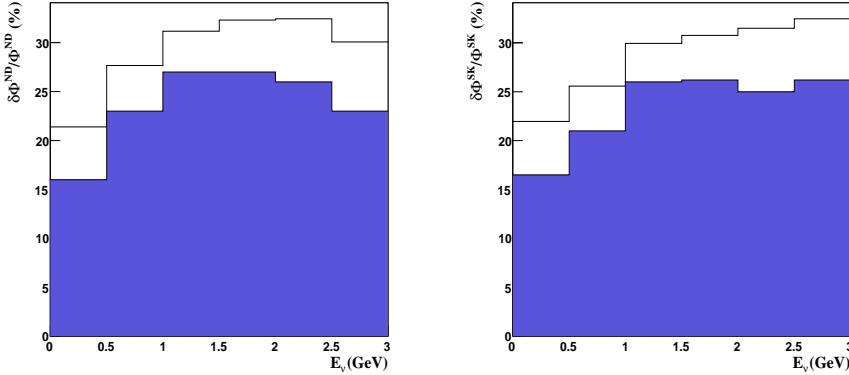


Figure 4.22: Uncertainties in the muon neutrino flux predictions as a function of neutrino energy E_ν associated with the systematic uncertainties in the multiplicity and kinematics of π^+ production in primary hadronic interactions. Left: uncertainties on the near flux. Right: uncertainties on the far flux. The filled and empty histograms show the errors from this error source alone and all errors in this error category (primary interactions), respectively. This systematic uncertainty is constructed from several variations, as discussed in the text. This systematic uncertainty is motivated in Ref. [61].

where, in $\phi_\alpha(c_{k \neq i}, c_i + \epsilon_i)$, only the single parameter c_i is varied by some amount, while the other parameters c_k are specified according to their best-fit values, as in $\phi_\alpha(c_i)$. The amounts ϵ_i are taken to be the 1σ error for 7 d.o.f. ($\Delta\chi^2 = 8.18$). This procedure does not account for non-linearities in the parameters' variations, and for asymmetric errors.

This procedure for translating the HARP π^+ production uncertainties into flux uncertainties yields the results shown in Fig. 4.22. This is the dominant uncertainty affecting both the absolute flux predictions, and the far-to-near flux ratio. The uncertainties on the absolute neutrino flux predictions vary between 15% at low neutrino energies, to about 25% at higher energies. Naively, we

would have expected uncertainties about half as large, based on the HARP π^+ production uncertainties given in Ref. [61] over the full pion phase space measured by HARP. It could be that larger uncertainties arise because of the needed extrapolation to phase space regions not covered by HARP, or because the linear approximation used in propagating the uncertainties is not a good approximation in this case. As a conservative approach, we take the uncertainties obtained by the method outlined above.

Given the importance of HARP-based π^+ production multiplicity and kinematics uncertainties in primary hadronic interactions in relation to the K2K flux prediction uncertainties, we inspected more closely this error source. In particular, we studied the following two points:

1. which Sanford-Wang π^+ parameter error derived from the HARP measurement contributes the most to the K2K flux prediction uncertainties,
2. which uncertainty source limits the accuracy of the HARP measurement itself.

First, we concluded that the largest contributions to the absolute muon neutrino flux predictions and to the far-to-near flux ratio prediction are due to Sanford-Wang π^+ parameters c_2 , c_3 and c_4 in Eq. 4.13. These parameters are the ones describing the shape of the π^+ momentum distribution in the forward pion production region. In particular, we conclude that the uncertainty in the π^+ production angular distribution is negligible compared to the momentum shape uncertainty. Second, the uncertainties in the HARP π^+ measurement that have the biggest impact on the absolute flux prediction uncertainties are the ones related to the HARP momentum reconstruction capability, where by momentum reconstruction uncertainties we consider both momentum scale and momentum resolution uncertainties. For more details on HARP systematic uncertainties, see Table 3 in Ref. [61].

We also estimated an uncertainty associated with kaon production in primary hadronic interactions. In this case, given that the corresponding HARP measurement is not yet available, and given the paucity of experimental data, we assign a large, 50%, uncertainty to the overall kaon production normalization, for both charged and neutral kaons. We do not apply to kaons the full procedure described above for pions to assign uncertainties also to the kinematics of the production. This 50% uncertainty is motivated by comparisons shown in Fig. 4.23 on K^+ production in p-Al and p-Be interactions, between the beam

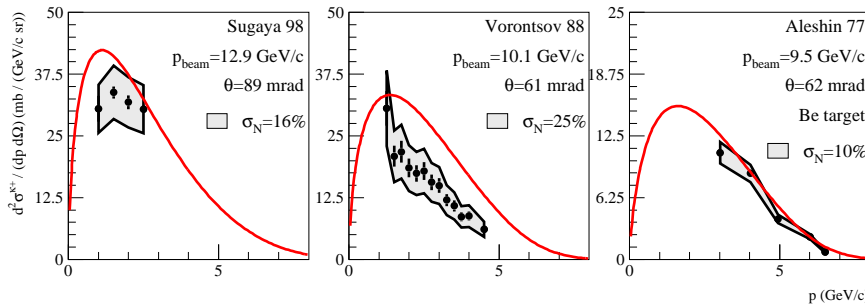


Figure 4.23: Comparisons on K^+ production, as a function of kaon momentum and for a fixed kaon angle, in proton-nucleus interactions. The left and middle panels refer to an aluminum target, the right panel to a beryllium target. The black points are the production data from Refs. [75, 82, 83]. The red curve is the Sanford-Wang parameterization used by the beam Monte Carlo simulation to describe K^+ production in p-Al and p-Be interactions at the beam momentum, kaon momentum, and kaon angle indicated. The normalization uncertainty quoted by the experiments is also given.

Monte Carlo simulation on one side, and experimental data on the other, considering also the normalization uncertainties quoted by the experiments.

The resulting flux prediction uncertainties due to kaon production are shown in Fig. 4.24. Generally, this uncertainty has a negligible effect on the flux predictions, except in the high energy part of the far-to-near flux ratio prediction.

Secondary Hadronic Interactions

Given the target dimensions, reinteraction effects for the secondaries produced in primary hadronic interactions can potentially have a large effect on neutrino flux predictions, and therefore a flux systematic uncertainty associated with an uncertainty in secondary hadronic interactions has been estimated. Ideally one would estimate reinteraction effects from the π^+ production from the K2K target replica measured at HARP. Since this measurement is not yet available, we estimate this uncertainty by looking at the flux prediction variations be-

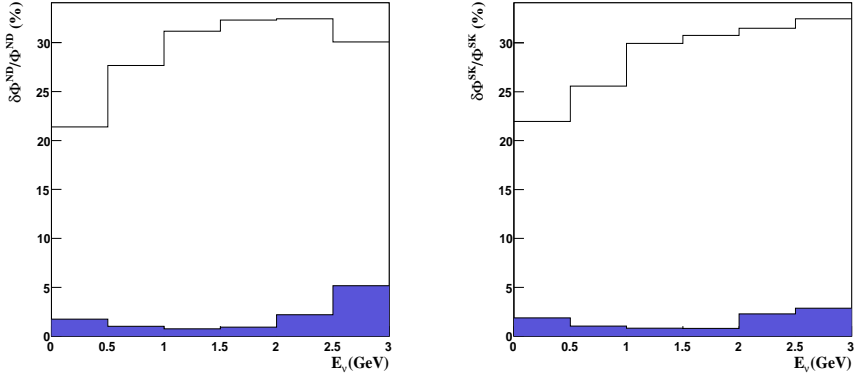


Figure 4.24: Uncertainties in the muon neutrino flux predictions as a function of neutrino energy E_ν associated with a systematic change in the description of primary hadronic interactions, corresponding to increasing the charged and neutral kaon production normalization in primary hadronic interactions by 50%. Left: uncertainties on the near flux. Right: uncertainties on the far flux. The filled and empty histograms show the errors from this error source alone and all errors in this error category (primary interactions), respectively. This systematic variation is motivated in the text and by Fig. 4.23.

tween the default GCALOR model to describe the rate and the final state of secondary hadronic interactions, and the GHEISHA model. In particular, this means calling the `GPGHEI` and `GHEISHA` routines for secondary hadronic interactions instead of the `CALSIG` and `GCALOR` ones. No changes to the treatment of primary hadronic interactions are made.

Figure 4.25 shows the total π^+ -Al inelastic cross-section as a function of pion momentum, as predicted by the GCALOR, GHEISHA and GFLUKA models, and as measured in Refs. [84, 85]. The GHEISHA and GFLUKA inelastic cross-sections are close to the experimentally measured values, while the GCALOR interaction rate is about a factor of two higher. This anomalous behavior should be,

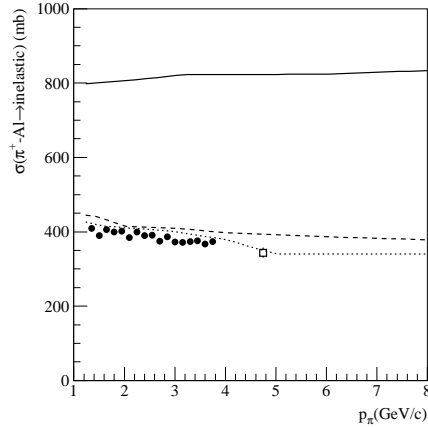


Figure 4.25: Comparisons on the π^+ -Al inelastic cross-section, as a function of pion momentum. The solid, dashed, and dotted lines are the GCALOR, GFLUKA, and GHEISHA predictions in the beam Monte Carlo simulation, respectively; the data points shown with full circles are from Ref. [84], while the open square point is from Ref. [85].

at least somewhat, compensated by the fact that GCALOR predicts particle multiplicities in pion-nucleus interactions that are about a factor of two too low (see, for example, Tables 1 and 2 in Ref. [86]). We concluded that the large differences in the description of secondary hadronic interactions between the GCALOR and GHEISHA models can be, conservatively, considered representative of the uncertainties associated with secondary hadronic interactions.

The flux prediction uncertainties due to secondary hadronic interaction uncertainties are shown in Fig. 4.26. Uncertainties as high as 10-20% in both the low-energy and high-energy tails of the energy spectrum are obtained; nevertheless, this uncertainty plays a less important role than the one associated to primary hadronic interactions.

Horn Magnetic Fields

Finally, we estimated the flux uncertainties due to non-perfect knowledge of the magnetic field in the two-horn system, both related to the magnetic field strength, and to the field homogeneity in azimuth.

The uncertainty in the magnetic field strength (or in the peak horn current) quoted in Ref. [87], estimated from measurements during horn testing phase, corresponds to about 5% [88]. The design uncertainty during horn operation is 10% [88]. To be conservative, we use the latter number, and we study how the flux predictions change by changing the peak horn current by 10% in a fully correlated way in the two horns. The results are shown in Fig. 4.27. The flux variation is only a few percent at low neutrino energies, and reaches about 20% at higher energies. Similarly, the uncertainty in the far-to-near flux ratio due to the magnetic field uncertainty is more pronounced in the high energy region.

Magnetic field measurements made during horn testing phase with an inductive coil showed some perturbations in the magnetic field strength as a function of azimuth for the first horn, while the radial dependence predicted by the calculation was confirmed [89]. It was found that the magnetic field strength varies periodically in azimuth, with a perturbation of $\pm 15\%$ with respect to the nominal strength predicted by the calculation, and with a period of $2\pi/4$ [89]. The central value flux predictions are not corrected to account for this perturbation, which is however included as an additional systematic uncertainty. The resulting uncertainty on the fluxes is shown in Fig. 4.28. This perturbation in the magnetic field of the horns has a negligible effect on the flux predictions.

Systematic Uncertainties Summary

The evaluation of systematic uncertainties affecting the neutrino flux predictions are summarized in Tab. 4.9 and Fig. 4.29.

In Tab. 4.9, the uncertainties in the total flux predictions integrated over all neutrino energies is given, both for the muon neutrino fluxes at the near and far detector. The table shows both the individual contributions, and the total flux systematic uncertainties. The total uncertainty on the fluxes is estimated to be about 30%; the dominant uncertainty is the one associated with the primary hadronic interactions, mainly due to the π^+ production and the interaction rate.

Figure 4.29 shows instead the flux predictions systematic uncertainties for a

Error Category	Error Source	δ_N (%)	δ_F (%)
Primary Beam Optics	Mean centering	0.35	0.32
	Mean aiming	0.14	0.16
	Spread and angular divergence	4.84	4.05
	Sub-total	4.86	4.07
Primary Hadronic Int.	Interaction rate	16.05	15.52
	Multiplicity and kinematics of π^+ prod.	23.73	21.93
	Multiplicity of K^\pm, K_0, \bar{K}_0 production	1.22	1.45
	Sub-total	28.67	26.91
Secondary Hadronic Int.	Rate, tertiary multiplicity and kinematics	6.80	6.04
	Sub-total	6.80	6.04
Horn Magnetic Fields	Magnetic field strength	5.97	5.42
	Azimuthal field perturbations	0.93	0.60
	Sub-total	6.05	5.45
All	Total	30.47	28.40

Table 4.9: Summary of systematic uncertainties in the total muon neutrino flux predictions integrated over all neutrino energies. The symbols δ_N and δ_F indicate the fractional errors on the fluxes at the near and far detector, respectively. Both the total errors and the individual error contributions considered in this section are listed.

given neutrino energy bin, both for the near and far fluxes. The total uncertainties, as well as the contributions from the four error categories discussed above (beam optics, primary hadronic interactions, secondary hadronic interactions, horn magnetic fields), are shown.

The uncertainties for the absolute flux predictions in a given neutrino energy bin range varies from about 25% at low energies, to about 50% at high energies. The uncertainty due to the description of primary hadronic interactions is the dominant one.

Finally and summarizing all this study, figure 4.30 shows central values for flux prediction at far and near detectors, along with the uncertainties computed in this section. For comparison purposes, also flux predictions based on the Cho/CERN model are plotted in the same figure.

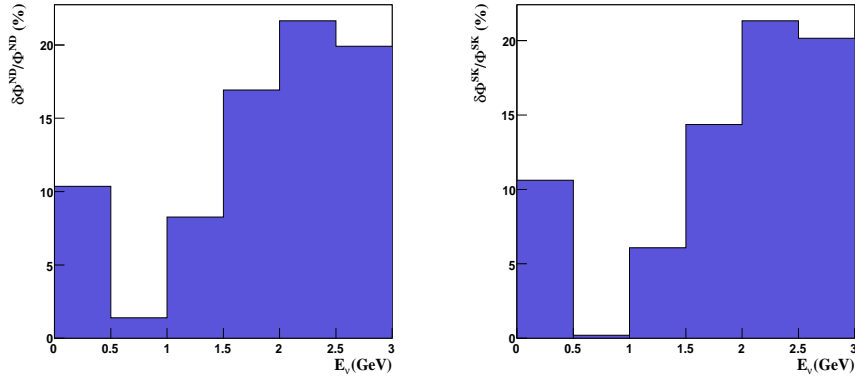


Figure 4.26: Uncertainties in the muon neutrino flux predictions as a function of neutrino energy E_ν associated with a systematic change in the description of secondary hadronic interactions, corresponding to varying the default GFLUKA/CALOR model to the GHEISHA model, both for what concerns the rate of secondary hadronic interactions and the description of the final state in secondary hadronic interactions (multiplicities and kinematics of tertiaries). Left: uncertainties on the near flux. Right: uncertainties on the far flux. The filled and empty histograms show the errors from this error source alone and all errors in this error category (primary interactions), respectively. This systematic variation is motivated in the text and by Fig. 4.25.

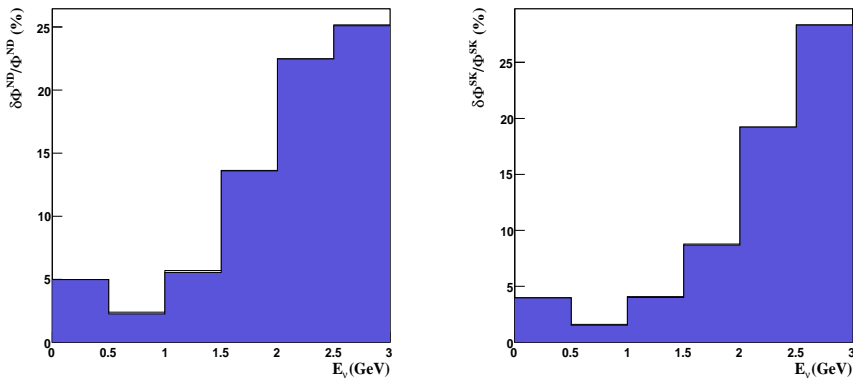


Figure 4.27: Uncertainties in the muon neutrino flux predictions as a function of neutrino energy E_ν associated with a systematic change in the description of the magnetic field of the horns, corresponding to varying the magnetic field amplitude (peak horn current) by 10% in both horns. Left: uncertainties on the near flux. Right: uncertainties on the far flux. The filled and empty histograms show the errors from this error source alone and all errors in this error category (primary interactions), respectively. This systematic variation is motivated in Ref. [87, 88].

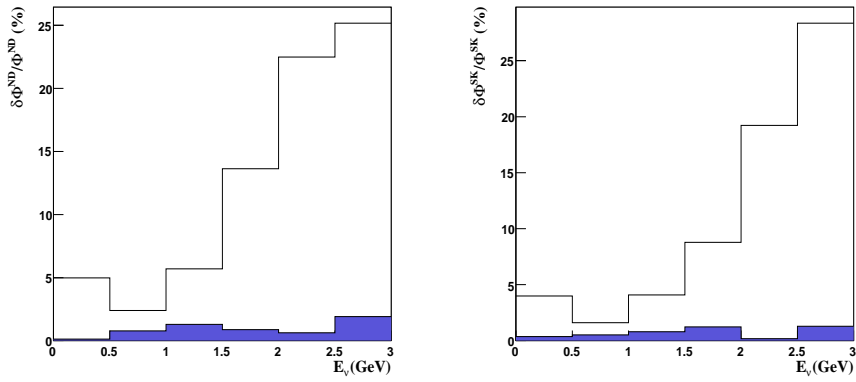


Figure 4.28: Uncertainties in the muon neutrino flux predictions as a function of neutrino energy E_ν associated with a systematic change in the description of the magnetic field of the horns, corresponding to introducing azimuthal perturbations in the magnetic field of both horns, with an amplitude of 15% and a period of $2\pi/4$ in ϕ . Left: uncertainties on the near flux. Right: uncertainties on the far flux. The filled and empty histograms show the errors from this error source alone and all errors in this error category (primary interactions), respectively. This systematic variation is motivated in Ref. [89].

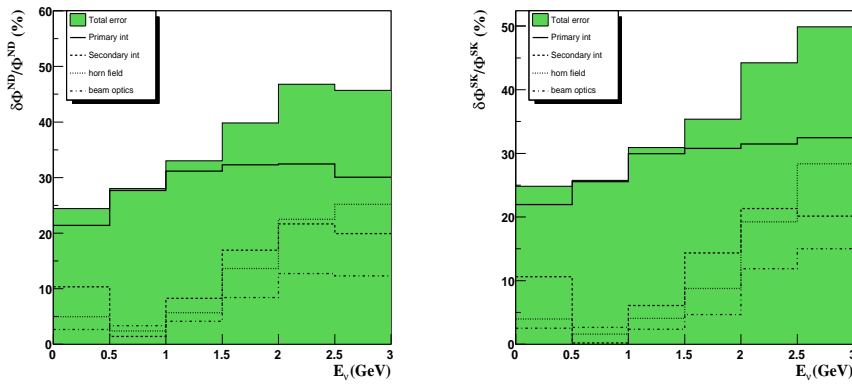


Figure 4.29: Summary of systematic uncertainties in the muon neutrino flux predictions as a function of neutrino energy E_ν . Left: near flux uncertainties. Right: far flux uncertainties. The solid, dashed, dotted, and dot-dashed lines show the contributions due to all uncertainties related to primary hadronic interactions, secondary hadronic interactions, horn magnetic fields and beam optics, respectively. The filled histogram shows the total systematic uncertainty.

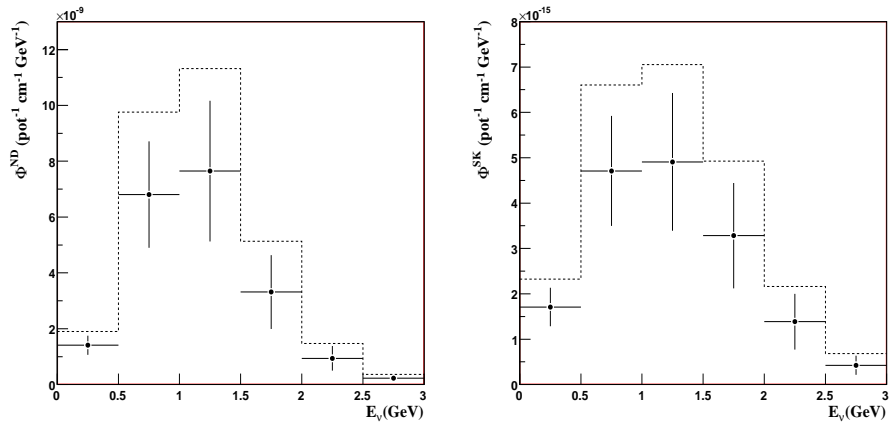


Figure 4.30: Summary of flux predictions for (left) the near detector of K2K and (right) the SK far detector, based on the HARP inputs and the full systematic error evaluation described in this section. The points with error bars show the HARP-based central value and the total systematic uncertainties given in Fig. 4.29. The dashed histogram shows the central value flux predictions based on the Cho/CERN model for π^+ production.

4.6.3 Prediction of the far-to-near ratio from the HARP result

We compute now the F/N ratio based on neutrino flux predictions presented in previous section. The first think to notice is that absolute flux normalization does not play any role in the F/N ratio. Therefore, one can consider flux predictions with relative normalization. In this case, flux prediction uncertainties related to absolute normalization are not taken into account (corresponding to the error in parameter c_1 of Sanford-Wang formula). Relatively-normalized flux predictions are shown in figure 4.31, along with Cho/CERN model predictions and PIMON measurements above 1 GeV. As can be seen, all of them agree within errors, being the HARP prediction the most accurate. Note also that for the K2K analysis, the last bin has been integrated from 2.5 up to 10 GeV.

The F/N ratio ($\Phi^{\text{SK}}/\Phi^{\text{ND}}$) in absence of oscillations is then computed with the predicted fluxes. Prediction from HARP π^+ production measurement, with systematic errors according to the discussion in previous section, can be seen in figure 4.32 as a function of neutrino energy. For comparison purposes, Cho-CERN and PIMON results are also shown. A summary of uncertainties in the F/N ratio integrated over all neutrinos energies is presented in table 4.10.

Error Category	Error Source	$\delta_{F/N}$ (%)
Primary Beam Optics	Mean centering	0.03
	Mean aiming	0.03
	Spread and angular divergence	0.75
	Sub-total	0.76
Primary Hadronic Int.	Interaction rate	0.63
	Multiplicity and kinematics of π^+ prod.	1.43
	Multiplicity of K^\pm, K_0, \bar{K}_0 production	0.23
	Sub-total	1.58
Secondary Hadronic Int.	Rate, tertiary multiplicity and kinematics	0.71
	Sub-total	0.71
Horn Magnetic Fields	Magnetic field strength	0.52
	Azimuthal field perturbations	0.34
	Sub-total	0.62
All	Total	1.99

Table 4.10: Summary of systematic uncertainties in the F/N ratio flux prediction integrated over all neutrino energies. The symbol $\delta_{F/N}$ indicate the fractional errors on the F/N ratio. Both the total errors and the individual error contributions considered in section 4.6.2 are listed.

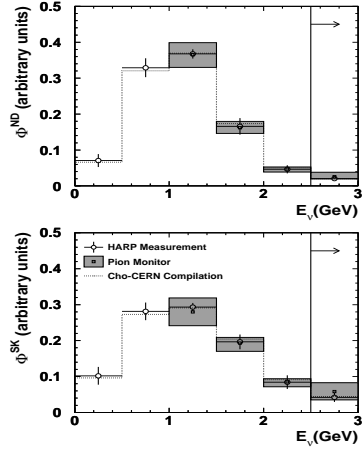


Figure 4.31: Relatively-normalized muon neutrino flux predictions at the near (top) and far (bottom) detectors. The empty circles with error bars show the central values and shape-only errors based on the HARP π^+ production measurement, the empty squares with shaded error boxes show the central values and errors from the pion monitor (PIMON) measurement, and the dotted histograms show the central values from the Cho-CERN compilation of older (non-HARP) π^+ production data. The PIMON predictions are normalized such that the integrated fluxes above 1 GeV neutrino energy match the HARP ones, at both the near and far detectors.

We estimate that the flux ratio uncertainty as a function of the neutrino energy binning used in this analysis is at the 2-3% level below 1 GeV neutrino energy, while it is of the order of 4-9% above 1 GeV. We find that the dominant contribution to the uncertainty in F/N comes from the HARP π^+ measurement itself. In particular, the uncertainty in the flux ratio prediction integrated over all neutrino energies is 2.0%, where the contribution of the HARP π^+ production uncertainty is 1.4%. Table 4.11 shows the contributions of all systematic uncertainty sources discussed above on the far-to-near flux ratio prediction for each neutrino energy bin.

The dotted histograms in Figures 4.31 and 4.32 show the central value pre-

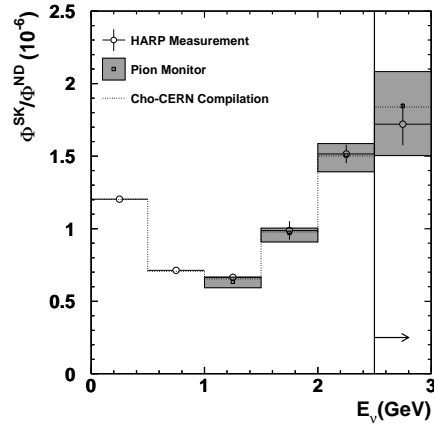


Figure 4.32: Prediction for the K2K muon neutrino F/N flux ratio in absence of oscillations. The empty circles with error bars show the central values and systematic errors on the muon neutrino flux predictions from the HARP π^+ production measurement, the empty squares with shaded error boxes show the central values and errors from the pion monitor measurement, and the dotted histograms show the central values from the Cho-CERN compilation of older (non-HARP) π^+ production data.

dicted by using the “Cho-CERN” compilation for primary hadronic interactions, which was used in K2K prior to the availability of HARP data. We find that the predictions of F/N flux ratio by HARP and Cho-CERN are consistent with each other for all neutrino energies. Note that the difference between Cho-CERN and HARP central values represents a difference in hadron production treatment only.

However, HARP results provide a much more accurate F/N ratio since uncertainties have been reduced with respect to the old error evaluation based on Cho/CERN model and PIMON measurement (described in section 4.4), as can be seen in last row of table 4.11.

Error Source	0.0–0.5	0.5–1.0	1.0–1.5	1.5–2.0	2.0–2.5	2.5–
Hadron interactions						
Primary int. rate	0.3	0.9	0.9	2.1	0.2	0.3
π^+ mult. and kinemat.	0.7	2.0	1.8	2.1	2.9	4.7
Kaon multiplicity	0.1	<0.1	0.1	<0.1	0.1	4.9
Secondary interactions	0.3	1.2	2.0	2.1	0.4	0.7
Horn magnetic field						
Field strength	1.1	0.8	1.4	4.2	2.8	3.9
Field homogeneity	0.3	0.2	0.5	0.3	0.6	0.3
Primary beam optics						
Beam centering	0.1	<0.1	<0.1	<0.1	0.1	0.1
Beam aiming	0.1	<0.1	<0.1	0.1	0.4	0.2
Beam spread	0.1	0.7	1.7	3.4	1.0	3.2
Total Error	1.4	2.7	3.6	6.5	4.2	8.5
Total Error Cho+PIMON	2.6	4.3	4.9	10	11	12

Table 4.11: Contributions to the uncertainty in the far-to-near flux ratio prediction. The uncertainties are quoted in %. The six columns refer to different bins in neutrino energy, as shown in the table in units of GeV. Last row shows *old* systematic evaluation from Cho/CERN model plus PIMON measurements, as described in section 4.4, used in [68].

4.6.4 Summary of flux predictions based on HARP

In this section, we have presented flux predictions for the K2K experiment based on the recent measurement by HARP of the inclusive production cross-section of positive pions, in the collisions of protons at the K2K beam momentum with a thin aluminum target [61]. These predictions are based on the official K2K beam Monte Carlo simulation code, where we have varied the π^+ production hadronic model to make use of the HARP results, while keeping all other aspects of the simulation unchanged, such as beamline geometry, primary beam optics, description of secondary hadronic interactions, horn focusing, meson and muon decays. In addition to the central value predictions, we have also re-evaluated the systematic uncertainties affecting those predictions, both for what concerns the absolute fluxes at the near and far detectors, and for the far-to-near flux ratio prediction. Finally, we compared these new results with the previous beam Monte Carlo flux predictions, based on the Cho/CERN hadronic model for π^+ production.

The F/N flux ratio used to extrapolate the measurements in ND to the ex-

pectation in SK is obtained in three independent ways: using the HARP measurement, the Cho-CERN model, and the PIMON measurement, as described in the previous sections. We find that all three predictions of the F/N ratio are consistent with each other within their measurement uncertainties. Among these measurements, we use the one predicted by the HARP measurement in the current neutrino oscillation analysis, since the HARP pion production measurement was done for the same conditions as K2K experiment: the proton beam momentum and the relevant phase space of pions responsible for the neutrinos in K2K are the same. In particular, the measured momentum region by the HARP experiment reaches below $2 \text{ GeV}/c$ down to $0.75 \text{ GeV}/c$ where the PIMON is insensitive. The HARP measurement also gives us the most accurate measurements on hadron production.

The central values for the F/N flux ratio as a function of neutrino energy obtained from the HARP π^+ production results, \bar{R}_i , are given in Tab. 4.12, where the index i denotes an energy bin number. The total systematic uncertainties on the F/N flux ratio as a function of neutrino energy are given in Tab. 4.13, together with the uncertainty correlations among different energy bins, expressed in terms of the fractional error matrix $\langle \delta R_i \delta R_j \rangle / (\bar{R}_i \bar{R}_j)$, where i, j label neutrino energy bins. The F/N central values and its error matrix are used in the analysis for neutrino oscillation described later.

Energy Bin Number i	E_ν [GeV]	$\bar{R}_i (\times 10^{-6})$
1	0.0–0.5	1.204
2	0.5–1.0	0.713
3	1.0–1.5	0.665
4	1.5–2.0	0.988
5	2.0–2.5	1.515
6	2.5–	1.720

Table 4.12: Predictions for the F/N muon neutrino flux ratio as a function of neutrino energy, for the HARP model for π^+ production in primary hadronic interactions. The neutrino energy binning is also indicated.

While the neutrino flux predictions given in this section are appropriate for most of the protons on target used in this analysis, a small fraction of the data was taken with a different beam configuration. The K2K-Ia period differed from the later configuration, as described in Sec. 4.2.2. As a result, the far/near flux

Energy Bin	1	2	3	4	5	6
1	0.187	0.002	-0.036	-0.372	-0.281	0.240
2	0.002	0.728	0.868	1.329	0.698	-1.398
3	-0.036	0.868	1.304	2.122	1.041	-2.040
4	-0.372	1.329	2.122	4.256	2.165	-3.799
5	-0.281	0.698	1.041	2.165	1.779	-2.678
6	0.240	-1.398	-2.040	-3.799	-2.678	7.145

Table 4.13: Fractional error matrix $\langle \delta R_i \delta R_j \rangle / (\bar{R}_i \bar{R}_j)$ obtained from the systematic uncertainties on the F/N flux predictions. The neutrino energy binning is the same as in Tab. 4.12. The values are given in units of 10^{-3} .

ratio for June 1999 is separately estimated, in the same manner as described above for later run periods. We find that the flux ratio predictions for the two beam configurations, integrated over all neutrino energies, differ by about 0.4%. The flux ratio prediction for the June 1999 beam configuration and the ND spectrum shape uncertainties are used to estimate the expected number of neutrino events in SK and its error for the June 1999 period.

4.7 Measurements at near and far detectors

4.7.1 Measurement at the near detector system

Two main measurements are performed in the near detector site:

1. neutrino event rate (1KT measurement)
2. neutrino energy spectrum (combination of 1KT, SciFi and SciBar detectors)

Moreover, beam stability is also monitored with the measurements done at the near detector site. This section briefly summarizes the role of the near site data in the K2K experiment.

Neutrino event rate measurement

The integrated flux of the neutrino beam folded with the neutrino interaction cross-section can be determined by measuring the neutrino event rate at the near site. We recall that the event rate at the 1KT is used in the oscillation analysis: since neutrinos have not oscillated yet (detector site is only 300 m away from the beam source), any difference between the measured rates in 1KT and SK can be treated in terms of neutrino oscillation. In addition, the stability of the neutrino beam can be monitored thanks to the MRD measurements, from which beam properties can be derived. Furthermore, LG and SciBar detectors are able to measure the electron neutrino contamination in the beam.

As described in section 4.3.1, the 1KT water cherenkov detector allows the measurement of the absolute number of neutrino interactions in the near site and the prediction of the number of neutrino interactions in the far site. Since the 1KT uses a water target and almost the same hardware and software as SK, the systematic error in the predicted number of interactions at the far site can be reduced.

The fiducial volume in the 1KT is defined as a horizontal cylinder with axis along the beam direction (z-axis). The radius is 200 cm and the z coordinate is limited to $-200 \text{ cm} < z < 0 \text{ cm}$, where the center of the 1KT ID is defined as $z = 0 \text{ cm}$, and the total fiducial mass is 25 tons. The fiducial volume cut results in an almost pure neutrino sample, rejecting cosmic rays or muons generated by the beam in the materials surrounding the 1KT (beam-induced muons).

These are the two major background sources considered. Cosmic ray events usually have a vertex near the upper wall of the inner tank, but some events contaminate the fiducial volume due to failure of the vertex reconstruction. It is found that cosmic rays in the fiducial volume are 1.0% of the neutrino data. The other important background source is beam-induced muons which can be tagged by PMTs located in the outer detector. After the vertex cut, the remaining events are estimated to be 0.5%.

Table 4.14 shows the total number of neutrino interactions and the number of protons on target for each period. N_{obs}^{1KT} stands for the number of observed events, while N_{int}^{1KT} is the total number of events, taking into account detection efficiency corrections.

The dominant error associated with the event rate is the uncertainty of the fiducial volume, which is 3%. This systematic is estimated from the comparison of neutrino interaction in data and MC simulation. Another non-negligible error is the uncertainty of the event rate stability. It is computed to be 2%. In total, a $\pm 4.1\%$ is quoted for the error on the number of 1KT neutrino events over the entire K2K run.

Neutrino spectrum at the near detector

Apart from the neutrino event rate, the near detector site (containing 1KT, SciFi and SciBar detectors) performs also a measurement of the neutrino energy spectrum before the oscillation, using a sample of CC events. The neutrino energy is reconstructed from the muon kinematic parameters p_μ and θ_μ assuming a QE interaction as given in Eq. 4.2. The two-dimensional distributions of p_μ

Period	$POT_{1KT}(10^{18})$	N_{obs}^{1KT}	N_{int}^{1KT}
Ia	2.6	4282	7206
Ib	39.8	75973	130856
IIa	21.6	43538	73614
IIb	17.1	34258	57308
IIc	2.9	5733	9346

Table 4.14: Number of neutrino interactions in the 1KT. N_{obs}^{1KT} stands for the number of observed events, while N_{int}^{1KT} is the total number of events, taking into account detection efficiency corrections.

versus θ_μ are used to measure the neutrino energy spectrum. The spectrum is fitted by using a χ^2 method to compare observed (p_μ, θ_μ) distributions to MC expectations.

The fitting method

In order to obtain the neutrino energy spectrum, the (p_μ, θ_μ) distribution is fit with the MC expectation. The neutrino energies are divided into eight bins as shown in Table 4.15. The free parameters in the fit are the neutrino energy spectrum parameters for eight energy bins ($f_1^\phi, \dots, f_8^\phi$) and a parameter, R_{nQE} , which represents the relative weighting of CC-nonQE events to CC-QE events. The systematic uncertainties, such as nuclear effects, the energy scale, the track finding efficiency, and other detector related systematics, are also incorporated as the fitting parameters (\mathbf{f}). The contents in (m, n) -th bin of the (p_μ, θ_μ) distribution, $N_{m,n}^{\text{MC}}$, is expressed with the 16 templates and the fitting parameters as,

$$N_{m,n}^{\text{MC}} \equiv P \cdot \sum_{i=1}^8 f_i^\phi \cdot \left[N_{m,n,i}^{\text{MC(QE)}} + R_{\text{nQE}} \cdot N_{m,n,i}^{\text{MC(nQE)}} \right], \quad (4.19)$$

where P , $N_{m,n,i}^{\text{MC(QE)}}$ and $N_{m,n,i}^{\text{MC(nQE)}}$ are a normalization parameter, the number of expected contents in the (m, n) -th bin for QE interaction and that for non-QE interaction for the i -th neutrino energy bin. We take the χ^2 between the observed distributions, $N_{m,n}^{\text{obs}}$, and $N_{m,n}^{\text{MC}}$.

During the fit, the flux in each energy bin and R_{nQE} are re-weighted relative to the nominal values in the MC simulation. The flux for $E_\nu = 1.0 - 1.5$ GeV bin is fixed to unity for the normalization, and another set of parameters are prepared for relative normalization of each detector.

The χ^2 functions are separately defined for each detector and then summed to build a combined χ^2 function as

$$\chi_{\text{ND}}^2 = \chi_{\text{IKT}}^2 + \chi_{\text{SF}}^2 + \chi_{\text{SB}}^2 \quad (4.20)$$

Further details about how these χ^2 terms are computed are given in [38]. Finally, a set of the fitting parameters ($f_i^\phi, R_{\text{nQE}} : \mathbf{f}$) is found by minimizing the χ^2 function. The best fit values, their error sizes and the correlations between them are used as inputs to the oscillation analysis, as described in section 4.8.

f_1^ϕ	f_2^ϕ	f_3^ϕ	f_4^ϕ	f_5^ϕ	f_6^ϕ	f_7^ϕ	f_8^ϕ
0.0–0.5	0.5–0.75	0.75–1.0	1.0–1.5	1.5–2.0	2.0–2.5	2.5–3.0	3.0–

Table 4.15: The E_ν (GeV) interval of each bin, used for the fit of the near detector site energy spectrum

Fit results

The minimum χ^2 point in the multi-parameter space is found by changing the spectrum shape, R_{nQE} and the systematic parameters. The central values and the errors of the fitting parameters are summarized in Table 4.16. All the systematic parameters stay within their estimated errors. The result of the spectrum measurement is shown in Fig. 4.33 with the prediction of the beam MC simulation.

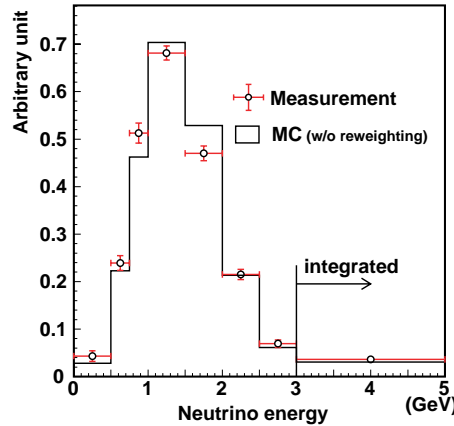


Figure 4.33: The neutrino energy spectrum measured at the near site, assuming CC-QE. The expectation with the MC simulation without reweighting is also shown. Figure from [38].

The errors of the measurement are provided in the form of an error matrix. Correlations between the parameters are taken into account in the oscillation analysis with this matrix. The full elements in the error matrix are shown in Table 4.17.

parameter	best fit
f_1 (0.00-0.50 GeV)	1.657 ± 0.437
f_2 (0.50-0.75 GeV)	1.107 ± 0.075
f_3 (0.75-1.00 GeV)	1.154 ± 0.061
f_4 (1.00-1.50 GeV)	$\equiv 1$
f_5 (1.50-2.00 GeV)	0.911 ± 0.044
f_6 (2.00-2.50 GeV)	1.069 ± 0.059
f_7 (2.50-3.00 GeV)	1.152 ± 0.142
f_8 (3.00- GeV)	1.260 ± 0.184
R_{nQE}	0.964 ± 0.035

Table 4.16: Results of the spectrum measurement. The best fit value of each parameter is listed. Data from [38].

	f_1	f_2	f_3	f_5	f_6	f_7	f_8	R_{nQE}
f_1	43.86	-3.16	7.28	-2.21	-0.76	-3.48	0.81	-8.62
f_2	-3.16	7.51	1.97	1.90	0.62	1.29	2.43	-5.68
f_3	7.28	1.97	6.00	3.38	1.63	3.44	1.71	-2.99
f_5	-2.21	1.90	3.38	4.04	-1.86	4.53	2.20	1.65
f_6	-0.76	0.62	1.63	-1.86	5.28	-5.85	5.11	0.94
f_7	-3.48	1.29	3.44	4.53	-5.85	13.67	-10.14	4.09
f_8	0.81	2.43	1.71	2.20	5.11	-10.14	18.35	-11.77
R_{nQE}	-8.62	-5.68	-2.99	1.65	0.94	4.09	-11.77	20.30

Table 4.17: The error matrix for f_i and R_{nQE} . The square root of error matrix (sign $[M_{ij}] \cdot \sqrt{|M_{ij}|}$) is shown here in the unit of %. Data from [38].

4.7.2 Measurement at Super-Kamiokande

Number of observed neutrino events

Events which are fully contained in the SK fiducial volume are reconstructed using similar methods to the SK atmospheric neutrino analysis and then used in the K2K oscillation analysis.

One has to ensure that neutrino event sample comes from the K2K beam and not from other sources, and consequently *timing* cut needs to be applied. In order to select those neutrino interactions which come from the accelerator at KEK, two Universal Time Coordinated time stamps from the worldwide GPS system are compared: time at the beam source (KEK-PS beam) and time at SK. The difference between both has to be compatible with the time of flight of beam neutrinos.

In addition to the timing criteria, additional cuts are required to ensure the quality of the event sample. The main goals of these cuts are to reject eventual sources of background (decay electrons, incoming external events, ...) and they rely mainly on the fiducial volume cut and the PMT response.

In total, 112 accelerator produced, fully contained events, are observed in the SK fiducial volume, with 58 events reconstructed as 1-ring μ -like. Tab. 4.18 summarizes the characterization of these events and the MC expectations with and without neutrino oscillation.

	K2K-I			K2K-II		
	data	expected		data	expected	
		w/o osc.	w/ osc.		w/o osc.	w/ osc.
Fully contained	55	80.8	54.8	57	77.3	52.4
1-ring	33	51.0	31.1	34	49.7	30.5
μ -like	30	47.1	27.7	28	45.2	26.7
e-like	3	3.9	3.4	6	4.5	3.8
multi-ring	22	29.8	23.7	23	27.6	21.9

Table 4.18: SK event summary. For oscillated expectations, $\sin^2 2\theta = 1$ and $\Delta m^2 = 2.8 \times 10^{-3} \text{ eV}^2$ are assumed. Table from [38].

The systematic uncertainties for estimating N_{SK} and the reconstructed neutrino energy in SK are evaluated using atmospheric neutrinos as a control sample. Tab. 4.19 shows the systematic errors for N_{SK} . As it occurs for the 1KT

	K2K-I	K2K-II
event selection	<1%	<1%
fiducial volume cut	2%	2%
decay electron background	0.1%	0.1%
MC statistics	0.6%	0.6%
Total	3%	3%

Table 4.19: Systematic errors for N_{SK} . Table from [38].

measurement, the dominant uncertainty on N_{SK} comes from the vertex reconstruction. Since a cut is made on fiducial volume a systematic shift in or out of this volume will either over or underestimate the number of events expected. It is evaluated comparing the number of events for atmospheric neutrino data with the MC expectation in the fiducial volume using two different vertex reconstruction programs.

Energy distribution

The energy distribution of the events is compared against expectation in several ways. Fig. 4.34 shows the visible energy distribution, which is estimated from the energy deposit in the inner detector for all of the fully contained fiducial volume events. In this figure, the observed data is compared with the MC expectation based on the ND measurement without neutrino oscillation.

Figure 4.35 shows the expected energy spectrum together with the observation for the one-ring μ -like events. The expectation is normalized by the number of observed events (58). The neutrino energy is reconstructed using the reconstructed muon momentum and the known beam-direction while assuming there was a QE interaction and ignoring the Fermi momentum. As can be seen, compared to the MC expectation there is a deficit of $1R\mu$ events in the low energy region, as is expected from the oscillation hypothesis.

Systematic errors on the energy spectrum come from reconstruction algorithms and energy scale and they are estimated also from atmospheric neutrinos. Both sources of systematics are taken into account in the oscillation analysis. The uncertainties associated to the reconstruction algorithms range between 3% and 6%, while that associated to the energy scale is 2%.

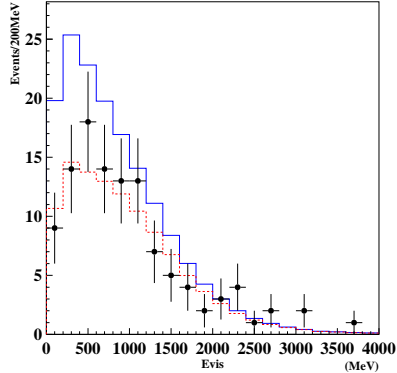


Figure 4.34: The visible energy distribution for fully contained fiducial-volume events in SK. The closed circles are the observed data. The solid histogram is the MC expectation based on the ND measurement without neutrino oscillation, and the dashed one is the MC expectation with neutrino oscillation of $\sin^2 2\theta = 1$ and $\Delta m^2 = 2.8 \times 10^{-3} \text{ eV}^2$. Figure from [38].

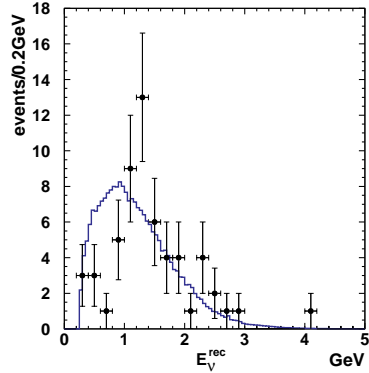


Figure 4.35: Reconstructed E_ν distribution for the SK 1-ring μ -like sample. Points with error bars are data. The solid line is the expectation without oscillation. The histogram is normalized by the number of events observed (58). Figure from [38].

4.8 Neutrino Oscillation Analysis

As previously said, the signatures of neutrinos oscillating from ν_μ to ν_τ are both a reduction in the total number of observed neutrino events and a distortion in the neutrino energy spectrum. Thus, one can perform a two-flavor neutrino oscillation analysis based on the comparison between the observation values and the expected ones in absence of oscillation. Such analysis has been developed in K2K using a maximum-likelihood method.

The likelihood \mathcal{L} is built from three different contributions:

1. $\mathcal{L}_{\text{norm}}$: takes into account the observed number of events at SK
2. $\mathcal{L}_{\text{shape}}$: takes into account the shape of the E_ν^{rec} spectrum at SK
3. $\mathcal{L}_{\text{syst}}$: takes into account systematic uncertainties

The systematics are also treated as fitting parameters in the likelihood. They are included in the constraint likelihood term ($\mathcal{L}_{\text{syst}}$) where they are varied within their uncertainties, thus modifying the expectation. The systematic parameters in the likelihood come from:

- neutrino energy spectrum at the near detector site
- F/N flux ratio
- neutrino-nucleus cross-section
- efficiency and energy scale of SK
- overall normalization

Summarizing, the total likelihood function can be written as:

$$\mathcal{L} = \mathcal{L}_{\text{norm}} \times \mathcal{L}_{\text{shape}} \times \mathcal{L}_{\text{syst}}. \quad (4.21)$$

The oscillation parameters, Δm^2 and $\sin^2 2\theta$, are obtained by maximizing the likelihood function. One-hundred twelve fully contained events are used in $\mathcal{L}_{\text{norm}}$ and fifty eight FC one-ring μ -like events are used for $\mathcal{L}_{\text{shape}}$, respectively.

4.8.1 Predictions at Super-Kamiokande

First step of the analysis is to predict the number of neutrino events at SK ($N_{\text{exp}}^{\text{SK}}$) and the reconstructed energy spectrum $\phi_{\text{exp}}^{\text{SK}}(E_{\nu}^{\text{rec}})$. We take advantage of the F/N flux ratio defined in section 4.4 to estimate the neutrino flux at SK (Φ^{SK}). Then, $N_{\text{exp}}^{\text{SK}}$ and can $\phi_{\text{exp}}^{\text{SK}}$ be derived from Φ^{SK} .

Predicted flux at SK

The neutrino flux at SK is estimated from the F/N flux ratio $R^{\text{F/N}}$ and the measured ND spectrum Φ^{ND} :

$$\Phi^{\text{SK}} = R^{\text{F/N}}(E_{\nu}) \cdot \Phi^{\text{ND}}(E_{\nu}) \cdot (1 - P(E_{\nu}; \Delta m^2, \sin^2 2\theta)),$$

where $P(E_{\nu}; \Delta m^2, \sin^2 2\theta)$ is the neutrino oscillation probability given by Eq. (4.1).

The uncertainties of Φ^{ND} and their correlation are obtained from the ND analysis as shown in Tab. 4.17. Those for $R^{\text{F/N}}$ are derived from the HARP π^+ measurement and the beam MC simulation, and are summarized in Tab. 4.13.

Number of neutrino events

The expected number of neutrino events in SK ($N_{\text{exp}}^{\text{SK}}$) is derived by extrapolating the measured number of interactions in the 1KT ($N_{\text{int}}^{\text{1KT}}$) with the ratio of the expected neutrino event rate per unit mass, $\rho^{\text{SK}}/\rho^{\text{1KT}}$. Taking into account the difference of fiducial mass (M) and the number of protons on target (POT) used in the analysis for 1KT and SK, $N_{\text{exp}}^{\text{SK}}$ is written as:

$$N_{\text{exp}}^{\text{SK}}(\Delta m^2, \sin^2 2\theta) \equiv N_{\text{int}}^{\text{1KT}} \cdot \frac{\rho^{\text{SK}}}{\rho^{\text{1KT}}} \cdot \frac{M^{\text{SK}}}{M^{\text{1KT}}} \cdot \frac{\text{POT}^{\text{SK}}}{\text{POT}^{\text{1KT}}} \cdot C_{\nu_e}, \quad (4.22)$$

where superscripts “1KT” and “SK” denote the variable for SK and 1KT, respectively, and C_{ν_e} is the correction factor for the difference of the electron neutrino contamination in the neutrino beam at 1KT and SK. The value of C_{ν_e} is estimated to be 0.996 with the MC simulation.

The expected event rate at each detector, ρ , is calculated from the neutrino flux Φ , the neutrino-water interaction cross-section σ , and the detector efficiency ϵ estimated with the MC simulation:

$$\rho = \int dE_{\nu} \Phi(E_{\nu}) \cdot \sigma(E_{\nu}) \cdot \epsilon(E_{\nu}).$$

In order to be insensitive to the absolute cross-section uncertainty, we incorporate the uncertainties in neutrino-nucleus cross-section as the cross-section ratio relative to CC-QE interactions. The uncertainty of the CC-nonQE/CC-QE cross-section ratio is taken from the ND measurements. The uncertainties from event reconstruction at SK are summarized in Tab. 4.19. The uncertainty of the overall normalization of the number of events in each period is estimated from the fiducial mass error of 1KT and SK and the uncertainty in the difference of the number of protons on target used for the analysis. In total, the normalization error is estimated to be $\pm 5.1\%$ for both Ib and II periods.

The number of FC events without neutrino oscillation is estimated to be $158.1^{+9.2}_{-8.6}$. We estimate the expected number of events without neutrino oscillation taking into account all of the known systematic uncertainties, using a MC technique. This technique allows us to determine the contributions from the individual systematics to the the total error by selectively including only some errors during the generation. We find that the dominant error sources are the fiducial volume uncertainties in 1KT and SK $(^{+4.9\%}_{-4.8\%})$ and the F/N ratio $(^{+2.9\%}_{-2.9\%})$. We recall error on the F/N ratio used to be $\pm 5\%$ before HARP prediction of the K2K neutrino flux, so it was comparable to one associated with fiducial volumes. Although uncertainty on $R^{F/N}$ is still one of the dominant errors in the K2K analysis, it is not the most relevant one any more after introduction of HARP results.

Reconstructed neutrino energy spectrum

The expected spectrum shape of the reconstructed neutrino energy at SK, $\phi_{\text{exp}}^{\text{SK}}(E_{\nu}^{\text{rec}})$, is calculated as:

$$\phi_{\text{exp}}^{\text{SK}} = \int dE_{\nu} \cdot \Phi^{\text{SK}}(E_{\nu}) \cdot \sigma(E_{\nu}) \cdot \epsilon_{1\text{R}\mu}^{\text{SK}}(E_{\nu}) \cdot r(E_{\nu}; E_{\nu}^{\text{rec}}), \quad (4.23)$$

where $\epsilon_{1\text{R}\mu}^{\text{SK}}$ is the detection efficiency for muon events in SK and $r(E_{\nu}; E_{\nu}^{\text{rec}})$ is the probability of reconstructing an event with true energy E_{ν} as E_{ν}^{rec} . Both of them are estimated with the MC simulation. In the actual procedure, the E_{ν} and E_{ν}^{rec} are binned with an interval of 50 MeV, and hence the integral over the true neutrino energy is replaced by a summation over true energy bins.

The uncertainties from the neutrino energy spectrum at the ND, the F/N flux ratio, and the cross-section ratios are incorporated as described above.

Apart from the other systematics described above, the uncertainties from muon event reconstruction at SK are also taken into account. The energy scale

uncertainty in SK is 2.1% for SK-I and 2.0% for SK-II, respectively, as described in section 4.7.2.

The expected E_ν^{rec} spectrum shape for null oscillation case and its error are estimated using the same technique as the number of events and shown in Fig. 4.36. The height of the box represents the size of estimated error in each bin. The contribution of each systematic uncertainty is estimated by turning each uncertainty on exclusively one by one, as shown in Fig. 4.37. We find that the error on the spectrum shape is dominated by the SK energy scale.

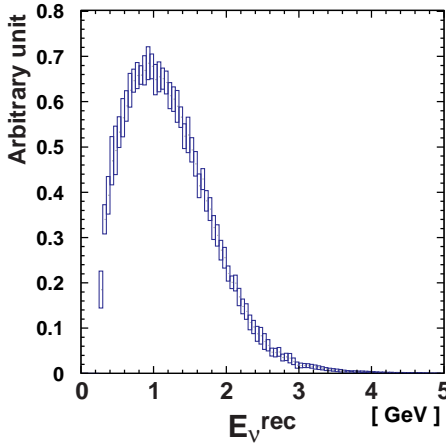


Figure 4.36: Expected reconstructed neutrino energy spectrum shape in the case of null oscillation. Height of boxes indicate the size of error. Figure from [38].

4.8.2 Likelihood definition

We describe now briefly each term of likelihood function defined in 4.21.

The normalization term, $\mathcal{L}_{\text{norm}}$, is defined as the Poisson probability to observe N_{obs} events when the expected number of events is N_{exp} :

$$\mathcal{L}_{\text{norm}} = \frac{(N_{\text{exp}})^{N_{\text{obs}}}}{N_{\text{obs}}!} e^{-N_{\text{exp}}} \quad (4.24)$$

The energy spectrum shape term is defined as the product of the probability for each muon event to be observed at reconstructed neutrino energy E_ν^{rec} . We use the expected neutrino energy spectrum, given in Eq. (4.23), as the probability density function. The probability density function is separately defined for each experimental period:

$$\mathcal{L}_{\text{shape}} = \prod_{i=1}^{N^{\text{obs}}} \phi_{\text{exp}}^{\text{SK}}(E_{\nu,i}^{\text{rec}}; \Delta m^2, \sin^2 2\theta) \quad (4.25)$$

Finally, the systematic parameters are treated as fitting parameters, and are assumed to follow a Gaussian distribution. They are constrained within their uncertainties by constraint terms expressed as:

$$\mathcal{L}_{\text{syst}} \equiv \prod_{j=1}^{N_{\text{syst}}} \exp(-\Delta \mathbf{f}_j^T (M_j)^{-1} \Delta \mathbf{f}_j), \quad (4.26)$$

where N_{syst} is the number of parameter sets, $\Delta \mathbf{f}_j$ represents the deviations of the parameters from their nominal values and M_j is the error matrix for j -th set of parameters.

4.8.3 Results

From the likelihood analysis two main results are obtained: best fit point for the $\Delta m^2 - \sin^2 2\theta$ space and the allowed region for the oscillation parameters. The following summarizes oscillation analysis results published in [38], along with the impact of the various systematics discussed in this work.

Best fit oscillation parameters

The point which maximizes the likelihood in the $\Delta m^2 - \sin^2 2\theta$ space within the physical region is:

$$(\Delta m^2, \sin^2 2\theta) = (2.8 \times 10^{-3} \text{eV}^2, 1.0). \quad (4.27)$$

At this point, the expected number of events is 107.2, which agrees well with the 112 observed within the statistical uncertainty. The observed E_ν^{rec}

distribution is shown in Fig. 4.38 together with both the expected distributions for the best-fit parameters, and the expectation without oscillations.

The probability that the observations can be explained equally well by the no oscillation and by the oscillation hypotheses is estimated by computing the difference of log-likelihood between the null oscillation case and the best fit point with oscillation. The null oscillation probability is calculated to be 0.0015 % (4.3σ). When only normalization (shape) information is used, the probability is 0.06% (0.42%).

Table 4.20 shows the effect of each systematic uncertainty on the null oscillation probability. The effect is tested by turning on the error source written in the first column in the table. As shown in the table, the dominant contributions to the probabilities for the normalization information are from the F/N flux ratio and the normalization error, while the energy scale is the dominant error source for the probability with the E_ν^{rec} shape information consistent with the results found using the MC test described in Sec. 4.8.1.

	Norm-only	Shape-only	Combined
Stat. only	0.01%	0.22%	0.0001%
FD spectrum	0.01%	0.24%	0.0002%
nQE/QE, NC/CC	0.01%	0.23%	0.0002%
Far/Near	0.02%	0.23%	0.0003%
ϵ^μ	—	0.23%	0.0002%
Energy scale	—	0.38%	0.0002%
Normalization	0.03%	—	0.0005%
All errors	0.06%	0.42%	0.0015%

Table 4.20: Effect of each systematic uncertainty on the null oscillation probability. The numbers in the table are null oscillation probabilities when only the error written in the first column is turned on. Table from [38].

Allowed region of oscillation parameters

The allowed region of oscillation parameters is evaluated computing the difference in the log-likelihood between each point and the best fit point:

$$\begin{aligned}
\Delta \ln \mathcal{L}(\Delta m^2, \sin^2 2\theta) &\equiv \ln \left(\frac{\mathcal{L}_{\max}^{\text{phys}}}{\mathcal{L}(\Delta m^2, \sin^2 2\theta)} \right) \\
&= \ln \mathcal{L}_{\max}^{\text{phys}} - \ln \mathcal{L}(\Delta m^2, \sin^2 2\theta),
\end{aligned} \tag{4.28}$$

where $\mathcal{L}_{\max}^{\text{phys}}$ is the likelihood at the best-fit point and $\mathcal{L}(\Delta m^2, \sin^2 2\theta)$ is the likelihood at $(\Delta m^2, \sin^2 2\theta)$ with systematic parameters that maximize the likelihood at that point.

The allowed regions in the neutrino oscillation parameter space, corresponding to the 68%, 90% and 99% confidence levels (CL) are shown in the left panel of Fig. 4.39. For comparison purposes, right panel of the same figure shows results of the previous K2K analysis ([68]).

The 90% C.L. contour crosses the $\sin^2 2\theta = 1$ axis at $\Delta m^2 = 1.9$ and 3.5×10^{-3} eV².

This result is compared with the parameters found by the measurement of atmospheric neutrino oscillation by the Super-Kamiokande collaboration [27]. Figure 4.40 shows the allowed regions of oscillation parameters found in this analysis together with the SK result. The K2K result is in good agreement with the parameters found using atmospheric neutrinos, thereby confirming the neutrino oscillation result reported by SK.

4.9 K2K Summary

The K2K experiment is a long-baseline neutrino experiment, that measures neutrino fluxes from an accelerator-based beam. A primary proton beam of 12 GeV/c collides with an aluminum target, where light hadrons are produced. Neutrinos from hadron decay constitute the neutrino beam. The fluxes are measured first in a detector site placed 300 meters away from the target station, where neutrinos have not yet oscillated. A second measurement of the neutrino flux takes place at Super-Kamiokande (SK) detector, 250 km away from the beam source, where a signature of oscillation is expected to be observed.

In order to measure the oscillation parameters, the energy spectrum and the flux normalization are used to predict the un-oscillated signal measured at SK. By means of Monte-Carlo (MC) techniques, a far-to-near flux ratio $R^{\text{F/N}}$ is computed to obtain such a prediction. The uncertainties associated with the

$R^{F/N}$ strongly depend on the MC description of the hadron production-cross section on aluminum. K2K beam MC used to rely on old cross-section measurements [64] and *in-situ* measurements to parameterize hadron production. This implied big errors on the $R^{F/N}$ estimation. In fact, $R^{F/N}$ used to be one of the dominant errors in previous K2K oscillation analysis [68]. However, in the current analysis [38] a new description of the hadron production coming from the HARP results has been introduced into K2K beam MC, leading to much more accurate estimation of the $R^{F/N}$.

HARP is an experiment meant to develop a systematic study of hadron production for beam momenta from $1.5 \text{ GeV}/c$ to $15 \text{ GeV}/c$ for a large range of target nuclei. Its first published result [61] is the measurement of the π^+ production on an aluminum target, for a proton beam momentum of $12.9 \text{ GeV}/c$. This measurement is relevant for the K2K experiment since it generates the neutrino beam under the same conditions. In this work, we describe the analysis performed to obtain the double-differential production cross-section of pions of positive charge. Then, results are used to describe pion production in the K2K beam MC and we predict the corresponding K2K neutrino flux, along with its uncertainties. We analyze a full set of systematics affecting the neutrino flux, including the ones coming from the HARP measurement. Finally, $R^{F/N}$ is computed. Overall error in this ratio is only 2%.

K2K took data from June 1999 to November 2004 and it has been used to compute neutrino oscillation parameters. One hundred and twelve beam-originated neutrino events are observed in the fiducial volume of Super-Kamiokande with an expectation of $158.1^{+9.2}_{-8.6}$ events without oscillation. The error coming from far-to-near ratio is $\pm 2.9\%$ (while it was $\pm 5\%$ before the HARP input to the beam MC) and it is not the dominant one anymore. The spectrum distortion expected from oscillation is also seen in fifty-eight muon-like events which have had their energy reconstructed. A likelihood analysis is performed and the probability that the observations are explained by a statistical fluctuation with no neutrino oscillation is 0.0015% (4.3σ). In a two flavor oscillation scenario, the allowed Δm^2 region at $\sin^2 2\theta = 1$ is between 1.9 and $3.5 \times 10^{-3} \text{ eV}^2$ at the 90 % C.L. with a best-fit value of $2.8 \times 10^{-3} \text{ eV}^2$. These results are consistent with the neutrino oscillation parameters previously measured by the Super-Kamiokande collaboration using atmospheric neutrinos.

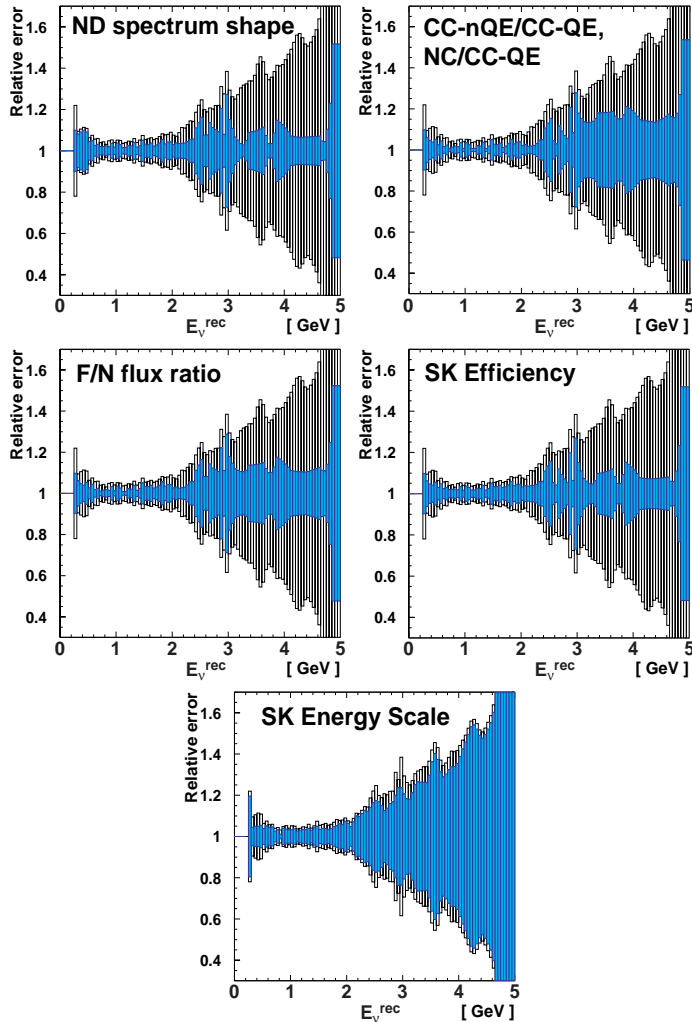


Figure 4.37: Contribution of each systematic error to the reconstructed neutrino energy spectrum. Vertical axis is relative error of the spectrum. Source of uncertainty is indicated in each plot. Blank and filled bars represent the sizes of the total error and the contribution from the source being considered, respectively. Figure from [38].

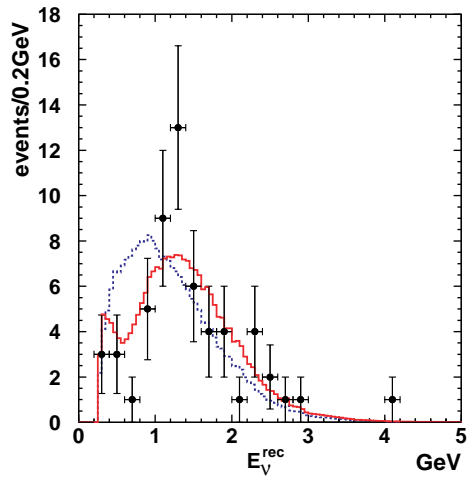


Figure 4.38: The reconstructed E_ν distribution for the 1-ring μ -like sample. Points with error bars are data. The solid line is the best fit spectrum with neutrino oscillation and the dashed line is the expectation without oscillation. These histograms are normalized by the number of events observed (58). Figure from [38].

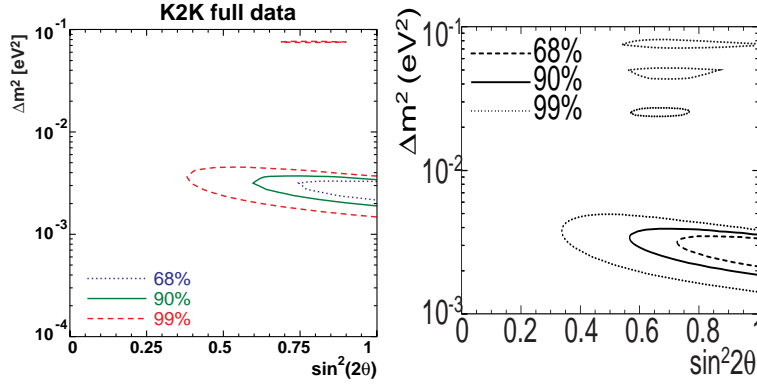


Figure 4.39: Allowed regions of oscillation parameters. Left: final K2K results as described in this work; three contours correspond to the 68% (dotted line), 90% (solid line) and 99% (dashed line) CL. allowed regions, respectively (Figure from [38]). Right: results from previous analysis, before HARP contribution and period IIc of data taking (Figure from [68]) .

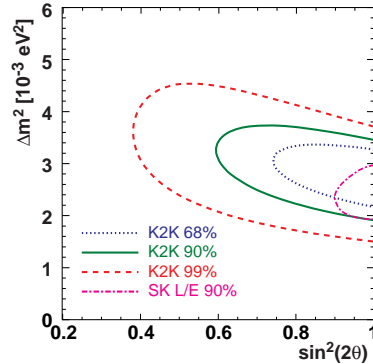


Figure 4.40: Comparison of K2K results with the SK atmospheric neutrino measurement [27]. Dotted, solid, dashed and dash-dotted lines represent 68%, 90%, 99% C.L. allowed regions of K2K and 90% C.L. allowed region from SK atmospheric neutrino, respectively. Figure from [38] .

Chapter 5

Nature of neutrino mass: SuperNEMO experiment

5.1 Overview

Results of oscillation experiments in the past few years have demonstrated that neutrinos are massive particles and that lepton number is not conserved. This is a proof of physics beyond the standard model. In addition, tritium β -decay experiments have established a very low limit on the electron neutrino mass. Grand unified theories can provide a natural framework for neutrino masses and lepton number violation. In particular, the seesaw model explains the smallness of the neutrino mass by requiring the existence of a Majorana neutrino. This kind of neutrino may also explain naturally the mechanism of leptogenesis.

A direct consequence of the above new physics is the renewed interest in the double beta decay experiments, since the discovery of the $\beta\beta^{0\nu}$ decay would prove the Majorana nature of the neutrino. In addition, double beta decay experiments offer a chance to measure the mass scale in combination with other kind of experiments, and the verification of the mass hierarchy.

The search for neutrino-less double beta decay processes ($\beta\beta^{0\nu}$) has been traditionally carried out with high resolution devices, such as germanium calorimeters [53, 90], characterized by a high efficiency for the signal, approaching 100%, and an impressive energy resolution, of the order of 0.1% at the end point of the two electron distribution.

The signal for this type of detectors is an event with total deposited energy

in a narrow window (of only a few keV) around $Q_{\beta\beta}$. This excellent energy resolution allows a powerful discrimination between $\beta\beta^{0\nu}$ and $\beta\beta^{2\nu}$ events, but is not sufficient to fully eliminate non- $\beta\beta$ backgrounds (e.g, the U and Th decay chains) since *any* energy deposition in the signal region will fake the signal.

On the other hand, since most of the backgrounds arising from natural radioactivity and other sources (cosmogenic activation, etc.) are photons or single electrons, an additional handle to reduce non- $\beta\beta$ backgrounds is to use the characteristic *topological signature* of a double $\beta\beta$ event, that is, the presence of two electrons of negative charge. This signature has been amply exploited by experiments such as ELEGANT [91] and the NEMO detector series [92, 93]. In particular, NEMO-2 measured the double beta decay mode of several nuclei, ranging from Molybdenum to Zirkonium [94]. The last incarnation of this series, the successful NEMO-3 apparatus [95], is still in operation at Modane. Among the results published by NEMO-3 there are the searches for $\beta\beta^{0\nu}$ processes [96] in Molybdenum (using 7 kg, of ^{100}Mo) and in Selenium (using 1 kg of ^{82}Se).

The principle of operation of NEMO3 is based on the use of thin foils of the isotope to be studied. Those foils are surrounded by a tracker and a calorimeter. The key concepts are: a) source and detector are different (unlike the case of Germanium crystals, for example), b) reconstruction of the two negative electron tracks provides the topological signature, useful to discriminate double beta events from backgrounds, and c) energy measurement is provided by the calorimeter surrounding the tracker. In addition to the ability to reject non- $\beta\beta$ backgrounds, the use of foils allows the study of different nuclei. However, the price to pay is a poor energy resolution (due to fluctuations of energy losses in the foil itself), resulting in a weak energy signature. Consequently, $\beta\beta^{2\nu}$ events are a potentially serious background for foil-based detectors.

The SuperNEMO detector is a proposed Goliath-version of the NEMO concept for the next-generation of $\beta\beta^{0\nu}$ experiments. It consists of several large modules. Each module hosts a foil of about 12 m^2 surface and 40 mg/cm^2 thickness (thus about 5 kg). The foil is surrounded by a tracker and a calorimeter, very similar in design to the NEMO-3 devices. A sketch of one of the modules is shown in Figure 5.1. The main improvement with respect to NEMO3 comes from: a) thinner foil, b) improved calorimeter resolution, and c) improved geometrical acceptance.

There are a number of questions that need to be addressed to properly evaluate the physics reach and the optimal design of SuperNEMO. A good starting point is to consider the discrimination that can be attained between the $\beta\beta^{0\nu}$ and $\beta\beta^{2\nu}$ modes as a tool to fix the detector parameters. Clearly, non- $\beta\beta$ backgrounds are also important, but can be considered at a later stage. Many of the

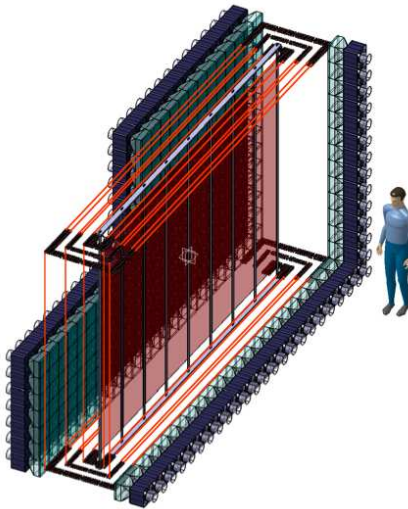


Figure 5.1: A sketch of an open SuperNEMO module. The foil, placed in the middle, is surrounded by a tracker with a lever arm of about 1 m. Tracker and foil are enclosed by a calorimeter.

SuperNEMO design parameters will be dictated by the necessity to discriminate as much as possible between the two $\beta\beta$ modes, while the radio-purity issues, in particular those concerning the foil, will affect to the performance against non- $\beta\beta$ backgrounds.

Regarding the reconstruction efficiency, it is mainly dominated by geometrical acceptance. Although our study is based on a realistic simulation of the detector and full reconstruction of the events, the simple topology and good lever arm of the modules result in a tracking efficiency (in the region of good geometrical acceptance) close to 90%. The geometrical acceptance, on the other hand, limits the overall efficiency to reconstruct a $\beta\beta^{0\nu}$ event to about 50%. Taking into account backscattering of electrons in the calorimeter wall and other *pathological* effects, this efficiency is reduced to about 30%. No significant improvement can be achieved here unless the geometry or technology is changed.

The rest of the relevant parameters studied in this work are: a) chosen isotope, b) calorimeter resolution, c) total exposure (mass of isotope times years of measurement), d) foil thickness, and e) level of backgrounds others than $\beta\beta^{2\nu}$

spectrum.

This chapter is organized as follows: Section 5.2 describes the NEMO3 experiment, since it is somehow the father of SuperNEMO. In Section 5.3 we introduce the SuperNEMO experiment in further detail, its goals and technology. Then simulation and reconstruction algorithms are described in Section 5.4, meanwhile event selection cuts are defined in 5.5. Section 5.6 reviews the ingredients needed to obtain a measurement (or a limit) of $T_{1/2}^{0\nu}$ (or $\langle m_\nu \rangle$), if one observes (does not observe) the $\beta\beta^{0\nu}$ mode, assuming the exchange of a light Majorana neutrino. Our results concerning the standard SuperNEMO design are presented in Section 5.7. Finally, 5.8 concludes and summarizes sensitivity results.

5.2 The NEMO experience

NEMO-3 [95] is the third generation of the NEMO $\beta\beta$ detectors. Its main goal is to search for the neutrino-less double beta decay in several isotopes. It is running since 2003 at the Modane Underground Laboratory (LSM), in the Frejus tunnel (France).

NEMO3 is what we call a *tracko-calor* experiment. It means that apart from measuring the total energy of a given $\beta\beta$ event, like in germanium experiments, particles are also tracked. Detector and $\beta\beta$ source are separated: a foil of the studied source is placed inside the detector, being surrounded by a tracking and a calorimeter device. NEMO3 detector has somehow a particle physics-like approach in the sense that the main goal is to reconstruct the final state topology and kinematics of the two beta particles. Tracking of beta particles provides the following features (or *observables*):

- single electron energy measurement
- time of flight of each particle
- electron angular correlations
- particle charge thanks to a magnetic field
- vertex reconstruction
- extra handles for background rejection

The NEMO-3 detector has two great advantages. First, it can perform measurements on many different nuclei, and in fact has studied seven isotopes, mainly ^{100}Mo (6.914 kg) and ^{82}Se (932 g). Apart from searching for the $\beta\beta^{0\nu}$ decay, NEMO collaboration is also measuring $T_{1/2}^{2\nu}$ of the isotopes placed in the detector. Secondly, reconstruction of the two negative electron tracks provides the topological signature, useful to discriminate double beta events from backgrounds.

5.2.1 NEMO detector

The detector has cylindrical shape and it is divided into 20 segments of thin source planes, with a total area of 20 m^2 , that can support about 10 kg of source material. The sources are within a wire drift chamber filled with a gas mixture of He, ethyl alcohol, argon and water. Three blocks of drift cells on either side of the source foils operate in Geiger mode for tracking. The tracking volume is surrounded by plastic scintillator-block calorimeters. A solenoid generates a 25 G magnetic induction field which allows the differentiation between positive and negative charged tracks. The detector is surrounded by 18 cm of low-background iron to reduce the external γ -ray flux. Fast neutrons from the laboratory environment are suppressed by an external shield of water, and by wood and polyethylene plates. The air in the experimental area is constantly flushed and has a radon-free purification system serving the detector volume. Fig. 5.2 shows a cartoon of the NEMO3 detector.

The choice of the isotopes ($\beta\beta$ emitters) to study was affected by several parameters. Two of the main ones were the $Q_{\beta\beta}$ value with respect to backgrounds and the natural isotope abundance, since the higher abundance, the easier the enrichment process. At the end it was decided to use 9 different isotopes with 3 different purposes:

- to study $\beta\beta^{0\nu}$ decay: ^{82}Se ($Q_{\beta\beta} = 2.995 \text{ MeV}$) and ^{100}Mo ($Q_{\beta\beta} = 3.034 \text{ MeV}$),
- to measure $\beta\beta^{2\nu}$ half-life: ^{130}Te , ^{116}Cd , ^{150}Nd , ^{96}Zr and ^{48}Ca ,
- to analyze backgrounds: natural Cu and Te (due to its high purity).

Fig. 5.3 shows the distribution of source foils in the NEMO-3 detector.

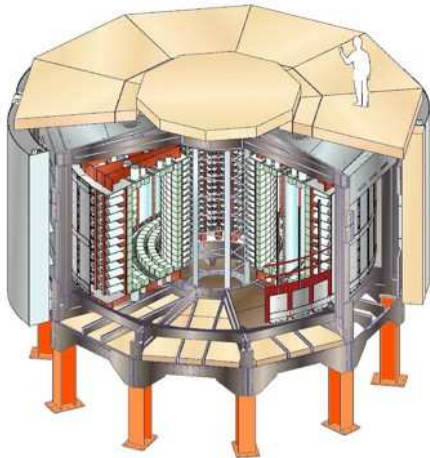


Figure 5.2: NEMO3 detector

5.2.2 NEMO (and SuperNEMO) backgrounds

The most significant concern in the NEMO (and therefore SuperNEMO) experiment is the background. The calorimeter measures the energy of the two electrons emitted from a common vertex in the source foil. The energy region of interest regarding the $\beta\beta^{0\nu}$ signal is around 3 MeV ($Q_{\beta\beta}$ of ^{82}Se is 2.995 MeV, as an example). The first kind of background to be considered is the tail of the $\beta\beta^{2\nu}$ spectrum, intrinsic to this kind of experiments, which overlaps this energetic region depending on the calorimeter resolution. Apart from this, the energy region is also shared by some energetic natural radioactivity, which can produce two electrons in the source (or close to it) thus mimicking $\beta\beta$ decays. The success of experiments searching for processes with such a high half-life, as the $T_{1/2}^{0\nu}$ of the $\beta\beta^{0\nu}$ decay, relies on the identification of these background events with a really good efficiency.

Natural radioactivity comes in general from long half-life isotopes of Potassium (^{40}K), Uranium (^{238}U and ^{235}U) and Thorium (^{232}Th). These isotopes appear in different abundances in all materials, in particular in those from which detectors are built, and therefore their decay chains are a potential source of background. In the case of NEMO and SuperNEMO, the ^{40}K and ^{235}U chains do not lead to an effective background for the $\beta\beta^{0\nu}$ search: the energy range

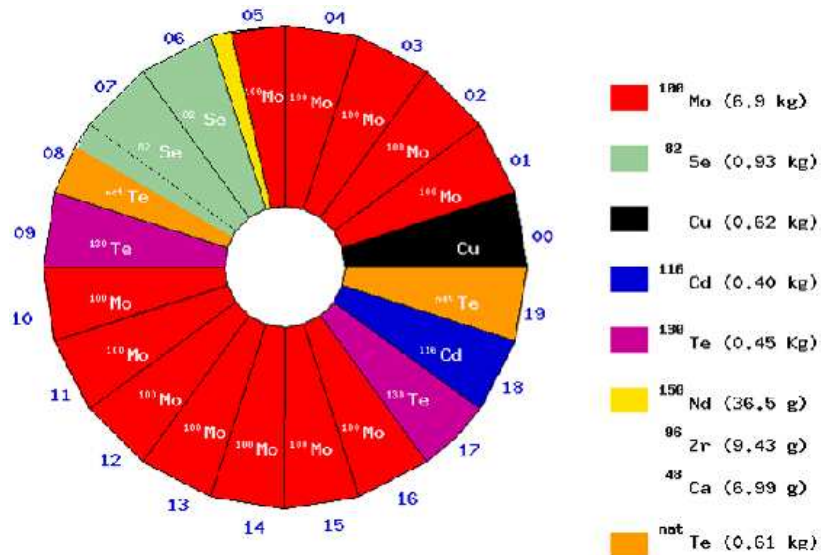


Figure 5.3: The source distribution in the 20 sectors of NEMO-3.

of the K decays are far below the $Q_{\beta\beta}$ of both ^{82}Se and ^{100}Mo , meanwhile the natural abundance of the ^{235}U isotope is negligible (0.7%). On the other hand, decay chains of ^{238}U and ^{232}Th are two of the major concerns in NEMO and SuperNEMO. Respectively, ^{214}Bi and ^{208}Tl isotopes are β -decay products of these two chains. Both have a Q_β above 3 MeV ($Q_\beta(^{214}\text{Bi})=3.270$ MeV and $Q_\beta(^{208}\text{Tl})=4.992$ MeV), thus being a source of background for a possible $\beta\beta0\nu$ signal in ^{82}Se and ^{100}Mo . Decays of these two isotopes produce, in addition to the β particle, γ rays with enough energy to interact with matter and generate new electrons. Fig. 5.4 shows a simplified view of ^{238}U and ^{232}Th decay chains, as far as NEMO-3 backgrounds are concerned, meanwhile Fig. 5.5 and 5.6 show simplified decay schemes of ^{214}Bi and ^{208}Tl , respectively. It is important to notice that ^{214}Bi decays into ^{214}Po , which in turn decays into ^{210}Pb via alpha emission with a branching ratio of 100%. This is the so-called Bi-Po process. The half-life of the ^{214}Po isotope is $164\ \mu\text{s}$, and consequently the ^{214}Bi decay can be tagged by means of the detection of the delayed alpha particle.

In this work, we distinguish between internal and external backgrounds. By internal we mean radioactive impurities inside the $\beta\beta$ source foil, while

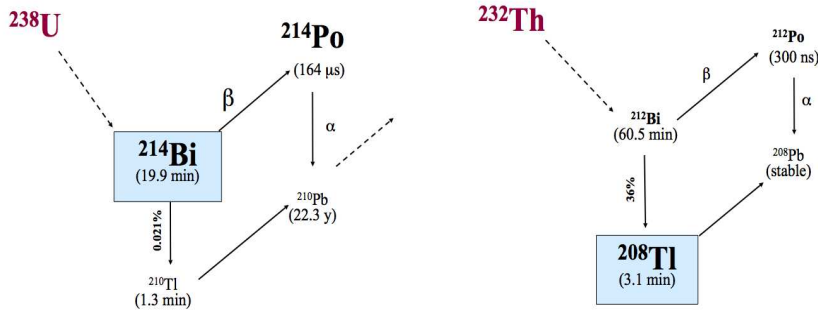
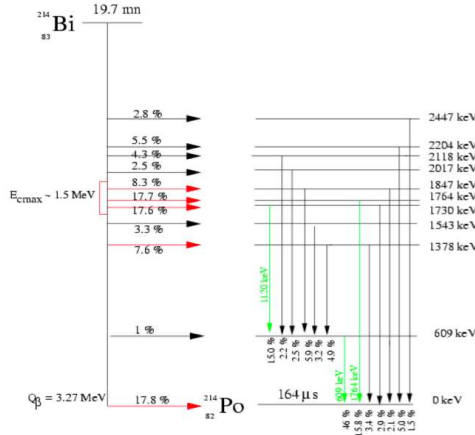


Figure 5.4: Simplified view of ^{238}U and ^{232}Th decay chains. Left: ^{214}Bi is a product of the ^{238}U series; it decays ($Q_\beta = 3.270 \text{ MeV}$) into ^{214}Po , which in turn decays into ^{210}Pb via alpha emission with a branching ratio of 100%: this is the so-called Bi-Po process. Right: ^{208}Tl is a β -emitter ($Q_\beta = 4.992 \text{ MeV}$) product of the ^{232}Th decay chain; it decays into stable ^{208}Pb .

for external we mean radioactive contaminants from outside the foils. The most important internal background is the tail of the $\beta\beta^{2\nu}$ which ultimately defines the limits of the half-life of the $\beta\beta^{0\nu}$ decay that can be searched for. In addition, we have impurities of ^{214}Bi and ^{208}Tl from the decay chains of ^{238}U and ^{232}Th , respectively. These isotopes can fake a $\beta\beta$ event by three different mechanisms. First of them is a beta decay accompanied by an electron of conversion process, second is a Moller scattering of the β -decay electron (two electrons are generated) inside the source foil, and third one is a beta decay emission to an excited state followed by a Compton scattered γ ray. Fig. 5.7 summarizes these three kind of processes leading to a faked $\beta\beta$ event. It is worth noticing here that the only general way to avoid the internal background is by means of ultra-pure foils, although the last mechanism can be tagged if one manages to detect the γ ray.

The source purity requirements in NEMO-3 to ensure that limiting background is $\beta\beta^{2\nu}$ spectrum were estimated in [96]. It was found that such requirements for ^{82}Se and ^{100}Mo foils were the following activities A :

Figure 5.5: ^{214}Bi decay scheme.

$$^{100}\text{Mo} : A(^{214}\text{Bi}) \leq 300 \mu\text{Bq/kg}, \quad A(^{208}\text{Tl}) \leq 20 \mu\text{Bq/kg} \quad (5.1)$$

$$^{82}\text{Se} : A(^{214}\text{Bi}) \leq 700 \mu\text{Bq/kg}, \quad A(^{208}\text{Tl}) \leq 50 \mu\text{Bq/kg} \quad (5.2)$$

However, foil sources did not reach these values at the end. As published in [96], the measured activities of ^{214}Bi and ^{208}Tl are:

$$\begin{aligned} ^{100}\text{Mo} : A(^{214}\text{Bi}) &= 350 \mu\text{Bq/kg} \text{ (upper limit)}, \\ A(^{208}\text{Tl}) &= 80 \pm 20 \mu\text{Bq/kg} \end{aligned} \quad (5.3)$$

$$\begin{aligned} ^{82}\text{Se} : A(^{214}\text{Bi}) &= 1200 \pm 500 \mu\text{Bq/kg}, \\ A(^{208}\text{Tl}) &= 300 \pm 50 \mu\text{Bq/kg} \end{aligned} \quad (5.4)$$

External backgrounds are impurities of ^{214}Bi and ^{208}Tl in the detector materials, along with external neutrons and high energy γ rays. One of the main sources of the background concerning detector impurities are the photomultipliers (PMT's): electrons generated inside them can cross the whole tracking

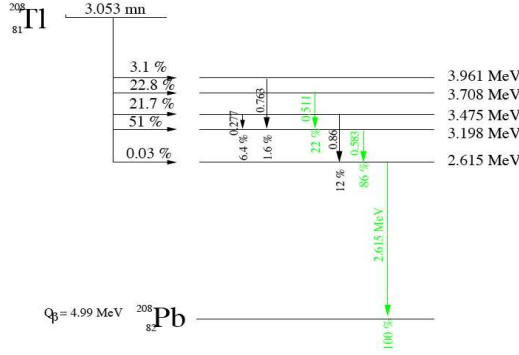


Figure 5.6: ^{208}Tl decay scheme.

chamber and be reconstructed as two different tracks, one in each side of the foil. The other major source of detector impurities is Radon gas inside the tracking chamber. ^{222}Rn and ^{220}Rn belong to the ^{238}U and ^{232}Th decay chains respectively, and they lead to the corresponding ^{214}Bi and ^{208}Tl isotopes. Indeed, the dominant background in the first period of data taking [96] was ^{222}Rn gas in the detector chamber. Radon level was estimated to be about 30 mBq/m³, and at first glance it was thought to come from the laboratory. Radon comes from the rocks and is also present in varying concentrations in all buildings as well in the free air; as it is a very diffusive gas, it can enter the detector. However, it has been discovered by the NEMO collaboration that Radon also comes from degassing of detector materials. Thus, even using an anti-Radon tent surrounding the detector, ^{222}Rn concentration inside the tracking chamber is currently:

$$A(^{222}\text{Rn}) = 5 \text{ mBq/m}^3 \quad (5.5)$$

Daughters of Radon are ionized and chemically active, and they stick to geiger wires and foil surface leading to a surface contamination of ^{214}Bi . If contamination is placed on the wires, it may be eventually identified with a good vertex

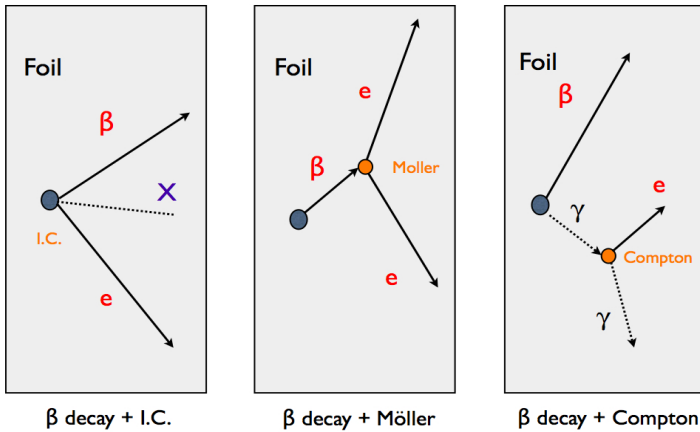


Figure 5.7: Mechanisms leading to internal background: the common outcome is two electrons leaving the source foil, thus mimicking a $\beta\beta$ decay. Left: β decay accompanied by an internal conversion (I.C.) process. Middle: Moller scattering of the β particle inside foil. Right: β decay to an excited state followed by a Compton scattering of the corresponding γ rays.

reconstruction algorithm. But contamination on foil surface faking $\beta\beta$ events is more difficult to treat. As previously said, since ^{214}Bi decays into ^{214}Po which is an alpha emitter with a short half-life ($1.64 \times 10^{-4}\text{s}$), tagging the α particle is a possible way to detect background coming from ^{214}Bi .

Regarding external photons entering the detector, γ rays can interact with the foil and lead to two electrons by e^+e^- pair creation, double Compton scattering, or Compton scattering followed by Moller scattering. In the NEMO-3 detector, two shields suppress neutrons and γ rays coming from outside the detector down to a negligible level with respect to other sources of background.

Finally, we stress again the fact that all the sources of background introduced in this section will be the same for the SuperNEMO experiment, and therefore we will study the impact of all of them in further sections, when analyzing

SuperNEMO sensitivity.

5.2.3 Limitations of the NEMO-3 experiment

Although NEMO-3 is a successful experiment regarding the measurement of $T_{1/2}^{2\nu}$ in several nuclei and the development of the tracko-calor technique, it is not a competitive $\beta\beta^{0\nu}$ experiment in the context of the next generation of $\beta\beta$ experiments, since it is background limited. On one side, energy resolution is about 14% FWHM at 1 MeV due to the poor resolution of the plastic scintillators used in the calorimeter device. This is not enough to have a good separation between the $\beta\beta^{2\nu}$ spectrum and the expected $\beta\beta^{0\nu}$ one. On the other side, ^{222}Rn gas inside the tracking chamber leads to ^{214}Bi (from Radon decay chain) contamination on the internal detector surfaces, in particular on the foil surface, becoming the limiting background to the search for the $\beta\beta^{0\nu}$ decay. Summarizing, NEMO-3 is background dominated, meaning that even running for ten years would not provide much better results than the ones obtained within 5 years.

Another limiting factor for the sensitivity to the $\beta\beta^{0\nu}$ process is the poor detection efficiency ϵ of the $\beta\beta$ events. It is only 8%, due to the points that we discuss below. We recall that sensitivity to $T_{1/2}^{0\nu}$ is proportional to detection efficiency ϵ as shown in Eq.3.24, and consequently one wants to keep this value as high as possible.

NEMO-3 detection efficiency is mainly limited by the geometrical acceptance, defined as the ratio between particles reaching the calorimeter walls and the total amount of emitted particles. Particles which do not hit the calorimeter are typically stopped inside the source or escape the detector without passing through one of the calorimeter blocks. The geometrical acceptance per charged particle is roughly 80%, and $(80\%)^2 = 64\%$ for a $\beta\beta$ event (two particles). Fig. 5.8 shows the geometrical acceptance for β particles coming from ^{100}Mo foil at sector 13th (see Fig.5.3) and for particles coming from calibration source placed near sector 13th; the acceptance is shown as a function of Monte Carlo particle energy and as a function of the cylindrical azimuthal angle $\phi = \text{atan}(y/x)$ ($\phi \in [0, 2\pi]$) at creation vertex. As can be seen, acceptance drops to zero as energy decreases for particles generated in ^{100}Mo foil because the lower energy, the higher probability for absorption inside the source. On the other hand, acceptance for particles from calibration source, whose thickness is negligible, is almost flat as a function of energy. As can be also inferred from Fig. 5.8, particles emitted with $\phi \sim 2$ rad and $\phi \sim 2\pi$ rad have less chances to

reach the calorimeter: these are particles reentering the foil for a second time and therefore with higher probability of being stopped inside the foil. To illustrate this situation, Fig. 5.9 shows visualization of two events in which a β particle re-enters the foil.

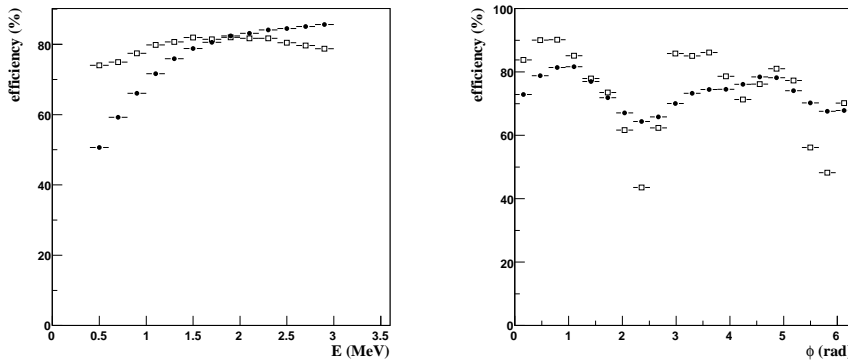


Figure 5.8: Geometrical acceptance or *intrinsic efficiency* (%) of the NEMO-3 detector to the β particles. Left: acceptance as a function of energy. Right: acceptance as a function ϕ angle as defined in the text. Black dots and empty squares show results for ^{100}Mo foil and calibration source, respectively.

Even if a given β particle reaches the calorimeter wall, it is not useful for analysis if it has crossed the foil for a second time. In such a case, the same particle is reconstructed as two different tracks, as shown in Fig. 5.9, thus faking itself a $\beta\beta$ event. This is another relevant source of detection inefficiency.

Finally, there is also a loss of detection efficiency due to the non-perfect reconstruction algorithms, as occurs in any experiment. For a given $\beta\beta$ event, reconstruction algorithms have to provide the corresponding tracks built from hits in the geiger wires, along with a set of parameters (like charge or intersection with the foil) which allows to select actual $\beta\beta$ events and reject background ones, by applying some selection cuts. Tracking efficiency in NEMO-3 is high, as corresponds to the large number of geiger cells layers (9 per side of the foil), but after applying the event selection cuts it turns out that the remaining events are only 8% of the total $\beta\beta$ events. As an example, we present in Fig. 5.10, the

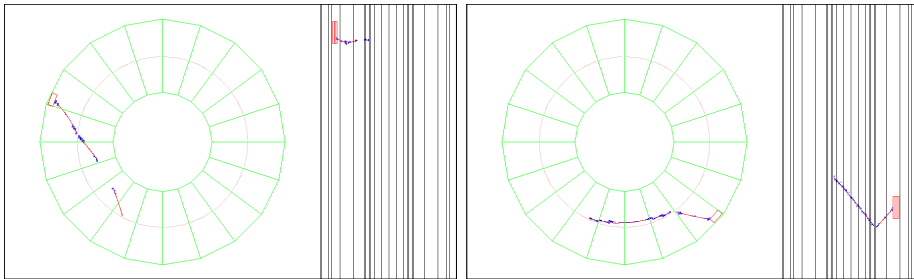


Figure 5.9: NEMO-3 events in which a β particle enters the foils for a second time. Left: visualization of the reconstructed tracks coming from a particle with $\phi = 1.75$ rad. Right: visualization of the reconstructed tracks coming from a particle with $\phi = 0.19$ rad.

charge identification efficiency of β particles: about 6% of the tracks are rejected because they are wrongly reconstructed as positive particles. In other words, since event selection requires two negative particles, $6\% + 6\% - (6\% \times 6\%) = 11.6\%$ of the $\beta\beta$ events are rejected due to a wrong charge identification.

5.2.4 Results of the search for the $\beta\beta^{0\nu}$ decay

NEMO collaboration presented its first results of the search for neutrino-less double beta decay in 2005 [96]. No $\beta\beta^{0\nu}$ signal was observed neither for ^{82}Se nor ^{100}Mo . A likelihood analysis was performed to get limits (90% C.L.) to the half-life of the process:

$$^{100}\text{Mo} : \quad T_{1/2}^{0\nu} > 4.6 \times 10^{23} \text{ years} \quad (5.6)$$

$$^{82}\text{Se} : \quad T_{1/2}^{0\nu} > 1.0 \times 10^{23} \text{ years} \quad (5.7)$$

corresponding to the following ranges of $\langle m_\nu \rangle$ (depending on the nuclear matrix elements considered):

$$^{100}\text{Mo} (7.369 \text{ kg} \cdot \text{year}) : \quad \langle m_\nu \rangle < 700 - 2800 \text{ meV} \quad (5.8)$$

$$^{82}\text{Se} (1.0 \text{ kg} \cdot \text{year}) : \quad \langle m_\nu \rangle < 1700 - 4900 \text{ meV} \quad (5.9)$$

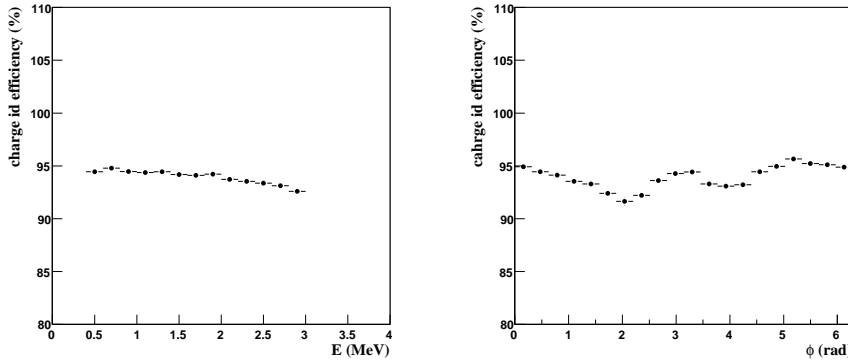


Figure 5.10: Charge identification efficiency (%) in the NEMO-3 experiment, as a function of particle energy (left) and ϕ angle (right) as defined in the text.

The analysis took into account three different measurements: the energy of each one of the electrons, the sum of both energy and the angle between the two tracks. Fig. 5.11 shows these variables for ^{100}Mo and $7.369 \text{ kg} \cdot \text{year}$ of exposure. Results were in good agreement with Monte Carlo simulations of $\beta\beta^{2\nu}$ spectrum.

As will be described in the following sections, one can estimate the sensitivity of an experiment like NEMO-3 by having an accurate knowledge of the signal and background energy distribution and the detection efficiency of the $\beta\beta$ process. Plots in Fig. 5.12 shows expected NEMO-3 sensitivity to $T_{1/2}^{0\nu}$ and $\langle m_\nu \rangle$, as a function of time, for both ^{100}Mo and ^{82}Se foils. These plots take into account the reduction in the Radon background after installation of the anti-Radon tent, and therefore sensitivity for 1 year shows slightly better results than published ones. As can be inferred, after 5 years of data taking sensitivity will be about

$$^{100}\text{Mo} : T_{1/2}^{0\nu} > 1.4 \times 10^{24} \text{ years}, \quad \langle m_\nu \rangle (QRPA) < 660 \text{ meV} \quad (5.10)$$

$$^{82}\text{Se} : T_{1/2}^{0\nu} > 2.7 \times 10^{23} \text{ years}, \quad \langle m_\nu \rangle (QRPA) < 1500 \text{ meV} \quad (5.11)$$

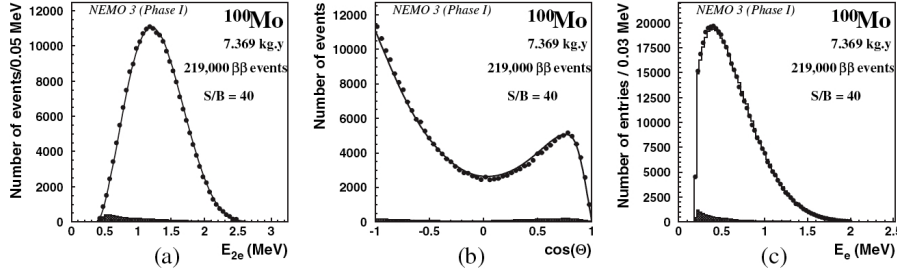


Figure 5.11: (a) Energy sum spectrum of the two electrons, (b) angular distribution of the two electrons, and (c) single energy spectrum of the electrons, after background subtraction from ^{100}Mo with 7.369 kg·y exposure. The solid line corresponds to the expected spectrum from $\beta\beta^{2\nu}$ simulations and the shaded histogram is the subtracted background computed by Monte Carlo simulations. The signal contains 219000 $\beta\beta$ events and the signal-to-background ratio is 40. From Ref.[96].

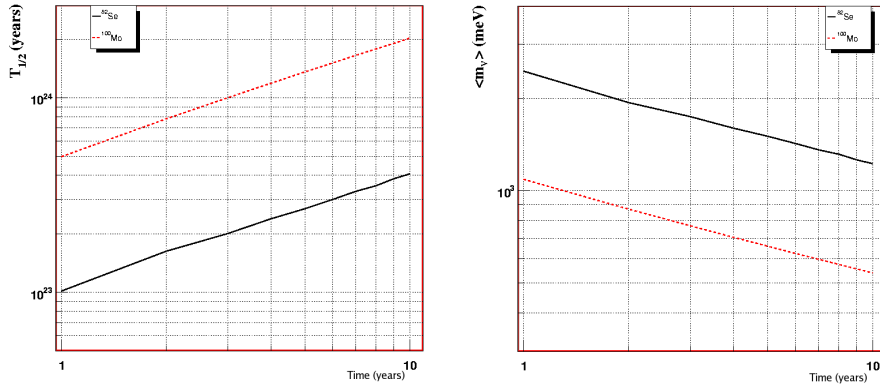


Figure 5.12: Expected NEMO-3 sensitivity at 90% C.L. as a function of time. Left: sensitivity to $T_{1/2}$. Right: sensitivity to $\langle m_\nu \rangle$ according to the Nuclear Matrix Elements quoted in [52]. Solid and dashed lines show results for ^{100}Mo and ^{82}Se , respectively.

5.3 SuperNEMO project

As in the NEMO3 experiment, the main goal of SuperNEMO is to search for the neutrino-less double beta decay ($\beta\beta^{0\nu}$). In order to do so, SuperNEMO detector has to fulfill some requirements. It has to provide energy measurement of the beta particles coming from the foil source and also a good identification of the creation vertex, to identify the $\beta\beta$ process. In addition, track reconstruction must provide enough information to reject all the possible backgrounds. The ability to distinguish electrons from positrons with the help of a magnetic field, and identification of gammas and alpha particles may be essential. On the other hand, choice of isotope to be used as a $\beta\beta$ emitter is also of major importance.

In this section we describe the goals of the SuperNEMO project and the kind of detector that is expected to be built in order to reach them.

5.3.1 SuperNEMO goals

SuperNEMO aims to extend and improve the experimental techniques used in the NEMO3 experiment. The main idea is to extrapolate the NEMO3 technology over one (or even two) orders of magnitude by studying about 100 kg of $\beta\beta$ decay isotopes, being the most reliable one ^{82}Se although ^{150}Nd is also under consideration. As described in Section 5.2, NEMO-3 best results for $T_{1/2}^{0\nu}$ limit are obtained with 7 kg of ^{100}Mo . In addition, it is expected that internal contamination of source foil (^{214}Bi and ^{208}Tl impurities) will be reduced by at least a factor of 10. Table 5.1 shows the improvements of SuperNEMO with respect to NEMO-3: first column shows SuperNEMO expected parameters, while second one shows NEMO-3 setup parameters.

The main goal of SuperNEMO is to search for the $\beta\beta^{0\nu}$ process in the 50–100 meV range. This would allow to cover the degenerate-hierarchy region of neutrino masses, as shown in Fig. 3.7. The motivation for reaching this scale has been strengthened by the claim of observation of $\beta\beta^{0\nu}$ decay in ^{76}Ge [4]; the only certain way to confirm or refute it is with another experimental result. To reach this scale and perform reliable measurements, some tens of kg of the decaying isotope with a corresponding reduction of the background should be enough.

SuperNEMO will also be able to study $\beta\beta^{0\nu}$ transitions to the 2^+ excited state of the nucleus, which involves a Majorana mass term through the $V + A$ interaction, instead of the $V - A$ one. Other mechanisms may contribute to the $\beta\beta^{0\nu}$ process, in particular the emission of a Majoron M^0 , the boson associated with the spontaneous symmetry breaking of the lepton number. The search for

the $\beta\beta M^0$ process involves a three body decay spectrum with no detection of the Majoron. SuperNEMO is expected to look for all these decay modes.

SuperNEMO sensitivity to the $\beta\beta^{0\nu}$ decay, via exchange of light Majorana neutrinos, will be studied in this work. The raw target is to increase the sensitivity to $T_{1/2}^{0\nu}$ of NEMO-3 experiment by two orders of magnitude, and therefore reach the sensitivities achieved in the Heidelberg-Moscow experiment [53]. SuperNEMO is expected to obtain higher sensitivities than past experiments (NEMO-3) thanks to an efficient background rejection and bigger exposure, and be at least competitive with present ones. Table 5.2 shows a summary of the proposed experiments for the near future, describing the isotope and the technology to be used; as can be seen, SuperNEMO is the only tracko-calorimeter approach.

5.3.2 Detector standard design

The SuperNEMO detector project has a modular design, promoting a proposal to distribute the fabrication over several collaboration sites. Each module is a *box* containing the foil source in the middle. The source is surrounded by the tracking device, composed of several geiger layers, as can be seen in Fig. 5.13. The walls of the tracking chamber are covered by plastic scintillators coupled to PMT's, which are meant to measure the energy of the tracks. The goal is to achieve an energy resolution of 7% FWHM at 1 MeV. The dimensions of each module are as follows: about 1 meter wide (so 0.5 meters per side of the foil), 4 meters high and 5 meters long. Foil thickness is between 20 and 80 mg/cm² (we assume 40 mg/cm² for the standard setup), and it is about 3 meters high and 4.5 meters long. With these dimensions, we expect to place about 5 kg of isotope per module. Thus, the idea is to build up to 20 modules to reach an exposure of 500 kg · year: 100 kg of isotope and 5 years of data taking.

All the above parameters must be optimized by means of Monte Carlo studies. It seems not feasible to reduce the width of the SuperNEMO module since accurate measurement of time of flight (performed thanks to the timing in the calorimeter device) relies on a minimum track length. However, this needs to be studied because the smaller distance between foil and calorimeter walls, the better acceptance, as will be demonstrated in Section 5.5. Dimensions of the SuperNEMO box have to be optimized depending on the foil thickness and technical issues, with the goal of maximizing the amount of isotope mass per module. Regarding the foil thickness, one needs to find a compromise: on one hand, the thinner the foil, the better energy resolution (due to energy losses in

experiment	SuperNEMO	NEMO-3
isotope	^{82}Se or ^{150}Nd	^{82}Se
isotope mass	100 kg	1 kg
$\beta\beta^{0\nu}$ detection efficiency	28%	8%
^{214}Bi contamination	10 $\mu\text{Bq}/\text{kg}$	1200 $\mu\text{Bq}/\text{kg}$
^{208}Tl contamination	2 $\mu\text{Bq}/\text{kg}$	300 $\mu\text{Bq}/\text{kg}$
energy resolution	7 % FWHM at 1 MeV	14% FWHM at 1 MeV
^{222}Rn level	0.5 mBq/m ³	5 mBq/m ³

Table 5.1: Differences between experimental parameters in SuperNEMO and NEMO-3 experiments. First column shows parameters for the target scenario of the SuperNEMO project. Second column shows experimental parameters of NEMO-3 experiment.

Experiment	Isotope	i.a. (%)	Mass (kg)	Technique
GERDA	^{76}Ge	86	40	Ge diodes liq. scint.
MAJORANA	^{76}Ge	86	120	Ge diodes
COBRA	^{116}Cd	nat.	418	CZT semiconductor
CUORE	^{128}Te	nat.	741	TeO_2 bolometers
CANDLES	^{48}Ca	nat.	tons	CaF_2 scint.
CAMEO	^{116}Cd	83	tons	CdWO_4 scint.
SNO+	^{150}Nd	nat.	500	Nd salt liquid scint.
SuperNEMO	^{82}Se (^{150}Nd)	90 (?)	100	Foils in tracko-calorimeter
EXO-200	^{136}Xe	80	200	LXe TPC

Table 5.2: A selection of the proposed experiments for the new generation grouped by the detection technique. SuperNEMO is the only tracko-calorimeter approach.

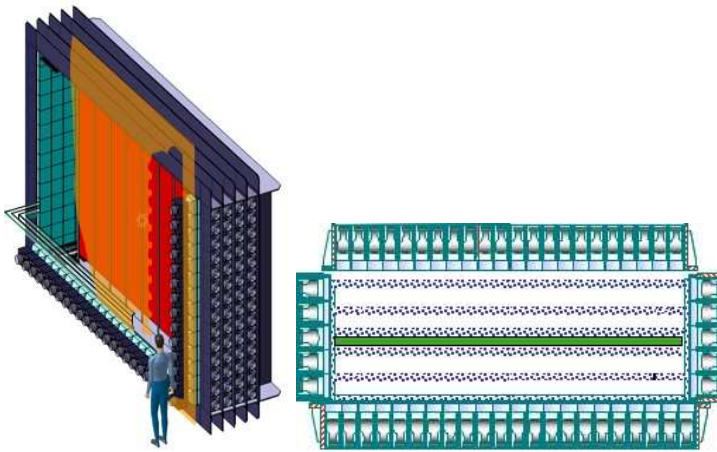


Figure 5.13: SuperNEMO module standard design. Left: general view of SuperNEMO module: box shape, of about one meter wide to allow time of flight measurement, 4 meters height and 5 meters length. Right: transverse section of a SuperNEMO module: foil is placed in the middle of the module and surrounded by geiger layers; tracking chamber walls are covered with scintillators coupled to PMT's.

side the foil); on the other, the thicker the foils the more mass per module, and therefore a higher exposure (mass per time) for a given number of SuperNEMO modules. Finally, different layouts of the geiger layers around the foil have to be analyzed, although it is clear that layers really close to both foil and scintillator walls are needed in order to get good vertex reconstruction and matching between tracks and calorimeter hits. In this work, we assume a NEMO-like layout for the tracker: three blocks of geiger layers (three layers each one), two of them almost attached to the foil and calorimeter walls, and the other in the middle of the chamber.

As in NEMO-3, the whole detector will be covered with a shield to protect it against neutron and gamma rays. The shield will be made of ultra-low radioactivity materials. All the components of electronics will need to be outside the shielding to minimize radioactivity near the source foil. Additionally, a very careful selection of all the detector materials will be required to achieve the

desired level of external contamination. The shielding will need to be effective at stopping gammas and neutrons from natural radioactivity in the laboratory. Thus a borated water shield is proposed. The possibility of an active shield for detection of secondaries from high energy muons is also of interest.

The highly modular structure of the detector will permit installation and operation of the first module while the others are being commissioned. So it is not necessary to wait for the completion of the construction of all SuperNEMO modules to start collecting data. On the contrary, it is advantageous to start data collection immediately after installing the first one: it provides an early handle on gaining experience on improving the construction of subsequent modules.

5.3.3 Choice of isotopes

The choice of the isotope to be used in SuperNEMO is a compromise between several factors. These include the transition energy $Q_{\beta\beta}$, the half-life $T_{1/2}^{2\nu}$, the phase space factor ($G^{0\nu}(E_0, Z)$) and nuclear matrix elements ($M_{0\nu}$) of the transitions for $\beta\beta^{0\nu}$ decay, the background in the energy regions surrounding the $Q_{\beta\beta}$ value, the possibility of reducing the radioactivity of the isotope to acceptable levels, and finally the natural isotopic abundance and the possibility of enrichment. Although it seems that the NME's would be a good criteria to select the isotope, uncertainties in their calculations do not allow the choice to depend only on this factor. The following list summarizes the desirable characteristics of the isotope:

- $Q_{\beta\beta}$ as high as possible in order to reject backgrounds of lower energies,
- $T_{1/2}^{2\nu}$ as high as possible to reduce the intrinsic background from the $\beta\beta^{2\nu}$ decay,
- isotope with a high natural isotopic abundance and suitable to be enriched, to increase exposure,
- small contaminations of U and Th to avoid internal backgrounds (^{214}Bi and ^{208}Tl),
- high $Q_{\beta\beta}$ and Z to provide large phase space factor $G^{0\nu}(E_0, Z)$,
- high nuclear matrix element to reach better sensitivity to $\langle m_\nu \rangle$.

Table 5.3 shows a list of the most commonly used isotopes in $\beta\beta$ decay experiments and their $Q_{\beta\beta}$, natural isotopic abundance, measured $\beta\beta^{2\nu}$ half-life [9] and QRPA evaluations of $T_{1/2}^{0\nu}$ for $\langle m_\nu \rangle = 50$ meV and $g_A = 1.25$ from Ref. [52]. It turns out that the only reliable choice is ^{82}Se , although ^{150}Nd could also be considered under certain assumptions. ^{48}Ca has a high $Q_{\beta\beta}$, but its natural isotopic abundance is poor and it cannot be enriched. Another isotope with high $Q_{\beta\beta}$ is ^{100}Mo , but its $\beta\beta^{2\nu}$ mode is too fast and would hide the $\beta\beta^{0\nu}$ signal. On the other hand, ^{76}Ge and ^{116}Cd have a $Q_{\beta\beta}$ too low and background levels coming from ^{214}Bi would be unacceptable.

Isotope	$Q_{\beta\beta}$ (keV)	i.a. (%)	$T_{1/2}^{2\nu}$ (y)	$T_{1/2}^{0\nu}$ ($\langle m_\nu \rangle = 50$ meV) (y)
^{48}Ca	4271 ± 4	0.187	$(4.2 \pm 1.2) \times 10^{19}$	—
^{76}Ge	2039.6 ± 0.9	7.8	$(1.3 \pm 0.1) \times 10^{21}$	$0.86_{-0.07}^{+0.08} \times 10^{27}$
^{82}Se	2995 ± 6	9.2	$(9.2 \pm 1.0) \times 10^{19}$	$2.44_{-0.26}^{+0.32} \times 10^{26}$
^{100}Mo	3034 ± 6	9.6	$(8.0 \pm 0.6) \times 10^{18}$	$2.37_{-0.32}^{+0.41} \times 10^{26}$
^{116}Cd	2802 ± 4	7.5	$(3.2 \pm 0.3) \times 10^{19}$	$2.86_{-0.39}^{+0.50} \times 10^{26}$
^{150}Nd	3367.1 ± 2.2	5.6	$(7.0_{-0.3}^{+11.8}) \times 10^{18}$	$2.23_{-0.21}^{+0.41} \times 10^{25}$

Table 5.3: A list of the most commonly used isotopes in $\beta\beta$ decay experiments and their $Q_{\beta\beta}$, natural isotopic abundance, measured $\beta\beta^{2\nu}$ half-life [9] and QRPA evaluations of $T_{1/2}^{0\nu}$ for $\langle m_\nu \rangle = 50$ meV and $g_A = 1.25$ from Ref. [52].

^{82}Se has high enough $Q_{\beta\beta}$ and acceptable $T_{1/2}^{2\nu}$. In addition, NME seems to be well understood since both QRPA and shell models are quite close in their calculations (from [52] and [101]). Moreover, ^{82}Se can be enriched and indeed it has been already used in NEMO-3 experiment, so it can be produced in a relatively easy way.

The other possibility is ^{150}Nd . It has a $Q_{\beta\beta}$ higher than the one for ^{82}Se (^{214}Bi decay would not be a background) and its NME seem to lead to a better sensitivity to $\langle m_\nu \rangle$, according to QRPA calculation (SHELL model has no prediction for this NME). However, there are some points regarding this isotope that remain unclear:

- NME calculation from QRPA model could not be reliable due to nucleus deformation,
- it is not known if it can be enriched in large quantities,

- it is not known which purity can be achieved concerning Th (^{208}Tl background).

In the present work, ^{82}Se foils are assumed to be the default choice, although results for ^{150}Nd are also given.

5.3.4 R&D and expected time scale

Although it is true that SuperNEMO will take advantage of NEMO experience, since the detector relies heavily on the very well known technology of NEMO-3, it is not less true that the new *scale* introduces new problems that we need to address. The following summarizes the most important tasks to develop in the R&D program of SuperNEMO:

- *calorimeter resolution*: target is to achieve 7% at FWHM. That means a factor 2 of improvement with respect to NEMO-3 detector. Previous experience shows that this task may be achievable either with plastic scintillators (as in NEMO 3), liquid scintillators or a hybrid detector combining plastic and non-organic scintillators. Studies of improvements in light yield and light collection are planned. The efficiency and uniformity of photocathodes in PMTs is also a concern to be addressed with the manufacturing firms.
- *production of source foils*: techniques to reach the required purity of the SuperNEMO foils are needed. The goal is to improve the radio purity of NEMO-3 by a factor 10-20. In addition, SuperNEMO also expects to use thinner foils: 40 mg/cm² are assumed to be the default ones, but using 20 mg/cm² foils will lead to a better energy resolution due to the lower energy losses inside them.
- *Radio purity measurements*: new tools are needed to ensure the radio purity of both foils and detector materials. A new detector called BiPo is being developed inside the SuperNEMO collaboration with the goal of providing purity measurements at few $\mu\text{Bq}/\text{kg}$ beyond the sensitivity of conventional Ge detectors. This detector has been already approved to operate at Canfranc underground laboratory (LSC).
- ^{222}Rn *background*: reduction of at least a factor 10 of radon levels with respect to NEMO-3 needs to be achieved. From NEMO-3 experience we know the radon comes from both air and degassing of detector materials.

That means that an anti-Radon tent surrounding SuperNEMO modules is not enough, so a new way of reducing radon levels needs to be found. In addition, tracking and reconstruction techniques have to be developed to tag ^{214}Bi background events (recall ^{214}Bi comes from ^{222}Rn). One clear way to do so is to detect the α particle from ^{214}Po decay (daughter of ^{214}Bi).

- *detection efficiency*: as it will be shown in Section 5.7, sensitivity of SuperNEMO detector depends strongly on the detection efficiency (the higher efficiency, the higher statistics). Consequently, one needs to search for the optimal setup of the detector, concerning the acceptance to the $\beta\beta$ events. In this work we will prove that the acceptance of the standard SuperNEMO module is only 50%, so it seems that alternative geometries must be analyzed.

Although the time scale is still unclear as it depends on several technical and political issues, one can image the following schedule. R&D stage of SuperNEMO will last until 2009-2010. In parallel, the work on the BiPo detector will carry on. Final design of BiPo is expected to be operating by 2010 at LSC, and by that time the construction of the SuperNEMO first module will start. Different modules will start taking data as they are built, since each one of them works independently.

5.4 Simulation and data reconstruction

A full simulation and a set of event reconstruction algorithms have been developed in order to obtain the response of the SuperNEMO detector to the $\beta\beta$ decays and optimize the information that can be inferred. Kinematics of the $\beta\beta$ process are simulated as a first step, and then event vertices in the foil are generated randomly. A GEANT4 application propagates particles inside the tracker and calorimeter. Later, the response of the SuperNEMO sub-detectors is mimicked by digitization algorithms. Finally, reconstruction algorithms build tracks from the geiger hits and associate them with calorimeter measurements and with an event vertex in the foil surface.

5.4.1 SuperNEMO simulation

Simulation is divided in various steps, from event simulation to detector response. Kinematics of $\beta\beta$ and other background events are simulated using a Monte Carlo (MC) generator that is being used in NEMO-3. Then, vertices for these events are created and particles are propagated all along the tracking chamber according to the following geometry of the SuperNEMO module. In the last step, digitization simulates the detectors response (tracker and calorimeter) according to the MC information of particles crossing the SuperNEMO module.

Geometry details

As explained in Section 5.3, SuperNEMO consists of several identical modules. Each module includes a $\beta\beta$ source in the form of a thin foil, a tracking volume and calorimeter walls surrounding the whole device.

The tracking chamber dimensions are 4 m high, 5 m long and 1 m wide. The foil is placed in the middle of the tracking volume, thus there is a 50 cm base between the foil and the calorimeter. The source foil dimensions are 3 m high and 4.5 m long. It is smaller than the module dimensions to increase the geometrical acceptance. Foil is made of pure ^{82}Se , with the density 5 g/cm³. Standard foil thickness is 40 mg/cm².

Tracking is performed by the array of Geiger cells. The cell diameter is equal to 3 cm. Design with 12 cathode wires per cell is chosen. Both anode and cathode wires are assumed to be made from steel. Wires diameter is 50 μm . Configuration chosen for the simulation is 3+3+3, which means three groups of Geiger cells with three layers of cells in each group. The distance between the foil and the first group is 0.5 cm. The distances between the 1st and 2nd, 2nd

and 3rd groups are 10 cm. The distance between the final group of cells and the calorimeter is 2.5 cm.

SuperNEMO tracking gas in this simulation is identical to the one in NEMO3 [96].

Calorimeter consists of four walls of plastic scintillator (polystyrene) surrounding the foil. The top and the bottom of the detector are not covered by the scintillator, since electronics will require this space. The walls are divided into smaller boxes of plastic, with the following dimensions: 25 cm height, 25 cm length and 5 cm thickness. Each block is wrapped in a 12 μm thick reflector film (mylar).

There is a vertical magnetic field of 25 Gauss.

Fast simulation

SNOVA [97] is the GEANT4 application that simulates a SuperNEMO module. Particles emerging from the source are propagated through the tracker and calorimeter where energy loss, production of secondaries, multiple scattering and decay are simulated. SNOVA was conceived as a fast and flexible simulation for detector design studies and therefore several geometric properties, as detector sizes or tracker configuration, can be set by means of parameters files. Fig. 5.14 shows a visualization of the SuperNEMO module geometry defined in the application. In the following an overview of SNOVA is given. Further details are described at [97].

SNOVA takes as an input $\beta\beta$ events, generated by the same algorithms used in NEMO-3, with all the required information, namely, number and type of particles, initial momenta, vertices and times of generation. All relevant physics processes, such as multiple scattering, ionization, Compton scattering, bremsstrahlung, etc., are considered. However, meaningless secondary particles (very short tracks) are not propagated but added as local energy depositions in order to speed up the simulation.

SNOVA produces output events with only true MC information. There are two types of true MC hits: geiger hits and calorimeter hits. Geiger hits are generated when a charge particle crosses a Geiger cell of the tracking volume. Information about the point of maximal approach to the anode wire as well as the particle's momentum in this point are saved as hit properties. Calorimeter hits are produced when any particle deposits its energy in a calorimeter block. The true MC hit contains the exact amount of energy deposited by the particle and the time of the hit. Fig. 5.15 shows simulated geiger and calorimeter hits, in a sort of event display.

Hit digitization

A calorimeter *DIGI* hit contains true total energy deposit per counter, so if few different particles hit the same calorimeter counter, their energy deposits are summed. This true energy is used later in the analysis for further smearing according to the calorimeter resolution function.

Calorimeter resolution is limited mainly by the fluctuations in the number of photoelectrons produced by scintillator light in the photocathode. Correspondingly, the simplest resolution function is just a Gaussian, with the energy dependent width:

$$\text{FWHM}_E = \frac{\text{FWHM}_{1\text{MeV}}}{\sqrt{E \text{ MeV}}} \quad (5.12)$$

Later on, to define the calorimeter resolution we will quote the width (FWHM) at 1 MeV only.

Along with the energy, a DIGI hit contains measured time of the hit, assuming similar timing characteristics (scintillator decay time, photomultiplier rise time, etc.) as in the NEMO-3 calorimeter. Obviously, it is only a rough approximation and more accurate description of SuperNEMO counter's timing properties will be needed later, when its design becomes fixed. This is especially important for external background simulations.

A DIGI Geiger hit contains time of anodic and cathodic signals as it should be seen in the SuperNEMO detector.

Further details about digitization have been given at [98].

5.4.2 Event reconstruction

Event reconstruction is divided in two different steps. First, geiger hits coming from a same MC particle are associated via pattern recognition algorithm. Then, particles are reconstructed starting from the sequences of associated hits.

Pattern recognition

The task is to connect geiger hits to form sequences of cells, to be later fitted in order to obtain final reconstructed tracks. One has to remember that, at this stage, a geiger hit is given by the position of the wire that was lit and the distance of maximum approach of the particle to the wire, thus identifying a circle centered at the wire: the track is passing tangentially to this circle,

but one doesn't know at which point on the circle it actually passed, so such information must be gathered by joining several hits into a sequence.

A hit that is not in the middle of two near hits is selected as a starting point for a new sequence; the sequence is then left evolving one hit at a time. Connection of hits is always made between nearby cells. If more than one connection is possible, all the possibilities are taken into account. When there are at least 3 cells associated, we try to find the actual coordinates of each hit. Sometimes this procedure is not successful since two different solutions for these coordinates are compatible with the three hit circles: in such cases, we choose one of them in a later stage, when trying to build bigger tracks by fitting the sequences of cells, as explained in next section.

A more detailed description about this algorithm has been given elsewhere [99].

Track reconstruction

Once tracker hits coming from the same particle have been associated, as explained above, next step aims at getting tracks by fitting the hits using the Kalman filter [73]. The goal of the track fit is to obtain information that offers an extra handle to reject backgrounds and to define the topology of a given event. In SuperNEMO, the following information is expected to be obtained from the fit:

- vertex reconstruction,
- charge of the track,
- track length,
- direction of track at vertex,
- association between tracks and calorimeter hits.

The output of the pattern recognition algorithm is a set of geiger hit chains or sequences placed in the six tracker blocks. Each one of these sequences can be treated as a track segment. A set of fitting algorithms from a Kalman-Filter based library [72] is then applied in order to join segments from different blocks and therefore build bigger tracks. These algorithms work as follows. First of all, a segment in one of the two first geiger blocks, the ones closest to the foil, is fitted with a Kalman filter. This segment is then propagated to the next blocks and the χ^2_m of matching with other segments there is computed. The

segment with the lower χ_m^2 is attached to the first segment and both are refitted as a whole track. This procedure is repeated until there are no unassociated segments, or until there are no more possible matchings between segments.

The outcome of the fitting algorithms is a set of tracks fitted according to a model: helix model if magnetic field is on and straight line model if it is off. Each one of the fitted tracks will be treated as a reconstructed particle. Fig. 5.16 shows the fit efficiency, defined as the ratio between the number of fitted tracks and the total amount of MC particles that fulfill the minimum requirements to be fitted. These requirements are to have more than 3 geiger hits, not to be backscattered in the plastic of the calorimeter wall, and not to enter the foil for a second time. Left plot in Fig. 5.16 shows fit efficiency as a function of the momentum p of the MC particle, meanwhile right plot shows efficiency as a function of the polar angle θ with respect to the foil normal direction. As can be seen, efficiency is quite flat and around 90%.

The inefficiency of 10% comes mainly from those events in which two tracks are so close in the first geiger block that we do not manage to get two different segments. To ensure the quality of the vertex reconstruction, tracks are not allowed to share a segment in the first block, so when this occurs one of the tracks is lost, leading to reconstruction inefficiency. There are two ways of fixing this situation: one is to improve the tracking resolution in the first geiger block (by using smaller geiger cells, for instance), and the other is to allow segment sharing between two tracks. The last solution needs to be studied since the amount of background events mimicking $\beta\beta$ events may increase.

When fitting to an helix model, one of the fitted parameters is the charge of the particle. Efficiency of the charge identification in this case is about 99%, as shown in Fig. 5.17.

Once the track has been fitted, the creation vertex on the foil is computed by trying to intersect the track with the foil surface, placed along $z = 0$. If intersection exists, its x and y coordinates are defined as the coordinates of the vertex (x_v, y_v) . As a first approximation, z coordinate of vertex is assumed to be 0. Top plots in Fig. 5.18 show efficiency of the vertex reconstruction, defined as the ratio of the fitted tracks with reconstructed vertex on the foil and the total amount of MC particles that indeed come from the foil. Efficiency is high (98%), as expected since first block of geiger layers is only 0.5 mm away from the foil. The resolution of the vertex reconstruction is computed by obtaining the residual between the intersection point and the actual position of the MC particle on the foil surface. This residual is presented in the bottom plots of Fig. 5.18. As expected, residuals in x and y coordinates are centered at 0 and the RMS of these distributions show resolutions of:

$$\text{RMS}_{v_x} = 1.5 \text{ mm} \quad \text{RMS}_{v_y} = 13 \text{ mm}$$

Apart from the vertex, propagation of the fitted track to the foil surface also provides the direction of the particle at that point, information which is needed for subsequent angular correlation studies.

Finally, the association between tracks and calorimeter hits is done evaluating a χ_m^2 of matching. Each track is propagated until it crosses any of the calorimeter walls, and then χ_m^2 is computed for any calorimeter hit placed in the same wall, as follows:

$$\chi_m^2 = \frac{(x_{tr} - x_{CAL})^2}{\sigma_{x_{tr}}^2 + \sigma_{x_{CAL}}^2} + \frac{(y_{tr} - y_{CAL})^2}{\sigma_{y_{tr}}^2 + \sigma_{y_{CAL}}^2} \quad (5.13)$$

where (x_{tr}, y_{tr}) is the intersection point between the track and the calorimeter wall, σ_x and σ_y are the errors of x_{tr} and y_{tr} , respectively, (x_{CAL}, y_{CAL}) is the position of the center of the calorimeter block, and $\sigma_{x_{CAL}}$ and $\sigma_{y_{CAL}}$ are the resolutions of x_{CAL} and y_{CAL} , respectively. According to a uniform distribution, $\sigma_{x_{CAL}}$ and $\sigma_{y_{CAL}}$ are defined as:

$$\sigma_{x_{CAL}} = \sqrt{\frac{1}{12}X}, \quad \sigma_{y_{CAL}} = \sqrt{\frac{1}{12}Y} \quad (5.14)$$

where X and Y are the calorimeter block dimensions of 25 cm in the x and y directions. For each track, the hit with lowest χ_m^2 is the one that remains associated. Fig. 5.19 shows efficiency of this matching procedure, defined as the ratio between the reconstructed tracks with associated hit and the total amount of MC particles hitting the calorimeter wall. As can be seen, this efficiency is about 98%.

Particle flight length is computed according to the model when both foil vertex and calorimeter hit association have been obtained. First, path distances between the geiger hits are added to obtain the length of the track itself. Then, distances between the extremes of the track and the vertex and the associated calorimeter hit are taken into account in order to get the final particle flight distance, from the foil to the calorimeter wall. Fig. 5.20, shows the flight length residual defined as the difference between reconstructed length and simulated one. As can be seen in the plot, reconstructed length is slightly bigger than the simulated: center of the residual distribution is about 5 mm instead of zero. The resolution of the flight length measurement is given by the RMS of the distribution: 33 mm.

Reconstructed information of a typical event can be seen in Fig. 5.21, where hits and track fit are plotted as a sort of event display.

5.5 Event selection

Once an event has been reconstructed, it has to fulfill some conditions in order to be considered for the analysis. The goals of event selection cuts are to select only those events which contains two tracked particles with measured energy, and to reject background events which may fake a $\beta\beta$ decay.

5.5.1 Event selection cuts

Since the search for the $\beta\beta^{0\nu}$ process relies on the energy spectrum, first requirement for a reconstructed event is to have two hits in the calorimeter providing the total energy. This ensures there are two particles or photons in the event.

Next step is to ensure that particles are charged. Charged particles are expected to be tracked thanks to the hits observed in geiger layers, so only events with two reconstructed tracks are selected. In case there is a magnetic field in the tracking chamber, charge sign can be measured from the fit procedure, and then tracks must have $q = -1$. In addition, events in which particles are backscattered in the plastic of the calorimeter walls, or in which secondary particles appear, need to be rejected. To do so, events with more than a maximum number of geiger hits not associated to any track, N_{ggfree}^{max} , do not pass the selection.

Both tracks in the event must have an associated calorimeter hit in order to set the energy of each particle, and this association must fulfill that the χ_m^2 of matching, is less than a maximum allowed value $\chi_{m_{max}}^2$.

Tracks are also required to have a reconstructed vertex on the foil surface, and both vertices have to be compatible, as expected in a $\beta\beta$ event. To establish that two tracks come from the same vertex, a cut on the χ^2 of the residual between them (χ_{vres}^2) forces it to be smaller than a maximum value $\chi_{vres_{max}}^2$:

$$\chi_{vres}^2 = \frac{(v_1 - v_1)^2}{\sigma_{v_1}^2 + \sigma_{v_1}^2} < \chi_{vres_{max}}^2 \quad (5.15)$$

where v_1 and v_2 are the vertices of the two tracks and σ_1 and σ_2 their errors. Since vertex resolution in x and y coordinates are different, as shown in Section 5.4.2, this cut is applied separately for each vertex coordinate.

In order to ensure the quality of the tracks, last requirements are to have a length L between a minimum and a maximum value, $(L_{min}; L_{max})$, and to fulfill that the χ^2_{fit} of the track fit is less than a maximum allowed value $\chi^2_{fit,max}$.

A typical source of background already seen in NEMO-3 experiment is the *crossing electrons*. An energetic photon from any external source (radioactive impurities of ^{214}Bi and ^{208}Tl in the detector, neutron capture, cosmic muons, etc.) can produce an electron in the plastic calorimeter via Compton scattering. This particle may give a signal in the same block of the calorimeter where it is generated and then cross the whole tracking chamber (and therefore the foil) until it reaches again the calorimeter. That process would be reconstructed as two charged tracks coming from the foil. Since the energy of the photon can be in the same energy region as the $\beta\beta$ process of ^{82}Se , it may fake a $\beta\beta^{0\nu}$ decay. There are two ways of rejecting these kind of events. The first one is the charge measurement. A crossing electron (e^-) is measured as a positive particle when flying towards the foil, since its sense of movement is opposite to the one of a particle coming from the foil. Hence, a crossing electron event is reconstructed as a e^-e^+ pair coming from the same vertex at the foil, and it can be rejected thanks to the charge measurement. The second way of identifying this kind of background events is using the time of flight (TOF) of both tracks, where the charge does not play any role. TOF for a particle coming from foil can be computed as follows:

$$TOF = \frac{L_{trk}}{c\sqrt{1 - 1/(E_e/m_e)^2}} = \frac{L_{trk}}{v_{trk}} \quad (5.16)$$

where E_e is the total energy of the electron, m_e is the electron mass, L_{trk} is the track length and v_{trk} is the velocity. If T_1 and T_2 are the times of the two calorimeter hits in an event, and TOF_1 and TOF_2 the times of flight for the two associated tracks, the observable $\Delta t = (T_1 - T_2) - (TOF_1 - TOF_2)$ must be compatible with zero for a $\beta\beta$ event coming from the foil. The probability for what is called *internal hypothesis* can be obtained using the χ^2 probability (P_{χ^2}) for one degree of freedom and the following χ^2 :

$$\chi^2_{int} = \frac{(\Delta t)^2}{\sigma_{\Delta t}^2} = \frac{[(T_1 - T_2) - (TOF_1 - TOF_2)]^2}{\sigma_{T_1}^2 + \sigma_{T_2}^2 + \sigma_{TOF_1}^2 + \sigma_{TOF_2}^2} \quad (5.17)$$

where σ_{T_1} and σ_{T_2} are the errors on the hit time measurements, and σ_{TOF_1} and σ_{TOF_2} are the errors on the time of flight calculation. For a given reconstructed event with two tracks associated to calorimeter hits, a minimum value for the internal hypothesis probability ($P_{\chi^2}^{int,min}$) is required, so $P_{\chi^2}(\chi^2_{int}, 1) > P_{\chi^2}^{int,min}$.

On the other hand, an *external hypothesis* probability is defined to take into account the probability of having a crossing electron event. In this case, the observable $\Delta t = (T_1 - T_2) - (TOF)$, where TOF is the total time of flight from one calorimeter hit to the other, must be compatible with zero, so the following χ^2 is built:

$$\chi^2_{ext} = \frac{(\Delta t)^2}{\sigma_{\Delta t}^2} = \frac{[(T_1 - T_2) - (TOF)]^2}{\sigma_{T_1}^2 + \sigma_{T_2}^2 + \sigma_{TOF}^2} \quad (5.18)$$

where σ_{TOF} is the error on the total time of flight. A maximum value for the external hypothesis probability ($P_{\chi^2}^{ext_{max}}$) is set, so any event must fulfill that $P_{\chi^2}(\chi^2_{ext}, 1) < P_{\chi^2}^{ext_{max}}$.

Taking all the above into account, a *good* reconstructed particle can be defined as follows:

- track is fitted with $\chi^2_{fit} < \chi^2_{fit_{max}}$,
- charge is $q=-1$,
- track length $L \in [L_{max}, L_{min}]$,
- track and calorimeter hit matched with $\chi^2_m < \chi^2_{m_{max}}$,
- track has a reconstructed vertex on the foil,

meanwhile a *good* reconstructed event has the following properties:

- two calorimeter hits,
- two good particles with common vertex, i.e, $\chi^2_{vres} < \chi^2_{vres_{max}}$,
- Number of not associated geiger hits is less than N_{ggfree}^{max} ,
- internal hypothesis probability larger than $P_{\chi^2}^{int_{min}}$,
- external hypothesis probability lower than $P_{\chi^2}^{ext_{max}}$.

Cuts applied for the event selection are summarized in Table 5.4. Specific values for the cuts used in the present work are also presented in the table. These cut values were set analyzing systematically the performance of the reconstruction. Note $P_{\chi^2}^{ext_{max}}$ is set to 1: crossing electrons have not been simulated yet, and therefore a realistic cut could not be evaluated in the current analysis.

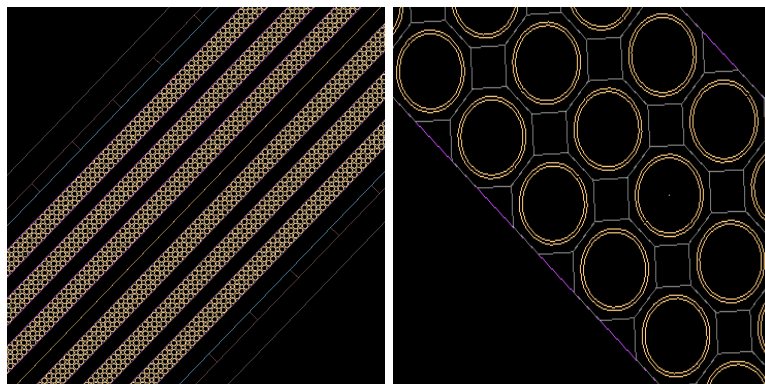


Figure 5.14: SuperNEMO module view as described in the GEANT4 application SNOVA. Left: view of the 6 blocks of geiger layers, three per side of the source foil. Right: detail of the three geiger cells layers in one of the blocks.

Number of calorimeter hits	2
Number of reconstructed tracks	2
Maximum value of χ^2_{fit}	30
Charge of the tracks	-1
Maximum value of χ^2_{vres}	10
Maximum value of the track length	3000 mm
Minimum value of the track length	300 mm
Maximum number of not associated geiger hits	3
Maximum value of χ^2_m	20
Minimum value for the internal hypothesis $P_{\chi^2}^{int\ min}$	0.01
Maximum value for the external hypothesis $P_{\chi^2}^{ext\ max}$	1

Table 5.4: Cuts applied for the $\beta\beta$ event selection.

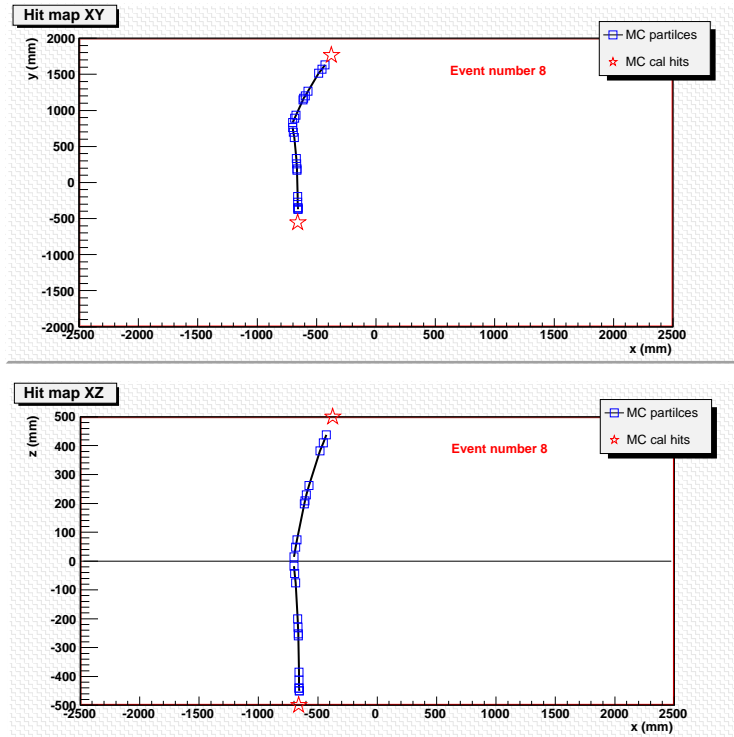


Figure 5.15: Simulated $\beta\beta^{0\nu}$ event. Squares, stars and lines show tracker hits, calorimeter hits and particle path, respectively. Top: XY hit map projection. Bottom: XZ hit map projection. Black line in $z = 0$ shows foil position.

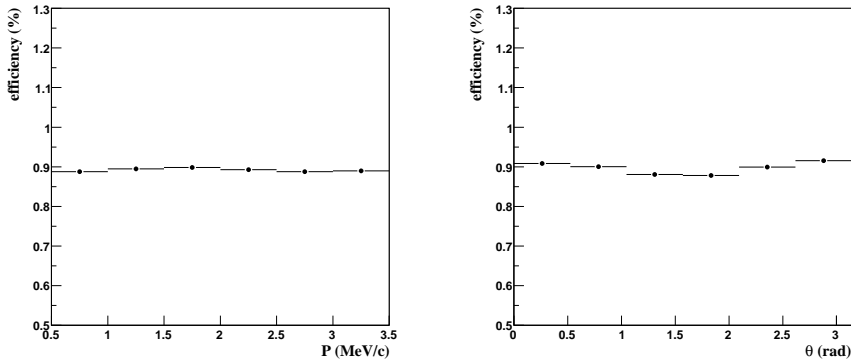


Figure 5.16: Reconstruction efficiency. Left: efficiency of track reconstruction as a function of momentum (MeV/c). Right: efficiency of track reconstruction as a function of polar angle (rad).

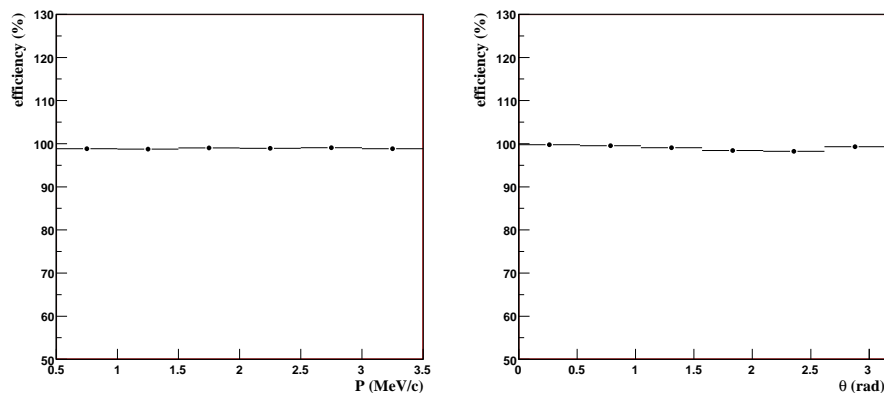


Figure 5.17: Charge identification efficiency. Left: efficiency as a function of momentum (MeV/c). Right: efficiency as a function of polar angle (rad).

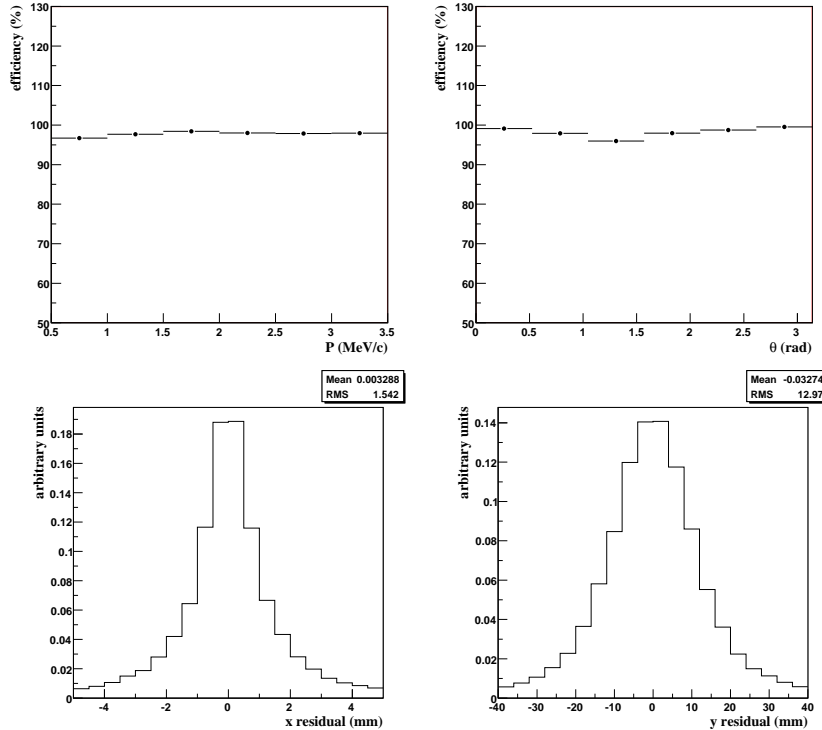


Figure 5.18: Vertex reconstruction. Top left: efficiency of vertex reconstruction as a function of momentum (MeV/c). Top right: efficiency of vertex reconstruction as a function of polar angle (rad). Bottom left: x coordinate of vertex residual (mm). Bottom right: y coordinate of vertex residual (mm).

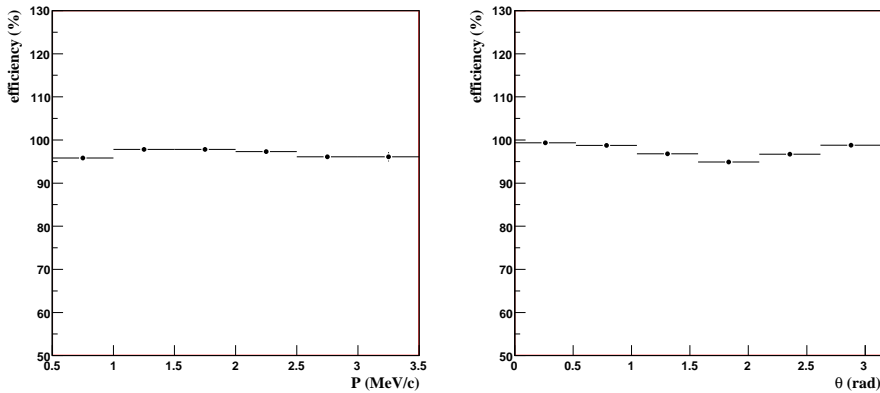


Figure 5.19: Efficiency of matching between tracks and calorimeter hits. Left: efficiency of matching with calorimeter hit as a function of momentum (MeV/c). Right: efficiency of matching with calorimeter hit as a function of polar angle (rad).

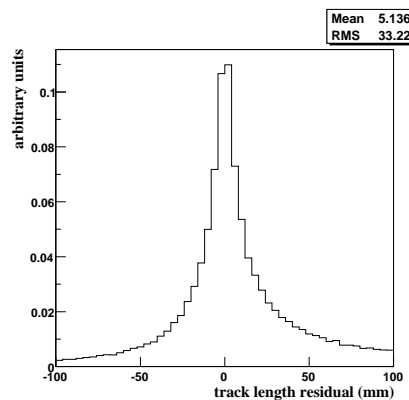


Figure 5.20: Particle flight length residual defined as the difference between reconstructed length and simulated length. Center of distribution is at 5 mm, being the RMS 33 mm.

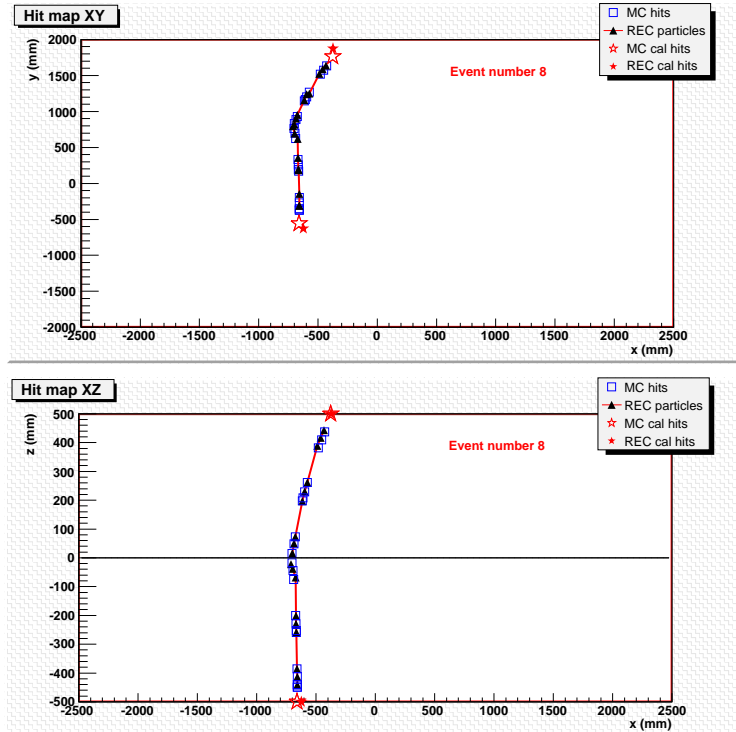


Figure 5.21: Reconstructed $\beta\beta^{0\nu}$ event. Squares and empty stars show simulated tracker and calorimeter hits, respectively, meanwhile, triangles, solid stars and lines show reconstructed tracked hits, reconstructed calorimeter hits and track fit, respectively. Top: XY hit map projection. Bottom: XZ hit map projection. Black line in $z = 0$ shows foil position.

5.5.2 Overall detection efficiency

The overall detection efficiency $\epsilon_{\beta\beta}$ for the $\beta\beta$ decay (both $\beta\beta^{0\nu}$ and $\beta\beta^{2\nu}$) is defined as the ratio between the number of events selected and the total number of $\beta\beta$ decays that actually took place. This efficiency can be treated as the convolution of three different factors:

1. topological acceptance $\epsilon_{\beta\beta}^{accep}$
2. reconstruction efficiency $\epsilon_{\beta\beta}^{rec}$
3. selection cuts efficiency $\epsilon_{\beta\beta}^{sel}$

$$\text{so } \epsilon_{\beta\beta} = \epsilon_{\beta\beta}^{accep} \cdot \epsilon_{\beta\beta}^{rec} \cdot \epsilon_{\beta\beta}^{sel}.$$

The geometrical acceptance takes into account the fraction of $\beta\beta$ events in which one of the electrons does not produce a hit in the calorimeter wall. This happens when the particle is stopped inside the foil or inside the tracking chamber, or when it goes through one of the detector walls where there are not calorimeter blocks. This is estimated to occur in 27% of the $\beta\beta$ decays, and therefore geometrical acceptance is 73%. The geometrical acceptance concept can be extended by taking into account all those events which would never pass, for topological reasons, the selection cuts even if the reconstruction algorithms were perfect. The following list summarizes these kind of events:

- a particle enters the foil for a second time and is tracked in both sides of the foil,
- a particle is backscattered in the calorimeter block and tracked in its way back,
- a secondary particle is generated in the chamber and tracked,
- there are more than two calorimeter hits in the event.

Putting all together, $\epsilon_{\beta\beta}^{accep}$ can be considered as a topological acceptance for $\beta\beta$ events and it is estimated to be 51% for ^{82}Se foils of 40 mg/cm^2 . Fig. 5.22 shows track acceptance of SuperNEMO as a function of momentum and the polar angle θ with respect to the foil normal direction, when a ^{82}Se foil of 40 mg/cm^2 is assumed. As can be observed, particles with low momentum are typically stopped inside the foil or in the tracking chamber due to the energy

losses. On the other hand, particles emitted with $\theta \sim 1.6 \sim \pi/2$ rad, i.e., parallel to the foil, have less chances to reach the calorimeter and more chances to cross again the foil.

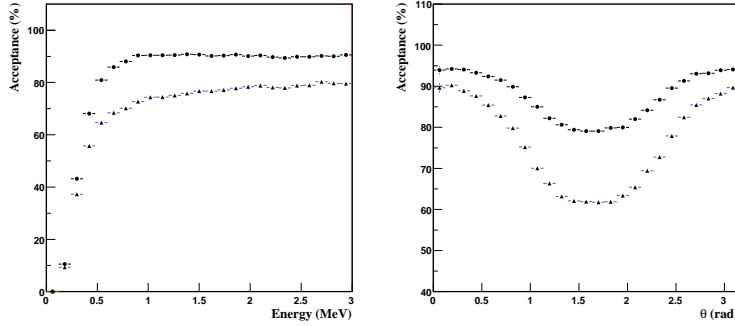


Figure 5.22: Track acceptance in SuperNEMO detector when ^{82}Se foils of 40 mg/cm^2 are used. Left: acceptance as a function of energy (MeV). Right: acceptance as a function of polar angle θ (rad). Squares show geometrical acceptance meanwhile triangles show topological acceptance, as defined in the text.

For a given geometry of the SuperNEMO detector, $\epsilon_{\beta\beta}^{accep}$ depends on two main factors: one is magnetic field and the other is the foil source. As expected, $\epsilon_{\beta\beta}^{accep}$ depends on the magnetic field B . It turns out that if B is turned off, event topological acceptance is increased up to 60%, as can be seen in Fig. 5.23, where acceptance per track is plotted for $B=0$. This is basically due to two effects. One is that the number of particles reentering the foil is lower when there is not magnetic field, and the other is that magnetic field leads to a higher energy loss. Topological acceptance $\epsilon_{\beta\beta}^{accep}$ also depends on the source material, since different density implies different energy losses inside the foil. For ^{150}Nd foils of 40 mg/cm^2 , $\epsilon_{\beta\beta}^{accep}$ is slightly higher than the one for ^{82}Se foils of the same thickness (54%), as can be seen in Fig. 5.24. Finally, $\epsilon_{\beta\beta}^{accep}$ depends on the foil thickness, since energy losses inside the foils also depend on it. To illustrate this fact, Fig. 5.25 shows acceptance per track for ^{82}Se foils of 40 mg/cm^2 and 80 mg/cm^2 .

Reconstruction efficiency $\epsilon_{\beta\beta}^{rec}$ takes into account the fact that fitting and reconstruction algorithms fail for some events which fulfill the requirements to be

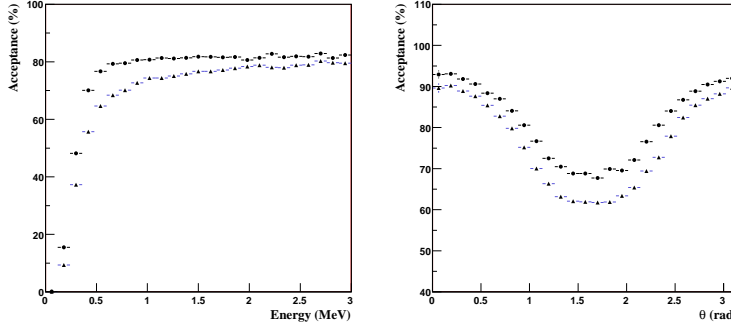


Figure 5.23: Track acceptance in SuperNEMO detector for $B=0$ Gauss and ^{82}Se foil of 40 mg/cm^2 . Left: acceptance as a function of energy. Right: acceptance as a function of polar angle θ (rad). Squares show acceptance when $B = 0$ Gauss, meanwhile triangles show acceptance for $B=25$ Gauss, as previously shown in Fig. 5.22.

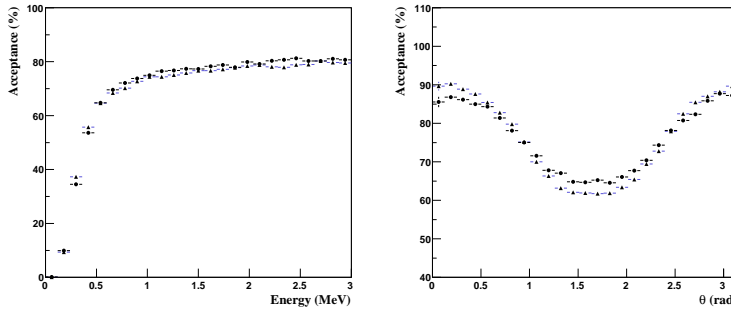


Figure 5.24: Track acceptance in SuperNEMO detector for ^{150}Nd and ^{82}Se foils of 40 mg/cm^2 . Left: acceptance as a function of momentum (MeV/c). Right: acceptance as a function of polar angle θ (rad). Circles show acceptance for ^{150}Nd foils, meanwhile triangles show acceptance for ^{82}Se foils, as previously shown in Fig. 5.22.

reconstructed and selected. In Section 5.4.2 efficiencies of these algorithms have been presented. The overall reconstruction efficiency for a particle, defined as a fitted track with vertex on the foil, associated calorimeter hit and good charge identification, is shown in Fig. 5.26 as a function of momentum p and polar angle θ . The integrated value of the particle reconstruction efficiency is about 85%, consistent with the efficiencies presented in Section 5.4.2. Reconstruction efficiency of the $\beta\beta$ event (i.e. two reconstructed particles) is 72%.

Finally, selection efficiency $\epsilon_{\beta\beta}^{sel}$ takes into account the fraction of events lost when the selection cuts are applied. Selection cuts defined in 5.5.1 provide an important handle to reject background events, but they also reject some $\beta\beta$ events which have been successfully reconstructed. It has been estimated that $\epsilon_{\beta\beta}^{sel}$ is about 78%.

From the above values of $\epsilon_{\beta\beta}^{accep}$, $\epsilon_{\beta\beta}^{rec}$ and $\epsilon_{\beta\beta}^{sel}$ one gets that final overall reconstruction efficiency for $\beta\beta$ events is $\epsilon_{\beta\beta} \sim 28\%$. Table 5.5 summarizes the efficiencies defined in this section.

	Event	Track
Acceptance $\epsilon_{\beta\beta}^{accep}$	51%	71%
Reconstruction $\epsilon_{\beta\beta}^{rec}$	72%	85%
Selection $\epsilon_{\beta\beta}^{sel}$	78%	99%
Overall efficiency $\epsilon_{\beta\beta}$	28%	60%

Table 5.5: Summary of overall reconstruction efficiency for $\beta\beta^{0\nu}$ events, assuming ^{82}Se foil of 40 mg/cm² and magnetic field of 25 Gauss, and geometry as defined in 5.4.1: detector of 4 m high, 5 m long and 1 meter wide.

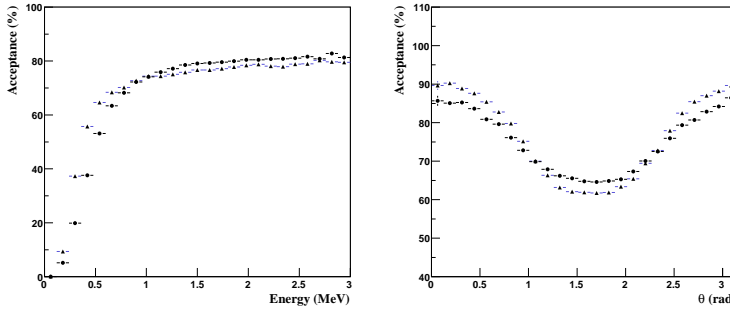


Figure 5.25: Track acceptance in SuperNEMO detector for ^{82}Se foils of $40 \text{ mg}/\text{cm}^2$ and $80 \text{ mg}/\text{cm}^2$ foils. Left: acceptance as a function of momentum (MeV/c). Right: acceptance as a function of polar angle θ (rad). Circles show acceptance for $80 \text{ mg}/\text{cm}^2$ foils, meanwhile triangles show acceptance for $40 \text{ mg}/\text{cm}^2$ foils, as previously shown in Fig. 5.22.

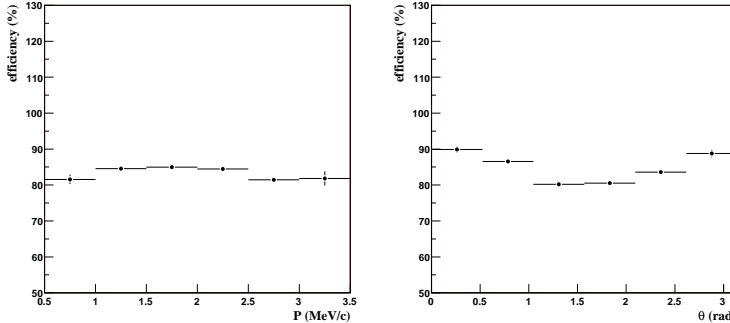


Figure 5.26: Particle reconstruction efficiency. Left: reconstruction efficiency as a function of momentum (MeV/c). Right: reconstruction efficiency as a function of polar angle θ (rad).

5.6 Computing SuperNEMO sensitivity

With the full simulation of the SuperNEMO standard module, the event reconstruction algorithms, and the set of event selection cuts described in previous sections, we are now in place to obtain the expected energy spectra in the SuperNEMO experiment, for both signal and background events. Moreover, we are able to estimate how many events we expect to detect for a given experimental setup and a time of measurement. In this section we describe how this information can be used to compute SuperNEMO sensitivity to $T_{1/2}^{0\nu}$, when one assumes the exchange of a light Majorana neutrino.

5.6.1 Sensitivity to a light Majorana neutrino

The $\beta\beta^{0\nu}$ signal is distributed around $Q_{\beta\beta}$ as a Dirac's delta convoluted with the detector resolution function, which in SuperNEMO can be well represented by a Landau (due to the fluctuations of energy losses in the foil and the tracking chamber) convoluted with a gaussian (due to the calorimeter resolution). On the other hand, the $\beta\beta^{2\nu}$ background, near the end-point, can be imaged as exponential convoluted with the detector resolution function (Fig. 5.27).

Since the topological signature does not discriminate between $\beta\beta^{0\nu}$ and $\beta\beta^{2\nu}$ events, $\beta\beta^{2\nu}$ events pass the event selection cuts and the only handle to separate one from the other is energy resolution. Therefore, assuming no other background is present in our experiment, sensitivity is ultimately limited by the calorimetric resolution. However, in the region near the end-point where signal and background overlap, one can improve the discrimination between one and the other by using the knowledge of the distributions in Fig. 5.27, taking advantage of the expected number of events of each kind.

The situation becomes even more complicated when other backgrounds are taken into account. Then spectrum of $\beta\beta^{2\nu}$ is convoluted with the one coming from the different sources of background, giving a sort of overall background spectrum. For that reason, one has to find also what is the shape of the background spectra and how many background events are going to pass the event selection cuts.

As soon as all spectrum shapes are well known, and estimation of the number of events of each type under given experimental conditions is possible, one can compute the sensitivity of the experiment. The main goal of the analysis is to look for an excess of events with respect to the expected background, but one also needs to estimate the confidence level of the results. If such an excess is found, we have a signal which can be translated in terms of a value of $T_{1/2}^{0\nu}$. On

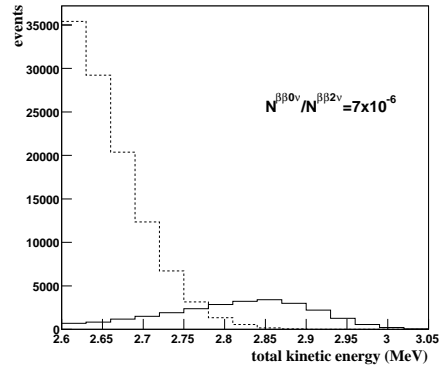


Figure 5.27: Distributions of the signal (solid line) and the $\beta\beta^{2\nu}$ background (dashed line), near $Q_{\beta\beta}$ in SuperNEMO. The simulated foil is ^{82}Se , with a thickness of 40 mg/cm^2 . Calorimeter resolution is 7% FWHM at 1MeV. Ratio between $\beta\beta^{0\nu}$ and $\beta\beta^{2\nu}$ events is 7×10^{-6} .

the other hand, if no signal is observed, a lower limit to $T_{1/2}^{0\nu}$ can be set.

5.6.2 Nuclear matrix elements

In order to determine an effective Majorana neutrino mass from a $\beta\beta^{0\nu}$ result, one requires input from nuclear theory. The matrix elements however are very hard to calculate and the various techniques and authors produce varying results. The two main techniques for calculating the matrix elements are the quasi-particle random phase approximation (QRPA) and the nuclear shell model (NSM). The discussion of these methods is out of the scope of this work. For further details, see Ref. [100] and [101].

Each approach has its advantages and disadvantages and hence critics and advocates. Due to this complicated situation, the spread in the calculations is commonly taken as a measure of the theoretical uncertainty. Some people have even begun to treat the calculations as a statistical sample from which to extract an error bar on the calculated matrix elements, reaching the conclusion that the matrix elements are only known to within an order of magnitude.

However, recent papers have addressed this issue in the context of the QRPA (e.g., [52]) arguing that almost all the latest QRPA-like calculations, give the same results to within about 30% (see Fig. 5.28). Though we have no way of knowing for sure that any of the calculations give results that are right, it is comforting to think that they agree with one another.

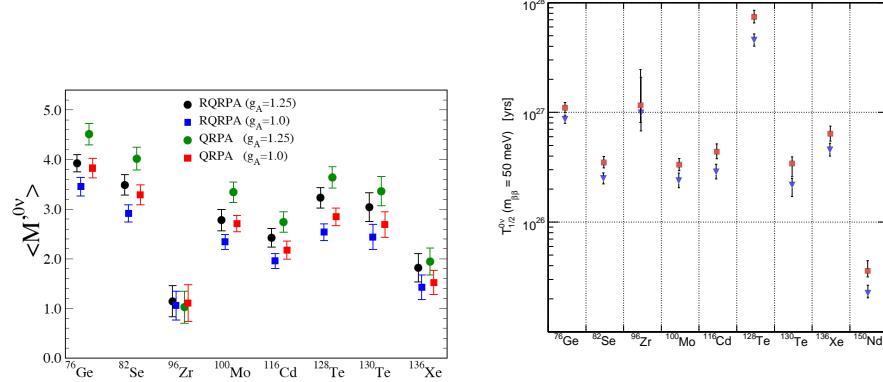


Figure 5.28: Left panel: Average nuclear matrix elements and their variance (including the uncertainty coming from the experimental error in $M^{2\nu}$) for QRPA and RQRPA methods, for the two customary values of the coupling constant g_A (parameterization of the Gamow-Teller strength) and for several nuclei. For ^{136}Xe the error bars encompass the whole interval related to the unknown rate of the $\beta\beta^{2\nu}$ decay. From [52]. Right panel: $\beta\beta^{0\nu}$ half-lives and their variance evaluated with the RQRPA average nuclear matrix elements and for assumed $\langle m_\nu \rangle = 50 \text{ meV}$. Red squares for $g_A = 1.00$; blue triangles for $g_A = 1.25$. ^{150}Nd is included for illustration. All calculations treated it as spherical nuclei; deformation will undoubtedly modify their matrix elements. Data from [52].

Anyway, the uncertainty in the nuclear matrix elements in no way reduces the attractiveness of double-beta decay experiments. And, of course, if the decay is seen, the theoretical work will increase dramatically.

NME used for ^{82}Se and ^{150}Nd

The $\beta\beta^{2\nu}$ mode has been measured for both ^{82}Se , and ^{150}Nd in several experiments, but in our work we will use the NEMO 3 results. Since SuperNEMO is going to use similar experimental technique, we believe that systematic effects should be similar as well, that is why usage of the NEMO 3 measurement seems to be more appropriate.

$T_{1/2}^{2\nu}$ used for the current analysis comes from the works [102] and [103]:

$$^{82}\text{Se} : \quad T_{1/2}^{2\nu} = 1.0 \times 10^{20} \text{ y} \quad (5.19)$$

$$^{150}\text{Nd} : \quad T_{1/2}^{2\nu} = 9.33 \times 10^{18} \text{ y} \quad (5.20)$$

For the $\beta\beta^{0\nu}$ mode one needs a theoretical calculation of the matrix element. While there is a reasonable agreement among different groups for ^{82}Se , the situation is more complicated for ^{150}Nd , which is very hard to treat theoretically.

A recent calculation in the context of the QRPA model [52] yields the following values for the $T_{1/2}^{0\nu}$ of ^{82}Se , depending on the value of the axial-vector coupling constant g_A used for the parameterization of the Gamow-Teller strength:

$$^{82}\text{Se} : \quad T_{1/2}^{0\nu}(\langle m_\nu \rangle = 50 \text{ meV}) = (2.44_{-0.26}^{+0.32} - 3.50_{-0.38}^{+0.46}) \times 10^{26} \text{ y} \quad (5.21)$$

where the upper values stand for $g_A = 1.00$ and the lower ones for $g_A = 1.25$. From the proton-neutron QRPA model (pnQRPA) [104] the following compatible values are obtained:

$$^{82}\text{Se} : \quad T_{1/2}^{0\nu}(\langle m_\nu \rangle = 50 \text{ meV}) = (1.81 - 2.76) \times 10^{26} \text{ y} \quad (5.22)$$

where the upper values stand for $g_A = 1.00$ and $g_{pp} = 1.00$, and the lower ones for $g_A = 1.25$ and $g_{pp} = 0.96$, being g_{pp} the particle-particle strength parameter that controls the magnitude of the proton two-body interaction. On the other hand, the shell model [101] and A. Poves [105] yield larger but quite close results for ^{82}Se :

$$NSM : \quad T_{1/2}^{0\nu}(\langle m_\nu \rangle = 50 \text{ meV}) = 9.6 \times 10^{26} \text{ y} \quad (5.23)$$

$$A.Poves : \quad T_{1/2}^{0\nu}(\langle m_\nu \rangle = 50 \text{ meV}) = 5.7 \times 10^{26} \text{ y} \quad (5.24)$$

For ^{150}Nd the scenario is much more unclear, with only a few predictions and bad agreement between them. The QRPA model computes the following values, depending again on g_A :

$$^{150}\text{Nd} : T_{1/2}^{0\nu}(\langle m_\nu \rangle = 50 \text{ meV}) = (2.23_{-0.21}^{+0.41} - 3.55_{-0.42}^{+0.87}) \times 10^{25} \text{ y} \quad (5.25)$$

However, the QRPA calculation treats ^{150}Nd as a spherical nucleus and this may not be a correct approach since ^{150}Nd is strongly deformed. A pseudo SU(3) model has been used in [106] to compute the NME of ^{150}Nd taking into account nucleus deformation. This model has provided results for the NME of the $\beta\beta^{2\nu}$ process in good agreement with experiments. From this model one obtains:

$$^{150}\text{Nd} : T_{1/2}^{0\nu}(\langle m_\nu \rangle = 50 \text{ meV}) = 4.2 \times 10^{26} \text{ y} \quad (5.26)$$

which is one order of magnitude away from the QRPA results. In fact, if one sticks to the latest result, ^{150}Nd is not such a suitable isotope for setting a limit to $\langle m_\nu \rangle$. In conclusion, there seems not to be yet a reliable calculation taking deformation into account, so sensitivity to $\langle m_\nu \rangle$ when using ^{150}Nd foil will be affected by this unquotable uncertainty.

Fig. 5.29 shows $T_{1/2}^{0\nu}$ versus $\langle m_\nu \rangle$ for ^{82}Se and ^{150}Nd and the different models used to compute the NME of the $\beta\beta^{0\nu}$ decay. Along the following sections of this work, several plots concerning the sensitivity of SuperNEMO to $T_{1/2}^{0\nu}$ will be shown. In order to obtain this sensitivity in terms of $\langle m_\nu \rangle$ according to a given model, plots in this figure must be used. For some experimental setups, we will also show sensitivity plots in terms of $\langle m_\nu \rangle$ and in such cases we will use the QRPA model as a reference, since it provides numbers for both ^{82}Se and ^{150}Nd .

5.6.3 Likelihood analysis

The main building block of the analysis is the probability density function f (p.d.f) that describes the SuperNEMO expected data. In our experiment, we consider only two kind of events: signal and background, characterized by a continuous variable x :

$$x = E/Q_{\beta\beta} \quad (5.27)$$

where E is the energy sum of both electrons in the event. This variable is limited within a range around $Q_{\beta\beta}$ in which we perform our analysis. In

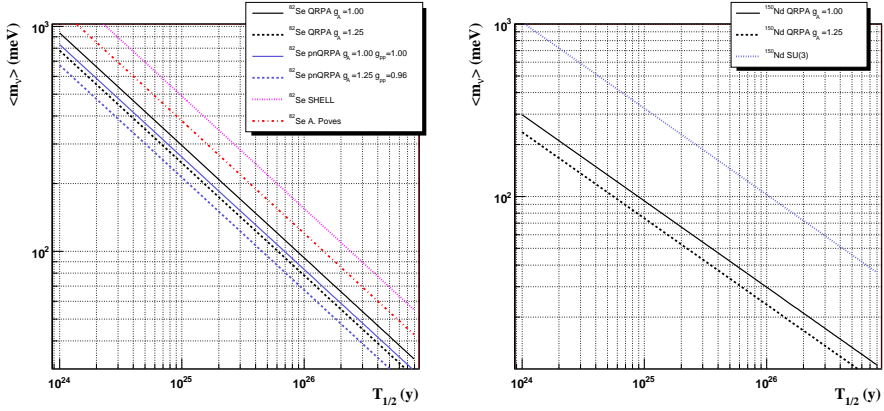


Figure 5.29: $T_{1/2}^{0\nu}$ versus $\langle m_\nu \rangle$ according to different models. Left: $T_{1/2}^{0\nu}$ versus $\langle m_\nu \rangle$ for ^{82}Se , according to QRPA model with $g_A=1.00$ (black solid line), QRPA model with $g_A=1.25$ (black dashed line), pnQRPA model for ($g_A = 1.00$, $g_{pp}=1.00$) (gray solid line) and for ($g_A = 1.25$, $g_{pp}=0.96$) (gray dashed line), NSM (dotted line), A. Poves model (dot-dashed line). Right: $T_{1/2}^{0\nu}$ versus $\langle m_\nu \rangle$ for ^{150}Nd according to QRPA model with $g_A=1.00$ (solid line), QRPA model with $g_A=1.25$ (dashed line), and SU(3) model (dotted line).

this work, we take $x \in [0.87, 1.07]$. Signal and background events have different p.d.f's ($f_s(x)$ and $f_b(x)$, respectively), which are obtained from the SuperNEMO simulation and the reconstruction chain (5.4) and have been already presented in Fig. 5.27. Only p.d.f for $\beta\beta^{2\nu}$ background is presented in that figure: in case of considering other kind of backgrounds, the corresponding p.d.f's are convoluted with it. The overall composite p.d.f of SuperNEMO experiment is built as follows:

$$f(x) = \alpha f_s(x) + (1 - \alpha) f_b(x) \quad (5.28)$$

where $\alpha = n_s/(n_s + n_b)$, being n_s the number of signal events ($\beta\beta^{0\nu}$), and n_b the number of background events, accepted by the topological selection. Both n_s and n_b are distributed according to a Poisson distribution, so the total

number of events $n = n_s + n_b$ is also Poisson distributed, with mean value ν . Notice that α parametrizes the ratio between signal and background events, and therefore it is the only variable that needs to be fitted. Since the number of signal events depends on the half-life of the $\beta\beta^{0\nu}$ process, we have that $\alpha = \alpha(T_{1/2}^{0\nu}) = \alpha(\langle m_\nu \rangle)$, and thus the p.d.f depends also on this parameter: $f(x) = f(x; T_{1/2}^{0\nu}) = f(x; \langle m_\nu \rangle)$.

In order to determine the value of the parameter α , one can maximize the extended Likelihood function [107] (with $\theta = T_{1/2}^{0\nu}$) defined as:

$$L(\nu, \theta) = \frac{e^{-\nu}}{n!} \prod_{i=1}^n \nu f(x_i; \theta) \quad (5.29)$$

where x_i is each one of the observed events. The use of the extended likelihood is justified by the fact that n is a random variable (poisson-distributed) with mean ν : one can not fix the number of events in a $\beta\beta$ experiment.

It is usually easier to work with $\ln L$, so in this analysis we maximize the logarithm of the extended likelihood:

$$\log L(\nu, \theta) = -\nu(\theta) + \sum_{i=1}^n \log(\nu(\theta) f(x_i; \theta)) \quad (5.30)$$

Moreover, we bin experiment data in $N = 20$ bins, so events are distributed in a vector of data $\mathbf{n} = (n_1, n_2, \dots, n_N)$, with expectation values $\boldsymbol{\nu}$ and probabilities $f(\mathbf{n}; \boldsymbol{\nu})$. Then minimization of likelihood function is based on the contents of the bins. Now equation 5.30 can be rewritten as:

$$\log L(\nu, \theta) = -\nu_{tot} + \sum_{i=1}^N n_i \log(\nu_i(\nu_{tot}, \theta)) \quad (5.31)$$

where $n_{tot} = \sum_{i=1}^N n_i$, $\nu_{tot} = \sum_{i=1}^N \nu_i$ and:

$$\nu_i(\nu_{tot}, \theta) = \nu_{tot} \int_{x_i^{\min}}^{x_i^{\max}} f(x_i; \theta) dx \quad (5.32)$$

being x_i^{\min}, x_i^{\max} the lower and upper bounds of the bin.

Maximizing 5.31 is equivalent to maximizing the likelihood ratio $\lambda(\theta) = f(\mathbf{n}; \boldsymbol{\nu})/f(\mathbf{n}; \mathbf{n})$, or to minimizing the quantity

$$L_R = -2\ln\lambda(\theta) = 2 \sum_{i=1}^N (n_i \log \frac{n_i}{\nu_i(\theta)} + \nu_i(\theta) - n_i) \quad (5.33)$$

The nice feature of equation 5.33 is that the value of L_R for the true parameter is zero (L_R^{min}). In addition, it allows for a goodness-of-fit test. This statistic follows a χ^2 in the large data sample limit, for $N - m$ degrees of freedom, being m the number of fitted parameters (m=1 in our analysis). Furthermore, L_R is well defined even if there are no events in a given bin (unlike the χ^2 statistic). This allows to bin the data with an arbitrarily high number of bins (in the limit of many bins one converges to the definition for unbinned data).

Fig. 5.30, shows the variation of the statistic defined in equation 5.33 with the parameter $\theta = \langle m_\nu \rangle$. The true values of $\langle m_\nu \rangle$ generated in the simulation are 200, 300, 500 and 700 meV, the isotope is ^{82}Se and the run conditions are those described above. Notice that one obtains, as expected, $L_R = 0$ for the true value of the parameter. To obtain the error on the determination of $\langle m_\nu \rangle$, recall that L_R is distributed like a χ^2 and thus one standard deviation error corresponds to $L_R^{min} + 1 = 1$.

5.6.4 Computing the discovery potential

To quantify the discovery potential of a given experiment one often builds an *exclusion plot*, defined as the region where one cannot distinguish a parameter with some finite value from the null hypothesis at some confidence level.

To compute the exclusion plot for SuperNEMO, we use again equation 5.33. The procedure is as follows. For a given experimental setup where everything but the exposure is fixed, run over a grid of exposures exp (kg · year) and $T_{1/2}^{0\nu}$ values. For each pair $(exp, \langle m_\nu \rangle)$, compute the number of $\beta\beta^{0\nu}$ signal events. In addition, for each value of exp , compute the number of $\beta\beta^{2\nu}$ events and any other kind of background events. This results in a value of L_R in each point of the grid. Since L_R is χ^2 distributed, one can now compute the C.L. corresponding to a variation of L_R above its minimum value ($L_R = 0$). Recall that a variation of 1.0 corresponds to one standard deviation error, that is a C.L. of 68.3%. The 90% C.L. corresponds to a variation of 2.71, 95% to 3.84 and 99% to 6.63.

Clearly, the choice of the C.L. to quantify the sensitivity of an experiment is somewhat arbitrary (one has simply to be consistent when comparing different options and/or experiments). Notice, however, that the rather extended practice of choosing 90% C.L. for an exclusion plot is rather ambiguous. Since one is

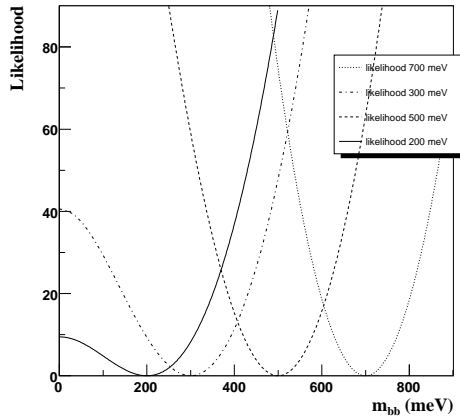


Figure 5.30: Variation of the L_R statistics defined in equation 5.33 with the parameter $\langle m_\nu \rangle$. Notice that one obtains, as expected, $L_R = 0$ for the true value of the parameter. To obtain the error on the determination of $\langle m_\nu \rangle$, recall that L_R is distributed like a χ^2 and thus one standard deviation errors correspond to $L_R^{min} + 1 = 1$.

rejecting the null hypothesis at 1.64 standard deviations, the region above the exclusion line cannot be interpreted as discovery region (one cannot claim a signal with 1.64 standard deviations evidence). Choosing 95% is more acceptable, but 99% guarantees that the area above the exclusion line is a discovery region, in which the signal is observed with more than 2 standard deviations.

However, since 90% C.L. is the value most commonly used, in this work we also present SuperNEMO sensitivity results for this confidence level. In the next section, exclusion (or sensitivity) plots will be shown as a function of several parameters. Area above lines in those plots will show the range of $T_{1/2}^{0\nu}$ values that would be excluded at 90% C.L. if no signal is found. Area below the lines will show the values of $T_{1/2}^{0\nu}$ that cannot be explored. The lines themselves will set the lower limit to $T_{1/2}^{0\nu}$ if no signal is observed.

In further sections, figures showing SuperNEMO sensitivity in terms of $\langle m_\nu \rangle$

will be obtained assuming nuclear matrix elements (NME) from QRPA model [52]; however, since there are several models in the market quoting different values for NME, we will also present numbers for sensitivity to $\langle m_\nu \rangle$ as a range between the upper and lower mass limits according to all of them ([52, 101, 104, 105, 106]. It turns out that for ^{82}Se highest values of $\langle m_\nu \rangle$ come from the Nuclear Shell Model (NSM) [101], while lowest ones come from proton-neutron QRPA model (pnQRPA) [104].

5.7 The physics case of SuperNEMO

ex

We are now equipped to quantify the impact of several relevant parameters in the SuperNEMO performance. We will address, in turn, the cases of ^{82}Se and ^{150}Nd . For the rest of this section we define the SuperNEMO standard setup as follows: foils of 40 mg/cm^2 , calorimeter resolution of $\text{FWHM} = 7\%$ at 1 MeV, and module geometry as defined in 5.3. Only mass mechanism of $\beta\beta^{0\nu}$ decay is considered in this work.

5.7.1 Physics case of ^{82}Se

We start analyzing the best case for the SuperNEMO experiment. Best case stands for no other backgrounds but $\beta\beta^{2\nu}$ spectrum, so ^{214}Bi and ^{208}Tl contaminations are considered to be negligible. In addition, best case also means reaching a calorimeter resolution of 7% FWHM at 1 MeV, although the feasibility of this has not been proved yet, either using plastic or liquid scintillators, as projected for the SuperNEMO detector. The expected spectra for 100 kg of ^{82}Se after 5 years of data taking (or $500 \text{ kg} \cdot \text{year}$ of exposure), assuming the standard setup, is shown in Fig. 5.31. Only $\beta\beta^{2\nu}$ background (filled histogram) is considered, and $\beta\beta^{0\nu}$ signal (empty histogram) is computed for $T_{1/2}^{0\nu} = 10^{26}$ years.

As explained in Section 5.6, exclusion plots are used to quantify the discovery potential of the SuperNEMO experiment. Left panel of Fig. 5.32 shows exclusion plots at 90% (dotted line), 95% (dashed line) and 99% (solid line) C.L., when the $\beta\beta^{2\nu}$ spectrum is the only background taken into account. Right panel of same figure shows same results in terms of sensitivity to $\langle m_\nu \rangle$ at 90% C.L., when QRPA nuclear matrix elements from [52] are considered.

For $500 \text{ kg} \cdot \text{year}$ of exposure and therefore correspondingly to the spectra shown in Fig. 5.31, the sensitivity limits are shown in Table 5.6. Second column on Table 5.6 shows limit to $T_{1/2}^{0\nu}$, and third one shows corresponding range of $\langle m_\nu \rangle$ (depending on nuclear models). Finally, on fourth column $\langle m_\nu \rangle$ value according to QRPA model (used in figures as a reference) is presented.

In the following sections, the dependence of these results with different parameters are analyzed: exposure, calorimeter resolution, magnetic field, detection efficiency and foil thickness. Then, impact of internal backgrounds others from the $\beta\beta^{2\nu}$ spectrum will also be studied.

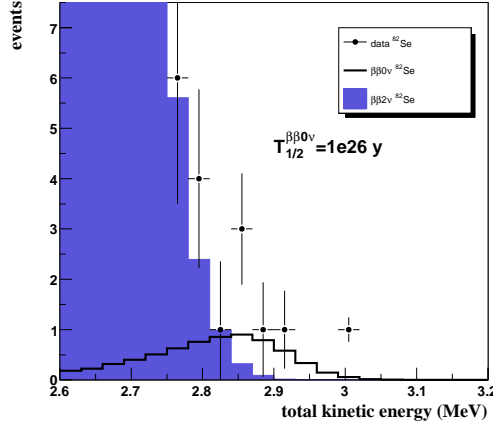


Figure 5.31: Expected spectra after 5 years of data taking with 100 kg of ^{82}Se foils and the SuperNEMO standard setup as defined in the text. $\beta\beta^{0\nu}$ signal assumes half-life of $T_{1/2}^{0\nu} = 10^{26}$ years.

Resolution	$T_{1/2}^{0\nu}$ (y)	$\langle m_\nu \rangle$ range (meV)	$\langle m_\nu \rangle$ (QRPA) (meV)
7%	1.6×10^{26}	53-123	61

Table 5.6: Sensitivity result for SuperNEMO best case: no other backgrounds but $\beta\beta^{2\nu}$ one are considered. Third column shows $\langle m_\nu \rangle$ sensitivity range corresponding to upper and lower limits from nuclear models in [52, 101, 104, 105, 106], meanwhile fourth one shows $\langle m_\nu \rangle$ sensitivity according to QRPA model [52]. Results at 90% C.L., for an exposure of 500 kg · year. Resolution given in FWHM at 1 MeV.

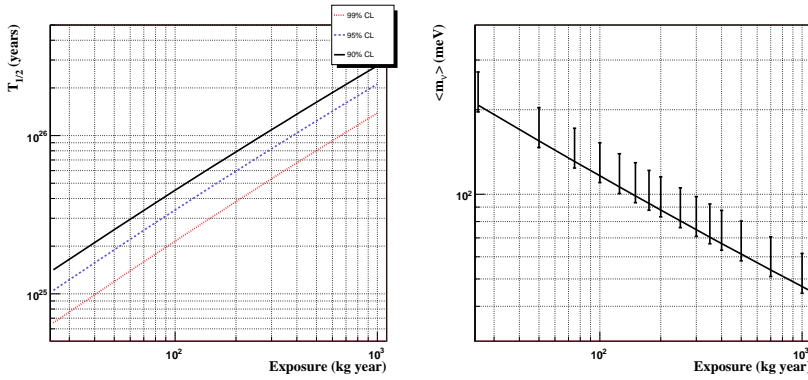


Figure 5.32: Sensitivity plots (exclusion plots) for ^{82}Se and the SuperNEMO standard setup: foil of 40 mg/cm^2 , calorimeter resolution of 7% FWHM at 1 MeV, and magnetic field of 25 Gauss. Left: sensitivity to $T_{1/2}^{0\nu}$ at 90% (solid line), 95% (dashed line) and 99% C.L., as a function of exposure. Right: sensitivity to $\langle m_\nu \rangle$ at 90% C.L. as a function of exposure, when NME value from QRPA model with $g_A = 1.25$ is used. Error bars take into account both QRPA uncertainties and discrepancy between $g_A = 1$ and $g_A = 1.25$ results.

5.7.2 Dependence of the sensitivity with the exposure

As can be seen in Fig. 5.32, the sensitivity improves gradually with the experiment exposure (source mass M by the data taking time t). Normally half-life sensitivity is proportional to exposure, since $N_{\beta\beta} \propto Mt$, in the no-background case, and proportional to \sqrt{Mt} if an experiment has non-zero background (see Sec. 3.3.3):

$$\text{zero - background : } \langle m_\nu \rangle \propto (T_{1/2}^{0\nu})^{-1/2} \propto (Mt)^{-1/2} \quad (5.34)$$

$$\text{background - dominated : } \langle m_\nu \rangle \propto (T_{1/2}^{0\nu})^{-1/2} \propto (Mt)^{-1/4} \quad (5.35)$$

In general it is useful to introduce the factor R , which measures the power law of the dependence of the sensitivity with the exposure:

$$\langle m_\nu \rangle \sim (Mt)^{-1/R} \quad (5.36)$$

Likelihood analysis used here, unlike simple window counting methods, mixes background dominated regions with almost zero-background regions of the energy spectrum. Therefore actual value of R will be somewhere between 2 and 4. As the exposure is increased, so does the R factor, until the point in which the experiment becomes fully dominated by background. When this happens, sensitivity cannot be improved significantly by increasing the exposure.

For practical applications, R can be approximately calculated as:

$$R = \frac{\frac{\Delta Mt}{Mt}}{\frac{\Delta \langle m_\nu \rangle}{\langle m_\nu \rangle}} \approx \frac{\frac{(Mt)_1 - (Mt)_2}{(Mt)_1 + (Mt)_2}}{\frac{\langle m_\nu \rangle_1 - \langle m_\nu \rangle_2}{\langle m_\nu \rangle_1 + \langle m_\nu \rangle_2}} \quad (5.37)$$

Fig. 5.33 shows dependence of R with exposure for the case of only $\beta\beta^{2\nu}$ background and ^{82}Se foils. For the standard SuperNEMO design and expected exposure (500 kg · year), $R \approx 2.55$, which means that background level is still low.

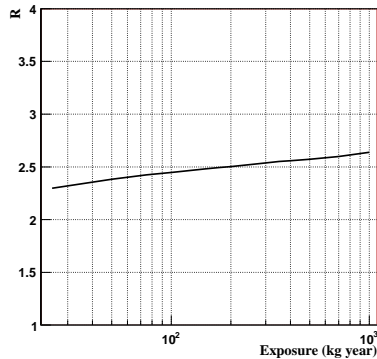


Figure 5.33: R factor for ^{82}Se sensitivity results at 90% C.L., and the SuperNEMO standard setup: ^{82}Se foil of 40 mg/cm^2 , calorimeter resolution of 7% FWHM at 1 MeV, and magnetic field of 25 Gauss.

5.7.3 Dependence of the sensitivity with the experimental setup

Apart from the mass of isotope to be placed in SuperNEMO, there are four other parameters related to the experimental setup that may have a big impact on the sensitivity to the $\beta\beta^{0\nu}$ process:

- calorimeter energy resolution,
- foil thickness,
- detection efficiency,
- magnetic field.

The following analyzes the dependence of the sensitivity with the above variables.

Dependence with calorimeter resolution: $\beta\beta^{0\nu}$ background

$\beta\beta^{2\nu}$ is the ultimate background for the $\beta\beta^{0\nu}$ process. It cannot be reduced by any means but detector energy resolution. To illustrate this fact, Fig. 5.34 shows SuperNEMO sensitivity dependence on calorimeter energy resolution: left plot shows sensitivity to $T_{1/2}^{0\nu}$ as a function of exposure for three different energy resolution (7%, 9%, and 14%), meanwhile right plot shows same sensitivity as a function of the energy resolution, for a fixed exposure of 500 kg · year. We recall that only $\beta\beta^{2\nu}$ background is considered here. As previously remarked, SuperNEMO goal for calorimeter resolution is 7% FWHM at 1MeV, and if this target is met, $T_{1/2}^{0\nu}$ sensitivity will be 1.6×10^{26} years after 5 years of running with 100 kg source. This sensitivity must be treated as a limit when no other background is present. Table 5.7 shows sensitivity results for various energy resolutions, assuming an exposure of 500 kg · year.

Reduction of the $\beta\beta^{2\nu}$ background level by means of the energy resolution can be seen in Fig. 5.35, where dependence of R factor with exposure for calorimeter resolutions of 7, 9 and 14% (FWHM at 1MeV) is shown. It is clear that SuperNEMO starts to be dominated by the $\beta\beta^{2\nu}$ background very quickly, as the calorimeter resolution is degraded.

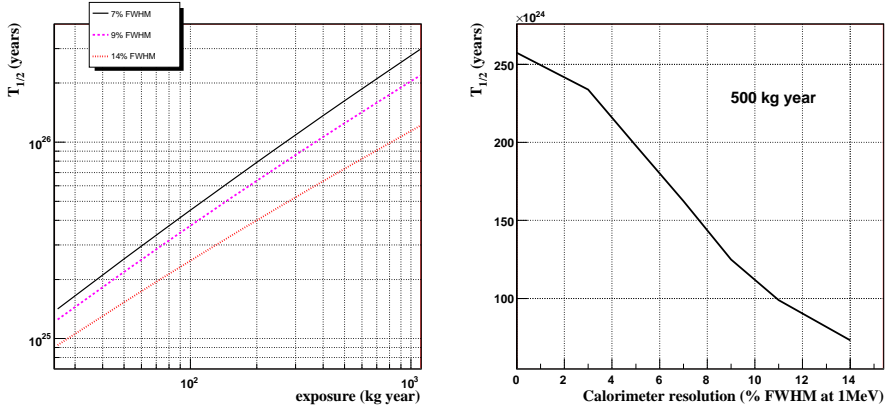


Figure 5.34: Dependence of the sensitivity with calorimeter resolution, assuming ^{82}Se foils and the standard setup. Left: sensitivity to $T_{1/2}^{0\nu}$ at 90% C.L. as a function of exposure, for calorimeter resolutions of 7% (solid line), 9% (dashed line) and 14% FWHM at 1 MeV (dotted line). Right: sensitivity to $T_{1/2}^{0\nu}$ at 90% C.L. as a function of calorimeter resolution, for an exposure of 500 $\text{kg} \cdot \text{year}$.

Dependence with foil thickness

Energy losses within the source have significant contribution to the final detector energy resolution, hence the $\beta\beta^{2\nu}$ background. Thus the foil thickness is an important parameter to optimize. Default choice for SuperNEMO is 40 mg/cm^2 , but one may want to use thinner foils in order to improve energy resolution or, on the contrary, to use thicker ones to increase exposure for a given number of SuperNEMO modules since each one of them would contain a larger amount of isotope mass. Fig. 5.36 shows sensitivity results for ^{82}Se foils of 20, 40, 60 and 80 mg/cm^2 . As expected due to the energy losses, the best sensitivity is obtained for 20 mg/cm^2 foils. One may roughly say that a difference of 20 mg/cm^2 in SuperNEMO foils is equivalent to about 2% of energy resolution.

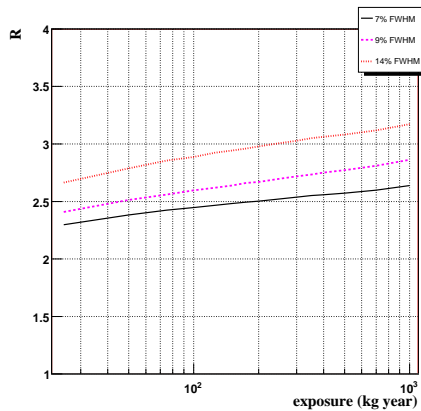


Figure 5.35: R factor for ^{82}Se sensitivity results at 90% C.L. for SuperNEMO standard setup: ^{82}Se foil of 40 mg/cm^2 and magnetic field of 25 Gauss. Solid, dashed and dotted lines show R factor for calorimeter resolutions of 7, 9 and 14% FWHM at 1 MeV, respectively.

Dependence with detection efficiency

Since number of observed $\beta\beta$ events in the experiment depends on the overall reconstruction efficiency, sensitivity to $T_{1/2}^{0\nu}$ also depends strongly on it.

It was shown previously (Sec. 5.4) that final efficiency calculated by SuperNEMO software is dependent on the SuperNEMO module setup. Section 5.4 proves that there is room for limited optimization of the reconstruction code once the tracking layout is fixed. Nevertheless, even assuming 100% efficiency of reconstruction algorithms, it turns out that overall detection efficiency is limited to 51% due to the acceptance of the SuperNEMO standard setup. Consequently, further improvement can only be achieved on the way of optimizing this detector acceptance. Removing the magnetic field and reducing the foil to calorimeter distance are some of the immediate ideas.

Fig. 5.37 shows sensitivity plots as a function of $\epsilon_{\beta\beta}$. As can be seen, sensitivity is limited to $2.5 \times 10^{26} \text{ y}$, since this is the number obtained for detection efficiency of 51% and $500 \text{ kg} \cdot \text{year}$. One has to notice the strong dependence of the sensitivity with the detection efficiency: as an example, an

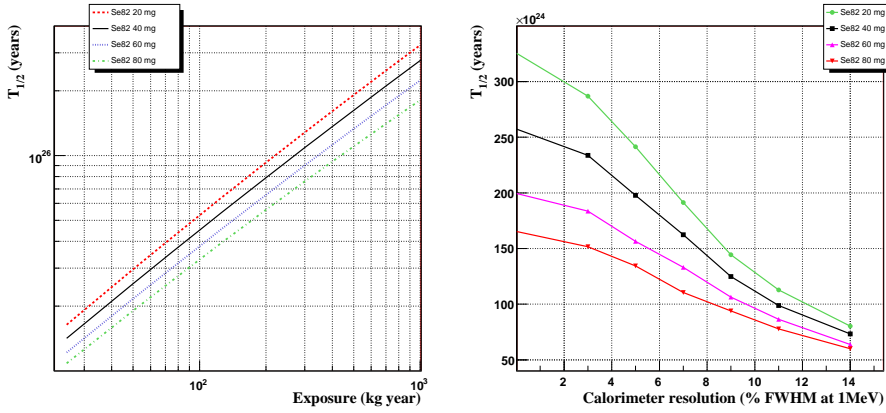


Figure 5.36: Dependence of the sensitivity with the foil thickness, assuming ^{82}Se foils and the standard setup: calorimeter resolution of 7% FWHM at 1MeV and magnetic field of 25 Gauss. Top left: sensitivity to $T_{1/2}^{0\nu}$ at 90% C.L. as a function of exposure, for foils of 20 mg/cm^2 (dashed line), 40 mg/cm^2 (solid line), 60 mg/cm^2 (dotted line) and 80 mg/cm^2 (dot-dashed line). Left: sensitivity to $T_{1/2}^{0\nu}$ at 90% C.L. as a function of calorimeter resolution, for an exposure of $500\text{ kg}\cdot\text{year}$ and foils of 20 mg/cm^2 (dashed line), 40 mg/cm^2 (solid line), 60 mg/cm^2 (dotted line) and 80 mg/cm^2 (dot-dashed line).

experimental setup with 7% of calorimeter resolution and 50% efficiency would yield the same results as one with 1% FWHM and 28% (the current value for SuperNEMO).

To B or not to B: magnetic field effect

Magnetic field is meant to measure the charge of the tracked particles. This allows to reject crossing electrons, but they also can be identified using the time of flight information as explained in 5.5. On the other hand, magnetic field makes the topological acceptance decrease about 5%, as shown in Fig. 5.23, and this leads to a worse sensitivity. Therefore, the need for the magnetic field

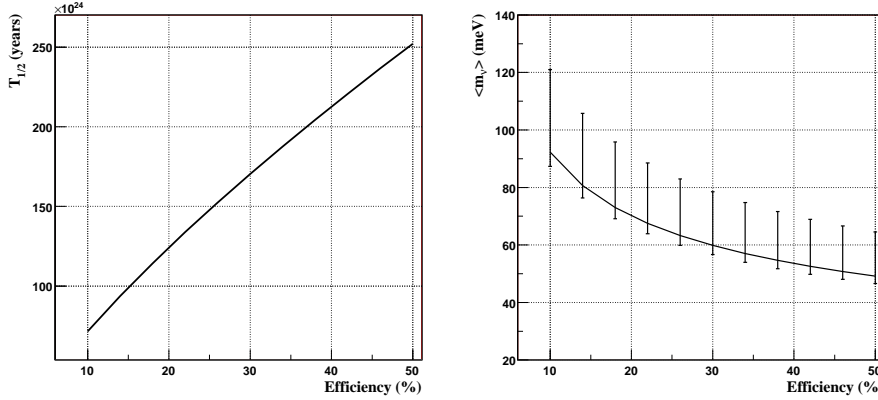


Figure 5.37: Sensitivity plots as a function of detection efficiency, for ^{82}Se and the SuperNEMO standard setup: foils of 40 mg/cm^2 , calorimeter resolution of 7% FWHM at 1MeV, and magnetic field of 25 Gauss. Left: sensitivity to $T_{1/2}^{0\nu}$ at 90% C.L., as a function of detection efficiency. Right: sensitivity to $\langle m_\nu \rangle$ at 90% C.L. as a function of detection efficiency, when NME value from QRPA model with $g_A = 1.25$ is used. Error bars take into account both QRPA uncertainties and discrepancy between $g_A = 1$ and $g_A = 1.25$ results.

still needs to be discussed.

Fig. 5.38 shows sensitivity plots when no magnetic field is applied in the tracking chamber. For comparison reasons, we also show there results with $B=25$ Gauss. As can be seen, small improvement of the sensitivity is consistent with a detection efficiency increase of about 5%, as derived from Fig. 5.37.

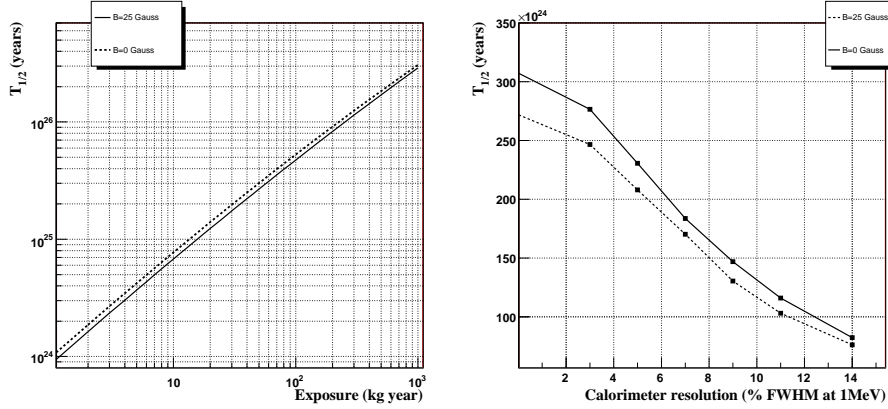


Figure 5.38: Magnetic field impact on the sensitivity, assuming ^{82}Se foils of 40 mg/cm^2 and calorimeter resolution of 7% FWHM at 1MeV. Left: sensitivity to $T_{1/2}^{0\nu}$ at 90% C.L. as a function of exposure for $B = 0$ Gauss (solid line) and $B = 25$ Gauss (dashed line). Left: sensitivity to $T_{1/2}^{0\nu}$ at 90% C.L. as a function of calorimeter resolution for $B = 0$ Gauss (solid line) and $B = 25$ Gauss (dashed line), assuming exposure of 500 kg·year.

Resolution	$T_{1/2}^{0\nu}$ (y)	$\langle m_\nu \rangle$ range (meV)	$\langle m_\nu \rangle$ (QRPA) (meV)
3%	2.3×10^{26}	44-102	51
7%	1.6×10^{26}	53-123	61
9%	1.2×10^{26}	61-141	70
14%	0.7×10^{26}	80-155	91

Table 5.7: Sensitivity result for SuperNEMO best case (no other backgrounds but $\beta\beta^{2\nu}$ one are considered) and various energy resolutions. Third column shows $\langle m_\nu \rangle$ sensitivity range corresponding to upper and lower limits from nuclear models in [52, 101, 104, 105, 106], meanwhile fourth one shows $\langle m_\nu \rangle$ sensitivity according to QRPA model [52]. Results at 90% C.L. for an exposure of 500kg·year. Resolution given in FWHM at 1 MeV.

5.7.4 Internal backgrounds

We consider now internal backgrounds. Recall by internal here we mean impurities inside foil, namely ^{214}Bi and ^{208}Tl isotopes. In the case of ^{82}Se source, both isotopes have an energy release above $Q_{\beta\beta}$ value, therefore they contribute as a background for $\beta\beta^{0\nu}$ decay since their decay may fake a $\beta\beta$ event, as explained in 5.2.

In order to obtain the energy spectra of these backgrounds and the ratio of events that mimic a $\beta\beta$ decay, we simulate ^{214}Bi and ^{208}Tl events and apply to them the same reconstruction algorithms and selection cuts as to the actual $\beta\beta$ events. It has been estimated that about 0.04% of the Bismuth and Thallium decays pass the event selection cuts, after generation of a second electron via one of the mechanisms described in Section 5.2. Regarding the energy distribution of the faked $\beta\beta$ events, Fig. 5.39 shows in arbitrary units the spectra of both kind of backgrounds.

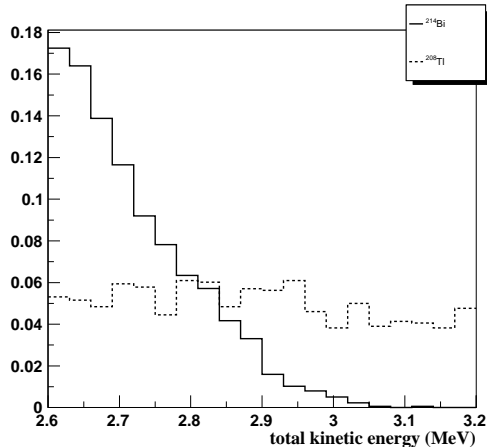


Figure 5.39: Normalized spectra of fake $\beta\beta$ events coming from ^{214}Bi (solid line) and ^{208}Tl (dashed line), for the SuperNEMO standard setup: ^{82}Se foils of 40 mg/cm^2 and calorimeter resolution of 7% FWHM at 1 MeV.

The following analyzes the impact of both ^{214}Bi and ^{208}Tl impurities inside

the foil, with the goal of finding an estimation for the maximum allowed levels of such contaminations.

^{214}Bi internal background

We assume different levels of ^{214}Bi contamination inside the ^{82}Se foils. The worst case is defined by the foil purity measured in the NEMO-3 experiment: 1200 $\mu\text{Bq}/\text{kg}$, as described in Section 5.2. Then we assume different scenarios in which ^{214}Bi impurities may be reduced by factors 10, 100 and 1000 (so background levels of 120, 12 and 1.2 $\mu\text{Bq}/\text{kg}$).

Fig. 5.40 summarizes sensitivity results for these different levels of ^{214}Bi , along with $\beta\beta^{2\nu}$ contribution. Note the fast decrease of sensitivity with worsening energy resolution when bismuth pollution is not too high. This accounts for exponential behaviour of the ^{214}Bi energy spectrum, as in the $\beta\beta^{2\nu}$ case (Fig. 5.39). On the other hand, for high values of bismuth contamination (120 and 1200 $\mu\text{Bq}/\text{kg}$), dependence with calorimeter resolution almost disappears. The impact of ^{214}Bi background can also be seen in Fig. 5.41, where the R factor is shown for the same levels of ^{214}Bi : the experiment becomes background dominated very rapidly as the exposure is increased.

From Fig. 5.40, one can conclude that a reduction of at least a factor 100 is needed with respect to ^{214}Bi levels in NEMO-3 ^{82}Se foil, in order to have a competitive SuperNEMO experiment. It would be a factor 1000 to make ^{214}Bi background negligible. It is also obvious that SuperNEMO cannot tolerate 1200 $\mu\text{Bq}/\text{kg}$ of bismuth contamination, since under these conditions it does not offer almost any improvement with respect to NEMO-3. As an example, notice that for 1 $\text{kg} \cdot \text{year}$ and a background of 1200 $\mu\text{Bq}/\text{kg}$ of ^{214}Bi , one obtains a limit of $T_{1/2}^{0\nu} = 5 \times 10^{23}\text{y}$. As presented in 5.2, NEMO published value is $T_{1/2}^{0\nu} = 1.0 \times 10^{23}\text{y}$. The small improvement in this value is due to the better calorimeter resolution (7% instead of 14%) and the higher detection efficiency (28% instead of 8%).

It is very difficult to set any criteria on the concrete desired limit of ^{214}Bi or any other impurities. A complex balance between the experiment goal, technical possibility and price should be achieved. It is beyond the scope of this work to discuss any of such criteria here. However, a rough number can be inferred from the following considerations.

First, one can assume that any desired purity level can be reached and then wonder which level of background would make the sensitivity decrease by 10%. It has been estimated that such a level is $\sim 4 \mu\text{Bq}/\text{kg}$.

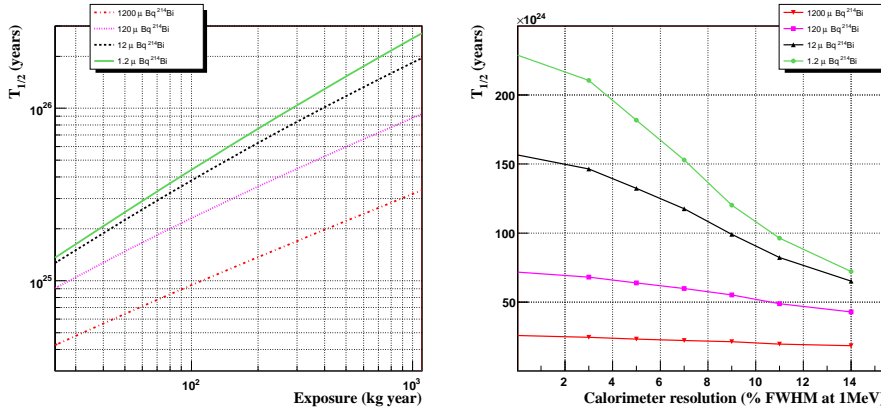


Figure 5.40: Sensitivity plots for various levels of ^{214}Bi , assuming ^{82}Se foils and the SuperNEMO standard setup. Left: sensitivity to $T_{1/2}^{0\nu}$ at 90% C.L. as a function exposure, for 1.2 $\mu\text{Bq}/\text{kg}$ (solid line), 12 $\mu\text{Bq}/\text{kg}$ (dashed line), 120 $\mu\text{Bq}/\text{kg}$ (dotted line) and 1200 $\mu\text{Bq}/\text{kg}$ (dot-dashed line) of ^{214}Bi . Right: sensitivity to $T_{1/2}^{0\nu}$ as a function of calorimeter resolution for for 1.2 $\mu\text{Bq}/\text{kg}$ (circles), 12 $\mu\text{Bq}/\text{kg}$ (triangles), 120 $\mu\text{Bq}/\text{kg}$ (squares) and 1200 $\mu\text{Bq}/\text{kg}$ (inverted triangles) of ^{214}Bi .

Second, one can look on the R factor (Fig. 5.35) in order to make the comparison between ^{214}Bi and $\beta\beta^{2\nu}$ backgrounds. Remember that R factor represents the level of background in the experiment. If R for ^{214}Bi plus $\beta\beta^{2\nu}$ is equal to doubled background due to $\beta\beta^{2\nu}$ only (in other words, to the value of R at the twice bigger exposure (1000 kg · year)), then ^{214}Bi background is comparable with the one from $\beta\beta^{2\nu}$. This happens when ^{214}Bi level is about 4 $\mu\text{Bq}/\text{kg}$.

A third criterion to set the maximum desired level of contamination may be the goal of reaching sensitivity values below 100 meV for $\langle m_\nu \rangle$. As shown in Fig. 3.7, sensitivities better than 100 meV would allow to cover almost completely the degenerate region of neutrino masses. For ^{82}Se sources, this means to reach at least values for the half-life of about 10^{26} years, as proved in Fig. 5.29. Under this criterion, it seems quite obvious from Fig. 5.40 that for levels above 120 $\mu\text{Bq}/\text{kg}$ of ^{214}Bi , sensitivity of SuperNEMO would be spoiled, while 12

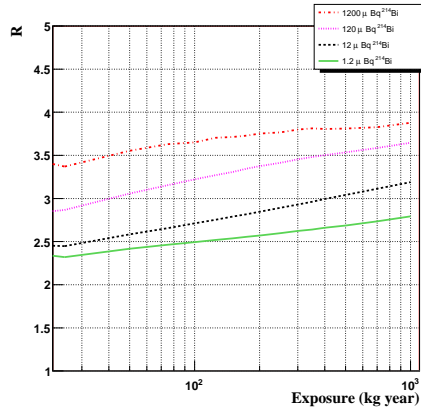


Figure 5.41: R factor for ^{82}Se sensitivity results at 90% C.L. and various levels of ^{214}Bi , assuming SuperNEMO standard setup. Solid, dashed, dotted and dot-dashed lines show R factor for 1.2, 12, 120 and 1200 $\mu\text{Bq}/\text{kg}$ of ^{214}Bi , respectively.

$\mu\text{Bq}/\text{kg}$ would be still tolerable.

Since the feasibility of reducing foil impurities of ^{214}Bi down to 1.2 $\mu\text{Bq}/\text{kg}$ (where this background is almost negligible) seems to be quite difficult, SuperNEMO collaboration takes the conservative value of 10 $\mu\text{Bq}/\text{kg}$ for Bismuth contamination, as the desired or target value of the SuperNEMO experiment. The corresponding $T_{1/2}^{0\nu}$ sensitivity is $1.22 \times 10^{26} \text{ y}$ for 500 $\text{kg} \cdot \text{year}$.

^{208}Tl internal background

A similar study can be done regarding the ^{208}Tl internal background. As said in Section 5.2, it was found in NEMO-3 that ^{208}Tl activity inside ^{82}Se foil is 300 $\mu\text{Bq}/\text{kg}$. Therefore, we take this value as the worst case for SuperNEMO. Then we study SuperNEMO sensitivities corresponding to purity improvements of factors 10, 100 and 1000 (so background levels of 30, 3 and 0.3 $\mu\text{Bq}/\text{kg}$). It has been set that SuperNEMO target is to reach 2 $\mu\text{Bq}/\text{kg}$.

Fig. 5.42 shows sensitivity results for the above ^{208}Tl activity levels (together with $\beta\beta^{2\nu}$ background), while Fig. 5.43 shows the corresponding R factor. Ex-

periment is background dominated for $300 \mu\text{Bq}/\text{kg}$ of ^{208}Tl even with small exposures.

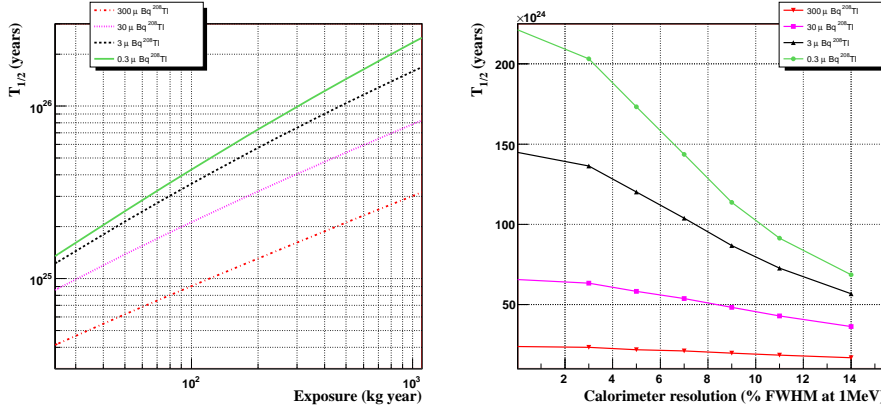


Figure 5.42: Sensitivity plots for various levels of ^{208}Tl , assuming ^{82}Se foils and the SuperNEMO standard setup. Left: sensitivity to $T_{1/2}^{0\nu}$ at 90% C.L. as a function exposure, for $0.3 \mu\text{Bq}/\text{kg}$ (solid line), $3 \mu\text{Bq}/\text{kg}$ (dashed line), $30 \mu\text{Bq}/\text{kg}$ (dotted line) and $300 \mu\text{Bq}/\text{kg}$ (dot-dashed line) of ^{208}Tl . Right: sensitivity to $T_{1/2}^{0\nu}$ at 90% C.L. as a function calorimeter resolution, for $0.3 \mu\text{Bq}/\text{kg}$ (circles), $3 \mu\text{Bq}/\text{kg}$ (triangles), $30 \mu\text{Bq}/\text{kg}$ (squares) and $300 \mu\text{Bq}/\text{kg}$ (inverted triangles) of ^{208}Tl .

As for the ^{214}Bi case, it seems obvious from Fig. 5.42 that a reduction of factor 100 in the levels of ^{208}Tl with respect to NEMO-3 is needed in order to achieve a competitive SuperNEMO sensitivity. A reduction of factor 1000 is necessary to make ^{208}Tl background almost negligible. Again, SuperNEMO is out of the game if one assumes a ^{208}Tl contamination level of $300 \mu\text{Bq}/\text{kg}$ (NEMO-3 value): for such a level of background and $1 \text{ kg} \cdot \text{year}$ of exposure, sensitivity limit is $T_{1/2}^{0\nu} = 4.7 \times 10^{23}$ years. The improvement with respect to NEMO-3 result (1.0×10^{23} y [96]) is poor.

From Fig. 5.42, where the sensitivity values for the various levels of ^{208}Tl contamination are presented, is inferred that the $0.5 \mu\text{Bq}/\text{kg}$ impurity of ^{208}Tl

would reduce the $T_{1/2}^{0\nu}$ sensitivity by 10% compared with the case of only $\beta\beta^{2\nu}$ background. Analyzing also Fig. 5.43, which shows R factor for different values of ^{208}Tl background, one can say that SuperNEMO can tolerate up to 2 $\mu\text{Bq}/\text{kg}$ of ^{208}Tl .

Applying the same kind of criteria as for the Bismuth background, it has been accepted by the SuperNEMO collaboration that the target for ^{208}Tl internal contamination is 2 $\mu\text{Bq}/\text{kg}$. This value would reduce $T_{1/2}^{0\nu}$ sensitivity down to 1.15×10^{26} years.

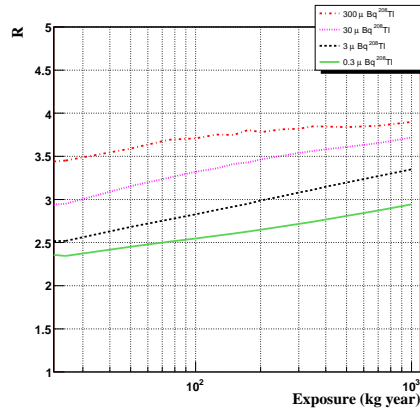


Figure 5.43: R factor for ^{82}Se sensitivity results at 90% C.L. and various levels of ^{208}Tl , assuming SuperNEMO standard setup. Solid, dashed, dotted and dot-dashed lines show R factor for 0.3, 3, 30 and 300 $\mu\text{Bq}/\text{kg}$ of ^{208}Tl , respectively.

5.7.5 Sensitivity for overall internal background

According to previous section, SuperNEMO goals for ^{214}Bi and ^{208}Tl impurities inside the source are to reach levels of 10 $\mu\text{Bq}/\text{kg}$ and 2 $\mu\text{Bq}/\text{kg}$, respectively. Under these conditions, Fig. 5.44 shows the expected spectra for the various backgrounds analyzed and a simulation of the expected number of events in the SuperNEMO detector for an exposure of 500 $\text{kg} \cdot \text{year}$. Sensitivity limits for

such an experiment are shown in Fig. 5.45. For $500 \text{ kg} \cdot \text{year}$ of exposure, the sensitivity limits are shown in Table 5.8.

Resolution	$T_{1/2}^{0\nu}$ (y)	$\langle m_\nu \rangle$ range (meV)	$\langle m_\nu \rangle$ (QRPA) (meV)
7%	1.0×10^{26}	67-154	78

Table 5.8: Sensitivity result for $10 \mu\text{Bq}/\text{kg}$ and $2 \mu\text{Bq}/\text{kg}$ of ^{214}Bi and ^{208}Tl internal contamination, respectively. Third column shows $\langle m_\nu \rangle$ sensitivity range corresponding to upper and lower limits from nuclear models in [52, 101, 104, 105, 106], meanwhile fourth one shows $\langle m_\nu \rangle$ sensitivity according to QRPA model [52]. Results at 90% C.L., for $500 \text{ kg} \cdot \text{year}$. Resolution given in FWHM at 1 MeV.

Fig. 5.46 shows also R factor for the levels of background described above. For $500 \text{ kg} \cdot \text{year}$, R is now about 3.3, while it was only 2.7 for only $\beta\beta^{2\nu}$ background.

Source thickness influences also the level of radioactive background. The biggest effect is observed for the surface pollution: it is directly proportional to the thickness and it will be discussed in Section 5.7.6, since it comes from an external background (^{222}Rn). In addition, there is small influence on the background from internal pollution. For instance, the Compton scattering probability is larger in the thick foil and so on.

On Fig. 5.47 sensitivity results for different foil thickness can be seen, when surface pollution is considered to be negligible. It is clear from the plot that foil thickness has significant influence on the SuperNEMO sensitivity. For instance, one can achieve the sensitivity to $T_{1/2}^{0\nu}$ of 0.7×10^{26} years with either $500 \text{ kg} \cdot \text{year}$ of data using $80 \text{ mg}/\text{cm}^2$ or $300 \text{ kg} \cdot \text{year}$ of data using $40 \text{ mg}/\text{cm}^2$ foil. In other words, if the size of SuperNEMO is fixed, similar result can be achieved using twice less expensive ^{82}Se isotope but measuring 6 years, instead of 5 (20% longer).

Another important conclusion from this plot is that one can compensate worse calorimeter resolution by decreasing the thickness of the foil. From this plot one can conclude that decreasing foil thickness from $40 \text{ mg}/\text{cm}^2$ to $20 \text{ mg}/\text{cm}^2$ one can compensate resolution loss by $\sim 2\%$ FWHM.

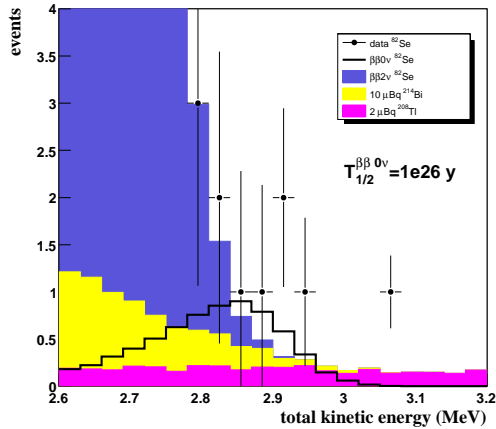


Figure 5.44: Expected spectra after 5 years of running with the SuperNEMO standard setup and radioactivities of $10 \mu\text{Bq}/\text{kg}$ of ^{214}Bi and $2 \mu\text{Bq}/\text{kg}$ of ^{208}Tl . $\beta\beta^{0\nu}$ signal assumes half-life of $T_{1/2}^{0\nu} = 10^{26}$ years. Background spectra are stacked to each other, being the total background histogram overlaid by the signal.

5.7.6 External backgrounds: ^{222}Rn

We consider now the external background coming from Radon gas inside the tracking chamber. As explained in Section 5.2, ^{222}Rn contamination leads to ^{214}Bi impurities placed on the foil surface and therefore to an extra source of background. We assume that other sources of external background (^{214}Bi and ^{208}Tl impurities in detector materials and external neutrinos and gammas) are negligible thanks to the tracking device and the detector shield.

Current Rn level in the NEMO 3 detector corresponds to $\sim 5 \text{ mBq}/\text{m}^3$ [108]. It has been estimated that, for the $40 \text{ mg}/\text{cm}^2$ foil thickness, this will correspond to ^{214}Bi surface contamination of $\sim 400 \mu\text{Bq}/\text{kg}$. This value has to be *added* to the internal bismuth contamination in order to get the total amount of ^{214}Bi background. Considering SuperNEMO targets for foil impurities ($10 \mu\text{Bq}/\text{kg}$ and $2 \mu\text{Bq}/\text{kg}$ of ^{214}Bi and ^{208}Tl , respectively) defined in previous section, total bismuth contamination would be $10+400=410 \mu\text{Bq}/\text{kg}$. It is clear from

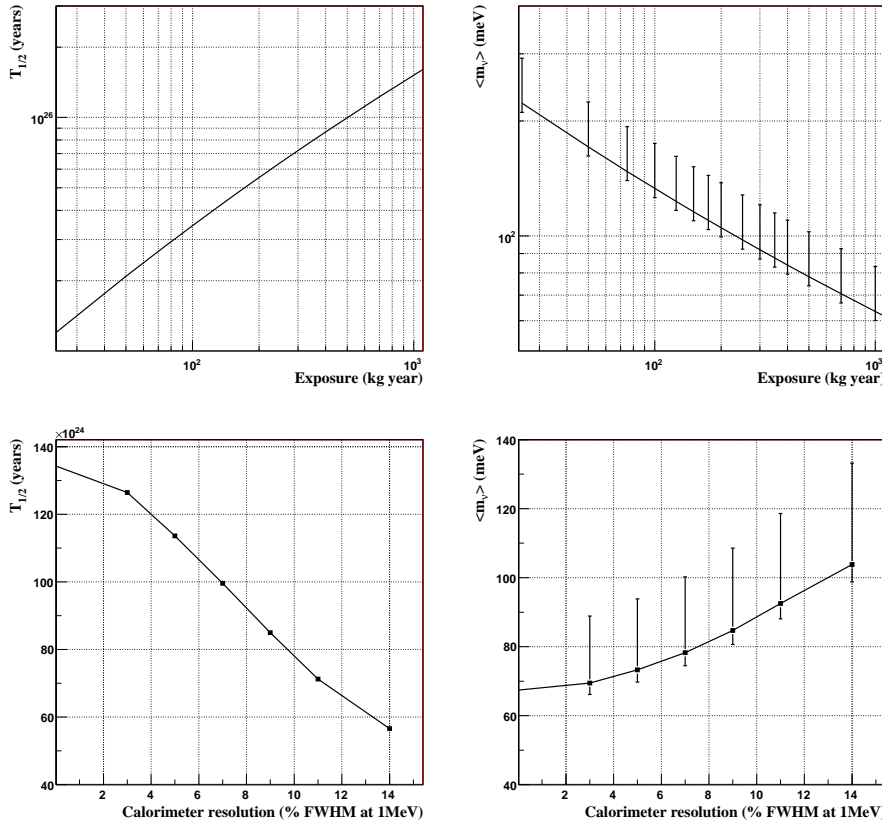


Figure 5.45: Sensitivity plots for $10 \mu\text{Bq}/\text{kg}$ of ^{214}Bi and $2 \mu\text{Bq}/\text{kg}$ of ^{208}Tl , assuming ^{82}Se foils and the standard setup: ^{82}Se foils of $40 \text{ mg}/\text{cm}^2$ and calorimeter resolution of 7% FWHM at 1 MeV. Top left: sensitivity to $T_{1/2}^{0\nu}$ at 90% C.L. as a function of exposure. Top right: sensitivity to $\langle m_\nu \rangle$ at 90% C.L. as a function of exposure. Bottom left: sensitivity to $T_{1/2}^{0\nu}$ at 90% C.L. as a function of calorimeter resolution, for an exposure of $500 \text{ kg} \cdot \text{year}$. Bottom right: sensitivity to $\langle m_\nu \rangle$ at 90% C.L. as a function of calorimeter resolution, for an exposure of $500 \text{ kg} \cdot \text{year}$. Error bars take into account both QRPA uncertainties and discrepancy between $g_A = 1$ and $g_A = 1.25$ results.

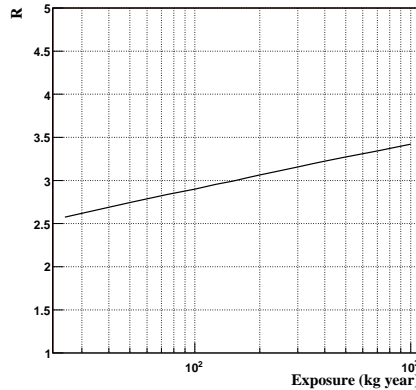


Figure 5.46: R factor for ^{82}Se sensitivity results at 90% C.L. assuming internal background of $10 \mu\text{Bq}/\text{kg}$ of ^{214}Bi and $2 \mu\text{Bq}/\text{kg}$ of ^{208}Tl and the SuperNEMO standard design.

figures 5.40 and 5.45 that such a level of background would spoil SuperNEMO sensitivity. Therefore, one can conclude that success of SuperNEMO experiment relies on a reduction of the Radon levels observed in NEMO-3 detector.

It is believed that main source of Rn in the NEMO-3 is degassing of photo-multipliers. However, we know from the NEMO-3 experience that eliminating one source of Radon will reveal another, which was not seen before. As an example, introduction of an anti-Radon factory in the NEMO-3 experiment lowered Rn level by factor of 6 only, instead of the expected factor 100. Therefore, one may take the conservative assumption of a factor 10 reduction in the Radon level, with respect to NEMO-3, for the SuperNEMO experiment. This corresponds to ^{214}Bi surface contamination of $40 \mu\text{Bq}/\text{kg}$ for $40 \text{ mg}/\text{cm}^2$ foils. Thus, total ^{214}Bi contamination is $10+40 = 50 \mu\text{Bq}/\text{kg}$. Corresponding $T_{1/2}^{0\nu}$ sensitivity is $0.75 \times 10^{26} \text{ y}$.

One can then imagine the following scenario for SuperNEMO: calorimeter resolution of 7% FWHM at 1 MeV, internal impurities of $10 \mu\text{Bq}/\text{kg}$ for ^{214}Bi and $2 \mu\text{Bq}/\text{kg}$ for ^{208}Tl , and surface pollution of ^{214}Bi due to Radon presence. Obviously, ^{214}Bi surface contamination per kg will be different depending on the foil thickness (the thicker the foil, the smaller the surface for a given mass of isotope). For $0.5 \text{ mBq}/\text{m}^3$ of ^{222}Rn inside the tracking chamber, it has been

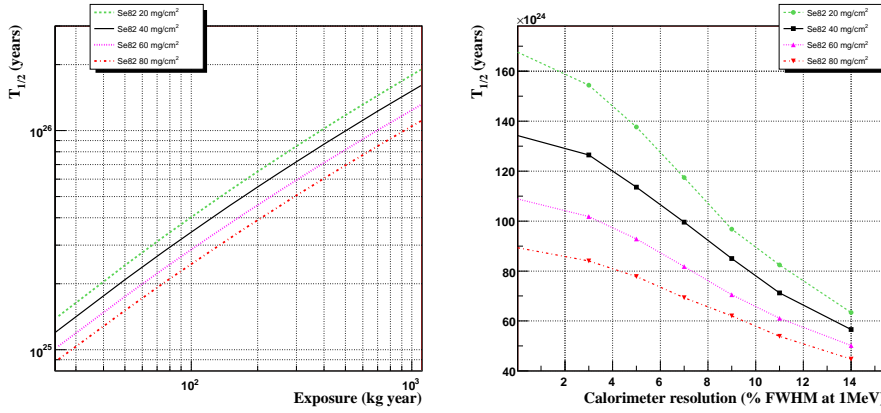


Figure 5.47: Dependence of the sensitivity with the foil thickness, assuming ^{82}Se foils, standard setup and contaminations 2 $\mu\text{Bq}/\text{kg}$ for ^{214}Bi and 10 $\mu\text{Bq}/\text{kg}$ for ^{208}Tl . Left: sensitivity to $T_{1/2}^{0\nu}$ at 90% C.L. as a function of exposure, for foils of 20 (circles), 40 (squares), 60 (triangles) and 80 (inverted triangles) mg/cm^2 thickness. Right: sensitivity to $T_{1/2}^{0\nu}$ at 90% C.L. as a function of calorimeter resolution, for an exposure of 500 $\text{kg} \cdot \text{year}$.

estimated that ^{214}Bi surface pollutions are 80, 40, 27 and 20 $\mu\text{Bq}/\text{kg}$ for the foil thicknesses of 20, 40, 60 and 80 mg/cm^2 , respectively.

On Fig. 5.48 results for this Radon scenario are shown. Obviously, in this case 20 mg/cm^2 foil has a poor performance due to huge surface background (not better than 40 mg/cm^2 foil).

To conclude, we stress the fact that foil thickness choice is totally dependent on the Radon background targets in the SuperNEMO experiment. Thinner foils help to reduce $\beta\beta^{2\nu}$ background but increase the contribution from surface contamination, which has to be controlled by some other means. To have negligible levels of contamination due to ^{222}Rn , NEMO-3 Radon levels need to be reduced by a factor 100.

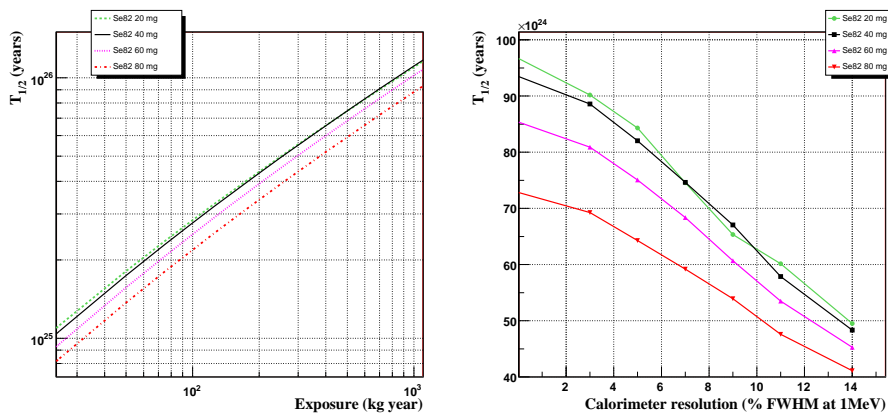


Figure 5.48: Dependence of the sensitivity with the foil thickness, assuming ^{82}Se foils, standard setup, internal contaminations 10 $\mu\text{Bq}/\text{kg}$ for ^{214}Bi and 2 $\mu\text{Bq}/\text{kg}$ for ^{208}Tl and surface contamination of ^{214}Bi . Left: sensitivity to $T_{1/2}^{0\nu}$ at 90% C.L. as a function of exposure at 7% calorimeter resolution, for foils of 20, 40, 60 and 80 mg/cm^2 . Right: sensitivity to $T_{1/2}^{0\nu}$ at 90% C.L. as a function of calorimeter resolution, for an exposure of 500 $\text{kg} \cdot \text{year}$.

5.7.7 Physics case of ^{150}Nd

So far, ^{150}Nd is considered as one of the possible $\beta\beta$ sources for the SuperNEMO experiment. In the current section, we carry out a similar study to the one presented for the ^{82}Se case: we analyze the dependence of the sensitivity with exposure, calorimeter resolution, internal backgrounds and foil thickness. However, we stress again the fact that ^{150}Nd foils suffer from a set of uncertainties (both theoretical and technical) that make them not to be a reliable choice for the SuperNEMO experiment. Further studies are needed in order to treat ^{150}Nd as an actual possibility for SuperNEMO. We recall the open technical issues regarding ^{150}Nd , which have been already pointed out in Section 5.3.3:

- it is not known if it can be enriched in large quantities,
- it is not known which purity can be achieved regarding ^{208}Tl background,
- production cost may be unaffordable.

In addition, the theoretical uncertainties in the estimation of the NME for ^{150}Nd play a major role, since different models yield quite different results. We remind that ^{150}Nd is a rather deformed nucleus and models typically do not take into account this fact. On the other hand, the major clear advantage of ^{150}Nd is its high $Q_{\beta\beta}$ (3.67 MeV): it is above Q_β of ^{214}Bi decay, and therefore this isotope is not a background when searching for the $\beta\beta^{0\nu}$ decay in this isotope.

In the current section, the SuperNEMO standard design as defined in 5.3 is assumed, as it was done for the ^{82}Se analysis. For this given setup, one has to notice that, since ^{150}Nd has a higher $Q_{\beta\beta}$, a slightly higher detection efficiency for the $\beta\beta$ process is obtained. It is 29.5% in comparison with 28% for $\beta\beta^{0\nu}$ decay of ^{82}Se . As described above, we only consider internal background from Thallium impurities, since Bismuth energy spectrum does not overlap the expected signal for the $\beta\beta^{0\nu}$ decay. Fig. 5.49 shows in arbitrary units the yields for the $\beta\beta^{0\nu}$ and $\beta\beta^{2\nu}$ decays, along with the ^{208}Tl decay events faking $\beta\beta$ ones, when a ^{150}Nd foil is used.

The $\beta\beta^{2\nu}$ background

The major disadvantage of ^{150}Nd with respect to ^{82}Se is its much faster rate of $\beta\beta^{2\nu}$ decay. Its half-life (Eq. 5.20) is 10 times smaller than ^{82}Se $T_{1/2}^{2\nu}$. That means that the ratio between $\beta\beta^{0\nu}$ and $\beta\beta^{2\nu}$ expected events is smaller, and

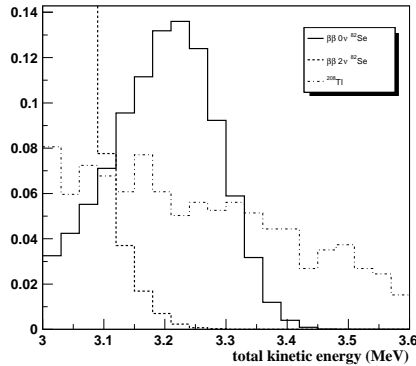


Figure 5.49: Energy spectra in arbitrary units for ^{150}Nd foils of 40 mg/cm^2 and calorimeter resolution of 7% FWHM at 1 MeV.

therefore the $\beta\beta^{2\nu}$ background becomes more important than in the ^{82}Se case. As can be seen in top left plot of Fig. 5.50, sensitivity to $T_{1/2}^{0\nu}$ at 90% C.L. is $8 \times 10^{25}\text{y}$ for $500 \text{ kg} \cdot \text{year}$, so the result is worse than for ^{82}Se . However, if one relies on QRPA values of the NME [52], the sensitivity to $\langle m_\nu \rangle$ is better than the one for ^{82}Se : 27 meV at 90% C.L., for $500 \text{ kg} \cdot \text{year}$, as presented in the top right plot of the same figure. R factor in Fig. 5.51 shows how much higher is the $\beta\beta^{2\nu}$ background for ^{150}Nd foils, with respect to the ^{82}Se ones. As explained in the previous section, this kind of background can only be reduced by means of calorimeter resolution. Bottom plots in Fig. 5.50 show the sensitivity dependence with the resolution.

Internal backgrounds

We consider now backgrounds coming from impurities inside the foil. As previously said, in the case of ^{150}Nd foils, ^{214}Bi isotope does not contribute as a background for $\beta\beta^{0\nu}$ decay. This is considered as a big advantage of ^{150}Nd source compared to the ^{82}Se one. On Fig. 5.52 SuperNEMO sensitivity is shown for different levels of ^{208}Tl background. Similar to ^{82}Se case, with $0.5 \mu\text{Bq/kg}$ of ^{208}Tl impurities we found that SuperNEMO sensitivity is 10% lower than the case in which no internal backgrounds are present.

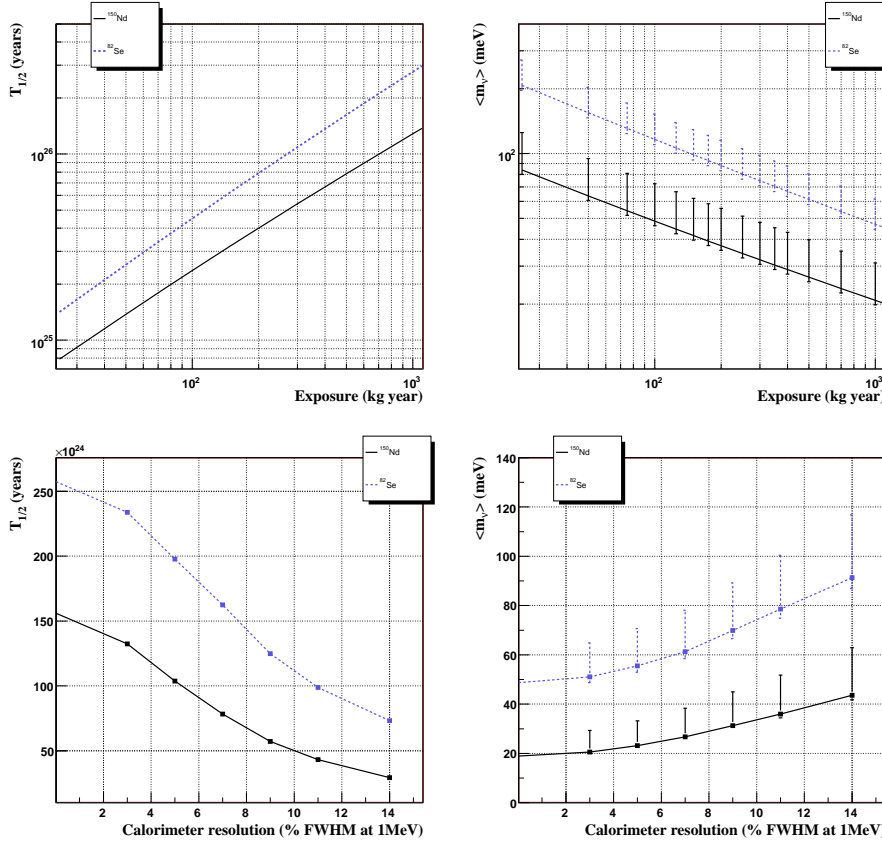


Figure 5.50: Sensitivity plots with only $\beta\beta^{2\nu}$ background, assuming ^{150}Nd foils of 40 mg/cm^2 and magnetic field of 25 Gauss. Top left: sensitivity to $T_{1/2}^{0\nu}$ at 90% C.L. as a function of exposure. Top right: sensitivity to $\langle m_\nu \rangle$ as a function of exposure, according to QRPA model [52]. Bottom left: sensitivity to $T_{1/2}^{0\nu}$ at 90% C.L. as a function of exposure. Bottom right: sensitivity to $\langle m_\nu \rangle$ at 90% C.L. as a function of exposure, according to QRPA model. Error bars take into account both QRPA uncertainties and discrepancy between $g_A = 1$ and $g_A = 1.25$ results. For comparison purposes, results for ^{82}Se foils of 40 mg/cm^2 are shown in dashed line.

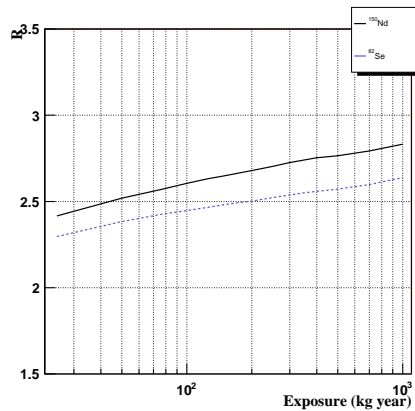


Figure 5.51: R factor for ^{150}Nd sensitivity results at 90% C.L. , assuming calorimeter resolution of 7% FWHM at 1 MeV and foil thickness of 40 mg/cm^2 . For comparison purposes, R for ^{82}Se foils of 40 mg/cm^2 are also shown in dashed line.

Effect of ^{208}Tl impurities in the R factor can be seen in Fig. 5.53, which shows a clear background saturation above $100 \text{ kg} \cdot \text{year}$ for Thallium levels above $2 \mu\text{Bq/kg}$. Applying the same kind of criteria as used for ^{82}Se foils, we assume the conservative requirement of $2 \mu\text{Bq/kg}$ of ^{208}Tl internal background for the SuperNEMO project in case the ^{150}Nd foils are used. For this level of ^{208}Tl background, SuperNEMO sensitivity to $T_{1/2}^{0\nu}$ is 6×10^{25} years.

Foil thickness

NEMO-3 has demonstrated that the level of Thorium (parent nucleus of ^{208}Tl) concentration in the tracking gas is very small [108]. That means that ^{208}Tl contamination deposited in the foil surface is expected to be negligible and therefore background coming from this isotope is only due to impurities inside the foil. Consequently, ^{208}Tl contamination does not depend on the foil thickness. Dependence of the sensitivity with the foil thickness is quite similar to the one obtained for the ^{82}Se source. Thinner foil allows SuperNEMO to achieve better overall energy resolution. Roughly, every 20 mg/cm^2 is equivalent to 1.5% of calorimeter resolution for thin foils ($\sim 40 \text{ mg/cm}^2$) and to 2% of calorimeter

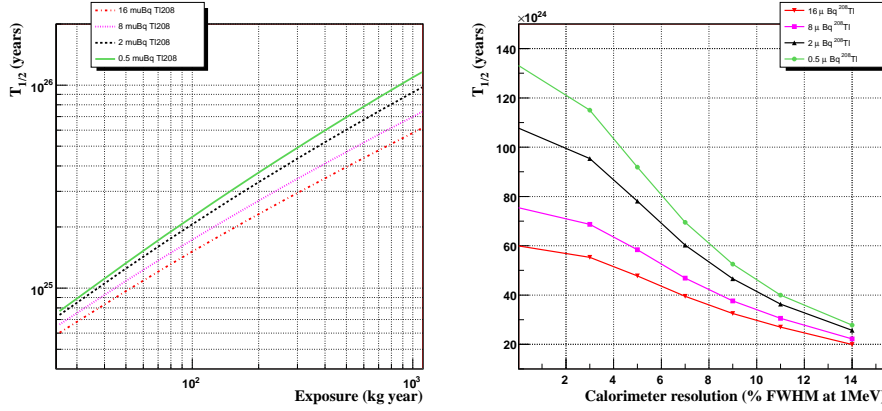


Figure 5.52: Sensitivity plots for various levels of ^{208}Tl , assuming ^{150}Nd foils and the SuperNEMO standard setup: foil of 40 mg/cm^2 , calorimeter resolution of 7% FWHM at 1 MeV and magnetic field of 25 Gauss. Left: sensitivity to $T_{1/2}^{0\nu}$ at 90% C.L. as a function exposure, for $0.5 \mu\text{Bq}/\text{kg}$ (solid line), $2 \mu\text{Bq}/\text{kg}$ (dashed line), $8 \mu\text{Bq}/\text{kg}$ (dotted line) and $16 \mu\text{Bq}/\text{kg}$ (dot-dashed line) of ^{208}Tl . Right: sensitivity to $\langle m_\nu \rangle$ at 90% C.L. as a function of exposure, for $0.5 \mu\text{Bq}/\text{kg}$ (circles), $2 \mu\text{Bq}/\text{kg}$ (triangles), $8 \mu\text{Bq}/\text{kg}$ (squares) and $16 \mu\text{Bq}/\text{kg}$ (inverted triangles).

resolution for thick foils ($\sim 80 \text{ mg/cm}^2$).

Comparison with ^{82}Se results

Fig. 5.54 shows the expected spectra in a SuperNEMO experiment using ^{150}Nd foils, with exposure of $500 \text{ kg} \cdot \text{year}$ and internal contamination inside foils of $2 \mu\text{Bq}/\text{kg}$ of ^{208}Tl . The standard SuperNEMO module is assumed, with a calorimeter resolution of 7% FWHM at 1 MeV. For such an experiment, sensitivities to $T_{1/2}^{0\nu}$ and $\langle m_\nu \rangle$ are shown in Fig. 5.55, together with ^{82}Se results when impurities of $10 \mu\text{Bq}/\text{kg}$ of ^{214}Bi and $2 \mu\text{Bq}/\text{kg}$ of ^{208}Tl are considered. For an exposure of $500 \text{ kg} \cdot \text{year}$, the following values are obtained:

$$T_{1/2}^{0\nu} = 6 \times 10^{25} \text{ y}, \quad \langle m_\nu \rangle = 30 - 132 \text{ meV} \quad (5.38)$$

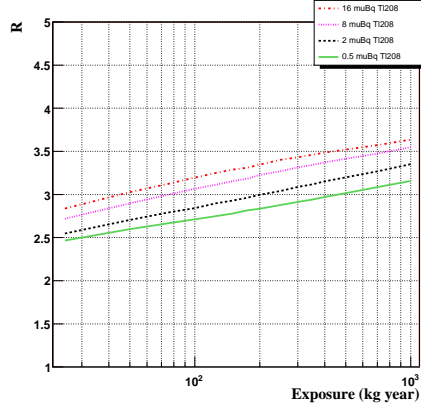


Figure 5.53: R factor for ^{150}Nd sensitivity results at 90% C.L. and various levels of ^{208}Tl , assuming SuperNEMO standard setup: foil of 40 mg/cm^2 and magnetic field of 25 Gauss. Solid, dashed, dotted and dot-dashed lines show R factor for 0.5, 2, 8 and 16 $\mu\text{Bq}/\text{kg}$ of ^{208}Tl , respectively.

where lower and upper limits of $\langle m_\nu \rangle$ correspond to NME from the QRPA model ($g_A=1.25$) and SU(3) model, respectively. As shown previously, ^{82}Se sensitivity to $T_{1/2}^{0\nu}$ (Table 5.8) is better than the ^{150}Nd one due to the bigger importance of the $\beta\beta^{2\nu}$ background in the last one. On the other hand, if NME coming from QRPA model are assumed, sensitivity to $\langle m_\nu \rangle$ is better using ^{150}Nd foils. It may reach 30 meV at 90% C.L., meanwhile it is only 78 meV for the ^{82}Se case.

However, one has to notice the significant differences between models estimating NME for ^{150}Nd , as can be observed in right panel of Fig. 5.55. As example, let's image that ^{150}Nd NME from SU(3) model [106] are the most accurate ones since they take into account nucleus deformation, while the best numbers for ^{82}Se are from QRPA. In this case, ^{82}Se would also provide better results of sensitivity to $\langle m_\nu \rangle$: ^{150}Nd would only reach 101 meV. Sticking to SU(3) numbers for ^{150}Nd , results of this isotope would beat the ^{82}Se ones only in case the SHELL [101] estimations for NME are used.

Summarizing the above discussion, we conclude that in order to consider

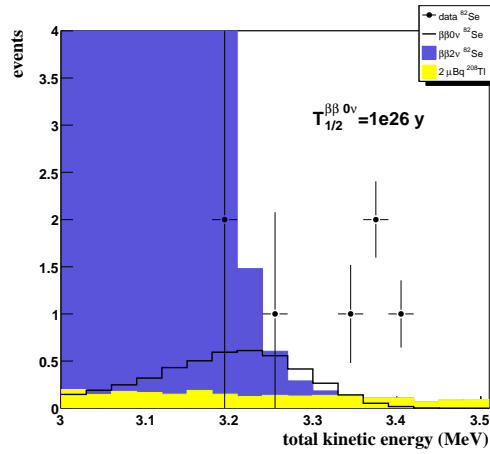


Figure 5.54: Expected spectra for 500 kg·year, running with ^{150}Nd foils and internal contamination of $2 \mu\text{Bq}/\text{kg}$ of ^{208}Tl . $\beta\beta^{0\nu}$ signal (empty histogram) assumes half-life of $T_{1/2}^{0\nu} = 10^{26}$ years.

^{150}Nd as an actual possibility for the SuperNEMO experiment, feasibility of foil production with the required radio-purity, high enrichment, and tolerable cost needs to be demonstrated as a first step. Even if this requirement is fulfilled some day, it turns out that further theoretical studies regarding the NME of ^{150}Nd are also needed in order to decide if it is a better choice than ^{82}Se . Taking into account all these considerations, and based on our current knowledge, the choice of ^{150}Nd foils is a more risky option for the SuperNEMO experiment.

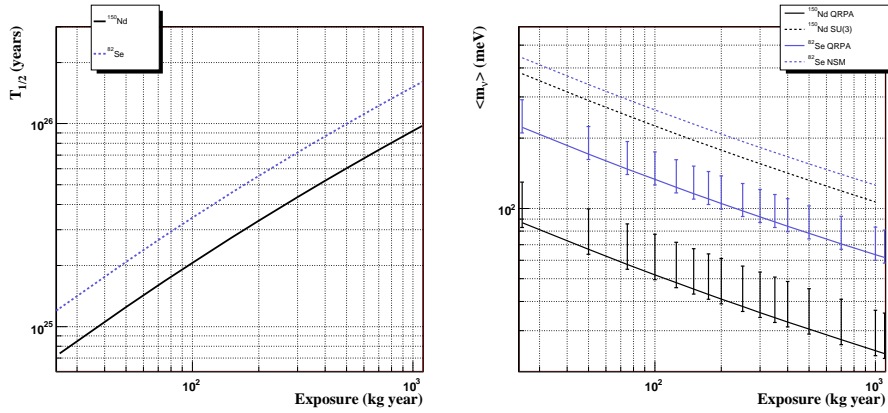


Figure 5.55: Sensitivity plots for ^{150}Nd foils with $2 \mu\text{Bq}/\text{kg}$ of ^{208}Tl of internal background, assuming the standard setup: foil of $40 \text{ mg}/\text{cm}^2$, 30% reconstruction efficiency, and magnetic field of 25 Gauss. Top left: sensitivity to $T_{1/2}^{0\nu}$ at 90% C.L. as a function of exposure. Top right: sensitivity to $\langle m_\nu \rangle$ at 90% C.L. as a function of exposure, according to NME from various models. For comparison purposes, results for ^{82}Se are also shown with grey (blue) lines.

5.7.8 Possible improvements to the standard setup

Along this section, an exhaustive analysis of the SuperNEMO sensitivity depending on several parameters has been described. This study provides information about SuperNEMO expected results for the standard design, but it also points out some experimental issues that may be improved in order to get better sensitivities.

First of all, we have shown the strong dependence of the results with the energy resolution. It is clear that SuperNEMO needs to have the best calorimeter resolution as possible, since this is the only way to reduce $\beta\beta^{2\nu}$ background. However, 7% FWHM at 1 MeV is the limit that can be achieved using the current technology (plastic scintillator coupled to PMT), so further improvements are only possible by means of a different calorimetric techniques (time projection chambers, as an example). The standard calorimeter device projected for the SuperNEMO experiment also has *timing* limitations. In order to compute time of flight of particles (using scintillator hit time), one needs flight distances of at least 50 cm and this forces the tracking chamber to be at least 1 meter wide (50 cm per side of the foil), leading to a really big module size.

Apart from size considerations, it turns out that the standard SuperNEMO module has a really poor acceptance mainly due to the big distance between foil and calorimeter walls (as explained in Section 5.5). It has been proved in Section 5.7 that detection efficiency has also a big impact on the sensitivity, and detection efficiency is dominated by the acceptance. Therefore, a clear way to improve SuperNEMO sensitivity is to optimize module geometry to increase the efficiency. This may be achieved by reducing the size of the module (but then time of flight resolution would suffer) or with a different geometry.

We have shown that magnetic field also reduces detector acceptance by a 5%, and consequently the detection efficiency. Further studies are needed to demonstrate whether magnetic field is needed or not. Although it is true that it provides a handle to reject crossing electrons (external particles crossing the chamber), they may also be identified by means of time of flight. On the other hand, if one assumes a more compact geometry of the SuperNEMO module in which measurement of time of flight is not possible, magnetic field would remain as the only way to veto this kind of background.

Another point that needs to be addressed in further studies is the Radon contamination. As previously said, Radon levels of NEMO-3 have to be reduced by a factor 100 if one wants to make this background negligible in the SuperNEMO experiment. In fact, a factor 10 reduction would lead to really disappointing results. It is not clear yet how to reduce Rn levels inside the de-

tector, but anyway ^{222}Rn is never going to disappear completely, so one needs to optimize the SuperNEMO detector to identify background events coming from ^{214}Bi decays. To do so, the main ideas are to develop good α tagging techniques (recall α comes from a bismuth daughter decay) and to optimize the tracker to achieve a high resolution in vertex reconstruction.

5.8 Summary of SuperNEMO sensitivity results

In this chapter we have described the standard setup of a SuperNEMO module. The whole SuperNEMO experiment consists of 20 modules. For such a setup, a full simulation has been developed. After generating the kinematics of a $\beta\beta$ event (both $\beta\beta^{2\nu}$ and $\beta\beta^{0\nu}$), a vertex is randomly placed in the source and beta particles are propagated inside the detector. Then, tracker and calorimeter response is simulated, so a set of geiger and scintillator hits are obtained for each event.

We have also shown how simulated $\beta\beta$ events are reconstructed. We apply two main algorithms to get reconstructed particles. One of them associates geiger hits from the same Monte Carlo particle and the other fits the whole track, associates it with a calorimeter hit and finds the vertex on the foil surface. Efficiency of particle reconstruction algorithm is high (85%), being the main source of inefficiency the resolution in the first block of geiger layers. Of course, this may be solved by allowing segment sharing between two tracks.

A set of event selection cuts have also been described. In order to ensure the correct identification of the $\beta\beta$ event, we require it to fulfill several conditions. These cuts lead to an extra loss of detection efficiency which has been estimated to be about 27%. This is the unavoidable price to pay if one wants to reject background events as much as possible.

We have shown that overall detection efficiency is about 28% for ^{82}Se foils, and 29.5% for ^{150}Nd ones. This efficiency is the convolution of three factors: topological acceptance of SuperNEMO detector, reconstruction efficiency, and event selection efficiency. It turns out that the overall efficiency is dominated by acceptance, since half of the $\beta\beta$ events are not useful for analysis due to topological reasons. Although reconstruction algorithms may be improved, this would only mean an increase of a few percent in the overall detection efficiency. The actual breakthrough to achieve better efficiency seems to be a different geometry for the SuperNEMO module.

Finally, we have performed a likelihood fit analysis to get SuperNEMO sensitivity to the $T_{1/2}^{0\nu}$ of the $\beta\beta^{0\nu}$ process, assuming the exchange of a light Majorana neutrino. We have studied this sensitivity in terms of several factors (exposure, calorimeter resolution, foil thickness and detection efficiency) and for two different foil sources (^{82}Se and ^{150}Nd). We also have taken into account various kinds of backgrounds. Apart from the intrinsic $\beta\beta^{2\nu}$ background, impurities of ^{214}Bi and ^{208}Tl inside the foil have been considered. We set the foil purity requirements as follows: 10 $\mu\text{Bq}/\text{kg}$ of ^{214}Bi and 2 $\mu\text{Bq}/\text{kg}$ of ^{208}Tl for ^{82}Se foils, and 2 $\mu\text{Bq}/\text{kg}$ of ^{208}Tl for ^{150}Nd . Table 5.9 summarizes the obtained sen-

sitivity values for exposure of $500 \text{ kg} \cdot \text{year}$ (as an example, equivalent to 100 kg of isotope and 5 years run), and 7% FWHM at 1 MeV of energy resolution. One has to keep in mind that the ^{150}Nd foils would only bring better results than ^{82}Se if QRPA values for NME are reliable.

Foil	$T_{1/2}^{0\nu}$ (y)	$\langle m_\nu \rangle$ (meV)	$T_{1/2}^{0\nu}$ (y)	$\langle m_\nu \rangle$ (meV)	$\langle m_\nu \rangle$ (QRPA) (meV)
^{82}Se	1.6×10^{26}	53 - 123	10^{26}	67 - 154	78
^{150}Nd	8×10^{25}	26 - 114	6×10^{25}	30 - 132	30

Table 5.9: Summary of sensitivity values to the $\beta\beta^{0\nu}$ process, for $500 \text{ kg} \cdot \text{year}$ and 7% FWHM at 1 MeV of energy resolution. First column shows used foil; second column shows sensitivity to $T_{1/2}^{0\nu}$ and $\langle m_\nu \rangle$ (lower and upper limits according to different NME models) when no backgrounds but $\beta\beta^{2\nu}$ one are assumed; third one shows sensitivity $T_{1/2}^{0\nu}$ and $\langle m_\nu \rangle$ when ^{214}Bi ($10 \mu\text{Bq}/\text{kg}$) and ^{208}Tl ($2 \mu\text{Bq}/\text{kg}$) impurities are taken into account; Finally, fourth column shows sensitivity to $\langle m_\nu \rangle$ for these levels of background according to QRPA ($g_A=1.25$) values for NME. Other sources of background have not been considered.

We remind that one of the goals of the SuperNEMO experiment is to check Klapdor's claim [4]. The Heidelberg-Moscow experiment claimed a first evidence of neutrino-less double beta decay. According to their results, $T_{1/2}^{0\nu}$ is 1.19×10^{21} in ^{76}Ge and the effective neutrino mass $\langle m_\nu \rangle$ (0.24-0.58) eV (99.73% C.L.). So far this has been, at least, a controversial result. As can be inferred from sensitivity plots (in terms of $\langle m_\nu \rangle$) of section 5.7, SuperNEMO can explore this range of neutrino effective mass with a few $\text{kg} \cdot \text{year}$ of exposure. Let's take $\langle m_\nu \rangle = 240 \text{ meV}$ from Klapdor's claim and ^{82}Se nuclear matrix elements from QRPA values. Then the left plot of Fig. 5.56 shows confidence levels of exclusion of such a $\langle m_\nu \rangle$ value as a function of exposure, according to SuperNEMO results. With only $20 \text{ kg} \cdot \text{year}$ SuperNEMO would exclude Klapdor's claim at 90% C.L. in case no signal is observed. It would be 99% C.L. for $50 \text{ kg} \cdot \text{year}$. On the other hand, if a signal is found for $\langle m_\nu \rangle = 240 \text{ meV}$, then SuperNEMO would be able to measure it with 2.9σ for $25 \text{ kg} \cdot \text{year}$ (5.7σ for $100 \text{ kg} \cdot \text{year}$), as can be seen in right plot of Fig. 5.56.

^{214}Bi contamination on foil surface due to the ^{222}Rn decay chain is an important issue that needs to be addressed in further studies. It is clear from the

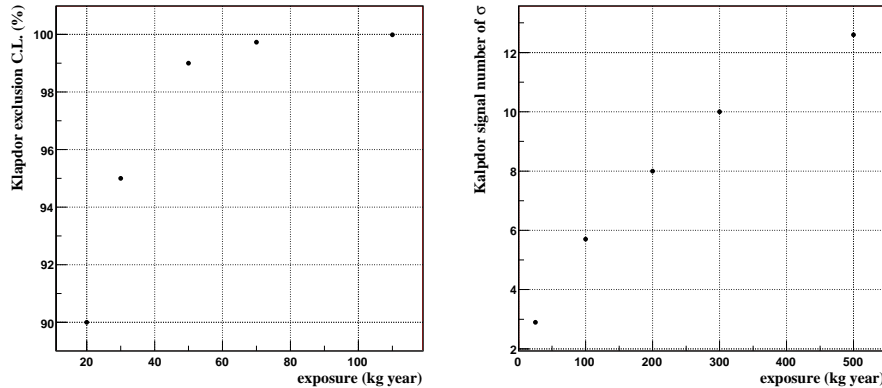


Figure 5.56: Sensitivity of SuperNEMO to Klapdor's claim [4], assuming the standard setup, ^{82}Se foils of 40 mg/cm^2 and calorimeter resolution of 7% FWHM at 1 MeV. Assumed internal background levels are $10 \mu\text{Bq/kg}$ of ^{214}Bi and $2 \mu\text{Bq/kg}$ of ^{208}Tl . Left: confidence level for exclusion of Klapdor's claim, as a function of exposure. Right: number of sigmas for an eventual Klapdor's signal, as a function of exposure.

analysis presented in this work that SuperNEMO sensitivity is spoiled if one takes into account current levels of Radon in NEMO-3 experiment. It has been estimated that a reduction of a factor 100 has to be achieved with respect to this level in order to make this background negligible. It is still not clear how to face this problem.

Improvements to the SuperNEMO sensitivities presented in this chapter are only possible with a different detector setup or with different technology. Sticking to tracker and calorimeter techniques described for the standard setup, the only way to increase the sensitivity is to change the geometry of the SuperNEMO module. The main goal would be to increase the acceptance to the $\beta\beta$ events, since, as it has been proved, it may be as important as achieving better energy resolution.

Chapter 6

Feasibility of the SuperNEMO physics case

In Section 5.7 we have defined the SuperNEMO targets regarding calorimeter resolution and background levels, and sensitivity results for such targets have been presented and analyzed. However, the feasibility of reaching the desired values has not been discussed. The SuperNEMO setup as described in 5.3 and 5.7 is somehow *ideal* and may be very optimistic if one compares the expected values for energy resolution and contamination levels with the values of NEMO-3 experiment. Therefore, we define in this chapter several scenarios for the SuperNEMO experimental setup, from the most pessimistic to the unreal one in which backgrounds are almost negligible. In this context, we describe a realistic set of parameters for the SuperNEMO experiment and present corresponding sensitivity results.

Apart from analyzing the most realistic physics case of SuperNEMO, one also needs to look for possible locations where this experiment can be placed. Canfranc Underground Laboratory (LSC) is an underground scientific facility dedicated to the research in Fundamental Physics, Particle Physics and Astrophysics. A new hall will be ready to hold experiments by 2009, and SuperNEMO proposal has been considered as an attractive possibility for the LSC. In this chapter, we analyze the physics case of SuperNEMO operating at LSC, for the various scenarios defined previously.

All along this chapter we refer to ^{82}Se foils, since it is the most realistic choice according to Sections 5.3.3 and 5.7.7.

6.1 Feasibility of SuperNEMO experimental targets

The SuperNEMO experimental parameters defined in Sections 5.3 and 5.7 have to be treated as the SuperNEMO goals. There are no experimental results proving that the desired energy resolution can be achieved, and the same happens for the radio-purity levels of the foils. In addition, it is still not known how to reduce the Radon levels measured in the NEMO-3 detector. Therefore, one may wonder whether the SuperNEMO targets are realistic or not. The following analyzes this issue and defines various scenarios for the SuperNEMO experimental setup.

Energy resolution

SuperNEMO aims at achieving calorimeter resolution of 7% FWHM at 1 MeV. So far, this value has never been reached with plastic or liquid scintillator. Recall the NEMO-3 calorimeter resolution is 14% FWHM, and since it was built only a few years ago, it is difficult to think of a factor 2 of improvement for the SuperNEMO detector if one sticks to the same technology (plastic scintillator coupled to PMT's). Consequently, 7% seems a quite optimistic approach, whose feasibility has not been demonstrated yet. A resolution of 9% FWHM at 1 MeV may be a more realistic value. Consequently, one can image three different scenarios for the SuperNEMO calorimetric device:

- *demonstrated*: 14% FWHM, so no improvements with respect to NEMO-3,
- *realistic*: resolution of 9% FWHM at 1 MeV is achieved,
- *optimistic*: SuperNEMO target of 7% FWHM at 1 MeV is achieved.

Foil radio-purity

We recall that the levels of ^{214}Bi and ^{208}Tl contamination inside NEMO-3 ^{82}Se foil are $1200 \mu\text{Bq}/\text{kg}$ and $300 \mu\text{Bq}/\text{kg}$, respectively (Eq. 5.3). Nevertheless, in Section 5.7 we have set SuperNEMO radio-purity requirements as:

$$A(^{214}\text{Bi}) = 10 \mu\text{Bq}/\text{kg} \quad (6.1)$$

$$A(^{208}\text{Tl}) = 2 \mu\text{Bq}/\text{kg} \quad (6.2)$$

Thus, SuperNEMO targets for foil internal background imply a reduction of about factor 100 with respect to NEMO-3 values. Again, there is no evidence that one can reduce the backgrounds measured in NEMO-3 by such a factor and therefore we conclude that SuperNEMO radio-purity targets are, at least, optimistic. We believe that an improvement of a factor 10 is a much more realistic assumption. As done for the calorimeter resolution, one can define various scenarios regarding internal contamination:

- *demonstrated*: no improvement with respect to NEMO-3 foil contamination,
- *realistic*: only a factor 10 of internal background reduction is achieved, so ^{214}Bi and ^{208}Tl activities inside ^{82}Se foil are 120 and 30 $\mu\text{Bq}/\text{kg}$, respectively,
- *optimistic*: levels of 10 $\mu\text{Bq}/\text{kg}$ and 2 $\mu\text{Bq}/\text{kg}$ for ^{214}Bi and ^{208}Tl are achieved (as already said, this is the SuperNEMO goal), so there is a reduction of about factor 100 with respect to NEMO-3,
- *unrealistic*: improvement of factor 1000 in radio-purity, so internal background becomes negligible.

^{222}Rn contamination

As described in Section 5.2, the measured level of ^{222}Rn inside the NEMO-3 detector is 5 mBq/m^3 . This value could not be reduced after surrounding the whole detector with an anti-Radon tent and that leads us to think that the main source of radon is degassing of materials inside the tracking chamber. On the other hand, SuperNEMO target regarding Radon contamination is to have at most 0.5 mBq/m^3 (see Section 5.7). How to achieve a reduction of factor 10 in ^{222}Rn level with respect to NEMO-3 is still not known, and therefore it seems one more time a very optimistic approach. We can image four different cases for the SuperNEMO experiment:

- *demonstrated*: same level of ^{222}Rn as in NEMO-3 detector,
- *realistic*: reduction of factor 5 in NEMO-3 ^{222}Rn level,
- *optimistic or SuperNEMO target*: reduction of factor 10 in NEMO-3 ^{222}Rn level,
- *unrealistic*: reduction of factor 100 in NEMO-3 ^{222}Rn level, which becomes negligible.

Possible scenarios for SuperNEMO setup

Combining the above considerations concerning energy resolution and backgrounds, one can build the following SuperNEMO scenarios:

1. *demonstrated or NEMO-like*: no improvement regarding background levels and calorimeter resolution are achieved with respect to NEMO-3. In fact, results are almost independent of calorimeter resolution since the experiment is fully background dominated due to Bismuth and Thallium foil impurities.
2. *realistic*: reduction of factor 10 in foil internal contamination and reduction of factor 5 in ^{222}Rn level inside tracking chamber, with respect to NEMO-3 measured values. Calorimeter resolution of 9% FWHM at 1 MeV, since 7% has been never achieved neither for plastic nor liquid scintillators.
3. *optimistic or SuperNEMO target*: reduction of about a factor 100 in foil internal contamination and reduction of factor 10 in ^{222}Rn level inside tracking chamber, with respect to NEMO-3 measured values. Really good calorimeter resolution for plastic or liquid scintillator: 7% FWHM at 1 MeV.
4. *unrealistic*: reduction of about factor 1000 in foil internal contamination and reduction of factor 100 in ^{222}Rn level inside tracking chamber, with respect to NEMO-3 measured values. Really good calorimeter resolution. Although this means an ideal experiment, it draws the best case scenario in which internal and Radon contaminations are negligible, being the tail of the $\beta\beta^{2\nu}$ spectrum the only background.

Notice that none of these scenarios takes into account external backgrounds other than ^{222}Rn . It is well known from the NEMO-3 experiment that PMTs contain a non-negligible amount of ^{214}Bi and ^{208}Tl impurities, which act as another source of external background. In this analysis we assume that this background can be identified with very high efficiency thanks to the tracking device. In addition, we also assume that external neutrons and gammas are fully stopped in the surrounding shield.

Table 6.1 shows background levels and calorimeter resolution of the four scenarios defined above. Recall the demonstrated scenario corresponds to a NEMO-like setup, in which the only improvement with respect to NEMO-3

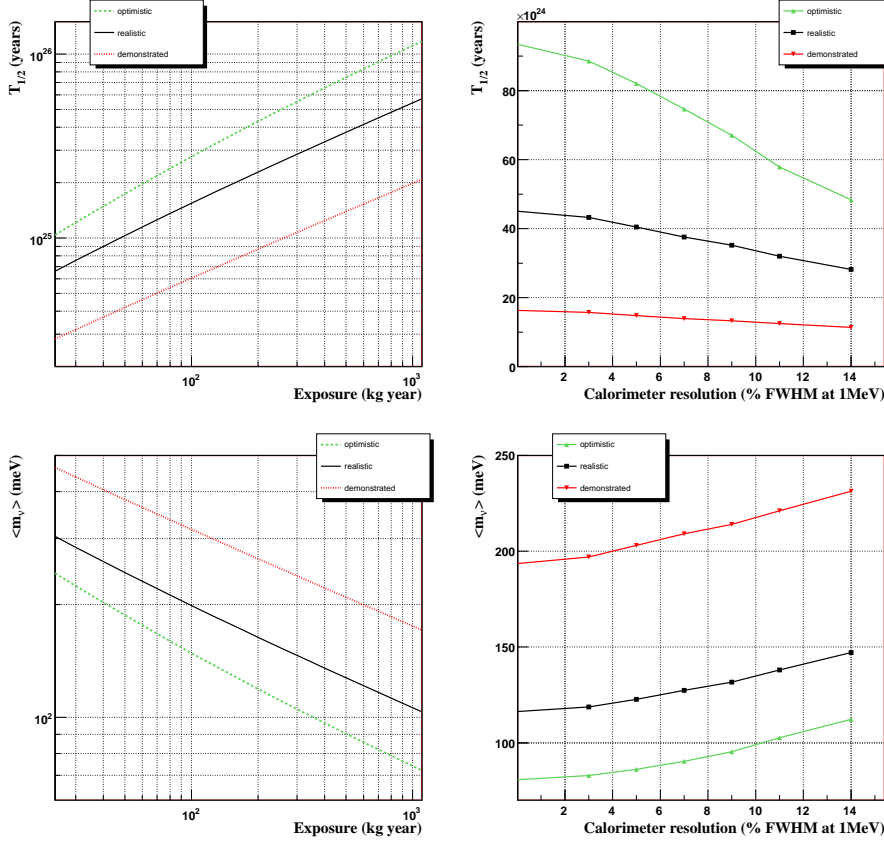


Figure 6.1: Sensitivity plots for the demonstrated, realistic and optimistic scenarios defined in the text, assuming ^{82}Se foils. Top left: sensitivity to $T_{1/2}^{0\nu}$ at 90% C.L. as a function of exposure. Top right: sensitivity to $T_{1/2}^{0\nu}$ at 90% C.L. as a function of calorimeter resolution, for an exposure of 500 kg · year. Bottom left: sensitivity to $\langle m_\nu \rangle$ at 90% C.L. as a function of exposure. Bottom right: sensitivity to $\langle m_\nu \rangle$ at 90% C.L. as a function of calorimeter resolution, for an exposure of 500 kg · year. Results according to QRPA values of NME [52].

experiments comes from a higher detection efficiency (28% instead of 8%) and exposure (up to 500 kg · year).

Fig. 6.1 shows sensitivity results for the demonstrated, realistic and optimistic scenarios. As can be inferred from the analysis presented in Section 5.7, the demonstrated one completely destroys the physics case of SuperNEMO. Table 6.2 summarizes the corresponding sensitivity results for 500 kg · year, in terms of $T_{1/2}^{0\nu}$ and $\langle m_\nu \rangle$ (for both mass ranges according to different nuclear models and value from QRPA). For comparison purposes, we also quote in Table 6.2 an estimation of the NEMO-3 sensitivity for 500 kg · year. Since NEMO-3 operates with only 1 kg · year of ^{82}Se , such an exposure would correspond to a data taking time of 500 years, which of course is impossible to achieve. However, this estimation offers a way to compare NEMO-3 and SuperNEMO experiments.

The physics case of SuperNEMO only starts to have interest for background reductions of a factor 10. The demonstrated (NEMO-like) scenario is out of the game since its sensitivity to $\langle m_\nu \rangle$ is above 200 meV (according to QRPA model), and therefore it is not capable of exploring the quasi-degenerate region of neutrino masses (see 3.3.3). It only offers an improvement of about a factor 3 in sensitivity to $\langle m_\nu \rangle$ with respect to NEMO-3 estimation. Assuming the realistic scenario, it turns out that the SuperNEMO capability of checking Klapdor's claim depends on the nuclear model used to obtain the NME. Even taking the QRPA value, the quasi-degenerate region is not explored completely. On the other hand, the optimistic scenario (SuperNEMO target) yields a really interesting sensitivity, capable of excluding or confirm Klapdor's signal with several sigmas. The point with this scenario is the feasibility of the background reduction assumed with respect to NEMO-3. A factor 100 improvement in foil radio-purity really seems an optimistic approach.

Looking at the R factor for these scenarios (Fig. 6.2) one realizes that the demonstrated one becomes fully background dominated for exposures above 100 kg · year ($R \sim 4$) and consequently sensitivity is not improved significantly by going above this exposure: as an example, for 100 kg · year, the sensitivity is about 300 meV, while multiplying the exposure by 5 (500 kg · year) only yields a sensitivity of about 200 meV.

To analyze the physics case of these SuperNEMO scenarios, it is also useful to compare their results with the NEMO-3 ones. Table 6.3 shows results of the four scenarios for 1.0 kg · year, along with the NEMO-3 published result. Notice that NEMO-3 $\langle m_\nu \rangle$ range is different from the one in Eq. 5.8 since we use different nuclear model references. As can be seen in the table, the demonstrated or NEMO-like scenario shows an improvement of factor 3.6 in sensitivity to $T_{1/2}^{0\nu}$

Scenario	Cal. Res. (FWHM at 1MeV)	^{214}Bi ($\mu\text{Bq/kg}$)	^{208}Tl ($\mu\text{Bq/kg}$)	^{222}Rn ($m\text{Bq}/m^3$)
Demonstrated	14%	1200	300	5
Realistic	9%	120	30	1
Optimistic	7%	10	2	0.5
Unrealistic	7%	1.2	0.3	0.05

Table 6.1: Experimental parameters of the scenarios defined in the text. Demonstrated scenario corresponds to NEMO-3 values, optimistic one to SuperNEMO targets. The unrealistic scenario stands for an ideal experiment with no other background apart from the $\beta\beta^{2\nu}$ one. Calorimeter resolution given in FWHM at 1 MeV.

Scenario	$T_{1/2}^{0\nu}$ (y)	$\langle m_\nu \rangle$ range (meV)	$\langle m_\nu \rangle$ (QRPA) (meV)
Demonstrated	0.11×10^{26}	199-459	231
Realistic	0.35×10^{26}	113-261	132
Optimistic	0.75×10^{26}	78-180	90
Unrealistic	1.26×10^{26}	59-138	70
NEMO-3	0.03×10^{26}	370-852	430

Table 6.2: Sensitivity result for various SuperNEMO scenarios, as defined in the text. An estimation of NEMO-3 sensitivity extrapolated to 500 kg · year is shown in last row. Demonstrated scenario corresponds to NEMO-3 values, while the optimistic one to SuperNEMO targets. The unrealistic scenario stands for an ideal experiment with no other background apart from the $\beta\beta^{2\nu}$ one. The $\langle m_\nu \rangle$ range corresponds to upper and lower limits from nuclear models in [52, 101, 104, 105, 106]. Results at 90% C.L, for 500 kg · year.

with respect to NEMO-3, due to the higher detection efficiency (28% instead of 8%). Optimistic and very optimistic scenarios yield improvements of factors 6.5 and 7.7, respectively.

Scenario	$T_{1/2}^{0\nu}$ (y)	$\langle m_\nu \rangle$ range (meV)	$\langle m_\nu \rangle$ (QRPA) (meV)
Demonstrated	3.6×10^{23}	1121-2582	1301
Realistic	6.5×10^{23}	834-1921	968
Optimistic	7.7×10^{23}	767-1765	890
Unrealistic	8.1×10^{23}	747-1721	867
NEMO-3	1.0×10^{23}	2128-4900	2470

Table 6.3: Sensitivity result for various SuperNEMO scenarios, as defined in the text for for 1 kg · year. NEMO-3 results are quoted in the last row. Demonstrated scenario corresponds to NEMO-3 values, while the optimistic one to SuperNEMO targets. The unrealistic scenario stands for an ideal experiment with no other background apart from the $\beta\beta^{2\nu}$ one. The $\langle m_\nu \rangle$ range corresponds to upper and lower limits from nuclear models in [52, 101, 104, 105, 106]. Results at 90% C.L, for 1 kg · year.

Comparing SuperNEMO expected sensitivity with NEMO-3 results also offers a way to validate the analysis presented in this work. If one assumes the pessimistic scenario (NEMO-like) and a detection efficiency of 8% for the $\beta\beta^{0\nu}$ events (NEMO-3 value), the corresponding sensitivity to $T_{1/2}^{0\nu}$ for 1 kg · year is 10^{23} y (as already shown in Fig. 5.12), recovering thus the value measured in NEMO-3.

6.2 Canfranc Underground Laboratory and BiPo

Canfranc Underground Laboratory (LSC) is an underground scientific facility dedicated to the research in Fundamental Physics, Particle Physics and Astrophysics, since 1985. It is located close to Canfranc (Spain), in the Somport Railway Tunnel which connects Spain and France across Central Pyrenees. The laboratory consists of several old small rooms and a new big experimental hall (since 2007), which is under Tobazo mountain (1980 meters high). The dimensions of this main hall are 40 meters long, 15 m wide (so 600 m²) and 12 m high. Figure 6.3 shows a picture of the main hall at the LSC. The general

characteristics of the laboratory are the following:

- Maximum depth: 2450 m.w.e. (equivalent meters of water) in the main hall.
- Composition of the rock: limestone, calcic carbonate and quartz plans
- Muon flow: $2 \times 10^{-7} \mu/cm^2s$
- Neutron flow: $\sim 10^{-6} n/cm^2s$
- Ambient photon flow: $2 \times 10^{-2} \gamma/cm^2s$
- Radon level: $50 - 100 Bq/m^3$

From 2008, proposals for several experiments will be submitted to the Scientific Advisory Committee of the LSC. The only project which has been already approved to operate at LSC is the BiPo detector, whose description is given below.

The BiPo detector

The aim of the BiPo detector is to measure the radio-purity of ultra thin materials regarding ^{214}Bi and ^{208}Tl contamination, and especially the double beta source foils of the SuperNEMO detector. The expected sensitivity is $A(^{208}\text{Tl}) < 2 \mu\text{Bq/kg}$ and $A(^{214}\text{Bi}) < 10 \mu\text{Bq/kg}$, thus covering the needs of SuperNEMO project, as described in Section 5.7. This detector is already approved by the Scientific Committee of the LSC, and it is conceived as a facility provided by the laboratory to all those projects which need to perform radio-purity measurements down to sensitivity levels that cannot be achieved by the typical Germanium detectors. The R&D phase has started building a modular BiPo prototype. The goal of this prototype is to study the background and particularly the surface contamination of scintillators. A first capsule was installed at the LSC in October 2006, although it has been moved temporally to the Fréjus underground laboratory (LSM). After 10.7 days of measurements, a preliminary upper limit on the surface radiopurity of the tested scintillators of $A(^{208}\text{Tl}) < 60 \mu\text{Bq/m}^2$ (90% C. L.) has been obtained.

In order to measure ^{214}Bi and ^{208}Tl contaminations, the main idea of the BiPo detector is to detect the so-called Bi-Po process, a double detection of an electron followed by a delayed alpha. The ^{214}Bi isotope is nearly a pure β emitter ($Q_\beta = 3.27 \text{ MeV}$) decaying into ^{214}Po , an α emitter with a half-life

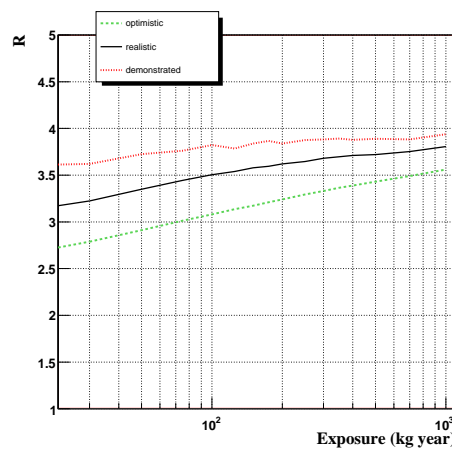


Figure 6.2: R factor as a function of exposure, for the demonstrated (dotted line), realistic (solid line) and optimistic (dashed line) scenarios defined in the text.



Figure 6.3: Main hall at Canfranc Underground Laboratory.

of $164 \mu\text{s}$. The ^{208}Tl isotope is measured by detecting its parent: the ^{212}Bi isotope. ^{212}Bi decays with a branching ratio of 64% via a β emission in ^{212}Po ($Q_\beta = 2.2 \text{ MeV}$) which is again an α emitter with a short half-life of 300 ns. Consequently, the BiPo signature of these two chains is an electron along with a delayed α particle, depending the delay time on the isotope contamination to be measured.

The first BiPo prototype (figure 6.4), consists of 20 low radioactive capsules made with Plexiglas or carbon fibers containing two organic plastic scintillators blocks face-to-face coupled with PMMA optical light guide to 5" low radioactive PMTs. The size of the scintillator blocks are $20 \times 20 \times 1 \text{ cm}^3$. Their entrance surface is covered with 200 nm of ultra-pure aluminum in order to avoid any scintillation light crosstalk. The capsules are filled by pure nitrogen in order to suppress Radon and Thorium contamination. Each capsule is shielded by the test facility consisting of a large tight mechanical structure with 10 cm of low activity lead (20 Bq/kg) and an inner layer of 4 cm of pure iron to suppress bremsstrahlung from the lead shielding.

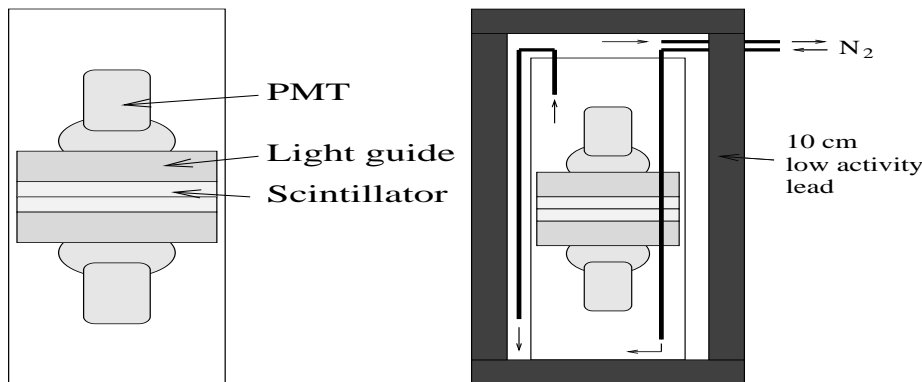


Figure 6.4: Scheme of a capsule of the BiPo-1 prototype and the first capsule with its own shielding in Canfranc.

6.3 Physics case at LSC

The LSC is a new laboratory. Concerning the search for the $\beta\beta^{0\nu}$ process, no commitments have been made yet and ideally, one would like to invest in

an experimental technique that would admit a progressive improvement of the sensitivity, in controlled steps. On a first step one should be able to reach sensitivities to the neutrino effective mass of about 100 meV and thus to confirm or firmly exclude Klapdor's claim. So far, the SuperNEMO project has been considered as an attractive possibility for this laboratory, but now we are in position to quantify the physics case of this experiment operating at LSC.

The first thing to take into account is the available space at LSC. The size of the main hall at LSC is 600 m². While the full SuperNEMO proposal envisions 100 kg of isotope mass (about 20 modules if one considers the standard design defined in this work), the maximum number of modules that the main LSC hall can hold is about 8. If one does not want to use all the available space, 5 or 6 modules seems to be more realistic. Hence we estimate that the SuperNEMO proposal for the LSC would have 1/3 of the total mass. We assume for the current analysis 6 modules containing foils of 5 kg, so total amount of 30 kg.

It is obvious from Sections 5.7 and 6.1 that the physics case of SuperNEMO relies on the radio-purity of the source foils, and consequently one of the main tasks of the R&D program is to figure out the actual value of ²¹⁴Bi and ²⁰⁸Tl activities in a ⁸²Se surface of 12 m². Moreover, one needs to measure the internal contamination of the foils before planning the final size of the SuperNEMO project, as the scalability of the detector strongly depends on the background. Due to all these considerations, the BiPo detector becomes of major importance. A clear first step in the R&D of SuperNEMO is to develop BiPo technology in order to measure foil purity, being this issue much more urgent than the energy resolution improvement.

Regarding radon levels at LSC (50-100 Bq/m³), one has to notice that it is much higher than the one in Fréjus underground laboratory (LSM), where the NEMO-3 detector is placed. Radon level at LSM is about 15 Bq/m³ [96], which means about a factor 3-6 less than the one at LSC. An efficient anti-Radon air system will be needed in order to protect SuperNEMO detector against ²²²Rn infiltration, and thus achieve at least the radon levels observed inside NEMO-3 detector. However, we recall that radon-induced backgrounds are not completely avoided by the so-called *anti-radon factory*: it indeed can reduce by a factor 100 the radon content in the air surrounding the detector (located inside a tent where air is passed by a Radon trap), but reduction is only of a factor 6 for the Radon *inside* the detector itself, as we know from the NEMO-3 experience. As previously described in this work, the reason is most likely degassing of PM tubes and other materials inside the SuperNEMO volume. The gas filling the tracking chamber of the detector is not recirculated and radon is accumulated due to degassing even if the external air has low radon levels. In order to find a

solution to this issue, one could build a first SuperNEMO module with the goal of understanding the Radon-induced background (distribution of background events, level of ^{222}Rn contamination in the gas volume, ...) and testing different techniques to reduce it (recirculation of the tracking gas, alpha tagging from BiPo events, ...).

Concerning overall background levels and calorimeter resolution, we believe that the realistic scenario defined in Section 6.1 is the most likely one meanwhile proofs of the feasibility of SuperNEMO targets do not show up. A NEMO-like scenario also needs to be treated as a possibility for SuperNEMO, since its parameters have been already achieved and do not depend on any assumption. Therefore, to study the physics case at LSC, we consider three sets of parameters for the SuperNEMO experiment: the optimistic SuperNEMO and the realistic targets, along with the demonstrated ones. These scenarios have been defined in Table 6.1.

A data taking time of 5 years seems to be quite reasonable for the SuperNEMO project at the LSC. Assuming 6 SuperNEMO modules holding 30 kg, the corresponding exposure would be 150 kg · year. Notice that for the demonstrated and realistic scenarios, longer times of measurement would not provide much better results since they are background dominated, as can be inferred from figures 6.1 and 6.2. Even assuming the optimistic scenario, doubling the data taking time (10 years and thus 300 kg · year) would only increase the sensitivity from 130 meV to 105 meV.

As a summary of the SuperNEMO case at LSC, we present sensitivity results for 150 kg · year in Table 6.4, where the demonstrated, realistic and optimistic scenarios are taken into account. Fig. 6.5 shows the corresponding expected spectra, assuming the realistic scenario. It turns out that none of the three scenarios are capable of exploring the quasi-degenerate neutrino mass region (see Fig. 3.7) completely. However, sensitivity in all of them would be enough to cover the range of neutrino effective mass quoted by Klapdor's claim.

Scenario	$T_{1/2}^{0\nu}$ (y)	$\langle m_\nu \rangle$ range (meV)	$\langle m_\nu \rangle$ (QRPA) (meV)
Demonstrated	0.62×10^{25}	271-624	314
Realistic	0.18×10^{26}	158-365	184
Optimistic	0.36×10^{26}	112-258	130

Table 6.4: Sensitivity results for the demonstrated, optimistic and very optimistic SuperNEMO scenarios, as defined in the text, operating at LSC. Results at 90% C.L. for $150 \text{ kg} \cdot \text{year}$.

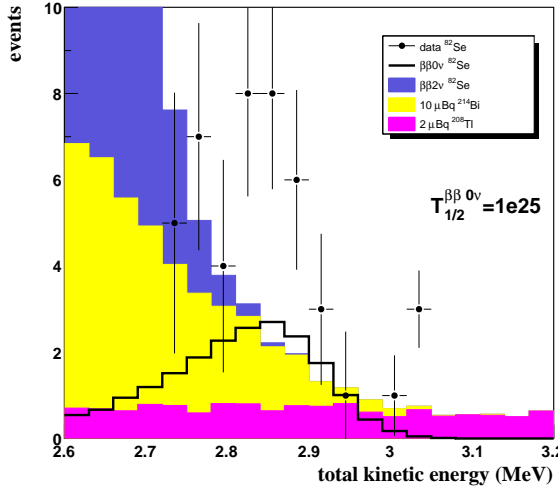


Figure 6.5: Expected spectra after 5 years of running with 6 modules of the SuperNEMO standard setup (30 kg of isotope) and assuming realistic scenario as defined in Section 6.1. $\beta\beta^{0\nu}$ signal assumes half-life of $T_{1/2}^{0\nu} = 10^{25}$ years. Background spectra are stacked to each other, being the total background histogram overlaid by the signal.

Chapter 7

Summary and Conclusions

In this work, we have described the current experimental techniques to study the neutrino nature, divided into two main groups: experiments measuring oscillation parameters, and therefore giving evidences of non-vanishing neutrino masses, and experiments searching for $\beta\beta^{0\nu}$ decay, and consequently for the nature of neutrino masses (Dirac or Majorana). Concerning neutrino oscillations, we focus on the K2K experiment, which confirmed oscillation effects inferred from atmospheric data, and the input to the K2K analysis provided by the HARP experiment. Regarding the nature of neutrino masses, we have described the NEMO experiment along with its published results, and the SuperNEMO project, meant to keep on searching for the $\beta\beta^{0\nu}$ decay. More specifically, this work has been organized as follows. After a brief introduction in Chapter 1, we have described in second chapter how the Standard Model can be extended in order to fit massive neutrinos, now that we have experimental proofs that they have non-vanishing masses. Chapter 3 summarizes the different experimental approaches to neutrino physics, from oscillation experiments to those trying to measure the neutrino masses m_i and paying particular interest in the $\beta\beta$ experiments, since they are the only known way to find out whether neutrinos are Dirac or Majorana particles. We describe in Chapter 4 the K2K experiment along with the HARP measurement of the pion production cross-section and its role in the K2K oscillation analysis. Then, we have discussed in Chapter 5 the NEMO-3 results regarding the search for the $\beta\beta^{0\nu}$ process, and the physics case of its natural evolution: the SuperNEMO experiment. An exhaustive analysis of its expected sensitivity has been presented. Since SuperNEMO has been traditionally considered as one possibility for the new LSC, we have analyzed in

Chapter 6 its case at this particular laboratory. Finally, in the current Chapter, we summarize all the above and review the main conclusions.

The current status of neutrino oscillation physics has been reviewed. As we stand now, we explain the Atmospheric neutrino data taken at Super-Kamiokande in terms of a maximum mixing between ν_μ and ν_τ neutrinos, along with the corresponding mass squared difference $|\Delta m_{atm}^2| \sim 2.4 \times 10^{-3} \text{ eV}^2$. This effect is confirmed by both K2K and MINOS experiments using accelerator-based ν_μ beams pointing to detectors where the oscillated flux is measured. A new set of high precision long-baseline oscillation experiments are being built in order to achieve better accuracy for the oscillation parameters.

On the other side, the deficit of solar neutrinos which has been observed for thirty years is now also understood in terms of oscillations between the ν_e and some combination of the ν_μ and ν_τ neutrinos. This conclusion comes mostly from the SNO and Super-Kamiokande experiments, along with the previous solar neutrino flux determination by gallium experiments. However, in order to establish the right pair of solar oscillation parameters, a reactor experiment has been decisive: the KamLAND experiment, where the disappearance of $\bar{\nu}_e$ and distortion of the flux from a nuclear plant has been detected at an average distance of 180 km from the source.

The minimum joint description of solar, atmospheric, long baseline and reactor data requires the mixing of the three known neutrinos. By combining the data from different sources, one can infer that the two corresponding mass square differences are $\Delta m_{21}^2 \simeq 7.9 \times 10^{-5} \text{ eV}^2$ and $|\Delta m_{31}^2| \simeq 2.6 \times 10^{-3} \text{ eV}^2$, meanwhile the mixing angles are $\theta_{12} \simeq 33.7$ deg and $\theta_{23} \simeq 43.3$ deg. Regarding the mixing between the solar and atmospheric sectors, the Chooz and Palo Verde reactor neutrinos experiments have led to an upper limit for the mixing angle θ_{13} , showing that indeed is really small or even vanishing: $\sin^2 2\theta_{13} \leq 0.1$.

This scenario of three mixed massive neutrinos is satisfactory as far as experimental data is concerned. However, this picture is not complete, since we have no direct evidence of the mixing angle θ_{13} and we do not have any kind of information about CP violation in the leptonic sector. Moreover, oscillation experiments do not provide information about the absolute magnitude of neutrino masses (that is, no information on the lightest mass), although they provide a lower bound on the heaviest neutrino mass ($\sqrt{\Delta m_{atm}^2} \simeq 0.05$ eV). In particular, by now they cannot separate two rather different scenarios, the hierarchical pattern of neutrino masses in which $m \sim \sqrt{\Delta m^2}$ and the degenerate pattern in which $m \gg \sqrt{\Delta m^2}$. At present, the most precise and model

independent bound on absolute mass scale comes from the tritium beta decay spectrum: $m_{\nu_e} < 2.2$ eV at 95% C.L.

In this work we have described one of the most important experiments regarding the quest of understanding neutrino oscillations, since it provided the first confirmation of atmospheric data using terrestrial neutrinos: the K2K experiment. The KEK to Kamioka long-baseline neutrino oscillation experiment (K2K) used an accelerator-produced beam of ν_μ with a neutrino flight distance of 250 km. The neutrinos were measured first by a detector located approximately 300 meters away from the beam source, where oscillation had not taken place yet. Then, the flux was measured again at Super-Kamiokande (SK) detector which is 250 km away from KEK.

We have described how oscillation effects are observed as both a suppression in the total number of ν_μ events observed at SK and a distortion of the measured energy spectrum. The observations of these two quantities (number of events and energy spectrum) are compared to their expectations at SK to study neutrino oscillation. Expectations at SK in absence of oscillation are obtained as follows. First, the near detector complex measures the neutrino flux and spectrum before neutrinos oscillate. Then, those measurements are extrapolated by the expected ratio of muon neutrino fluxes at the far and near detector locations, the far-to-near (F/N) flux ratio, to predict the number of neutrino events and energy spectrum in SK. The F/N ratio is computed by means of Monte-Carlo techniques, and consequently the accuracy of the K2K analysis relies on a good Monte-Carlo description of the neutrino beam.

In K2K, the neutrino beam is generated by the decay of pions produced on an Aluminum target, when a primary proton beam of 12 GeV/c collides with it. Thus, the yield of positive pions is responsible for the ν_μ beam profile and intensity. In the K2K simulation program, protons with a kinetic energy of 12.9 GeV are injected into the aluminum production target. Then, an empirical formula for the differential cross-section by J. R. Sanford and C. L. Wang is used to simulate the primary hadron production in the target. Parameters of this formula used to be obtained from a fit of an old data set (the Cho-CERN compilation) and this led to big uncertainties in the predicted fluxes and consequently in the final oscillation analysis. At this point HARP experiment plays a major role: HARP provides a much more accurate description of the pion production cross-section on an Aluminum target.

A precision measurement of the double-differential production cross-section, $d^2\sigma^{\pi^+}/dpd\Omega$, for pions of positive charge, performed in the HARP experiment has also been presented in this document. The incident particles are protons of

12.9 GeV/c momentum impinging on an aluminum target of 5% nuclear interaction length. The cross-section is fitted with a Sanford-Wang parameterization and the results are consistent with older data, but with much higher statistical accuracy. The results are given for secondaries within a momentum range from 0.75 GeV/c to 6.5 GeV/c , and within an angular range from 30 mrad to 210 mrad. This covers the region of interest for K2K, since 80% of the pions generated at KEK and decaying into neutrinos which reach the K2K detectors are within that phase space. The overall scale of the cross-section is known to better than 6%, while the average point-to-point error is 8.2%.

We have shown how neutrino flux predictions in the K2K experiment are obtained, using the measurement by the HARP experiment and the K2K beam Monte-Carlo. We have computed both flux central values and systematic uncertainties. For the central value predictions, we switch from a parameterization of π^+ production in the collisions of primary protons in aluminum based on a CERN compilation of p-Be data plus a nuclear correction to account for the different nuclear target material, to a parameterization based on the HARP result. Regarding the flux systematic uncertainties, we take into account those related to beam optics, primary and secondary hadronic interactions, and horn magnetic fields used to focus the beam towards the detectors. In particular, uncertainties coming from the HARP measurement have been carefully estimated, since they are the dominant ones in flux predictions. With both central values and corresponding errors we have computed the F/N ratio. Results are compatible with previous prediction from Cho-CERN compilation and with PIMON measurement (see Sec. 4.4.2), but much more accurate. We estimate that the flux ratio uncertainty as a function of the neutrino energy binning used in this analysis is at the 2-3% level below 1 GeV neutrino energy, while it is of the order of 4-9% above 1 GeV . We find that the dominant contribution to the uncertainty in F/N comes from the HARP π^+ measurement itself. In particular, the uncertainty in the flux ratio prediction integrated over all neutrino energies is 2.0%, where the contribution of the HARP π^+ production uncertainty is 1.4%.

Finally, we have described the results from the K2K oscillation analysis, taking into account the prediction of the F/N ratio provided by the HARP input. One hundred and twelve beam-originated neutrino events were observed in the fiducial volume of Super-Kamiokande with an expectation of $158.1^{+9.2}_{-8.6}$ events without oscillation. A distortion of the energy spectrum was also seen in 58 single-ring muon-like events with reconstructed energies. The probability that the observations are explained by the expectation for no neutrino oscillation is 0.0015% (4.3σ). In a two flavor oscillation scenario, the allowed Δm^2 region at $\sin^2 2\theta = 1$ is between 1.9 and $3.5 \times 10^{-3} \text{ eV}^2$ at the 90 % C.L. with a best-fit

value of 2.8×10^{-3} eV².

There is another major open issue to which oscillation experiments cannot contribute: they do not provide any information about the nature of neutrino masses, i.e., whether neutrinos are Dirac or Majorana particles. This arises from the fact that oscillations are not sensitive to the Majorana phases in the PMNS matrix. So far, the only way we now to address this question is the $\beta\beta$ decay. Such a process has been observed along with the emission of two neutrinos, but in case we detect the mode in which no neutrinos are involved ($\beta\beta^{0\nu}$), we will be sure that they are Majorana particles. Furthermore, it is hoped that the search for the neutrino-less double beta decay, reviewed in the current work, will help in determining, or at least narrowing down by setting an upper limit of $\langle m_\nu \rangle$, the absolute neutrino mass scale and in deciding which mass pattern (normal or inverted hierarchy, or even degenerate) is the right one. Currently, the best sensitivity to the neutrino effective mass $\langle m_\nu \rangle$ is provided by the Heidelberg-Moscow experiment, and in fact a subgroup of the collaboration led by Klapdor-Kleingrothaus has claimed a signal in the range of 0.24-0.6 eV with more than 4σ of statistical significance. Such a result has not been accepted by the whole community and thus one of the goals of the next round of $\beta\beta$ experiments is to test the so-called Klapdor's Claim by covering the range of $\langle m_\nu \rangle$ values corresponding to the degenerate neutrino mass pattern.

In this document, we have described an exhaustive analysis of the SuperNEMO project, meant to search for the $\beta\beta^{0\nu}$ decay as a natural evolution of the successful NEMO-3 experiment. The main goal of SuperNEMO is to achieve sensitivities to $\langle m_\nu \rangle$ of the order of 100 meV, by scaling up the NEMO-3 techniques. Consequently, SuperNEMO is conceived as a tracko-calor experiment in which a foil of a given $\beta\beta$ isotope is surrounded by tracking and calorimeter devices, thus providing both track and energy of emitted particles. We have described the standard setup of a SuperNEMO module, for which a full simulation has been developed. After generating the kinematics of a $\beta\beta$ event (both $\beta\beta^{2\nu}$ and $\beta\beta^{0\nu}$), a vertex is randomly placed in the source and beta particles are propagated inside the detector. Then, tracker and calorimeter response is simulated, so a set of geiger and scintillator hits are obtained for each event. We have also shown how simulated $\beta\beta$ events are reconstructed. We apply two main algorithms to get reconstructed particles. One of them associates geiger hits from a same Monte Carlo particle and the other fits the whole track, associates it with a calorimeter hit and finds vertex on foil surface. Efficiency of particle reconstruction algorithms is high (85%), being the main source of inef-

ficiency the resolution in the first block of geiger layers. A set of event selection cuts have also been described. In order to ensure the correct identification of the $\beta\beta$ event and high efficiency of background rejection, we require each event to fulfill several conditions. These cuts lead to an extra loss of detection efficiency which has been estimated to be about 27%. Finally, the overall detection efficiency is 28% for ^{82}Se foils, and 29.5% for ^{150}Nd ones. This efficiency can be understood as the convolution of three factors: topological acceptance of SuperNEMO detector, reconstruction efficiency, and event selection efficiency. We have proven that the overall efficiency is dominated by acceptance, since half of the $\beta\beta$ events are not useful for analysis due to topological reasons. The breakthrough to achieve better efficiency seems to be a different geometry for the SuperNEMO module.

With a sample of selected reconstructed events, we have performed a likelihood fit analysis to get SuperNEMO sensitivity to the $T_{1/2}^{0\nu}$ of the $\beta\beta^{0\nu}$ process, assuming the exchange of a light Majorana neutrino. We have studied the dependence with the exposure, calorimeter resolution, foil thickness and detection efficiency, and for two different foil sources (^{82}Se and ^{150}Nd). We also have taken into account various kind of backgrounds. Apart from the intrinsic $\beta\beta^{2\nu}$ background, impurities of ^{214}Bi and ^{208}Tl inside the foil have been considered. We have concluded that the foil purity requirements are as follows: 10 $\mu\text{Bq}/\text{kg}$ of ^{214}Bi and 2 $\mu\text{Bq}/\text{kg}$ of ^{208}Tl for ^{82}Se foils, and 2 $\mu\text{Bq}/\text{kg}$ of ^{208}Tl for ^{150}Nd . If these values are achieved along with an energy resolution of 7% FWHM at 1 MeV, sensitivities according to the QRPA model will be 67 (30) meV 90% C.L., for 100 kg of ^{82}Se (^{150}Nd) and a data taking time of 5 years. This results assume a best case in which Radon levels inside the detector are negligible. It seems clear that if SuperNEMO manages to achieve the calorimetric and background targets defined in this work, it will be capable of testing Klapdors's Claim with large significance and cover almost completely the quasi-degenerate range of neutrino masses.

Finally, we have analyzed the physics case of SuperNEMO at the Canfranc Underground Laboratory (LSC), along with the feasibility of the targets defined in the R&D program, mainly regarding energy resolution, radio-purity of source foils and Radon background. It turns out that 7% FWHM at 1 MeV may be too optimistic an approach given the fact that this resolution has never been achieved with plastic scintillator. Even for liquid scintillator, it seems more realistic to assume an energy resolution of 8-9%. Furthermore, the foil radio-purity requirements defined in the current analysis imply an improvement of factor 100 with respect to NEMO-3 values, and so far the feasibility of this has not been proven. The same happens with Radon contamination inside tracking chamber:

NEMO-3 values have to be reduced by at least a factor 10 if one wants to fulfill SuperNEMO requirements. Concerning the available space at LSC, one has to notice that 100 kg of isotope requires 20 SuperNEMO modules as defined in this work, and it is reasonable to think that only 6 can be fit in the main hall of the LSC (thus 30 kg). According to the above discussion, we have defined various scenarios. The *demonstrated* one is that in which NEMO values for background levels and calorimeter resolution are considered for SuperNEMO experiment. After 5 years of data taking with 6 SuperNEMO modules, the sensitivity will be 315 meV for ^{82}Se foils according to QRPA model. If one takes into account the optimistic scenario in which SuperNEMO targets are achieved, the sensitivity would be 130 meV, while assuming what we have defined as a more realistic approach would lead to 184 meV. Notice all these numbers stand for ^{82}Se foils: we do not consider ^{150}Nd foils case since the feasibility of their production is so far more than unclear.

Summarizing, we hope that this work had reviewed in a clear way the current status of the experimental approaches to understand the actual nature of neutrinos, those particles which offer us a main door towards physics beyond the Standard Model. Neutrinos have played in the last 70 years a major role in Particle Physics and consequently in the quest of understanding the Universe, and it is for sure that they will carry on providing revolutionary and fruitful information in the next decades.

Appendix A

Resumen en castellano

A.1 Introducción

El objetivo de este trabajo es estudiar desde un punto de vista experimental dos aspectos fundamentales de la naturaleza de los neutrinos, el fenómeno de las oscilaciones y su masa, centrándose en los experimentos en los que el grupo del IFIC (CSIC-UVEG) liderado por JJ Gomez-Cadenas, ha participado en los últimos 5 años. La física que estudia las propiedades de los neutrinos puede ser dividida en dos campos bien diferenciados: el de los experimentos de oscilación y el de los experimentos que tratan de medir la masa absoluta del neutrino. En cuanto a las oscilaciones de neutrinos, se describe en este documento el experimento K2K [38], que publicó en 2006 una fuerte evidencia de oscilación de neutrinos muónicos, y la aportación del experimento HARP al análisis de K2K. Por otra parte, en relación con el estudio de la naturaleza de la masa de los neutrinos, el presente documento se centra en el existoso experimento de desintegración doble beta sin emisión de neutrinos ($\beta\beta^{0\nu}$) NEMO-3 [96], y en el proyecto llamado SuperNEMO.

Este trabajo está organizado de la siguiente manera. El primer capítulo resume la historia de la física de neutrinos y describe el objetivo de la presente tesis. En el capítulo 2 se examina el Modelo Estándar y de qué manera los neutrinos masivos pueden ser introducidos en él con el fin de dar explicación a los datos experimentales que hoy en día poseemos. El capítulo 3 describe los diversos enfoques experimentales de la física de neutrinos, desarrollados desde el descubrimiento del anti-neutrino en 1956 por parte de Cowan y Reines, pre-

stando especial atención a los experimentos de oscilación y a los de búsqueda del proceso $\beta\beta^{0\nu}$. Con el objetivo de mostrar cómo se ha conseguido observar la oscilación de neutrinos, y por tanto probar que tienen una masa no nula, en el capítulo 4 se describe el análisis del experimento K2K y la contribución del experimento HARP. Dado que experimentos como K2K han demostrado la naturaleza masiva de los neutrinos, el capítulo 5 se centra en el experimento de $\beta\beta^{0\nu}$ NEMO-3, y en el caso de física de su evolución natural: el proyecto SuperNEMO. Un detallado estudio de la sensibilidad de SuperNEMO a la desintegración $\beta\beta^{0\nu}$ en función de diversos parámetros experimentales se presenta en el citado capítulo. Hasta la fecha, SuperNEMO ha sido considerado como una interesante posibilidad para el nuevo laboratorio subterráneo de Canfranc (LSC), así pues se analiza en el capítulo 6 su caso de física en el citado laboratorio. Por último, el capítulo 7 resume el presente trabajo y se remarcán las principales conclusiones y el estado actual de la física experimental encaminada a entender la verdadera naturaleza de los neutrinos.

A.2 Modelo Estándar y neutrinos masivos

En el Modelo Estándar los neutrinos fueron introducidos como partículas sin masa. Hoy en día sabemos que en realidad son masivos y por lo tanto el modelo debe ser modificado o extendido para dar cabida a este hecho. En particular, la oscilación de neutrinos implica que estas partículas tienen masa (aunque muy pequeña) y por tanto son una prueba de física más allá del Modelo Estándar. El hecho de que los neutrinos sean masivos abre las puertas a la eventual desintegración $\beta\beta^{0\nu}$, que se daría en el caso de que los neutrinos fueran partículas de Majorana, es decir, idénticos a sus anti-partículas. Descubrir si los neutrinos son o no de tipo Majorana, es de crucial importancia para obtener un modelo que explique su masa.

Mezcla y oscilación de neutrinos

Las tres especies activas de neutrinos pueden expresarse en términos de los autoestados de sabor ν_ℓ ($\ell = e, \mu, \tau$) o de los autoestados de masa ν_i ($i = 1, 2, 3$). Estas dos bases están relacionadas a través de la matriz de Pontecorvo-Maki-Nakagawa-Sakata(PMNS), análoga a la de Cabibbo-Kobayashi-Maskawa en el sector de quarks:

$$\nu_\ell = \sum_{i=1}^3 U_{\ell i} \nu_i \quad (\text{A.1})$$

Dicha matriz U puede parametrizarse en términos de tres ángulos θ_{ij} ($0 \leq \theta_{ij} \leq \pi/2$) y una fase δ ($0 \leq \delta \leq 2\pi$):

$$U = \begin{pmatrix} 1 & 0 & 0 \\ 0 & c_{23} & s_{23} \\ 0 & -s_{23} & c_{23} \end{pmatrix} \begin{pmatrix} c_{13} & 0 & s_{13}e^{-i\delta} \\ 0 & 1 & 0 \\ -s_{13}e^{-i\delta} & 0 & c_{13} \end{pmatrix} \begin{pmatrix} c_{12} & s_{12} & 0 \\ -s_{12} & c_{12} & 0 \\ 0 & 0 & 1 \end{pmatrix} \quad (\text{A.2})$$

siendo $c_{ij} \equiv \cos \theta_{ij}$ y $s_{ij} \equiv \sin \theta_{ij}$.

En esta descomposición la matriz U resulta del producto de tres rotaciones independientes: una en el plano 23, responsable de las transiciones atmosféricas; otra en el plano 12, responsable de las solares; y una tercera que conecta ambas. La fase δ , en el caso de ser no nula, describe la violación de CP en las oscilaciones de neutrinos.

Si los neutrinos son Majorana, se añaden dos fases adicionales, ϕ_1 y ϕ_2 , que describen la violación del número leptónico en procesos como el $\beta\beta^{0\nu}$:

$$U = \begin{pmatrix} c_{12}c_{13} & s_{12}c_{13} & s_{13}e^{-i\delta} \\ -s_{12}c_{23} - c_{12}s_{23}s_{13}e^{i\delta} & c_{12}c_{23} - s_{12}s_{23}s_{13}e^{i\delta} & s_{23}c_{13} \\ s_{12}s_{23} - c_{12}c_{23}s_{13}e^{i\delta} & -c_{12}s_{23} - s_{12}c_{23}s_{13}e^{i\delta} & c_{23}c_{13} \end{pmatrix} \cdot \begin{pmatrix} 1 & 0 & 0 \\ 0 & e^{i\phi_1} & 0 \\ 0 & 0 & e^{i\phi_2} \end{pmatrix} \quad (\text{A.3})$$

Estos seis parámetros de la matriz PMNS (3 ángulos y tres fases) y las tres masas m_i representan 9 incógnitas de la teoría. Los experimentos de oscilaciones nos han proporcionado medidas de las Δm_{ij}^2 y de los ángulos de mezcla.

A partir de la matriz PMNS se define la siguiente matriz de masa:

$$m_\nu^{\alpha\beta} = \sum_{i=1}^3 (U^*)_{\alpha i} m_i (U^\dagger)_{i\beta} \quad (\text{A.4})$$

La mayor parte de las teorías supersimétricas (SUSY) o de los modelos de gran unificación (GUT) incluyen neutrinos de Majorana ligeros y pesados. El mecanismo *see-saw* permite explicar el pequeño valor de la masa de los neutrinos ligeros (los neutrinos pesados tienen masa del orden de la escala de gran unificación).

Los autoestados débiles ν_α producidos en interacciones débiles son una combinación lineal de los autoestados de masa ν_i que evoluciona en el tiempo. La

probabilidad de que un estado ν_α de energía E sea detectado como ν_β tras propagarse una distancia L viene dada por:

$$P_{\alpha\beta} = \delta_{\alpha\beta} - 4 \sum_{i<j}^n \text{Re}[U_{\alpha i} U_{\beta i}^* U_{\alpha j}^* U_{\beta j}] \sin^2 X_{ij} + 2 \sum_{i<j}^n \text{Im}[U_{\alpha i} U_{\beta i}^* U_{\alpha j}^* U_{\beta j}] \sin 2X_{ij}, \quad (\text{A.5})$$

donde

$$X_{ij} = \frac{(m_i^2 - m_j^2)L}{4E}. \quad (\text{A.6})$$

Esta probabilidad de transición tiene un comportamiento oscilatorio, con amplitudes que son proporcionales a los elementos de la matriz de mezcla y a las longitudes de oscilación:

$$L_{0,ij}^{\text{osc}} = \frac{4\pi E}{\Delta m_{ij}^2}, \quad (\text{A.7})$$

donde $\Delta m_{ij}^2 \equiv m_i^2 - m_j^2$.

Desintegración doble beta sin neutrinos

Es un raro proceso de desintegración nuclear que modifica el número atómico (Z) en dos unidades sin cambiar el número másico (A). Implica, por tanto, la transformación de dos neutrones en protones. Energéticamente sólo puede suceder si el núcleo padre está menos ligado que el hijo, y ambos más ligados que el núcleo intermedio. En la naturaleza, estas condiciones tan sólo las cumplen unos 30 núcleos par-par. En general, el proceso transcurre entre los estados fundamentales (de espín y paridad 0^+) de los núcleos padre e hijo, aunque en ocasiones también es posible la transición a estados excitados (0^+ o 2^+). Experimentalmente, son de especial interés aquellos con una $Q_{\beta\beta}$ superior a los 2 MeV, dado que la probabilidad de desintegración depende fuertemente de ella.

La desintegración con dos neutrinos ($\beta\beta^{2\nu}$),

$$(Z, A) \rightarrow (Z + 2, A) + e_1^- + e_2^- + \bar{\nu}_{e1} + \bar{\nu}_{e2}, \quad (\text{A.8})$$

conserva la carga eléctrica y el número leptónico. Por contra, la desintegración sin neutrinos ($\beta\beta^{0\nu}$),

$$(Z, A) \rightarrow (Z + 2, A) + e_1^- + e_2^-, \quad (\text{A.9})$$

conserva la carga, pero viola el número leptónico; por tanto, está prohibida en el Modelo Estándar. Asimismo, podrían existir las transiciones $\beta\beta\chi$ en las que es emitido un majorón (esto es, un bosón ligero de carga neutra postulado en diversas extensiones de la teoría electrodébil estándar):

$$(Z, A) \rightarrow (Z + 2, A) + e_1^- + e_2^- + \chi, \quad (\text{A.10})$$

El espectro de energías de los dos electrones del $\beta\beta^{2\nu}$ es continuo, dado que la energía disponible, $Q_{\beta\beta}$, se reparte entre cuatro partículas. Por contra, en el proceso $\beta\beta^{0\nu}$ los electrones se reparten la totalidad de la energía, y, por tanto, el espectro es un pico situado en $Q_{\beta\beta}$. Así pues, es posible distinguir ambas señales a partir de sus espectros.

Son varios los procesos elementales que podrían ser responsables de la desintegración doble beta sin emisión de neutrinos. El más simple y probable es el intercambio de dos neutrinos Majorana ligeros que interaccionan mediante corrientes débiles $V - A$. En ese caso, la inversa del periodo de semidesintegración es:

$$[T_{1/2}^{0\nu}(0^+ \rightarrow 0^+)]^{-1} = \langle m_\nu \rangle^2 \left| M^{0\nu} \right|^2 G^{0\nu}(E_0, Z) \quad (\text{A.11})$$

donde $G^{0\nu}$ es la integral de espacio fásico de dos electrones, calculable analíticamente.

El término

$$\left| M^{0\nu} \right| = \left| M_{GT}^{0\nu} - \frac{g_V^2}{g_A^2} M_F^{0\nu} \right| \quad (\text{A.12})$$

es el elemento de matriz nuclear (NME) del isótopo que se desintegra a través del proceso $\beta\beta^{0\nu}$. $M_{0\nu}^{GT}$ y $M_{0\nu}^F$ son, respectivamente, los elementos de matriz nuclear de Gamow-Teller y Fermi; g_V y g_A son las constantes vectorial y axial de acoplamiento de la interacción débil. Existen dos métodos diferentes para la evaluación de los NME: la *quasiparticle random phase approximation* (QRPA) y el modelo nuclear de capas. Ambas aproximaciones están afectadas de importantes incertidumbres de origen teórico.

La masa efectiva del neutrino, $\langle m_\nu \rangle$, es el elemento m_{11} de la matriz de masa (ecuación A.4):

$$\begin{aligned} \langle m_\nu \rangle &= m_{11} \equiv m_{ee} = \left| \sum_j m_j U_{ej}^2 \right| \\ &= \left| |U_{e1}|^2 m_1 + |U_{e2}|^2 m_2 e^{i\phi_1} + |U_{e3}|^2 m_3 e^{i\phi_2} \right| \quad (\text{A.13}) \end{aligned}$$

donde U_{ej} son coeficientes de la matriz de PMNS. Esta masa efectiva es de gran importancia debido a su dependencia respecto de los autovalores másicos m_i y su

relación con los parámetros de las oscilaciones. De hecho es el único observable conocido en el que aparecen las fases de violación de CP de Majorana, $\phi_{1,2}$.

Sustituyendo en (A.13) los coeficientes correspondientes de (A.3):

$$|\langle m_\nu \rangle| = \left| \cos^2 \theta_{13} (|m_1| \cos^2 \theta_{12} + |m_2| e^{2i\phi_1} \sin^2 \theta_{12}) + |m_3| e^{2i(\phi_2 - \delta)} \sin^2 \theta_{13} \right| \quad (\text{A.14})$$

Si CP se conserva, $\phi_{1,2} = k\pi$, aunque, en general, será posible cualquier valor. Así, $\langle m_\nu \rangle$ puede ser compleja, y las cancelaciones en la suma son posibles.

Pueden definirse dos cantidades, límites superior e inferior de $\langle m_\nu \rangle$, independientes de las fases de Majorana:

$$\langle m_\nu \rangle_{\text{max}} = \sum_i |U_{ei}|^2 m_i \quad (\text{A.15})$$

$$\langle m_\nu \rangle_{\text{min}} = \max[(2|U_{ei}|^2 m_i - \langle m_\nu \rangle_{\text{max}}), 0] \quad (\text{A.16})$$

Con lo cual, si experimentalmente se detectara el proceso $\beta\beta^{0\nu}$ obteniéndose un valor de $\langle m_\nu \rangle$, podría deducirse el rango de valores absolutos de la masas del neutrino, utilizando los ángulos de mezcla $|U_{ei}|^2$ y las Δm_{ij}^2 conocidas a partir de los experimentos de oscilaciones. Estas son las dos situaciones posibles:

- Jerarquía normal:

$$(\langle m_\nu \rangle_{\text{min}} \equiv m_1) \ll (m_2 \simeq \sqrt{\Delta m_\odot^2}) \ll (m_3 \simeq \sqrt{\Delta m_{\text{atm}}^2})$$

- Jerarquía inversa: $(\langle m_\nu \rangle_{\text{min}} \equiv m_3) \ll m_1 \lesssim m_2$ con $m_{1,2} \simeq \sqrt{\Delta m_{\text{atm}}^2}$

Obviamente, si se dispusiera de algún dato adicional (un resultado positivo de los experimentos de desintegración beta de tritio, por ejemplo), sería posible determinar o acotar el valor de las fases $\phi_{1,2}$.

A.3 Situación actual de la física experimental de neutrinos

En 1998, la Colaboración Super-Kamiokande aportó la primera evidencia de oscilaciones de neutrinos; desde entonces, diversos experimentos han confirmado el resultado en los distintos sectores: K2K y MINOS en el atmosférico y Kamland y SNO en el solar. Así pues, los neutrinos pueden cambiar de sabor y, por tanto, tienen masa.

Sin embargo, en los experimentos de oscilaciones sólo pueden medirse las diferencias entre los cuadrados de las masas del neutrino, $\Delta m_{ij}^2 \equiv |m_i^2 - m_j^2|$.

Con lo cual, no permiten determinar la escala másica absoluta; tan sólo, una cota inferior: $m_{\text{scale}} = \sqrt{\Delta m^2}$. Además, en estos experimentos son indistinguibles las dos jerarquías de masa posibles: la normal, en la que las m_i y/o m_j son similares a $\sqrt{\Delta m^2}$; y la inversa, donde $m_i \gg \sqrt{\Delta m^2}$. La información que nos permita decidir cuál es la correcta sólo podrá obtenerse de experimentos en los que se realice una medida directa de la masa del neutrino, como en la búsqueda de la desintegración doble beta sin emisión de neutrinos o en el estudio de la desintegración beta del tritio.

La desintegración doble beta permitiría contestar también una pregunta fundamental concerniente a la naturaleza del neutrino. Mientras que los leptones cargados son partículas de Dirac, distintas de sus antipartículas, todo indica que los neutrinos podrían ser partículas de Majorana.

La explicación más simple para los datos de neutrinos solares es la de oscilaciones de ν_e a ν_μ y/o ν_τ . De igual modo, la explicación más directa para los datos de neutrinos atmosféricos es la de oscilación de ν_μ . La descripción mínima de todos los datos de manera conjunta requiere la implicación de los tres neutrinos conocidos, de manera que tenemos dos Δm^2 diferentes, provenientes de los sectores atmosférico y solar:

$$\Delta m_{21}^2 = \Delta m_{\text{sol}}^2 \ll \Delta m_{\text{atm}}^2 = |\Delta m_{31}^2| \simeq |\Delta m_{32}^2|. \quad (\text{A.17})$$

De un análisis global de todos los datos disponibles se obtienen los siguientes valores para los seis parámetros de oscilación, a 1σ (3σ) [5]:

$$\begin{aligned} \Delta m_{21}^2 &= 7.9_{-0.28}^{+0.27} ({}^{+1.1}_{-0.89}) \times 10^{-5} \text{ eV}^2, \\ |\Delta m_{31}^2| &= 2.6 \pm 0.2 (0.6) \times 10^{-3} \text{ eV}^2, \\ \theta_{12} &= 33.7 \pm 1.3 ({}^{+4.3}_{-3.5}), \\ \theta_{23} &= 43.3_{-3.8}^{+4.3} ({}^{+9.8}_{-8.8}), \\ \theta_{13} &= 0.0_{-0.0}^{+5.2} ({}^{+11.5}_{-0.0}), \\ \delta_{\text{CP}} &\in [0, 360]. \end{aligned} \quad (\text{A.18})$$

Aunque los experimentos de oscilación no permiten la determinación de la escala absoluta de la masa de los neutrinos, test cinemáticos y datos cosmológicos ponen límites superiores a las masas de los tres neutrinos conocidos:

$$\begin{aligned}
 m_{\nu_e} &< 2.2 \text{ eV} & \text{from } & {}^3\text{H} \rightarrow {}^3\text{He} + e^- + \bar{\nu}_e \\
 m_{\nu_\mu} &< 190 \text{ keV} & \text{from } & \pi^- \rightarrow \mu^- + \bar{\nu}_\mu \\
 m_{\nu_\mu} &< 18.2 \text{ MeV} & \text{from } & \tau^- \rightarrow n\pi + \nu_\tau \\
 \sum m_\nu &< 0.3 - 3.0 \text{ eV} & \text{from } & \Omega_\nu h^2 = \sum_i m_i / (94 \text{ eV})
 \end{aligned}$$

Finalmente, un subgrupo de la colaboración Heidelberg-Moscow ha publicado resultados positivos en la búsqueda del proceso $\beta\beta^{0\nu}$ [4]. Afirman que han observado una señal con 4σ en el isótopo ${}^{76}\text{Ge}$, correspondiente a la siguiente masa efectiva del neutrino:

$$\langle m_\nu \rangle = 0.24 - 0.58 \text{ eV} \quad (\text{A.19})$$

Sin embargo, la comunidad científica no ha aceptado de manera unánime este resultado, y por lo tanto entre los objetivos de la siguiente generación de experimentos $\beta\beta^{0\nu}$ está el de comprobar esta señal.

A.4 Evidencia de neutrinos massivos: K2K

El experimento K2K es un experimento de oscilación de neutrinos a gran distancia. El haz de neutrinos estudiado se genera a partir de un acelerador de protones que colisiona con un blanco de aluminio; la desintegración de hadrones ligeros producidos en el choque (principalmente piones) conforma un haz de ν_μ casi puro. El flujo de neutrinos se mide en un primer complejo de detectores situado a 300 metros de la fuente del haz, donde los neutrinos aún no han oscilado. Una segunda medida del flujo se realiza a 250 km, en el detector Super-Kamiokande (SK), donde se observa el doble efecto de la oscilación: supresión en el número esperado de eventos y distorsión del espectro energético del haz.

Para medir los parámetros de oscilación, el espectro energético y la normalización del flujo son usados para predecir la señal en ausencia de oscilación en SK. Mediante técnicas de Monte Carlo (MC), la relación entre el flujo cercano y el lejano $R^{F/N}$ se calcula para obtener dicha predicción. Los errores asociados a la estimación de $R^{F/N}$ dependen fuertemente de la descripción en el MC de la producción hadrónica en el blanco de Aluminio, es decir, en la descripción de la sección eficaz de producción hadrónica. El MC del haz de K2K se basaba anteriormente en viejas medidas (compilación CHO-CERN [64]) para parametrizar la generación de hadrones, y esto implicaba grandes errores en $R^{F/N}$ que de

hecho eran dominantes en el análisis de K2K. Sin embargo, en el último estudio de K2K [38], una nueva descripción a partir de los datos del experimento HARP [61] ha sido introducida, con la consiguiente mejora en el cálculo del $R^{F/N}$.

A.4.1 Predicción de flujos en K2K: el experimento HARP

El objetivo del experimento HARP es el estudio sistemático de producción hadrónica en un gran número de blancos, y para energías del haz incidente desde $1.5 \text{ GeV}/c$ a $15 \text{ GeV}/c$. El primer resultado publicado es la medida de la sección eficaz de producción de π^+ en aluminio. Esta medida es de gran relevancia para K2K ya que reproduce las condiciones en las que el haz de ν_μ es generado. En este trabajo, se describe el análisis desarrollado para obtener dicha sección eficaz y cómo los resultados son utilizados para describir el haz de neutrinos en el MC de K2K. Con los citados resultados, se han estimado los flujos de neutrinos en los detectores cercano y lejano, así como los errores asociados. La predicción de los flujos puede observarse en la figura A.1, junto con las predicciones anteriores al experimento HARP. Finalmente, se ha calculado $R^{F/N}$, obteniéndose que es compatible con las estimaciones anteriores, pero con un error mucho menor, como puede verse en la figura A.2. El error total en $R^{F/N}$ es del 2%.

A.4.2 Análisis de oscilaciones

El experimento K2K tomó datos desde junio del 1999 hasta noviembre del 2004. Estos datos han sido usados para medir los parámetros de oscilación. 112 interacciones de neutrinos del haz se observan en SK, siendo el valor esperado en ausencia de oscilaciones de $158.1^{+9.2}_{-8.6}$. El error proviniente de la relación entre los flujos cercano y lejano ($R^{F/N}$) es de $\pm 2.9\%$ (mientras que era 5% antes de la contribución de HARP), y ha dejado de ser el error dominante en el análisis. La distorsión en el espectro es también estudiada con 58 eventos en los que la energía del ν_μ ha sido reconstruida. Un estudio de verosimilitud (*likelihood*) ha sido desarrollado dando como resultado que la probabilidad de que la observación se explique por una fluctuación estadística y no por la oscilación es de 0.0015% (4.3σ). En el escenario de oscilaciones entre sólo dos sabores de neutrinos, la región permitida de Δm^2 para $\sin^2 2\theta = 1$ está entre 1.9 y $3.5 \times 10^{-3} \text{ eV}^2$ con 90% C.L. El mejor resultado del ajuste de los datos se obtiene con $2.8 \times 10^{-3} \text{ eV}^2$. La figura A.3 muestra un resumen de los resultados obtenidos.

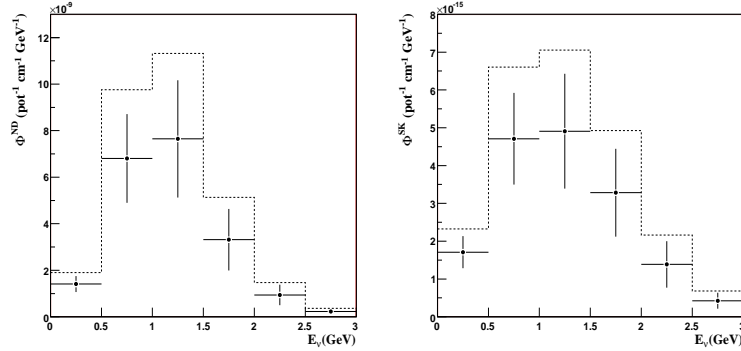


Figure A.1: Predicción de los flujos de ν_μ basados en los resultados de HARP y en una completa estimación de los errores sistemáticos. Los puntos con barras de error muestran estos resultados, mientras que el histograma de línea discontinua muestra el valor central de los anteriores resultados basados en [64]. Izquierdo: flujo en el detector cercano. Derecha: flujo en el detector lejano: Super-Kamiokande.

A.5 Naturaleza de la masa de los neutrinos: SuperNEMO

Dado que los resultados de los experimentos de oscilación han demostrado en los últimos años que los neutrinos son partículas masivas, actualmente hay un renovado interés por los experimentos de búsqueda de la desintegración $\beta\beta^{0\nu}$.

El experimento NEMO (*Neutrino Ettore Majorana Observatory*) permite la detección directa de los dos electrones de la desintegración doble beta mediante un sistema de trazado y un calorímetro. La Colaboración construyó previamente dos prototipos, NEMO-1 y NEMO-2, para comprobar la viabilidad del diseño. Desde junio de 2002, NEMO-3 está instalado en el Laboratorio Subterráneo de Modane (LSM, Francia), a una profundidad equivalente a 4800 m de agua. En la cavidad, un sistema de purificación del aire mantiene los niveles de radón por debajo de los $20 \text{ Bq} \cdot \text{m}^{-3}$.

El detector, de forma cilíndrica, está dividido en 20 sectores radiales. Cada uno de ellos consta de una fuente radiactiva laminar delgada ($30\text{-}60 \text{ mg/cm}^2$),

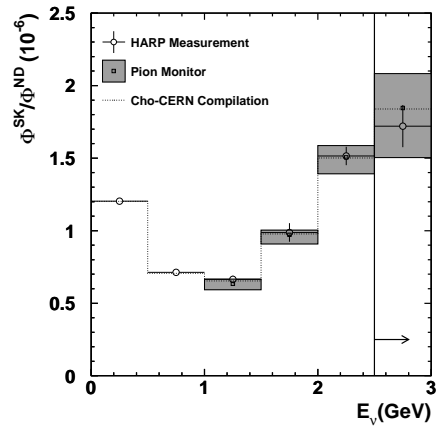


Figure A.2: Predicción de la relación entre los flujos cercano y lejano de ν_μ en el experimento K2K, en ausencia de oscilaciones. Los círculos con barras de error muestran los resultados obtenidos en el presente trabajo con los datos de HARP. La línea punteada muestra la anterior predicción obtenida con los datos de la compilación CHO-CERN [64]. Los cuadrados muestran los resultados del detector PIMON, que realizó dos medidas *in situ* de los piones generados en el blanco de aluminio.

de 2,5 m de altura, fijada verticalmente a 1,55 m del centro, entre dos volmenes de trazado concéntricos compuestos por 6180 cámaras de deriva, que operan en modo Geiger. Rodeando todo el sistema de trazado hay 1940 bloques de centellador plástico acoplados a fotomultiplicadores de 3" y 5". Este calorímetro permite la medida de la energía y tiempo de vuelo de las partículas. Un solenoide produce un campo magnético de 25 Gauss paralelo al eje del cilindro, con el propósito de identificar la carga de las partículas. Finalmente, un blindaje externo de hierro de 20 cm de grosor protege al detector de la radiación γ y de los neutrones térmicos.

Aunque la técnica desarrollada parece ser muy prometedora y ha realizado ya contribuciones significativas al campo, tiene su reto pendiente en lo concerniente a la resolución energética y a la eficiencia de detección, que en NEMO-3 son, respectivamente, 14% y $\sim 8\%$. Se han iniciado los estudios que permitirán la

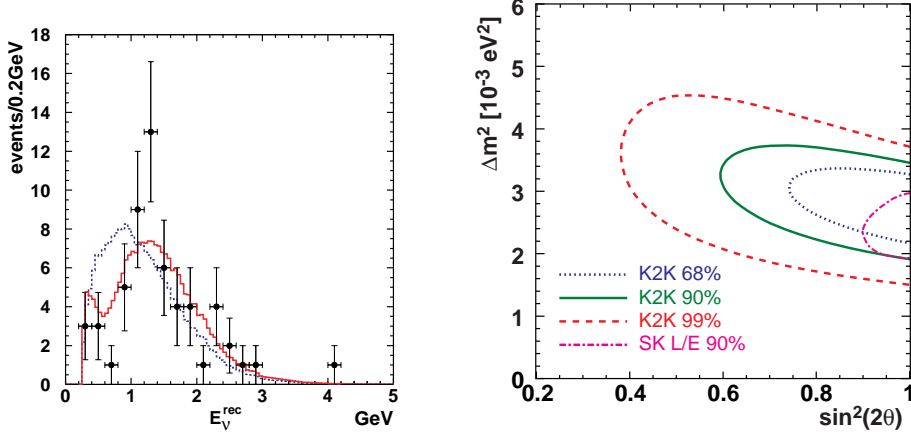


Figure A.3: Resultados del análisis de oscilaciones de K2K. Izquierdo: espectro energético en SK; los puntos con barras de error muestran los datos reales, el histograma de línea discontinua muestra la predicción en ausencia de oscilaciones, y el de línea continua el mejor ajuste al caso de oscilación. Derecha: región permitida para los parámetros de oscilación, a diferentes niveles de confianza (C.L.); se muestra también el resultado del análisis de SK con neutrinos atmosféricos.

construcción de un nuevo detector, SuperNEMO, de similar tecnología, aunque con geometría rectangular y capacidad para 100 kg de material radiactivo. SuperNEMO pretende mejorar principalmente la eficiencia de detección, la resolución energética y los niveles de contaminación dentro del detector.

El detector SuperNEMO está dividido en módulos que contienen una fuente de unos 12 m² de superficie y 40 mg/cm² de grosor, y por lo tanto unos 5 kg de material radiactivo. La fuente está rodeada por un dispositivo para detectar la traza de las partículas y un calorímetro para medir su energía. Se estima la construcción de unos 20 módulos, obteniendo así una masa total de unos 100 kg de isótopo. En la figura A.4 se puede observar un esquema de un módulo de SuperNEMO.

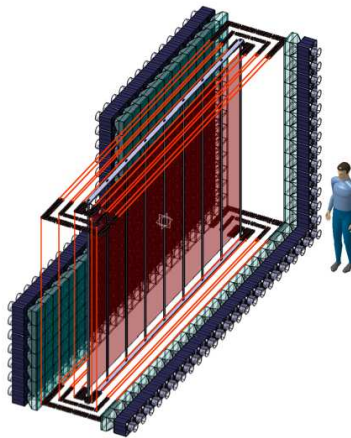


Figure A.4: Esquema de un módulo del detector SuperNEMO. La fuente se sitúa en el centro y es rodeada por el dispositivo para reconstruir trazas. Un calorímetro para medir la energía de las partículas cubre las paredes del módulo.

A.5.1 Simulación y reconstrucción de datos

En este trabajo se ha descrito el módulo estándar de SuperNEMO. Una simulación completa del experimento se ha desarrollado para este módulo. Tras la generación de la cinemática del evento $\beta\beta$, el vértice del evento se sitúa aleatoriamente en la fuente y las partículas son propagadas dentro del detector. Posteriormente, la respuesta del dispositivo de trazado y el calorímetro son simuladas, generándose una colección de medidas para cada evento.

Con el objetivo de reconstruir las partículas de eventos $\beta\beta$, dos algoritmos principales son aplicados a las medidas simuladas. Uno de ellos asocia las medidas del dispositivo Geiger que provienen de una misma partícula de MC, mientras que el otro ajusta las medidas a un trazo de modelo helicoidal, asocia la traza a una señal del calorímetro y extrae la traza a la superficie de la fuente para reconstruir el vértice. La eficiencia de reconstrucción de partículas es de 85%, como puede observarse en la figura A.5.

Un conjunto de cortes de selección se aplica entonces a los eventos reconstruidos para asegurar la correcta identificación de la desintegración $\beta\beta$ y el rechazo de los eventos de ruido. Dichos cortes llevan una pérdida adicional

de eficiencia, que ha sido estimada en 27%.

Finalmente, la eficiencia total de detección de eventos $\beta\beta$ es de 28% para fuentes de ^{82}Se y 29.5% para fuentes de ^{150}Nd . Esta eficiencia es la convolución de tres factores: la aceptancia topológica del detector, la eficiencia de reconstrucción, y la eficiencia de la selección de eventos. La eficiencia total resulta estar dominada por la aceptancia del módulo, que es $\sim 50\%$.

A.5.2 Sensibilidad al proceso $\beta\beta^{0\nu}$

En esta tesis doctoral se ha descrito un análisis mediante el principio de máxima verosimilitud para obtener la sensibilidad a la semi-vida $T_{1/2}^{0\nu}$ del proceso $\beta\beta^{0\nu}$, asumiendo el intercambio de un neutrino ligero de Majorana. Para ello, se ha usado la reconstrucción de datos anteriormente descrita y el valor de la eficiencia de detección obtenida. Se ha estudiado la sensibilidad en función de varios factores experimentales (exposición, resolución energética, grosor de la fuente y eficiencia de detección) y para dos fuentes diferentes: ^{82}Se y ^{150}Nd . Se han tenido en cuenta varias fuentes de contaminación. Además del ruido intrínseco debido a la cola del espectro $\beta\beta^{2\nu}$, se ha considerado la existencia de impurezas de ^{214}Bi y ^{208}Tl en las fuentes, que pueden simular mediante su desintegración beta un evento $\beta\beta$ (tras la generación de un segundo electrón en una interacción con el material de la fuente). Se han estimado los límites aceptables para la pureza de las fuentes: 10 $\mu\text{Bq}/\text{kg}$ de ^{214}Bi y 2 $\mu\text{Bq}/\text{kg}$ de ^{208}Tl para ^{82}Se , y 2 $\mu\text{Bq}/\text{kg}$ de ^{208}Tl para ^{150}Nd (como se recalca en este trabajo, el ^{214}Bi no supone un ruido para el experimento si se usan fuentes de ^{150}Nd , ya que el espectro energético de su desintegración beta no se extiende a la región de búsqueda del proceso $\beta\beta^{0\nu}$).

La tabla A.1 muestra la sensibilidad esperada para una exposición de 500 $\text{kg}\cdot\text{year}$ (equivalente a 100 kg de isótopo y 5 años de toma de datos) y resolución energética de 7% FWHM a 1 MeV. La figura A.6 muestra la correspondiente sensibilidad de SuperNEMO en función de la exposición. Bajo estas condiciones, SuperNEMO sería capaz de comprobar o excluir el resultado positivo publicado en [4].

A.6 SuperNEMO en el Laboratorio Subterráneo de Canfranc

El Laboratorio Subterráneo de Canfranc dispone de una nueva sala para la instalación de experimentos de bajo fondo. SuperNEMO ha sido considerado

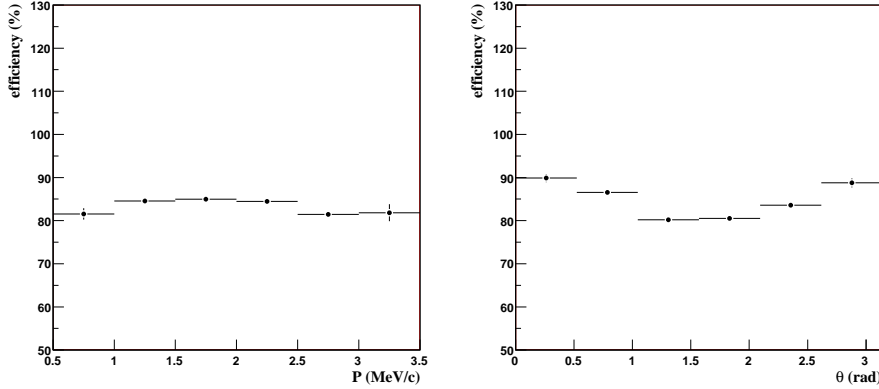


Figure A.5: Eficiencia de reconstrucción de partículas (%) en función del momento (izquierda) y en función del angulo polar definido respecto de la dirección normal a la fuente (derecha).

Foil	$T_{1/2}^{0\nu}$ (y)	$\langle m_\nu \rangle$ (meV)	$T_{1/2}^{0\nu}$ (y)	$\langle m_\nu \rangle$ (meV)
^{82}Se	1.6×10^{26}	53 - 123	10^{26}	67 - 154
^{150}Nd	8×10^{25}	26 - 114	6×10^{25}	30 - 132

Table A.1: Sensibilidad de SuperNEMO al proceso $\beta\beta^{0\nu}$, para 500 kg · year y 7% FWHM a 1 MeV de resolución energética. La primera columna muestra la fuente considerada; la segunda, la sensibilidad a $T_{1/2}^{0\nu}$ y $\langle m_\nu \rangle$ en ausencia de impurezas en las fuentes; finalmente, la tercera columna muestra la sensibilidad a $T_{1/2}^{0\nu}$ y $\langle m_\nu \rangle$ asumiendo impurezas correspondientes a 10 $\mu\text{Bq}/\text{kg}$ de ^{214}Bi y 2 $\mu\text{Bq}/\text{kg}$ de ^{208}Tl para ^{82}Se , y 2 $\mu\text{Bq}/\text{kg}$ de ^{208}Tl para ^{150}Nd . El rango de valores en $\langle m_\nu \rangle$ corresponde a las estimaciones de los elementos de matriz nuclear en [52, 101, 104, 105, 106]. Resultados para 90% C.L.

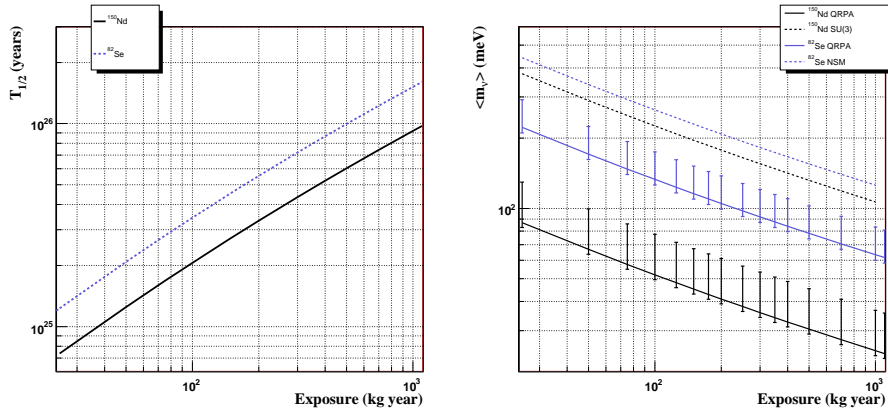


Figure A.6: Sensibilidad de SuperNEMO al proceso $\beta\beta^{0\nu}$ (90% C.L.) con fuentes de ^{82}Se y ^{150}Nd , asumiendo las siguientes condiciones experimentales: 7% FWHM a 1 MeV de resolución energética y contaminación en las fuentes de $10 \mu\text{Bq}/\text{kg}$ de ^{214}Bi y $2 \mu\text{Bq}/\text{kg}$ de ^{208}Tl . Izquierda: sensibilidad a $T_{1/2}^{0\nu}$ en función de la exposición. Derecha: sensibilidad a $\langle m_\nu \rangle$ en función de la exposición y para varias estimaciones de los elementos de matriz nuclear (modelos en [52, 101, 106]).

como una atractiva posibilidad para este laboratorio, pero su caso de física debe ser estudiado de una manera realista antes de tomar decisiones que comprometan el espacio disponible. En la sección anterior, se han expuesto resultados para unas determinadas condiciones, sin entrar a analizar si estas condiciones son o no factibles experimentalmente. En particular, se asume que el nivel de gas Radon dentro del detector es despreciable; sin embargo, en NEMO-3 el ^{222}Rn es la fuente dominante de ruido ya que su cadena de desintegración lleva al ^{214}Bi actuando pues como una contaminación adicional.

Atendiendo a la situación real del experimento NEMO-3, hemos definido tres posibles escenarios para SuperNEMO, en relación a la contaminación de la fuentes, la resolución energética, y el nivel de ^{222}Rn dentro del detector. Los citados escenarios se califican como *demostrado* (asume las condiciones experimentales alcanzadas en NEMO-3), *realista* (se consideran mejoras limitadas con respecto a NEMO-3) y *optimista* (objetivos de SuperNEMO para la fase de R&D, que aún no han sido alcanzados y que suponen una gran mejora con respecto a NEMO-3), y se resumen en la tabla A.2. Es importante destacar que no consideramos como alternativa real el uso de ^{150}Nd , ya que la posibilidad de su producción es más que dudosa. La figura A.7 muestra la sensibilidad alcanzada por los diferentes escenarios definidos en la tabla A.2, en función de la exposición y de la resolución energética.

Escenario	Cal. Res. FWHM a 1 MeV	^{214}Bi ($\mu\text{Bq}/\text{kg}$)	^{208}Tl ($\mu\text{Bq}/\text{kg}$)	^{222}Rn (mBq/m^3)
Demostrado	14%	1200	300	5
Realista	9%	120	30	1
Optimista	7%	10	2	0.5

Table A.2: Parámetros experimentales para tres posibles escenarios del experimento SuperNEMO. El escenario *demostrado* asume los parámetros del experimento NEMO-3, mientras que el llamado *optimista* asume los objetivos que SuperNEMO espera alcanzar en la fase de R&D, pero que aún no han sido alcanzados y que suponen una gran mejora con respecto a NEMO-3. La resolución calorimétrica se da en FWHM a 1 MeV.

Por otra parte, también hay que tener en cuenta el espacio disponible en el LSC. Los módulos estándar de SuperNEMO que han sido descritos en este trabajo tienen un gran tamaño, y sólo cabrían unos 6 de los 20 proyectados.

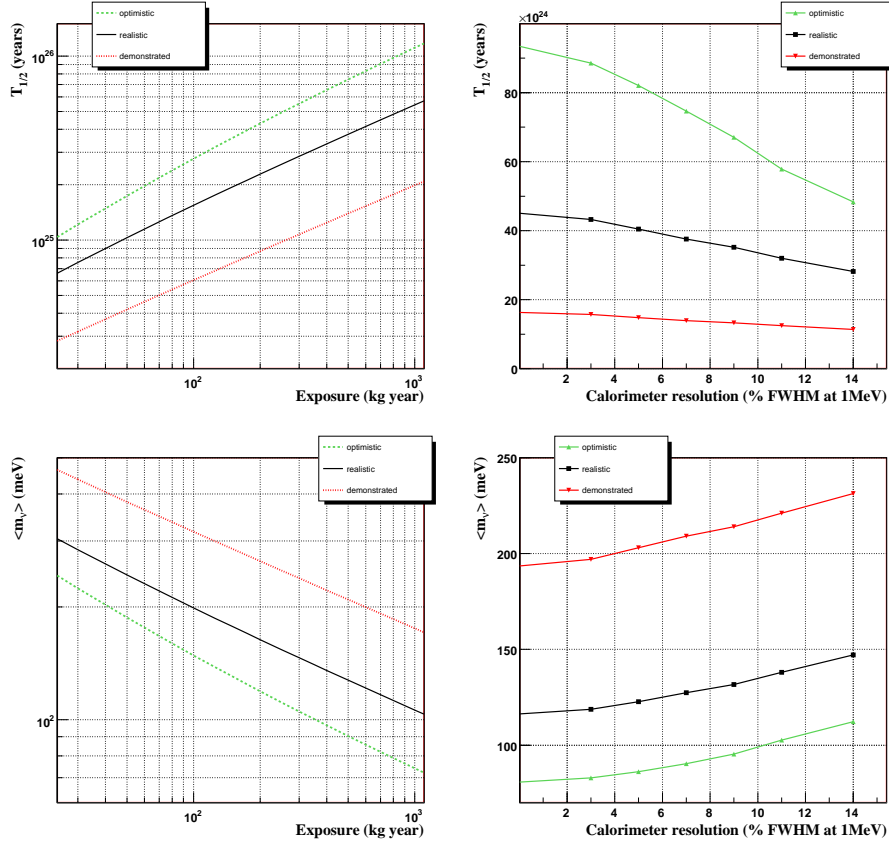


Figure A.7: Sensibilidad al proceso $\beta\beta^{0\nu}$ al 90% C.L., para los tres escenarios definidos en A.2, asumiendo fuentes de ^{82}Se . Arriba izquierda: sensibilidad a $T_{1/2}^{0\nu}$ en función de la exposición. Arriba derecha: sensibilidad a $T_{1/2}^{0\nu}$ en función de la resolución energética, para una exposición fija de 500 kg·year. Abajo izquierda: sensibilidad a $\langle m_\nu \rangle$ en función de la exposición. Abajo derecha: sensibilidad a $\langle m_\nu \rangle$ en función de la resolución energética, para una exposición fija de 500 kg·year.

Esto supone que la masa total de isótopo sería de 30 kg. Asumiendo un tiempo razonable de 5 años para la toma de datos, se tendría una exposición total de $150 \text{ kg} \cdot \text{year}$. La figura A.8 muestra una simulación de los espectros energéticos esperados en el experimento SuperNEMO bajo estas condiciones, asumiendo el escenario realista definido en la tabla A.2. Por otro lado, la tabla A.3 muestra las sensibilidades alcanzadas para los diferentes escenarios descritos en la tabla A.2 y para una exposición de $150 \text{ kg} \cdot \text{year}$.

Escenario	$T_{1/2}^{0\nu}$ (y)	$\langle m_\nu \rangle$ range (meV)	$\langle m_\nu \rangle$ (QRPA) (meV)
Demostrado	0.62×10^{25}	271-624	314
Realista	0.18×10^{26}	158-365	184
Optimista	0.36×10^{26}	112-258	130

Table A.3: Sensibilidad de SuperNEMO para los tres escenarios definidos en la tabla A.2. El rango de valores en $\langle m_\nu \rangle$ corresponde a las estimaciones de los elementos de matriz nuclear en [52, 101, 104, 105, 106]. Resultados al 90% C.L. y para $150 \text{ kg} \cdot \text{year}$.

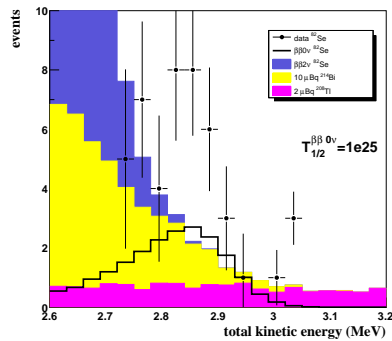


Figure A.8: Espectros energéticos esperados tras 5 años de toma de datos con 6 módulos de SuperNEMO, asumiendo el escenario realista definido en la tabla A.2. La señal $\beta\beta^{0\nu}$ asume una vida media de $T_{1/2}^{0\nu} = 10^{25}$ años.

A.7 Recapitulación y conclusiones

En la presente tesis se ha descrito la situación actual de la física experimental de neutrinos, dividida en dos frentes claramente distintos, aunque conectados. Por una parte, la física de oscilaciones que hoy en día ha demostrado que los neutrinos son partículas masivas. Por otra parte, los experimentos de búsqueda de la desintegración doble beta sin emisión de neutrinos, que tienen el principal objetivo de averiguar si los neutrinos son de tipo Majorana y proporcionar en combinación con los resultados de otros experimentos, un valor para la masa absoluta de estas partículas.

En particular, esta tesis describe el experimento K2K y la contribución a su análisis de oscilaciones por parte del experimento HARP. Los datos de éste último han sido utilizados para la predicción de los flujos de neutrinos en K2K, y ha permitido demostrar la existencia de oscilaciones con una significación estadística de 4.2σ . De igual manera, HARP ha permitido a K2K medir los correspondientes parámetros de oscilación con mejor precisión.

Por otro lado, este trabajo de investigación también ha analizado el caso de física del proyecto para la búsqueda del proceso $\beta\beta^{0\nu}$ llamado SuperNEMO. Se ha estudiado la sensibilidad de SuperNEMO a la citada desintegración en función de varios parámetros experimentales. De esta manera, se han fijado límites en los niveles de contaminación de las fuentes de ^{82}Se y ^{150}Nd . De acuerdo con estos niveles y con una resolución energética de 7% FWHM a 1 MeV, se ha estimado la sensibilidad de SuperNEMO a la semi-vida $T_{1/2}^{0\nu}$: $T_{1/2}^{0\nu} = 1 \times 10^{26}$ años para ^{82}Se ($\langle m_\nu \rangle_{QRPA} = 78$ meV) y $T_{1/2}^{0\nu} = 6 \times 10^{25}$ años ($\langle m_\nu \rangle_{QRPA} = 30$ meV) para ^{150}Nd . Finalmente, se ha estudiado la factibilidad de los objetivos experimentales de SuperNEMO, que deben ser alcanzados en la fase de R&D, y el potencial de este experimento operando en el LSC. Se concluyen con este análisis los siguientes puntos principales: 1) el limitado número de módulos que podrían ser instalados en el LSC hace que la sensibilidad de SuperNEMO esté limitada, 2) el caso de física de SuperNEMO depende fuertemente de la supresión en los niveles de ruido que se alcance. La sensibilidad de SuperNEMO operando en el LSC al proceso $\beta\beta^{0\nu}$ estaría entre $0.62 - 3.6 \times 10^{25}$ años ($\langle m_\nu \rangle_{QRPA} = 130 - 314$ meV).

Bibliography

- [1] F. Reines and C. L. Cowan, Phys. Rev. **113** (1959) 273.
- [2] B. Pontecorvo, Sov. Phys. JETP **26** (1968) 984 [Zh. Eksp. Teor. Fiz. **53** (1967) 1717].
- [3] V. N. Gribov and B. Pontecorvo, Phys. Lett. B **28** (1969) 493.
- [4] H. V. Klapdor-Kleingrothaus, A. Dietz, I. V. Krivosheina, Found. Phys. **32** (2002) 1181 [Erratum-ibid. **33** (2003) 679].
- [5] M. C. Gonzalez-Garcia and M. Maltoni, arXiv:0704.1800 [hep-ph].
- [6] F. Boehm and P. Vogel, *Physics of Massive Neutrinos*, Cambridge University Press (1992).
- [7] W. M. Yao *et al.* [PDG], J. Phys. G **33** (2006) 1.
- [8] P. Minkowski, Phys. Lett. B **67** (1977) 421.
- [9] P. Vogel, [arXiv:hep-ph/0611243v1].
- [10] S. R. Elliott and P. Vogel, Ann. Rev. Nucl. Part. Sci. **52** (2002) 115 [arXiv:hep-ph/0202264].
- [11] M. Doi, T. Kotani and E. Takasugi, Prog. Theor. Phys. Suppl. **83** (1985) 1.
- [12] J. Schechter and J. W. F. Valle, Phys. Rev. D **25** (1982) 2951.
- [13] J. Martin-Albo, Master Thesis, IFIC-UVEG, September 2007
- [14] J. N. Bahcall, N. A. Bahcall and G. Shaviv, Phys. Rev. Lett. **20** (1968) 1209.
- [15] J. N. Bahcall and R. Davis, Science **191** (1976) 264.
- [16] J. N. Bahcall, A. M. Serenelli and S. Basu, Astrophys. J. **621** (2005) L85 [arXiv:astro-ph/0412440].
- [17] R. J. Davis, D. S. Harmer and K. C. Hoffman, Phys. Rev. Lett. **20** (1968) 1205.
- [18] B. T. Cleveland *et al.*, Astrophys. J. **496** (1998) 505.
- [19] J. N. Abdurashitov *et al.* [SAGE Collaboration], J. Exp. Theor. Phys. **95** (2002) 181 [Zh. Eksp. Teor. Fiz. **122** (2002) 211] [arXiv:astro-ph/0204245].

- [20] W. Hampel *et al.* [GALLEX Collaboration], *Phys. Lett. B* **447** (1999) 127.
- [21] M. Altmann *et al.* [GNO Collaboration], *Phys. Lett. B* **616** (2005) 174 [arXiv:hep-ex/0504037].
- [22] M. B. Smy *et al.* [Super-Kamiokande Collaboration], *Phys. Rev. D* **69** (2004) 011104 [arXiv:hep-ex/0309011].
- [23] Y. Fukuda *et al.* [Kamiokande Collaboration], *Phys. Rev. Lett.* **77** (1996) 1683.
- [24] Q. R. Ahmad *et al.* [SNO Collaboration], *Phys. Rev. Lett.* **87** (2001) 071301 [arXiv:nucl-ex/0106015].
- [25] Q. R. Ahmad *et al.* [SNO Collaboration], *Phys. Rev. Lett.* **89**, 011301 (2002) [arXiv:nucl-ex/0204008].
- [26] Q. R. Ahmad *et al.* [SNO Collaboration], *Phys. Rev. Lett.* **89**, 011302 (2002) [arXiv:nucl-ex/0204009].
- [27] Y. Ashie *et al.* [Super-Kamiokande Collaboration], *Phys. Rev. Lett.* **93** (2004) 101801 [arXiv:hep-ex/0404034].
- [28] Y. Ashie *et al.* [Super-Kamiokande Collaboration], *Phys. Rev. D* **71** (2005) 112005 [arXiv:hep-ex/0501064].
- [29] M. C. Sanchez *et al.* [Soudan 2 Collaboration], *Phys. Rev. D* **68** (2003) 113004 [arXiv:hep-ex/0307069].
- [30] M. Ambrosio *et al.* [MACRO Collaboration], *Phys. Lett. B* **517** (2001) 59 [arXiv:hep-ex/0106049].
- [31] M. Apollonio *et al.* [CHOOZ Collaboration], *Phys. Lett. B* **466** (1999) 415 [arXiv:hep-ex/9907037].
- [32] K. Eguchi *et al.* [KamLAND Collaboration], *Phys. Rev. Lett.* **90** (2003) 021802 [arXiv:hep-ex/0212021].
- [33] G. Zacek *et al.* [CALTECH-SIN-TUM Collaboration], *Phys. Rev. D* **34** (1986) 2621.
- [34] G. S. Vidyakin *et al.*, *JETP Lett.* **59** (1994) 390 [*Pisma Zh. Eksp. Teor. Fiz.* **59** (1994) 364].
- [35] Y. Declais *et al.*, *Nucl. Phys. B* **434** (1995) 503.
- [36] A. Piepke [Palo Verde Collaboration], *Prog. Part. Nucl. Phys.* **48** (2002) 113.
- [37] I. Shimizu [KamLAND Collaboration], talk given at the TAUP 2007 conference, Sendai, Japan, September 2007.
- [38] E. Aliu *et al.*, *Phys. Rev. D* **74**, 072003 (2006)
- [39] E. Ables *et al.* [MINOS Collaboration], FERMILAB-PROPOSAL-P-875 (1995).
- [40] D. G. Michael *et al.* [MINOS Collaboration], *Phys. Rev. Lett.* **97** (2006) 191801 [arXiv:hep-ex/0607088].

- [41] A. Aguilar *et al.* [LSND Collaboration], Phys. Rev. D **64** (2001) 112007 [arXiv:hep-ex/0104049].
- [42] B. Armbruster *et al.* [KARMEN Collaboration], Phys. Rev. D **65** (2002) 112001 [arXiv:hep-ex/0203021].
- [43] A. A. Aguilar-Arevalo *et al.* [MiniBooNE Collaboration], Phys. Rev. Lett. **98** (2007) 231801 [arXiv:0704.1500 [hep-ex]].
- [44] J. Bonn *et al.*, Nucl. Phys. Proc. Suppl. **91** (2001) 273.
- [45] V. M. Lobashev *et al.*, Nucl. Phys. Proc. Suppl. **91** (2001) 280.
- [46] S. Cole *et al.* [2dFGRS Collaboration], Mon. Not. Roy. Astron. Soc. **362** (2005) 505 [arXiv:astro-ph/0501174].
- [47] M. Tegmark *et al.* [SDSS Collaboration], Phys. Rev. D **69** (2004) 103501 [arXiv:astro-ph/0310723].
- [48] D. N. Spergel *et al.* [WMAP Collaboration], arXiv:astro-ph/0603449.
- [49] R. A. C. Croft *et al.*, Astrophys. J. **581** (2002) 20 [arXiv:astro-ph/0012324].
- [50] N. Y. Gnedin and A. J. S. Hamilton, Mon. Not. Roy. Astron. Soc. **334** (2002) 107 [arXiv:astro-ph/0111194].
- [51] F. Vissani, JHEP **9906** (1999) 022 [arXiv:hep-ph/9906525].
- [52] V.A. Rodin *et al.*, Nucl. Phys. A **766**, 107-131 (2006)
- [53] H. V. Klapdor-Kleingrothaus *et al.*, Eur. Phys. J. A **12** (2001) 147
- [54] C. E. Aalseth *et al.*, Mod. Phys. Lett. A **17** (2002) 1475. Yu. G. Zdesenko, Rev. Mod. Phys. **74** (2002) 663.
- [55] F. Feruglio, A. Strumia and F. Vissani, Nucl. Phys. B **637** (2002) 345 [arXiv:hep-ph/0201291].
- [56] Y. Itow *et al.*, arXiv:hep-ex/0106019.
- [57] F. Ardellier *et al.* [Double Chooz Collaboration], arXiv:hep-ex/0606025.
- [58] P. Zucchelli, Phys. Lett. B **532** (2002) 166.
- [59] S. Geer, Phys. Rev. D **57** (1998) 6989 [Erratum-ibid. D **59** (1999) 039903] [arXiv:hep-ph/9712290].
- [60] A. G. Cocco [OPERA Collaboration], Nucl. Phys. Proc. Suppl. **85** (2000) 125.
- [61] M.G. catanesi *et al.*, Nucl. Phys. B **732**, 1-45 (2006)
- [62] R. Brun, F. Bruyant, M. Maire, A.C. McPherson, P. Zanarini (CERN) . CERN- DD/EE/84-1, Sep 1987.
- [63] J. R. Sanford and C. L. Wang, Brookhaven National Laboratory, AGS internal report, 1967 (unpublished); C. L. Wang, Phys. Rev. Letters 25, 1068 (1970); ibid. 25, 1536(E) (1970).

- [64] Y. Cho *et al.*, *Phys. Rev. D* **4**, 1967 (1971).
- [65] A Monte Carlo Program Package for the Design and Analysis of Calorimeter Systems. T.A. Gabriel, J.D. Amburgey, B.L. Bishop (Oak Ridge) . ORNL/TM-5619, Apr 1977.
- [66] A. Fasso, A. Ferrari, J. Ranft and P. R. Sala, *Given at 4th International Conference on Calorimetry in High-energy Physics, La Biodola, Italy, 19-25 Sep 1993.*
- [67] S. Buontempo *et al.*, *Nucl. Instrum. Meth. A* **349**, 70 (1994).
- [68] E. Aliu *et al.*, *Phys. Rev. Lett.* **94**, 081802 (2005)
- [69] M.G. Catanesi *et al.*, HARP Collaboration, CERN-SPSC/99-35, 15 November 1999.
- [70] L. Durieu *et al.*, CERN/PS 2001-037;
- [71] HARP collaboration, *Nucl. Instrum. Methods A* **571**, 527-561 (2007)
- [72] A. Cervera, J.J. Gomez-Cadenas and J.A. Hernando, *Nucl. Instrum. Methods A* **534**, 180 (2004).
- [73] P. Billoir, *Nucl. Instrum. Methods A* **225**, 352 (1984)
- [74] M.G. catanesi *et al.*, *Nucl. Instrum. Methods A* **572**, 899-921 (2007)
- [75] Y. Sugaya *et al.*, *Nucl. Phys. A* **634**, 115 (1998).
- [76] I. A. Vorontsov *et al.*, ITEP-11-1988.
- [77] I. A. Vorontsov *et al.*, ITEP-85-1983.
- [78] T. Abbott *et al.*, E-802 Collaboration, *Phys. Rev. D* **45**, 3906 (1992).
- [79] D. S. Barton *et al.*, *Phys. Rev. D* **27**, 2580 (1983).
- [80] T. Inagaki, Ph.D. Thesis, Kyoto University (2001), available from http://www-he.scphys.kyoto-u.ac.jp/theses/doctor/inagaki_dt.ps.gz
- [81] Y. P. Gorin, S. P. Denisov, S. V. Donskov, R. N. Krasnokutskii, A. I. Petrukhin, Y. D. Prokoshkin and D. A. Stoyanova, *Yad. Fiz.* **18**, 336 (1973).
- [82] I. A. Vorontsov, G. A. Safronov, A. A. Sibirtsev, G. N. Smirnov and Y. V. Trebukhovsky, “A-Dependence Of Fragmentation Of 9.2-Gev Protons On Nuclei. (In Russian),” <http://www.slac.stanford.edu/spires/find/hep/www?irn=191563> (1988)
- [83] Aleshin, <http://www-spires.dur.ac.uk/cgi-bin/hepdata/testreac/2884/FULL/query> (1977)
- [84] V. V. Gachurin *et al.*, ITEP-59-1985 <http://www.slac.stanford.edu/spires/find/hep/www?r=itep-59-1985> (1985)
- [85] Lykhacev, <http://www-spires.dur.ac.uk/cgi-bin/hepdata/testreac/4163/FULL/query> (1981)

- [86] A. Ferrari and P. R. Sala, “*GEANT Hadronic Event Generators: a comparison at the single interaction level*” (1996), available from <http://www.fluka.org/references/papers/geant.ps.gz>
- [87] Kohama, Masters Thesis (1998), available from <http://neutrino.kek.jp/internal/k2knote/BEAM/HORN/98-001/kohama-mt.ps.gz>
- [88] I. Kato, private communication.
- [89] T. Maruyama, Ph.D. Thesis, Tohoku University (2000), available from <http://neutrino.kek.jp/publications/theses/maruyama-dt.ps.gz>
- [90] Aalseth CE *et al.*, Phys. Rev. C **59**: 2108 (1999)
- [91] Ejiri H *et al.*, Phys. Rev. C **63** (2001)
- [92] D. Dassie *et al.*, Nucl. Instr. and Meth. A **309** (1991) 465-475
- [93] R. Arnold *et al.*, Nucl. Instr. Meth. A **354** (1995) 338
- [94] V. Vasilev *et al.* [NEMO Collaboration], Part. Nucl. Lett. **108** (2001) 68.
- [95] R. Arnold *et al.* [NEMO Collaboration], *Nucl. Instrum. Methods A* **536** , (2005)
- [96] R. Arnold *et al.* [NEMO Collaboration], Phys. Rev. Lett. **95**, 182-302 (2005) [arXiv:hep-ex/0507083].
- [97] J. Muñoz-Vidal *et al.*, SuperNEMO internal note (2006)
- [98] V. Vasiliev, SuperNEMO internal note (2006); <http://evalu29.ific.uv.es/SuperNemoSW/docs/gg.ps>
- [99] F. Nova, SuperNEMO internal note (2006)
- [100] J. Suhonen, O. Civitarese, Phys. Rep. **300** (1998) 123.
- [101] E. Caurier, G. Martinez-Pinedo, F. Nowacki, A. Poves and A. P. Zuker, Rev. Mod. Phys. **77** (2005) 427 [arXiv:nucl-th/0402046].
- [102] V. Vasiliev, Analysis of 2β signal from ^{100}Mo and ^{82}Se for Phase I and Phase II NEMO 3 data; NEMO 3 internal note, March 2006.
- [103] N. Fatehmi-Ghomi, “Double beta decay of ^{150}Nd in the NEMO 3 detector”, NEMO 3 internal note, 2007. Available from http://www.hep.man.ac.uk/u/nasim/paper/note_v4.ps
- [104] M. Kortelainen, J. Suhonen Phys. Rev. C **75** (2007)
- [105] A. Poves, talk at “Physics of Massive neutrinos”, Blaubeuren, 2007
- [106] H.G. Hirsch, O. Castanos, P.O. Hess, Nucl. Phys A**582** (1995)
- [107] R. Barlow, *Nucl. Instrum. Methods A* **297**, 496 (1990)
- [108] R. Arnold *et al.*, [NEMO Collaboration], Paper in preparation.
- [109] Laboratorio Subterraneo de Canfranc, <http://www.unizar.es/lfnae/>